Stimulated Resonant Inelastic X-ray Scattering in Transition Metal Systems

Doktorarbeit

zur Erlangung des akademischen Grades

Dr. rer. nat. *doctor rerum naturalium*

Erstgutachter:

Prof. Alexander Föhlisch

Zweitgutachter:

Prof. Birgit Kanngiesser

Mentor:

Prof. Markus Gühr

Eingereicht von

Markus Hantschmann

March 27, 2022

Eidesstattliche Erklärung

Hiermit erkläre ich, dass ich die vorliegende Arbeit selbstständig und eigenhändig sowie ohne unerlaubte fremde Hilfe und ausschließlich unter Verwendung der aufgeführten Quellen und Hilfsmittel angefertigt habe.

Die selbstständige und eigenständige Anfertigung versichert an Eides statt:

Berlin, den March 27, 2022

To the love of my live.

This journey was only possible thanks to your
encouragement, persistence, support, and energy!

Abstract

With the implementation of intense, short pulsed light sources throughout the last years, the powerful technique of resonant inelastic X-ray scattering (RIXS) became feasible for a wide range of experiments within femtosecond dynamics in correlated materials and molecules. In this thesis I investigate the potential to bring RIXS into the fluence regime of nonlinear X-ray-matter interactions, especially focusing on the impact of stimulated scattering on RIXS in transition metal systems in a transmission spectroscopy geometry around transition metal L-edges. After presenting the RIXS toolbox and the capabilities of free electron laser light sources for ultrafast intense X-ray experiments, the thesis explores an experiment designed to understand the impact of stimulated scattering on diffraction and direct beam transmission spectroscopy on a CoPd multilayer system. The experiments require short X-ray pulses that can only be generated at free electron lasers (FEL). Here the pulses are not only short, but also very intense, which opens the door to nonlinear X-ray-matter interactions. In the second part of this thesis, we investigate observations in the nonlinear interaction regime, look at potential difficulties for classic spectroscopy and investigate possibilities to enhance the RIXS through stimulated scattering. Here, a study on stimulated RIXS is presented, where we investigate the light field intensity dependent CoPd demagnetization in transmission as well as scattering geometry. Thereby we show the first direct observation of stimulated RIXS as well as light field induced nonlinear effects, namely the breakdown of scattering intensity and the increase in sample transmittance. The topic is of ongoing interest and will just increase in relevance as more free electron lasers are planned and the number of experiments at such light sources will continue to increase in the near future. Finally we present a discussion on the accessibility of small DOS shifts in the absorption-band of transition metal complexes through stimulated resonant X-ray scattering. As these shifts occur for example in surface states this finding could expand the experimental selectivity of NEXAFS and RIXS to the detectability of surface states. We show how stimulation can indeed enhance the visibility of DOS shifts through the detection of stimulated spectral shifts and enhancements in this theoretical study. We also forecast the observation of stimulated enhancements in resonant excitation experiments at FEL sources in systems with a high density of states just below the Fermi edge and in systems with an occupied to unoccupied DOS ratio in the valence band above 1.

Deutsche Zusammenfassung

In dieser Arbeit wird die Weiterentwicklung der Technik 'Resonante Inelastische Röntgenstreuung' (RIXS) thematisiert. Vor allem wird das Thema der nichtlinearen Röntgen-Materie-Wechselwirkung an Freien Elektronenlasern wird ausführlich diskutiert. Mit der Etablierung von intensiven kurzpulsigen Röntgenquellen auf Basis von freien Elektronenlasern, ist die Möglichkeit entstanden, zeitaufgelöste Experimente im Femtosekundenbereich mit Röntgenstrahlung durchzuführen. Die dort erzeugten Pulse sind so intensiv und kurz, dass neue Effekte, die analogien in der nichtlinearen Optik haben, auftreten können. Diese neu auftretenden Effekte sind für die Röntgengemeinschaft vollkommen neu und müssen verstanden werden um freie Elektronenlaser sinnvoll auf größerer Skala, sinnvoll nutzen zu können. Außerdem könnten diese Effekte auch ganz neue experimentelle Möglichkeiten eröffnen. Deswegen beschäftigt sich diese Arbeit vor allem mit der potentiellen Möglichkeit, die RIXS Technik im nicht-linearen Licht-Materie Wechselwirkungsbereich zu bringen, die geänderten Interaktionen zu verstehen und vielleicht sogar nutzbar zu machen.

Zu Beginn werden die Möglichkeiten der RIXS Technik vorgestellt. Im Anschluss wird ein von uns in Kollaboration mit dem SLAC entwickeltes und durchgeführtes Experiment vorgestellt, welches unter anderem die erste direkte Beobachtung von stimulierter resonanter inelastischer Röntgenbeugung an dünnen CoPd Multischichtsystemen ermöglicht hat. Außerdem sind intensitätsabhängige Veränderungen der Licht-Materie Wechselwirkung beobachtet worden. Speziell konten wir einen klaren Zusammenhang zwischen dem Zusammenbruch von Streuintensität (entspricht etwa der Intensität, die nicht in direkter Strahlrichtung abgestrahlt wird) und der Vergrößerung der Transmittivität (Intensität, die in Strahlrichtung durch die Probe propagiert) feststellen. Dies konnte mit der Verschiebung von Auger und Streueffekten zu stimulierten Effekten verknüpft werden.

Um das Experiment besser zu verstehen wunrde ein Ratengleichungsmodell entwickelt, das intensitätsabhängige Wirkungsquerschnitte inkludiert und damit intensitätsabhängige Puls-induzierte Effekte abschätzen kann. Es konnte gezeigt werden wie die Intensitätsabhängikeit von Puls-Induzierter Transparenz, Puls-induziertem zusammenbruch der Röntgenstreuung, und die Verstärkung von Teilen des Pulses mit stimulierten Emissionen verknüpft sind. Außerdem konnten einige Aspekte identifiziert werden, die dabei helfen können um neue Exper-

imente zu designen, die in der lage wären durch das Ausnutzen von stimulierter Emission und damit verbundenen Spektralen verschiebungen zusätzliche Informationen aus den zu untersuchenden Systemen zu gewinnen, wie zum Beispiel über die elektronische Zustandsdichte in einer Oberflächen- oder Interface-Schicht.

Preface

Before I begin to present the work of my PhD, I would like to start with a personal note. It was a great opportunity and a lifelong lasting experience for me to work in this international scientific environment. There were so many challenges along the way that I really got the chance to grow in different fields and learned how to adapt ones mindset to changing situations. Thanks for the opportunity to do my PhD and to work in science, especially in a field of science that is unique in various aspects! Not only to push the knowledge of humanity towards new boundaries, but also in being able to collaborate throughout the globe and creating interdisciplinary communities that work jointly on bigger goals than only their own topics. I can not imagine to be able to learn more than in a field, where physicists work with engineers, chemists, biologists, from life science and engineering questions to deep scientific questions and theories. Also this field is honored with the first Arabian Nobel prize holder which shows, that science is a powerful tool to overcome cultural boundaries and bring together the clever minds of the whole world. It was an honor to be given the opportunity to perform my PhD work in a group with so many different characters and so many collaborators. I got the opportunity to work in five countries with people from about 15 countries which can not be highlighted enough.

Science is more than just pushing the limits of our knowledge. It is the creation of goals for humanity that enable us to forget about quarrels and overcome frontiers to work together, and I am proud to have been a part of that.

In this Thesis I present the main project I worked on during my PhD time. There was a variety of other projects and Ideas, but for this Thesis I tried to concentrate on the project to detect and understand stimulated scattering in transition metal systems through the example of a CoPd multilayer system. I also worked on chemical reaction dynamics in transition metal complexes, and the Aluminum phase transition from metal to the liquid phase, with the latter frankly not succeeding as a lot of projects at free electron lasers do. We are still one of the first groups that push this frontier of experimental capabilities at free electron lasers and it takes a lot of time to understand even a single experiment. Another topic I worked on for quite some time was magnetic switching with plasmonic antennas. I was also involved in a project investigating CO to CO2 dissociation on Ru surfaces, which is a process in heterogeneous catalysis. However, most of the projects were glimpses into different directions within

the field of time resolved X-ray science such as for example the experiment to investigate the different electron transfers in ferri- and ferro-cyanide. The majority of my time in the first years went into this project. The publications from this and other projects can be found in the attachments. In those, I participated in the experiments, the planing and preparation stages and partially in the understanding and discussions of the results.

The projects presented within this thesis are selected because they run like a golden thread towards the understanding of stimulated RIXS for free electron laser experiments.

This thesis is a mere step towards the understanding nonlinear X-ray matter interactions within the soft X-ray regime. As always in science, we did not finish the project completely, but me, my collaborators and supervisors gained knowledge along the way which will help the next generation of experiments run smoother than the last.

Thank you all for the ride, the fun, and experience along the way.

So long and thanks for all the fish!

Contents

Chapter 1

Summary of Papers

Paper A

Stimulated resonant inelastic X-Ray scattering in a solid

D. Higley*, M. Hantschmann* et al. March 2022, Communications Physics, COMMSPHYS-21-0537-T

When materials are exposed to X-ray pulses with sufficiently high intensity various nonlinear effects can occur. Among the most fundamental of these is stimulated inelastic X-ray scattering, where inelastic scattering of one X-ray photon is stimulated by another X-ray photon with a different energy. Here, we report observations of stimulated Resonant Inelastic X-ray Scattering (RIXS) near the Co L_3 edge in solid Co/Pd multilayer samples. The stimulated RIXS is observed through the X-ray fluence and photon energy dependence of the transmission of high intensity X-ray pulses through the samples. With 1330 mJ/cm^2, 5 fs duration X-ray pulses the number of stimulated RIXS photons we detect per X-ray photon incident on our samples is nearly a million times more than that which could be detected for spontaneous RIXS using standard grating-based X-ray spectrometers. These results pave the way for the development of nonlinear X-ray techniques that use stimulated RIXS in condensed matter.
My contribution: I participated in the planning, design and performance of the experiment. I wrote the model to simulate the spectral changes and understand the interplay of the auger and stimulated decay. I extracted the scattering data and wrote the algorithms to sort for successful data-points, and bin by different fluence and incident spectra data-sets. I also wrote the manuscript together with Dan Higley.

Paper B

A rate model approach for FEL pulse-induced transmissions changes, saturable absorption, X-ray transparency and stimulated emission

As the use of FEL sources increases, so do the findings mentioning nonlinear phenomena occurring at these experiments, such as saturable absorption, induced transparency and scattering breakdowns. These are well known among the laser community, but are still rarely understood and expected among the X-ray community and for now lack tools and theories to accurately predict the experimental parameters and results. We present a simple theoretical framework to access short X-ray pulse induced light matter interactions which occur at intense short X-ray pulses as available at free electron laser sources. This easy to access/repeat theoretical framework is build to access effects such as saturable absorption, induced transparency and scattering suppression, stimulated emission, and transmission spectra. This computationally efficient rate model based approach is implemented in a straightforward way and intuitively adaptable to most solid state sample systems with the potential to be extended for liquid and gas sample systems. The feasibility of the model to estimate the named effects is demonstrated using the example of transition metal systems such as CoPd multi-layers and metal systems such as Al films. We believe this work is an important contribution for the preparation, performance and understanding of FEL based high intensity and short pulse experiments.

My contribution: I developed the algorithm, conducted the simulations and wrote the manuscript.

Paper C

Ultrafast self-induced X-ray transparency and loss of magnetic diffraction

Using ultrafast 2.5 fs and 25 fs self-amplified spontaneous emission pulses of increasing intensity and a novel experimental scheme, we report the concurrent increase of stimulated emission in the forward direction and loss of out-of-beam diffraction contrast for a CoPd multilayer sample. The experimental results are quantitatively accounted for by a statistical description of the pulses in

conjunction with the optical Bloch equations. The dependence of the stimulated sample response on the incident intensity, coherence time, and energy jitter of the employed pulses reveals the importance of increased control of x-ray free electron laser radiation.

My contribution: I participated in the planning, design and execution of the experiment, performed the pre-analysis and wrote the algorithms to bin by fluence data-sets. I extracted one of the two successful data-sets and cleaned the data with GMD information. I also helped to write the manuscript with Zhao Chen.

Paper D

Disentangling transient charge density and metal-ligand covalency in photo-excited ferricyanide with femtosecond resonant inelastic soft X-ray scattering

R. Jay, J. Norell, S. Eckert, M. Hantschmann et al., JPCL 9 (12), pp. 3538 (2018)

Soft X-ray spectroscopies are ideal probes of the local valence electronic structure of photocatalytically active metal sites. Here, we apply the selectivity of time-resolved resonant inelastic X-ray scattering at the iron L-edge to the transient charge distribution of an optically excited charge-transfer state in aqueous ferricyanide. Through comparison to steady-state spectra and quantum chemical calculations, the coupled effects of valence-shell closing and ligand-hole creation are experimentally and theoretically disentangled and described in terms of orbital occupancy, metal–ligand covalency, and ligand field splitting, thereby extending established steady-state concepts to the excited-state domain. π-Back-donation is found to be mainly determined by the metal site occupation, whereas the ligand hole instead influences σ-donation.

My contribution: I participated in the planning, design and execution of the experiment. Performed the pre-analysis onsite, wrote the algorithms to sort and bin the datasets, and conducted the first full analysis. I also conducted the test experiments at BESSY II.

Paper E

Fingerprints of electronic, spin and structural dynamics from resonant inelastic soft X-ray scattering in transient photo-chemical species,

J. Norell, R. Jay, M. Hantschmann et al., PCCP 20, pp. 7243 (2018).

We describe how inversion symmetry separation of electronic state manifolds in resonant inelastic soft X-ray scattering (RIXS) can be applied to probe excited-state dynamics with compelling selectivity. In a case study of Fe L3-edge RIXS in the ferricyanide complex Fe(CN)6, we demonstrate with multi-configurational restricted active space spectrum simulations how the information content of RIXS spectral fingerprints can be used to unambiguously separate species of different electronic configurations, spin multiplicities, and structures, with possible involvement in the decay dynamics of photo-excited ligand-to-metal charge-transfer. Specifically, we propose that this could be applied to confirm or reject the presence of a hitherto elusive transient Quartet species. Thus, RIXS offers a particular possibility to settle a recent controversy regarding the decay pathway.

My contribution: I participated in the planning, design and execution of the experiment. Performed the pre-analysis onsite, wrote the algorithms to sort and bin the datasets, conducted the first full analysis and wrote the first manuscript. I also conducted the test experiments at BESSY II.

Paper F

Ultrafast independent N-H and N-C bond deformation investigated with resonant inelastic X-ray scattering

S. Eckert, . . . , M. Hantschmann et al., Angew. Chemie 56 (22), pp. 6088 (2017).

The femtosecond excited state dynamics following resonant photoexcitation enable the selective deformation of $N-H$ and $N-C$ chemical bonds in 2-thiopyridone in aqueous solution with optical or X-ray pulses. In combination with multiconfigurational quantum-chemical calculations, the orbital-specific electronic structure and its ultrafast dynamics accessed with resonant inelastic X-ray scattering at the N 1s level using synchrotron radiation and the soft X-ray free-electron laser LCLS provide direct evidence for this controlled photoinduced molecular deformation and its ultrashort timescale.

My contribution: I participated in the planning, design and execution of the

experiment. I conducted the test experiments at BESSY II and was involved in the discussions to understand the experimental results.

Paper G

Untersuchung unabhängiger N-H- und N-C-Bindungsverformungen auf ultrakurzen Zeitskalen mit resonanter inelastischer Röntgenstreuung,

S. Eckert, . . . , M.Hantschmann et al., Angewandte Chemie 129 (22), 6184-6188 (2017).

Die Femtosekundendynamik nach resonanten Photoanregungen mit optischen und Röntgenpulsen ermöglicht eine selektive Verformung von chemischen N-H- und N-C-Bindungen in 2-Thiopyridon in wässriger Lösung. Die Untersuchung der orbitalspezifischen elektronischen Struktur und ihrer Dynamik auf ultrakurzen Zeitskalen mit resonanter inelastischer Röntgenstreuung an der N1s-Resonanz am Synchrotron und dem Freie-Elektronen-Laser LCLS in Kombination mit quantenchemischen Multikonfigurationsberechnungen erbringen den direkten Nachweis dieser kontrollierten photoinduzierten Molekülverformungen und ihrer ultrakurzen Zeitskala.

My contribution: I participated in the planning, design and execution of the experiment. I also helped with the test experiments at BESSY II.

Paper H

Chemical bond activation observed with an X-ray laser,

M. Beye, . . . , M. Hantschmann et al., JPCL 7 (18), pp. 3647 (2016).

The concept of bonding and antibonding orbitals is fundamental in chemistry. The population of those orbitals and the energetic difference between the two reflect the strength of the bonding interaction. Weakening the bond is expected to reduce this energetic splitting, but the transient character of bond-activation has so far prohibited direct experimental access. Here we apply time-resolved soft X-ray spectroscopy at a free-electron laser to directly observe the decreased bonding-antibonding splitting following bond-activation using an ultrashort optical laser pulse.

My contribution: I participated in the planning, design and execution of the experiment, and helped with the test experiments at BESSY II.

Paper I

Stimulated resonant X-Ray emission in solids,

Z. Chen, D. Highley, M. Hantschmann et al., APS Meeting (2016).

http://meetings.aps.org/link/BAPS.2016.MAR.C46.4

We present direct evidence of resonant stimulated X-Ray emission in magnetically patterned CoPd multilayers. At a free electron laser, we measure X-Ray transmission through CoPd of ultrafast (2fs) X-Ray pulses at the Co L-3 edge for fluences of up to 2 J/cm 2/fs simultaneously in the transmission and scattering geometries. With increasing fluence, we observe a nonlinear decrease in first-order scattering intensity together with a compensating increase in transmitted forward intensity for all energies within the Co resonant absorption edge. At high enough fluences (> 1 J/cm^2/fs), the sample absorption spectrum and scattering intensity are both suppressed by over two orders of magnitude, leaving the sample effectively transparent to X-Rays. In our geometry, these two effects are indicative of elastic stimulated scattering, which favors forward transmission at the cost of scattered intensity in all other directions.

My contribution: I participated in the planning, design and execution of the experiment, performed the pre-analysis and wrote the algorithms to bin data-sets by fluence. I extracted one of the two successful data-sets and cleaned the data with GMD information. I also helped to write the manuscript with Zhao Chen.

Paper J

Nanoscale confinement of all-optical magnetic switching in TbFeCo-competition with nanoscale heterogeneity,

T. Liu, . . . , M. Hantschmann et al., Nano Lett. 15 (10), pp. 6862 (2015).

Single femtosecond optical laser pulses, of sufficient intensity, are demonstrated to reverse magnetization in a process known as all-optical switching. Gold two-wire antennas are placed on the all-optical switching film TbFeCo. These structures are resonant with the optical field, and they create a field enhancement in the near-field which confines the area where optical switching can occur. The magnetic switching that occurs around and below the antenna is imaged using resonant X-ray holography and magnetic circular dichroism. The results not only show the feasibility of controllable switching with antenna as-

sistance but also demonstrate the highly inhomogeneous nature of the switching process, which is attributed to the process depending on the material's heterogeneity.

My contribution: I participated in the planning and execution of the experiment at SSRL, helped to fabricate the nano-structured gold antennas and holographic masks, and helped with the data analysis.

Paper K

Probing the transition state region in catalytic CO oxidation on Ru,

H. Öström, ..., M. Hantschmann et al., Science 347 (6225), pp. 978 (2015).

Femtosecond x-ray laser pulses are used to probe the carbon monoxide (CO) oxidation reaction on ruthenium (Ru) initiated by an optical laser pulse. On a time scale of a few hundred femtoseconds, the optical laser pulse excites motions of CO and oxygen (O) on the surface, allowing the reactants to collide, and, with a transient close to a picosecond (ps), new electronic states appear in the O K-edge x-ray absorption spectrum. Density functional theory calculations indicate that these result from changes in the adsorption site and bond formation between CO and O with a distribution of OC–O bond lengths close to the transition state (TS). After 1 ps, 10% of the CO populate the TS region, which is consistent with predictions based on a quantum oscillator model.

My contribution: I helped with the preparation and execution of the experiment, as well as the test experiments at BESSY II.

Paper L

Principles of femtosecond X-ray/optical cross-correlation with X-ray induced transient optical reflectivity in solids,

S. Eckert, ..., M. Hantschmann et al., APL 106 (6), pp. 061104 (2015).

The discovery of ultrafast X-ray induced optical reflectivity changes enabled the development of X-ray/optical cross correlation techniques at X-ray free electron lasers worldwide. We have now linked through experiment and theory the fundamental excitation and relaxation steps with the transient optical properties in finite solid samples. Therefore, we gain a thorough interpretation and an optimized detection scheme of X-ray induced changes to the refractive index and the X-ray/optical cross correlation response.

My contribution: I helped with the execution of the experiment and was involved in the result discussions.

Paper M

Following Metal-to-Ligand Charge-Transfer Dynamics with Ligand andd Spin Specificity Using Femtosecond Resonant Inelastic X-ray Scattering at the Nitrogen K-Edge,

R.M.Jay, S. Eckert, B.Van Kuiken, . . . , M. Hantschmann et al., J.Phys. Chem. Lett. (revised and approved)

We demonstrate for the case of photoexcited Ruthenium-tris-bipyridine how femtosecond resonant inelastic X-ray scattering at the ligand K-edge allows one to uniquely probe changes in the valence electronic structure following a metal-to-ligand charge-transfer excitation. Metal-ligand hybridization is probed by nitrogen 1s resonances providing information on both the electron-accepting ligand in the MLCT state and the hole density of the metal center. By comparing to spectrum calculations based on DFT, we are able to distinguish the electronic structure of the electron-accepting ligand and the other ligands and determine a temporal upper limit of (250 ± 40) fs for electron localization following the charge-transfer excitation. The spin of the localized electron is deduced from the selection rules of the RIXS process establishing new experimental capabilities for probing transient charge and spin densities.

My contribution: I helped with the planning, preparation, and execution of the experiment, and was involved in the result discussions as well as the RIXS map analysis.

List of Abbreviations

HZB	Helmholtz Zentrum Berlin
RIXS	Resonant Inelastic X-Ray Scattering
Fermi	Free Electron Laser Radiation for Multidisciplinary Investigations
BESSY	Berliner Elektronenspeicherring-Gesellschaft für Synchrotronstrahlung
SACLA	Spring-8 Angstrom Compact free electron LAser
XAS	X-Ray absorption spectroscopy
XES	X-Ray emission spectroscopy
LCLS	Linear Coherent Light Source
XFEL	European X-Ray Free-Electron Laser Facility
FEL	Free Electron Laser
SLAC	Stanford Linear Accelerator Center
SSRL	Stanford Synchrotron Radiation Lightsource
SXR	Soft X-Ray Materials Endstation
SASE	Self Amplified Spontaneous Emission
NEXAFS	Near Edge X-Ray Absorption Fine Structure
CoPd	Cobalt Paladium
GMD	Gas Monitor Detector
CCD	Charge coupled device
PnCCD	Pinhole CCD
MCP	Multi Channel Plate
YAG	Yttrium Aluminum Garnet Crystal
SiN	Silicium Nitrid
XUV	Extreme Ultra Violett Light
AMO	Atomic Molecular and Optical Science Instrument
FWHM	Full Width Half Maximum (Gaussian pulse)
Flash	Free Electron LASer in Hamburg
DOS	Density Of States

Chapter 2

Introduction

One of modern science's greatest challenges is the understanding of the very matter that forms the basis of living organisms and technology on an atomic level. The physical foundation of all matter is given by its chemical composition within time and space. During the last centuries, the basics of structure in matter were investigated, but it was only due to the development of the laser in the late fifties that science could start to gain insight into the time evolution of chemical reactions on a quantum mechanical level. With modern laser pulse lengths of a few femtoseconds, the possibility to observe the breaking and forming of chemical bonds and the changing electron densities throughout matter appeared. This development culminated in the establishment of the field of femtochemistry, which is the study of 'molecular motions in the transition states of physical, chemical and biological changes', and was awarded with a Nobel prize to Ahmed H. Zewail in 1999 [1].

Although this research field started off with the investigation of simple systems of a few atoms, the real interest lies in the understanding of complex systems, which build the backbone for function within matter. These functions can range from effects such as magnetism [2], over catalytic behavior [3, 4], photosynthesis [5], to the oxygen transport within hemoglobin [6], and many more. However different the function, the basis that connects most of these is the presence of a transition metal ion. Transition metals consist of a partially filled d-shell that forms reactive, long range orbitals, which are the foundation for correlated materials and the respective functions. The understanding of functional materials we have today is largely based on the investigation of potential energy surfaces and the insights gained from ultrafast spectroscopic techniques

within the field of femtochemistry.

The recent development of modern X-ray sources and the availability of femtosecond X-ray pulses enable the combination of the time resolution of optical spectroscopy with the selectivity and the spatial resolution of X-ray spectroscopy simultaneously. Techniques such as stimulated Raman scattering and resonant inelastic X-ray scattering (RIXS) proved themselves to be powerful tools that pushed the understanding of nature's structure and function even further [7, 8, 9, 10]. The development of pulsed X-ray sources from the slicing technique [11, 12] to free electron lasers (FEL) [13] introduced the possibility of ultrafast experiments in the X-ray regime and are continuously being improved today. The possibilities emerging with the short, intense and coherent pulses produced by FELs range from nanocrystallography and femtosecond diffractive imaging [14, 15], over real time observations of chemical reactions [10, 16] to the development of new nonlinear spectroscopic techniques [17, 18]. The capabilities of non-linear spectroscopies are well known to be compelling tools through the combination of high temporal and spectral resolution [19, 20]. Techniques such as stimulated Raman scattering [21] or multidimensional spectroscopies [22, 23] enabled the investigation of a variety of problems within the field of femtochemistry and set the basis for Ahmed Zewail's Nobel prize [1]. The achievements of these methods make it desirable to expand them into the X-ray regime, where their capabilities could be combined with the selectivity and spatial resolution of X-rays.

In order to do so, we need to understand how the onset of non-linear effects affects modern spectroscopy and how we can plan and control their occurrence. Additionally, the light source has to be controlled to the finest detail and the sample system has to enable certain transitions for spectroscopies such as four wave mixing, or stimulated Raman scattering. The FEL light sources are currently developing extremely controlled conditions, reducing the statistical nature of self amplified spontaneous emission (SASE) pulses while enabling seeded [24, 25], or even multi-colour operations [26, 27]. Now that the light sources are available with the relevant precision and control, we can focus to utilize these to improve our experimental spectroscopic capabilities.

In this thesis, the focus lies on the spectroscopic RIXS technique, where a photon scatters inelastically with matter and allows to probe the unoccupied valence states through the initial absorption, and the occupied valence states

through the inelastic scattering [28]. But however powerful the used technique is, the corresponding fluorescence channel signal tends to lack signal ratios due to the competing Auger decay channel. Within optical spectroscopic techniques, the problem of low signal rates was tackled through the development of nonlinear spectroscopy such as stimulated Raman scattering, which enhances the signal of interest through resonant stimulation. It is, therefore, of major interest to transfer the possibilities of optical spectroscopy to the X-ray regime, especially as there are indications of its feasibility [29, 30, 31] and discussions how it could potentially impact the experimental capabilities [32]. This thesis utilizes on these discussions and provides a proof of principle for stimulated RIXS in solid state transmission experiments and develops a rate model approach to improve our understanding of FEL pulse driven light-matter interactions. As stimulated emission will be the driving force in experiments stimulating the weak photon signal in low signal rate experiments, this dissertation and the model presented therein focuses on this effect, contrary to other theories focusing on pulse propagation or higher order non-linear light-matter interactions. The potential of nonlinear X-ray spectroscopy for the field of femtochemistry is enormous, and the experiments and discussions presented in this thesis provide a step towards its understanding and utilization.

Experiments with intense FEL pulses are promising to enable the observation of nonlinear X-ray matter interactions. These effects are well known in nonlinear optical spectroscopies, but rather unconventional for the X-ray community. Chapter 4.2 looks into some recent observations in this field and provides a view on the influence of stimulated scattering on classical experiments performed at high intensities. The emergence of stimulated scattering within one X-ray pulse creates new side effects which are investigated in this chapter. Namely the increase of forward scattering at the cost of first and third order scattering and a saturation effect in the absorption are expected. To better understand these effects, chapter 5, presents a study on the feasibility of stimulated RIXS within a single pulse geometry. Using a thin CoPd magnetic film, the first direct observation of a stimulated signal within a solid sample is shown. By investigating the scattering as well as transmission signal of single pulse experiments, we can show a connection between stimulated emission and the change of scattering and transmission signals. This hopefully leads to a better understanding of all light matter interactions for high intensity FEL experiments.

This thesis is organized as follows: First, this thesis discusses the concept of time resolved RIXS at FEL sources in chapter 3. Here the concept of time resolved RIXS is introduced as well as the experimental conditions and requirements of this technique. Secondly, chapter 4 reviews the non-linear phenomena surrounding RIXS at FEL sources from the experimental point of view. This chapter also discusses the occurrence of nonlinear phenomena, such as induced transparency and scattering breakdown observed in classic experiments at FEL sources. In chapter 5, our experimental approach to understand the occurrence, possibilities and side effects of stimulated RIXS is presented. This chapter is split into the discussion of an FEL experiment, measuring RIXS and scattering of intense short pulses at the Co L3-edge, and the experimental results. In the next chapter 6, this thesis develops a rate model approach to understand and estimate the effects observed in this and other experiments, and create a tool for estimations around stimulated RIXS in the soft X-ray spectrum. Lastly, this thesis finishes with a discussion on the question whether stimulated RIXS could be a tool to reveal hidden channels of surface states in well designed FEL experiments.

Chapter 3

The Toolbox of Time Resolved Resonant Inelastic X-Ray Scattering

Resonant inelastic X-ray scattering (RIXS) is an ever expanding experimental technique in which an X-ray photon is inelastically scattered off the investigated complex. This photon-in, photon-out type of spectroscopy is capable of measuring the energy, momentum, and polarization change of the scattered photon, which in turn offers information about the intrinsic excitations of the material under study [33]. These include crystal-field excitations, magnons, molecular vibrations, phonons, and charge transfers [34]. Additionally, RIXS is also element- and orbital-selective, which is because the incident photon can be tuned resonantly to specific atomic transitions and absorption edges, and can even be fine tuned to differentiate between different chemical environments of the same element [28]. In principle, RIXS can probe any intrinsic excitation as long as it is on overall charge neutral. Although this makes for impressive reading, the main drawback of this technique is the fact that it is limited by a low fluorescence yield, and demands thus highly intense light sources. However, the most recent achievements with new generation synchrotrons, and the establishment of X-ray FELs, this technique becomes ever more relevant and feasible.

This chapter aims at providing a summary of the aspects of RIXS relevant for this thesis in order to gain a better understanding of this technique and its abilities. First, the basic X-ray-matter interactions are introduced in Sec. 3.1, followed by a quantum mechanical description of the RIXS process in Sec. 3.1.2.

Finally, the experimental procedure and the corresponding main components, such as the sample delivery system, the spectrometer, and the X-ray light source, are introduced in Sec. 3.2.

3.1 Soft X-Ray Matter Interaction

The so-called soft X-ray regime is commonly referred to as the energy range approximately indicated by the excitation of the L-shell in a material system. Therefore, soft X-ray radiation covers the energy range between about 100 eV and 1000 eV. The fundamental interactions, however, do not change for other energies, so there is no clear definition of the soft X-ray range as a consequence. X-ray spectroscopy is the study of interactions between light and matter in order to understand the properties of a medium [35]. In soft X-ray spectroscopy, a photon or light pulse interacts with a material usually through absorption, which induces a core excited state. The consecutive relaxation process is then monitored through a variety of methods that evaluate the emitted photons or electrons in various possible ways. In the following, the basic interactions relevant for soft X-ray spectroscopy, and especially the RIXS process, are introduced.

3.1.1 Beer-Lambert Law

When a photon beam passes through a medium, the light intensity decreases and the corresponding energy is transferred to the medium [36]. The energy loss of the radiation is directly proportional to the incident intensity I_0, and decreases exponentially with the absorber concentration C and the path length through the medium of length l. This is a well known process expressed through Beer-Lambert's law in terms of transmitted intensity:

$$I_{trans} = I_0 e^{-\epsilon Cl}, \tag{3.1}$$

where ϵ describes the absorption coefficient containing all processes occurring between light and matter and the product ϵCl describes the optical density of the medium. In soft X-ray spectroscopy, resonant excitations from the core level to an empty valence state are the dominant excitation channel, hence the Beer-Lambert law can be rewritten in terms of the atomic scattering length f and

the absorption cross section σ_{abs} as

$$I_{trans} = I_0 e^{-\sigma_{abs}\rho_a d},$$ (3.2)

where ρ_a is the atomic number density and d the thickness of the interaction region [37]. While the X-ray absorption cross section will be introduced in greater detail in Sec. 3.1.3, it should here be noted that the *resonant* X-ray absorption cross section $\sigma_{abs} = 2\lambda f''$ depends on the atomic scattering length f. This dispersion correction depends on the resonant photon energy ε_0, the total spontaneous decay width $\Gamma = \Gamma_x + \Gamma_A$ with the radiative transition width Γ_x and the Auger width Γ_A as follows:

$$f'' = \frac{\lambda}{2\pi}\frac{\Gamma_x}{\Gamma}\frac{(\Gamma/2)^2}{(\hbar\omega - \varepsilon_0)^2 + (\Gamma/2)^2} \; [37].$$ (3.3)

λ, $\hbar$, ω havee their usual meaning. This expression will be of importance in Chapter. 5, since the basic Beer-Lambert law seems to fail for intense incident X-ray pulses and can be expanded, as shown later on.

3.1.2   An Insight into the Quantum Mechanical Picture

The Beer-Lambert law describes the average transmission of light through a material as stated in Eq. 3.2, yet it does not explain the respective mechanisms on a quantum mechanical level. When describing the interaction of soft X-rays with matter at a higher level, it can be understood as a two-step scattering process, where the two steps are an excitation step and a relaxation step, respectively. Thomson scattering, which is the only known mechanism differing from the further described types of interactions, has a cross section orders of magnitude smaller than the X-ray absorption cross section and is, therefore, disregarded, as it is unlikely to impact RIXS.

Fig. 3.1 shows a scheme of the X-ray-matter interactions relevant for RIXS, depicted for the interaction with a generic orbital energy diagram of a typical atom or molecule. The radiative processes can be separated into the absorption process in Fig. 3.1 a) and the radiative relaxation processes shown in Fig. 3.1 b). Fig. 3.1 c) depicts the Auger decay, which is a relaxation process under the emission of an Auger electron instead of a photon. From the RIXS point of

a)   Non-resonant absorption   Resonant absorption (NEXAFS)

Vacuum

                                                                      LUMO
                                                                      HOMO
                                                                      HOMO-1

Valence
orbitals

Core level

b) Radiative emission channels (RIXS)   **c)** Non-radiative relaxation

   Elastic Scattering   Inelastic Scattering
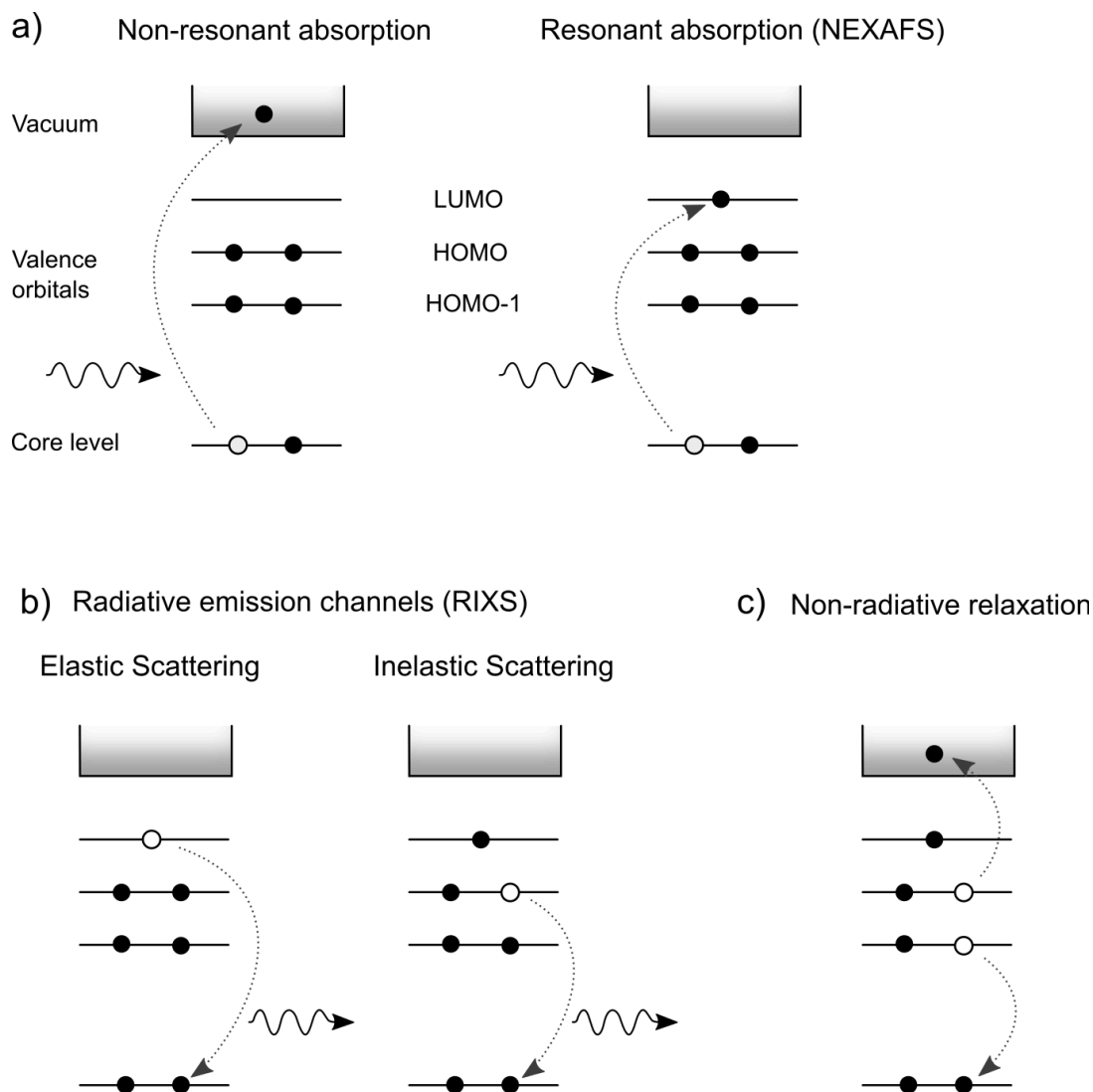
Figure 3.1: **The fundamental photon-matter interactions relevant for the RIXS process shown in a schematic molecular energy diagram. a)** shows the X-ray absorption process, where an initial X-ray photon is absorbed and a core level electron is promoted into the continuum (non-resonant, left) or an excited state (resonant, right). **b)** depicts the radiative emission process, where the electronic system relaxes under emission of an X-ray photon. This can be either the electron that was just excited (elastic scattering, left) or another valence electron (inelastic scattering, right). **c)** During the Auger process, the excited state relaxes under the emission of an Auger electron. Since either b) or c) can occur as a relaxation process, the two processes compete.

view, this process acts as a competitor to spontaneous emission, as it decreases the number of photons observable through the RIXS process, which is the combination of resonant absorption and a radiative relaxation, as further explained in Sec. 3.1.5 .

To understand the soft X-ray-matter interactions on a quantum mechanical level, the photon-matter interaction is treated as a time-dependent perturbation of an electromagnetic field to the unperturbed matter system and vice versa. The following quantum mechanical description follows the common literature, for example [38, 39, 40, 41, 42]. The Hamiltonian $\hat{H}$ describes the electron field system as

$$\hat{H} = \hat{H}_0 + \hat{H}_{int} \tag{3.4}$$

with $\hat{H}_0$ representing the unperturbed system of an electron in the field, defined by the nuclei and the other electrons, as well as the electromagnetic field in the vacuum, whereas the interaction of the two is described by $\hat{H}_{int}$. Following the Maxwell equations, the total Hamiltonian for the interaction of an electron at time t and position $\vec{r}$ with an electromagnetic wave is given by

$$\hat{H} = \underbrace{\frac{\vec{p}^2}{2m_e} + eU}_{\hat{H}_0} \underbrace{- \frac{e}{m_e}\vec{p}\vec{A} + \frac{e^2}{2m_e}\vec{A}^2}_{\hat{H}_{int}} \tag{3.5}$$

with the elementary charge e, the electron mass m_e, the momentum operator $\vec{p} = \frac{i}{\hbar}\nabla$ and the vector potentials $U(\vec{r})$ and $\vec{A}(\vec{r},t)$, respectively [40]. The vector potential of N_ω photons at frequency ω for a planar wave $\vec{A}$ can be writen as

$$\vec{A}(\vec{r},t) = \sqrt{\frac{8\pi N_\omega \hbar}{\omega V}}\hat{u}e^{i(\vec{k}\vec{r}-\omega t)} \ , \ \ |\vec{k}| = \omega, \ \ \vec{u}\vec{k} = 0 \tag{3.6}$$

with V being the volume the photons are in and $\vec{u}$ being a unity vector. To include the effect of superpositions and interference of planar waves, the vector potential is expanded by an incoming and a second incoming or outgoing wave as

$$\vec{A}(\vec{r},t) = \underbrace{A_1\hat{u}_1 e^{i(\vec{k}_1\vec{r}-\omega_1 t)}}_{\text{incident wave}} + \underbrace{A_2\hat{u}_2 e^{i(\vec{k}_2\vec{r}\pm\omega_2 t)}}_{\text{wave 2}} . \tag{3.7}$$

We assume that the unperturbed system is governed by the Hamiltonian $\vec{H}_0$

with known stationary states, defined through

$$\hat{H}_0|n\rangle = \epsilon_n|n\rangle \ , \ \langle n|m\rangle = \delta_{nm} \tag{3.8}$$

with the identity $\vec{u} = \sum_{n=0}^{\infty} |n\rangle\langle n|$. This expression indicates that the states $|n\rangle$ and $|m\rangle$ describe the whole system, including all electrons and nuclei that are considered in the stationary field.

If the eigenvalue differences near typical atomic bound states are much larger than the perturbation from the electromagnetic field, one can assume the first term of the interaction Hamiltonian from Eq. 3.5 to be much larger than the second, which reduces the interaction Hamiltonian to

$$\hat{H}_{int} \sim \left| \frac{e}{m_e} \vec{p}\vec{A} \right| \propto \frac{e}{m_e} \left| en_e \frac{p^2}{2m_e} \right|^{\frac{1}{2}} \sqrt{\frac{8\pi N_\omega \hbar}{\omega V}} \tag{3.9}$$

for a single planar wave, as given in Eq. 3.6. For the potential given by two planar waves, the perturbation on an electron system according to Eq. 3.5 and Eq. 3.7 is given by

$$\hat{H}_{int} = \left[\hat{V}_1 e^{-i\omega_1 t} + \hat{V}_2 e^{\pm i\omega_2 t} \right] e^{\lambda t} \ , \ \ \lambda \to 0+ \ , \ \ t_0 \to -\infty \tag{3.10}$$

with the time-independent operators

$$\hat{V}_j = \underbrace{\frac{e}{m_e} \sqrt{\frac{8\pi N_j \hbar}{\omega_j V}}}_{I} \ \underbrace{\vec{p}\vec{u}_j}_{II} \ \underbrace{e^{i\vec{k}\vec{r}}}_{III} \ . \tag{3.11}$$

The factor λ here does not represent the wavelength, but accounts for the introduction of the perturbation into the system at time $t = -\infty$, which then gradually increases. This is a mere mathematical introduction to ensure a continuous function. Factor I describes the radiation fields strength through the photon density N_j/V, factor II describes the polarization of the planar wave, and III describes the propagation of the wave with the propagation direction being determined by $\hat{k} = \vec{k}/|\vec{k}|$.

From time-dependent perturbation theory, which in general means the determination of the time-dependent Schrödinger equation, one can derive a transition probability of an initial state $|n\rangle$ into a final state $\langle m|$ through the interaction

with the electromagnetic potential $\vec{A}$. The time evolution over this transition probability is interpreted as the transition rate $\Gamma_{n \to m}$ from the initial to the final state under the influence of the photon field, and is typically called Fermi's Golden Rule

$$\Gamma_{n \to m} = \frac{2\pi}{\hbar} \left| \langle m | \hat{H}_{int} | n \rangle \right|^2 \delta(\epsilon_n - \epsilon_m) \quad [39, 36] \tag{3.12}$$

with the matrix element $\langle m | \hat{H}_{int} | n \rangle$ depicting the transition strength. From this rule, the cross sections for the transition between two states can be derived by dividing the transition rate through the incident photon flux, which is given by the number of photons N_ω in the volume V at the speed of light c as $F = \frac{N_\omega c}{V}$. Fermi's Golden Rule is exact, but inconveniently not solvable for the full interaction Hamiltonian $\hat{H}_{int}$. Therefore, the interaction term is typically expanded into a power series [43, 36, 39], leading to perturbations of first and second order, which are discussed in Sec. 3.1.3, 3.1.4, and Sec. 3.1.5, respectively.

In the soft X-ray regime, the so-called 'dipole approximation' is applied, assuming $e^{i\vec{k}\vec{r}} \approx 1$, as the photon wavelength ≈ 1 nm is approximately constant for the electron within the interaction length of ≈ 1 Å. This assumption expects the electromagnetic wave to oscillate so slowly that it can be assumed to be constant over the interaction length, hence the electron experiences a constant electric field. A further simplification can be introduced through the transition dipole moment $\vec{d}$ that reduces the differential momentum operator $\vec{p} = \frac{i}{\hbar} \nabla$ through the identity

$$\vec{p} = \frac{m_e}{i\hbar} [\vec{d}, \hat{H}_0] \ . \tag{3.13}$$

This simplifies the transition matrix element $\vec{M}$ to

$$\vec{M} = \langle n | \vec{p} e^{i\vec{k}\vec{r}} | m \rangle \approx \langle n | [\vec{d}, H_0] | m \rangle = \frac{m(\epsilon_0 - \epsilon_n)}{i\hbar} \langle n | \vec{d} | m \rangle. \tag{3.14}$$

This so-called transition dipole moment depicts the strength of a transition between two states. If this expression vanishes, typically due to geometric or symmetry reasons, one speaks of selection rules, which are further discussed in Sec. 3.1.6.

When applying these conceptual ideas to actual systems, two effects have to be considered. First, strictly monochromatic radiation cannot be provided, except for single photon sources, therefore the single photon frequency is replaced by the frequency distribution of the light source. And secondly, the states in atoms, molecules, or any material system have a non-delta-like energy distribution, which is caused by the lifetime broadening. Since all excited states decay, there is an excited state lifetime that is defined by the decay rates of all relaxation channels. For a core hole, as created within the soft X-ray regime, one speaks of the corresponding core hole lifetime. By applying Heisenberg's uncertainty principle to this excited state lifetime, the relation between the lifetime τ and the minimum energy width E_{nl} related to this time is

$$\tau E_{nl} \geq \hbar/2. \tag{3.15}$$

This energy width is called the natural lifetime broadening and has a characteristic Lorentzian energy profile. To include these for practical calculations, the δ-function in Eq. 3.12 is replaced by a respective distribution function.

In the following short descriptions, the different light-matter interactions with relevance for this thesis are introduced in the order of complexity regarding their degree of perturbation. First order perturbation is the interaction of matter with one photon through either absorption or emission described first. This is followed by a discussion of the second order perturbations, which involve all two-photon scattering processes and can be described by the Kramers-Heisenberg cross section [41]. This is introduced in Sec. 3.1.5, followed by a discussion of the scattering process between photons and electrons, so-called Raman scattering. Two-photon absorption and emission as well as Thomson scattering are not discussed in this thesis, because they are not of major importance for our discussion of RIXS.

3.1.3   X-Ray Absorption

Based on the theoretical background discussed above, the effects introduced in Fig. 3.1 can now be understood in greater detail. First, an expression for the X-ray absorption in terms of a one-photon absorption cross section is determined. For this process, only the first term of Eq. 3.11, that is the incoming wave,
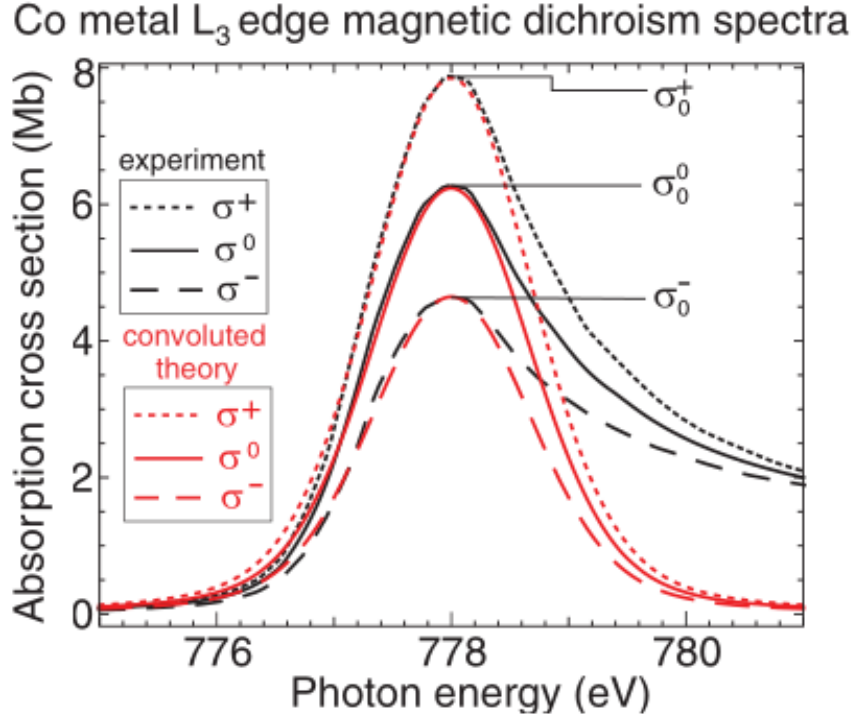
Figure 3.2: An example of a typical absorption cross section, in this case a Co metal L3 edge including the difference in cross section for the two different circular polarizations (magnetic dichroism). The theoretical cross section here has been calculated using Eq.3.3 ($*2\lambda$) convoluted with a 1.4 eV FWHM Gaussian to improve the fit with the experimental cross sections. The image is taken from the Lambert Beer expansion discussion by Stöhr et al. [37].

needs to be included. Under consideration of the above concepts, this yields the absorption cross section

$$\sigma_{abs} = \frac{\pi\omega}{c\xi_0} \left| \hat{u}\langle\hat{n}|\vec{d}|m\rangle \right|^2 \delta(\epsilon_n - \epsilon_0 - \hbar\omega) \tag{3.16}$$

between the initial state $|m\rangle$ and the final state $|n\rangle$, which is only different from zero if the energy difference between the states $\epsilon_n - \epsilon_0$ meets the condition $\epsilon_n - \epsilon_0 = \hbar\omega$. Note the different notation for the electric constant ξ_0. To determine a realistic absorption cross section, the natural lifetime broadening as well as the summation over all possible final states have to be included, giving the absorption cross section

$$\sigma_{abs} = \sum_n \frac{\pi\omega}{ce_0} |\hat{u}_n \hat{d}_n|^2 \frac{1}{(\epsilon_n - \epsilon_0 - \hbar\omega)^2 + \tau_n^2} \ . \tag{3.17}$$

23

As indicated in Fig. 3.1 a), this effect can occur in two variations. If the incident photon energy is larger than the orbital binding energy, the electron is excited into the continuum or vacuum and the atom is ionized, which is the so-called process of non-resonant absorption. For the situation where the photon energy is smaller than the orbital binding energy, the excitation can only occur in resonance with a specific absorption if the energy difference between the initial and final state are close to the incident photons energy. This process is called resonant absorption and is assumed to be the dominant excitation process for the material systems investigated in this thesis or through RIXS in general. The absorption process is described well through this concept of an absorption cross section. A typical example of such a cross section can be found in Fig. 3.2.

3.1.4   X-Ray Emission

The second one-photon interaction process is the emission of a photon from an excited system, as indicated in Fig. 3.1 b). However the notation in Fig. 3.1, in the case of the one-photon interaction, the system was already in the excited state, hence the term scattering does not apply here. In case of emission, only the second term of Eq. 3.7 contributes to the cross section. The calculation of the emission cross section proceeds in the same way as for the absorption cross section, however, there is one major difference. Due to the quantization of the photon field, the number of photons must be an integer, which poses a problem for the case of an empty photon field $N_\omega = 0$, since observations reveal that emission still occurs. A quantum mechanical treatment of this problem can be found in [44] and leads to the distinction between *spontaneous* and *stimulated emission*, where the spontaneous emission is understood as a stimulated emission of the vacuum or background field. The total emission cross section consists, therefore, of a spontaneous and a stimulated part and can be written as

$$\sigma_{em} \propto \underbrace{\left|\langle n|\vec{d}|m\rangle\right|^2}_{\text{spontaneous emission}} + \underbrace{N_\omega \left|\langle n|\vec{d}|m\rangle\right|^2}_{\text{stimulated emission}} . \qquad (3.18)$$

As can be seen from Eq. 3.18, the stimulated emission rate depends on the number of photons N_ω in the interaction volume before the emission occurs, while the spontaneous contribution is constant. For 'classical' RIXS experiments, this

distinction between spontaneous and stimulated emission is not relevant, but for experiments performed at intense X-ray sources it affects the light-matter interaction on a major scale, as shown in Chapter 5.

3.1.5   X-Ray Scattering

Now the discussion focuses on the actual scattering that is understood as a two-photon process. With the vector potential given in Eq. 3.7, two planar waves with wave vector $\vec{k}_i$ and polarization $\vec{u}_i$ are considered to interact with the system, given through the Hamiltonian $\hat{H}_0$ from Eq. 3.5. To further simplify the description, we consider the absorbed radiation to be given by the *incident wave* in Eq. 3.7, and the emitted radiation given by *wave2* in Eq. 3.7, respectively. Following this, the perturbation T is given through

$$\hat{H}_{int}(t,\vec{r}) = \frac{e}{2m_e}\vec{p}\left[A_1\vec{u}_1e^{i(\vec{k}_1\vec{r}-\omega_1 t)} + A_2\vec{u}_2e^{-i(\vec{k}_2\vec{r}-\omega_2 t)}\right] + $$
$$\frac{e^2}{4m_e}A_1A_2\vec{u}_1\vec{u}_2e^{i(\vec{k}_1-\vec{k}_2)\vec{r}-i(\omega_1-\omega_2)t}. \tag{3.19}$$

The solid angle element $d\Omega_2 = sin\theta_2 d\theta_2 d\phi$ with respect to the electron coordinate system is introduced to imply the emission direction, or for practical purposes the detector size. Following the discussion for Fermis Golden Rule (Eq. 3.12) and integrating over all possible radiation field modes that can interact to generate the emission, yields the so called Kramers-Heisenberg formula, which was first introduced in [41].

$$\sigma_{KH} = r_0^2\frac{\omega_2}{\omega_1}(N_2+1)d\Omega_2 \; \cdot$$
$$\left|\vec{u}_1\vec{u}_2\langle n|m\rangle \; - \frac{1}{m_e}\sum_f\left(\frac{\langle n|\hat{u}\vec{p}|f\rangle\langle f|\hat{u}_2\vec{p}|m\rangle}{\epsilon_f - \epsilon_m + \hbar\omega_2} + \frac{\langle n|\hat{u}_2\vec{p}|f\rangle\langle f|\hat{u}_1\vec{p}|m\rangle}{\epsilon_f - \epsilon_m - \hbar\omega_1}\right)\right|^2 \tag{3.20}$$

corresponds to the Kramers-Heisenberg formula written in terms of the cross section σ_{KH}. $r_0 = e^2/m_ec^2$ depicts the classical electron radius. Expression 3.20 includes all two-photon scattering processes that scatter with an incident photon with energy $\hbar\omega_1$ from the initial state $|m\rangle$ through the intermediate states $|f\rangle$ into a final state $|n\rangle$, implying the emission of a photon of the energy $\hbar\omega_2$ into the solid angle $d\Omega$. It also includes the polarization relation between the incident and the emitted photons.

Using this expression, the scattering process schematically shown in Fig. 3.1a) and b) can be described. The RIXS process is the combination of resonant absorption followed by a spontaneous (or stimulated as shown in Chapter 5) emission. This so-called Raman scattering includes elastic scattering, where the electronic systems remains unaltered, and inelastic scattering, where energy is transferred between the photon and the electronic system. If energy is absorbed by the system, the relevant process is called Stokes scattering, whereas if energy is released, one speaks of Anti-Stokes scattering. To expand the possible excitations within the electronic system, the states $|n\rangle$ have to represent nuclear motion for example, and therefore have to be expanded to include these degrees of freedom in the form $|n\rangle = |\phi(e)_n, \phi(vib)_n\rangle$. Considering an incident photon being absorbed in the system, and a second photon being emitted, the Raman scattering cross section is given by

$$\sigma_{Raman} = r_0^2 (N_2 + 1)\frac{\omega_2}{\omega_1}d\Omega_2 |\hat{u}_2 \boldsymbol{R}\hat{u}_1|^2, \qquad (3.21)$$

where $\boldsymbol{R}$ represents the matrix elements

$$R_{jk} = \frac{1}{m_e}\sum_f \left(\frac{\langle n|\hat{p}_j|f\rangle\langle f|\hat{p}_k|m\rangle}{\epsilon_f - \epsilon m + \hbar\omega_2} + \frac{\langle n|\hat{p}_k|f\rangle\langle f|\hat{p}_j|m\rangle}{\epsilon_f - \epsilon m - \hbar\omega_1}\right) \qquad (3.22)$$

with the relation $\omega_1 - \omega_2 = (\epsilon_n - \epsilon_m)\hbar = \Delta\epsilon_{n\ m}$. This condition gives the factor that a typical RIXS experiment probes, the energy difference between the initial and final state. If the incident photon energy matches one of the electronic excitations in the system, the cross section is largely enhanced and the process is called resonant Raman scattering. This is the case if the condition $\hbar\omega_1 = \epsilon_f - \epsilon_m$ is fulfilled and builds the foundation for RIXS spectroscopy.

We have to elaborate on a point mentioned earlier which is of critical importance for experiments performed at an FEL. It is the effect of the photon field on the scattering cross sections. For classical RIXS experiments, for instance at synchrotron sources, one assumes to have 'one-photon-at-a-time' experiments that reduce the factor $(N_2 + 1)$ to 1, with N_2 being the number of photons in the interaction volume within the emission wavelength. This assumption breaks down for FEL experiments, where the number of photons within the coherence volume, the volume in which the photons are indistinguishable and can interfere,

increases up to a magnitude of 10^9 [45].

A typical cross section estimation is another way of demonstrating the importance of the photons per pulse parameter. A typical soft X-ray cross section is around $\sigma = 1$ megabarn (Mb) [46]. Therefore, an estimation of the number of incident photons n_{inc} needed to absorb one photon per atom n_{abs} is given by

$$n_{inc} = \frac{n_{abs} A}{\sigma} = 10^{10} \tag{3.23}$$

for an X-ray focus of $A = 1$ μm^2. A typical synchrotron generates about 10^4 photons per pulse, which is far out of reach for multiple absorption processes. A typical FEL pulse, in contrast, contains $\approx 10^{12}$ photons [47], which clearly enters the regime where nonlinear and multi-photon effects have to be taken into account. The influence of the photon field on the RIXS experiments is further investigated in Chapter 5, where, depending on the incident field strength, the observed scattering changes substantially.

For elastic scattering, the incident photon energy and the emitted photon energy have to match, which reduces the Kramers-Heisenberg formula Eq. 3.20 to:

$$\sigma_{elastic} = r_0^2 m_e^2 \omega^4 (N_2 + 1) d\Omega_2 \times$$
$$\left| \sum_f \left(\frac{\langle n|\hat{u}_1 \vec{r}|m\rangle \langle m|\hat{u}_2 \vec{r}|n\rangle}{\epsilon_m - \epsilon_n} + \frac{\langle n|\hat{u}_2 \vec{r}|m\rangle \langle m|\hat{u}_1 \vec{r}|n\rangle}{\epsilon_m - \epsilon_n} \right) \right|^2, \tag{3.24}$$

This is the so-called Rayleigh cross section [39].

3.1.6   Selection Rules

As discussed in Sec. 3.1.2 around Eq. 3.14, the transition probability between two states depends on the transition dipole moment. The application of symmetry considerations to the two states can help determining whether the integral will be zero without solving it, which is the case for symmetry-forbidden transitions. This leads to the so-called selection rules. The expression for the transition dipole moment becomes zero if the two wave functions representing the initial and the final state are antisymmetric under symmetry operations of the system. Practically, this is expressed in terms of quantum numbers that can

be derived from the system wave function.

The selection rules dominating atomic and molecular electronic spectra are governed by the D3h point group, and can be written as $\Delta n = 0, 1, 2, ...$ with $\Delta L = \pm 1$ for single electron transitions, and $\Delta L = 0, \pm 1$, for multi-electron transitions, $\Delta S = 0$, and $\Delta J = 0, \pm 1$, except for the forbidden transition $J = 0 \rightarrow J = 0$. Here n is the principal quantum number, L the orbital angular momentum, S the spin angular momentum, and J the total angular momentum [48]. Note that these selection rules are strictly dependent on the assumptions made in Sec. 3.1.2 during the development of the quantum mechanical description, and are accordingly not omnipresent in any system. In general, if a transition takes place through a mechanism that does not involve the electrical dipole transition, or that is excluded from the description through simplifications, the transition might be observable as low intensity peaks in experimental spectra. Two examples for this are the mixing of states through vibronic coupling and a mixture of ligand orbitals with the d orbitals in transition metal complexes [38].

3.1.7 Auger Decay vs. RIXS

As indicated in Sec. 3.1, the Auger decay acts as a competitor for the RIXS process due to the fact that it reduces the number of excited systems available for the emission of photons. At soft X-ray energies for typical transition metal edges, the relation between Auger and radiative decay rates is shown in Fig. 3.3, where a gap of approximately two orders of magnitude can be seen between the radiative and the Auger decay rates, respectively. A detailed list of Auger and radiative decay rates can be found in [49], which is the origin of the shown figure. This implies that for the RIXS process, only a fraction of the excited systems decays radiatively. For the soft X-ray regime, this fraction is only about $0.1\,\% - 1\,\%$. This low photon yield of the RIXS process highlights the necessity to seek further improvements of this method, as presented in Chapter 5

3.2 Experimental Methods

A RIXS experiment requires three separate sections to work: an X-ray source to create the experimental conditions for the light beam or pulse, a sample delivery system defining the interaction region of the X-ray photons with the sample
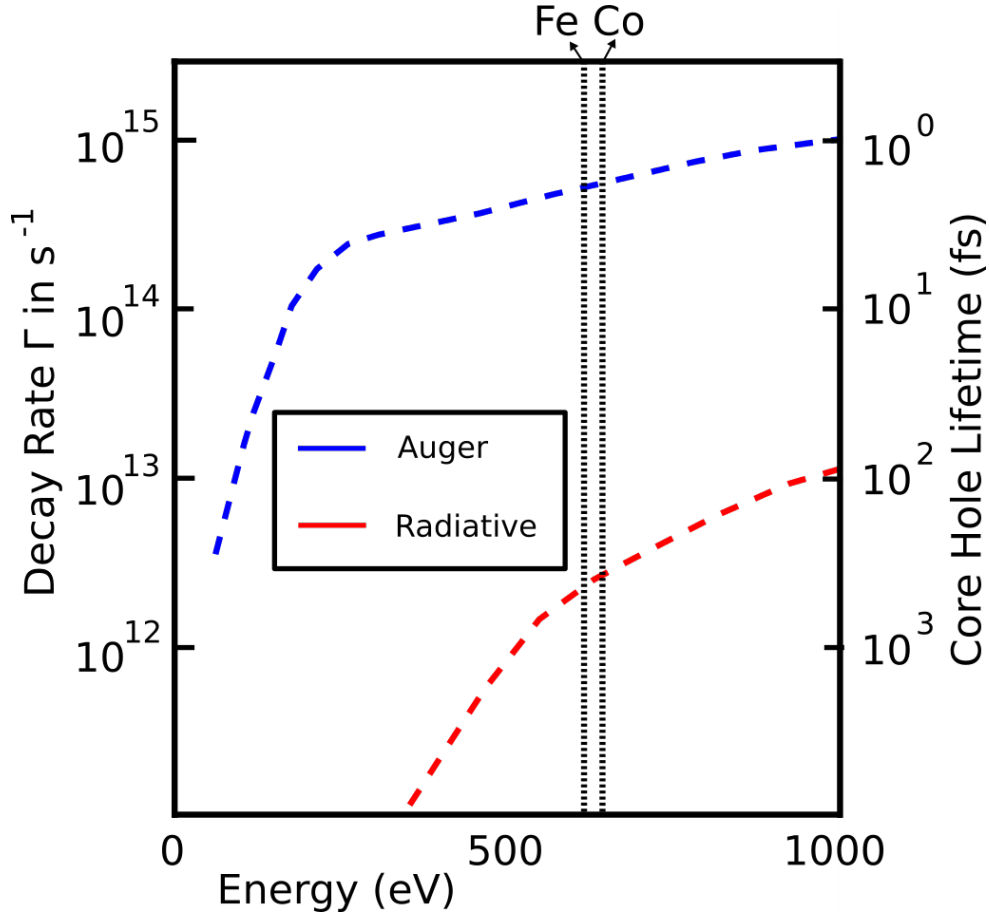
Figure 3.3: **Radiative (spontaneous emission) and Auger decay rates in the soft X-ray regime**. The ratio between Auger and radiative decay stays constant, whereas the overall decay rate depends mostly on the transition energy increasing with increasing energy. The transition metal L-edges of Iron and Cobalt are highlighted to indicate the soft X-ray region and the relations therein. The graph is adapted from [50] with values taken from [49].

and ensuring a timely sample renewal to reduce X-ray damage effects, and a spectrometer that captures the relevant information from the light-matter interaction region. In the following, these three parts are presented and explained in detail.

3.2.1   Fundamentals of X-Ray Generation

Synchrotron radiation is generated when a charged particle at relativistic speed is subject to a transverse acceleration [52]. This is valid for both synchrotron and FEL sources. Usually, the charged particle is provided in the form of electrons, but in principle other particles are also suitable for this purpose. The description of the total radiated power originated from the acceleration of a charged particle

in a vacuum is expressed through the Lamor formula, which is given as

$$P = \frac{q^2\gamma^4}{6\pi\epsilon_0 c}\left(\left(\frac{d\vec{\beta}}{dt}\right)^2(1-\beta^2) - \left(\vec{\beta} \times \frac{d\vec{\beta}}{dt}\right)^2\right) \tag{3.25}$$

under consideration of a relativistic generalization as explained in [53]. Here, $\gamma = \frac{1}{\sqrt{1-\beta^2}}$ is the Lorentz factor, q is the charge of the particle, and $\vec{\beta} = \frac{\vec{v}}{c}$ with the velocity $\vec{v}$ of the particle and c the speed of light. The acceleration source in a synchrotron is a magnetic field, hence the acceleration is perpendicular to the velocity, reducing it to $\vec{\beta}\frac{d\vec{\beta}}{dt} = 0$ and yielding the simplified equation

$$P_{a\perp v} = \frac{q^2 a^2 \gamma^4}{6\pi\epsilon_0 c^3}[53]. \tag{3.26}$$

Using the relativistic mass-velocity relationship $E = \gamma mc^2$ and the proportionality relationship $P_{a\perp v} \sim \gamma^4$, one receives

$$P_{a\perp v} \sim= \frac{E^4}{m^4 c^8}, \tag{3.27}$$

which explains why electrons are preferred to generate the radiation: since the radiated power is proportional to m^{-4}, electron radiation is approximately 10^{13} times higher compared with radiation produced by protons, for example [53]. The radiated power is proportional to the number of emitted photons and is also dependent on the charge, or rather the number of charges emitting radiation [53]. In typical X-ray facilities, the electrons are bunched together in order to increase the amount of emitted photons. Additionally, in a synchrotron the storage ring

Parameter	Bessy II	LCLS
Electron beam energy	1.7 GeV	2.5 - 14.7 GeV
Photon energy	1 eV - 10 keV	285 - 9600 eV
Repetition rate	$\approx$ 500 MHz	120 Hz
Pulse duration	60 ps	1-400 fs
Peak brilliance	10^{22}	10^{32}
Average brilliance	10^{20}	10^{20}

Table 3.1: A selection of parameters for the third generation synchrotron BESSY II [51] and the X-ray FEL LCLS [47]. Notable is the short pulse duration for the FEL light source compared to a third generation synchrotron. However, the overall flux in the experiment is about the same for the two sources. The choice which light source to use depends primarily on the required time resolution.

can contain many electron bunches, allowing a high repetition rate of the light pulses and thereby increasing the average brilliance, as shown in Tab. 3.1.

3.2.2   Intense X-ray Sources
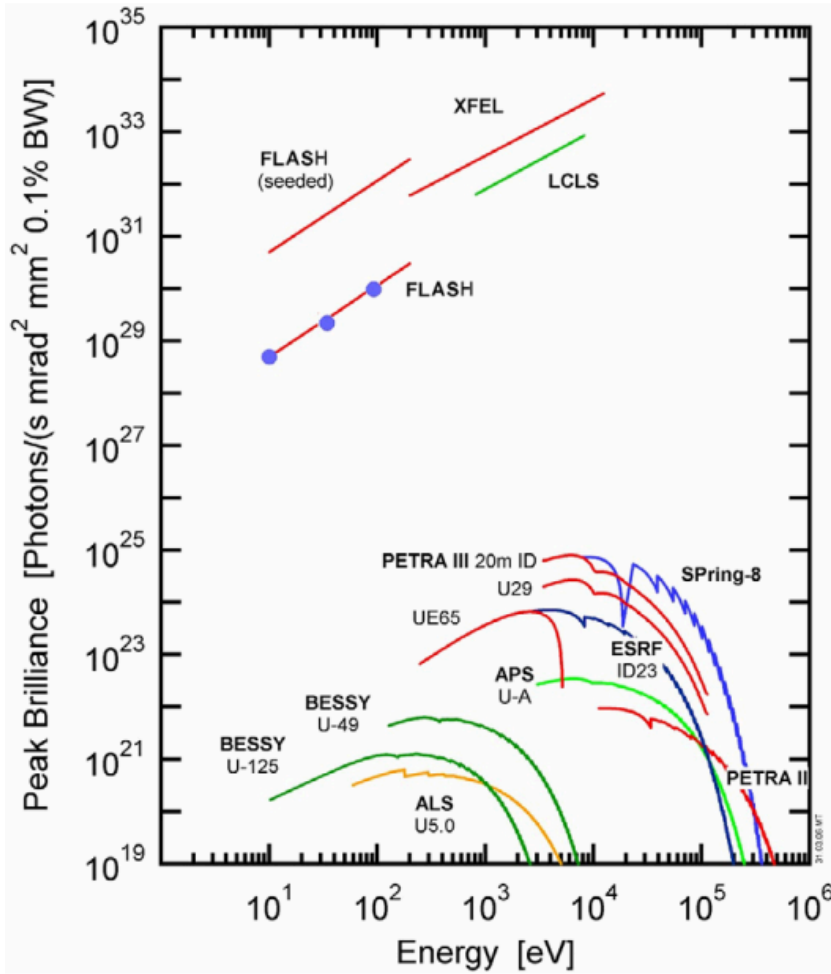
Figure 3.4: **The peak brilliance of a selection of modern light sources [54].** The difference in brilliance for synchrotrons and for FEL sources is obvious through the gap of about four orders of magnitude. However, the peak brilliance is the brilliance within one single pulse. The average brilliance of the sources only differs by a margin. The peak brilliance is an important measure for experiments that rely on single-pulse measurements.

The prerequisite for X-ray spectroscopy studies is the availability of well defined, tunable, coherent, and intense X-ray light sources. Modern facilities providing these are, for example, third generation synchrotron and FEL facilities [55, 53]. The key parameter used to compare the quality of different pulsed radiation

sources is the peak brilliance B_{Pk} of a light source. This quantity is defined as the number of photons per pulse $n_{photons}$ emitted into a transverse phase space with a relative bandwidth of 0.1%

$$B_{Pk} = \frac{n_{photons}}{(0.1\% BW)\sigma_x \sigma_y \sigma'_x \sigma'_y} \quad [53].$$ (3.28)

$\sigma_x \sigma_y$ is the transverse area representing the focal spot size, $\sigma'_x \sigma'_y$ is the solid angle into which the radiation is emitted, and $0.1\,\% BW$ is a relative bandwidth around the central wavelength of the emitted radiation. The peak brilliance of a selection of light sources is shown in Fig. 3.4. It can clearly be seen that FELs have a substantial higher peak brilliance compared with modern synchrotron sources. Another parameter commonly used to compare light sources is the average brilliance B_{avg} that describes the number of photons per second rather than the photons per pulse. Therefore, the average brilliance is related to the peak brilliance by the pulse length t_{pulse} and the frequency f of the pulses, as is evident from

$$B_{avg} = B_{Pk} \; t_{pulse} \; f.$$ (3.29)

A selection of typical parameters for a third generation synchrotron, namely BESSY II, and the FEL facility LCLS are shown in Tab. 3.1. While the average brilliance is the same for third generation synchrotrons (Bessy II, for instance) and FEL sources (LCLS, for example), there are distinct dissimilarities for the other parameters. The question which source to choose depends on the specific experimental requirements, especially in terms of timing. The main advantage of FEL sources is the very short pulse duration in the femtosecond range at high peak intensities as opposed to picosecond pulses at synchrotron facilities with a lower peak intensity, but overall similar photon counts per second.

3.2.3 From Bending Magnets to Free Electron Lasers: Generation of X-ray Radiation in Synchrotrons and FELs

The first implementation of X-ray radiation through the acceleration of an electron package traversing a magnetic field at relativistic velocity was performed with a bending magnet, as indicated in Fig. 3.5 a). The broad emission characteristics illustrated in orange were further improved by the implementation of

wigglers and undulators, as shown in Fig. 3.5 b) and c), respectively. Wigglers are a series of bending magnets with alternating fields, hence the emitted power P is proportional to the number of magnets $P \propto n_{mag}$ [56], whereas the emitted radiation has a broad spectrum whose center can be adjusted by changing the kinetic energy of the electron bunch. A comparable concept is given by the introduction of undulators, where the magnetic field is much weaker than for wigglers and alternates at an adjustable undulator period λ_U.

The two concepts are typically characterized by their strength parameter K, which depends on the maximum magnetic field B_{max} and their undulator period
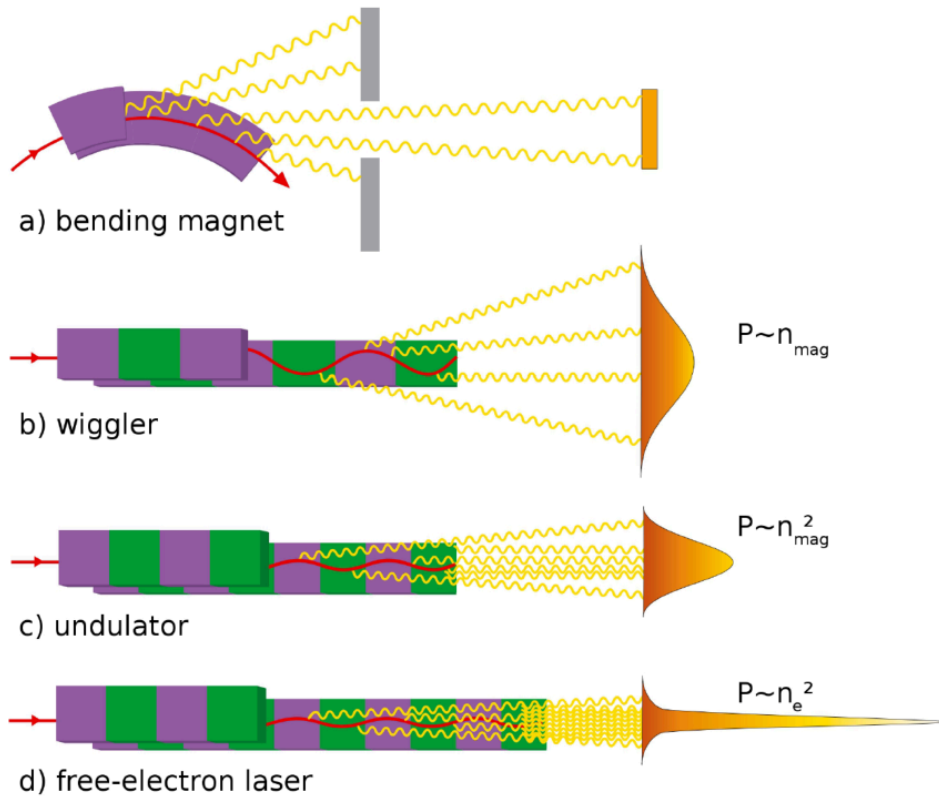
Figure 3.5: **Characteristic emission of different X-ray generating techniques which are based on electron bunch acceleration.** The different subfigures a) - d) represent X-ray generation through bending magnets, wigglers, undulators, and FELs. The red lines show the pathway of the electron bunch through the magnets indicated in violet and green for alternating field directions. The yellow lines represent the emitted X-rays and in orange the spatial power distribution P. The clear distinction from top to bottom is the increasing power distribution in a central beam. Also indicated is the (from top to bottom) increasing coherence, which is highest for a single SASE spike FEL pulse. The image is taken from [57] ©①⊖◎.

λ_U [58],

$$K = \frac{eB_{max}\lambda_U}{2\pi m_e c} \approx 0.93 B_{max}\lambda_U \quad \text{T·cm} \tag{3.30}$$

with c being the speed of light, m_e the electron mass, and e the elementary charge. Typically, wigglers have strength parameters of $K > 1$ Tcm, whereas $K \approx 1$ Tcm applies to undulators. However, as indicated in Fig. 3.5 b), in wigglers the electrons oscillate strongly, so that the emitted radiation is incoherently emitted into a wide angle and spectral distribution. Undulators, on the other hand, improve this by tuning the undulator period and the magnetic fields in a manner that their emitted radiation interferes constructively. Following Huang et al. [58], this resonance condition for the wavelength λ_r is given by

$$\lambda_r = \frac{\lambda_U}{2\gamma}(1 + \frac{K^2}{2} + \gamma^2\Psi^2), \tag{3.31}$$

where γ is the Lorentz factor of the electron bunch and Ψ the observation angle. Note that, although the undulators magnets are typically separated by a few centimeters [56], the emitted radiation is on the order of nanometers. This is originated in relativistic effects that shorten the magnetic field period the traversing electrons experience, and results in the relation between the emitted wavelength λ_r and the undulator period λ_U, as shown in Eq. 3.31. As another result, the emitted power P in an undulator scales with

$$P \propto n_{mag}^2, \tag{3.32}$$

which is also indicated in Fig. 3.5 c) [59]. From the resonance undulator wavelength Eq. 3.31 it becomes clear that an undulator can be tuned by either adjusting the magnetic field ($K \propto B$), by changing the undulator wavelength λ_U, or by tuning the electron energy ($E_e = \gamma m_e c^2$). This enables undulators to radiate with a very variable resonant wavelength depending on the conditions needed, which also explains the variation of the photon energy possible at different light sources, as shown in Tab. 3.1.

The difference between a third generation synchrotron undulator beamline and an FEL is the length of the undulator section. In a typical undulator, values here are from U49 at BESSY II, there are about 84 periods with a 49 mm

period length [60]. At the linear coherent light source FEL, the undulator section comprises 33 single undulator segments, each being comparable to one undulator section at a synchrotron. The LCLS undulator hall houses 33 undulators with 113 periods of 30 mm length, resulting in an undulator of effectively 112.8 m length [61]. Since the emitted power depends on the number of magnets as shown in Eq. 3.32, the radiation emitted from this source is significantly higher than that from a typical synchrotron beamline. However, the main difference in the pulse structure arises from the effect of self amplification by spontaneous emission (SASE), as further explained in the following section.

3.2.4 Self-Amplified Spontaneous Emission

If an electron bunch travels through an undulator, it emits radiation as explained above. With increasing undulator length, the emitted power is growing as shown in Fig. 3.6 by the blue line. Also indicated is an effect called microbunching, where, depending on the distance the bunch travels through the undulator, a modulation within the electron bunch appears until (for long undulator distances) it restructures the whole bunch to clearly separated microbunches. This effect is shown in Fig. 3.6 in form of the circled electron bunches. The effect originates from the interaction of the electron bunch with the so-called 'pondero-motive potential' from the combined undulator and radiation fields [58]. For a theoretical description of the process compare [58]. Here, both the radiation field and the electrons have a small component in the longitudinal direction that interacts depending on the relative position of the electrons to an initial electric field. This is given by the initial amplitude E_0 and the initial phase Ψ_0, respectively. It is shown to change the electron density distribution along the longitudinal direction $\frac{d\eta}{dz}$ depending on the relative time distance from the undulator entrance θ as

$$\frac{d\eta}{dz} = \frac{eK[JJ]}{2\gamma_0^2 mc^2} E_0 cos(\theta + \Psi_0). \qquad (3.33)$$

Here e is the electron charge, K the undulator's K parameter, and $\gamma_0 mc^2$ the reference energy of the interacting field, which can be slightly different from the electron energy γmc^2 [58]. As the electrons move along the undulator, their density distribution is modulated in a cosine form with the wavelength of the

initial radiation. This modulated electron density creates the microbunches that now continue to travel through the undulator and radiate photons, but instead of the broad distribution from a classical undulator, the photons radiated from one microbunch are now in phase. If the distance traveled through the undulator becomes long enough, the distance between the individual microbunches approaches the emitted wavelength, resulting in a coherent emission of all microbunches as indicated in Fig. 3.6 for the top right electron bunch. The lasing process saturates when the microbunching is fully developed. The radiation that starts the modulation is generated by the electron bunch itself, hence the name self amplification by spontaneous emission or SASE. The emitted power of such a pulse is now also proportional to the number of electrons n_e being in phase [43], scaling as

$$P \propto n_e^2 \tag{3.34}$$
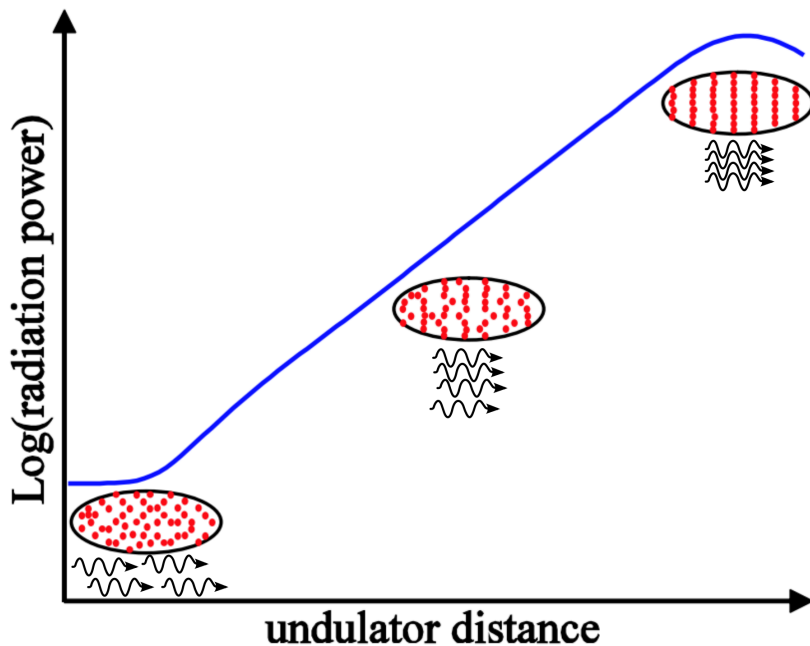
Figure 3.6: **The growth of radiation power in relation to the undulator length (blue curve).** The graphic indicates the change of the electron bunch structure with increasing undulator length and the emission characteristic of such a bunch, from unordered and out of phase for a short undulator to microbunched and coherent for a long one. When the whole electron bunch is microbunched as indicated by the top right graph, the radiation power saturates, since all radiated photons are in phase. The image is adapted from [58].

if running in SASE operation.

Since the SASE process is initiated by stochastic fluctuations of the electron bunch and spontaneous undulator induced radiation, the single SASE pulses vary in intensity, wavelength, and bandwidth, as indicated in Fig. 3.7 on the left. Here the black line shows the average spectrum over 3000 shots, which is comparable with the output spectrum of an undulator. However, the single pulses show strong fluctuations around the central wavelength. In Fig. 3.7 on the right, the temporal power profile of a SASE pulse is shown. The single-shot spectral profile in the frequency and temporal power domain are similarly spiky [58].

A special technique to gain control over the statistical fluctuations that define a SASE pulse is the seeding technique that has been recently demonstrated at the FERMI FEL in Italy [63]. As shown in Eq. 3.33, the microbunching depends on the initial field condition set by E_0 and Ψ_0. If this is now an external field, for example a high harmonic generation pulse as used in [63], one can 'seed' the initial fluctuations into the electron bunch. This technique is promising to further improve the control over the X-ray pulse parameters. However, the seeding technique is not yet available at soft X-ray sources, but will be implemented in future FEL designs such as LCLS II. The experiments discussed throughout this thesis have been performed in SASE operation at the
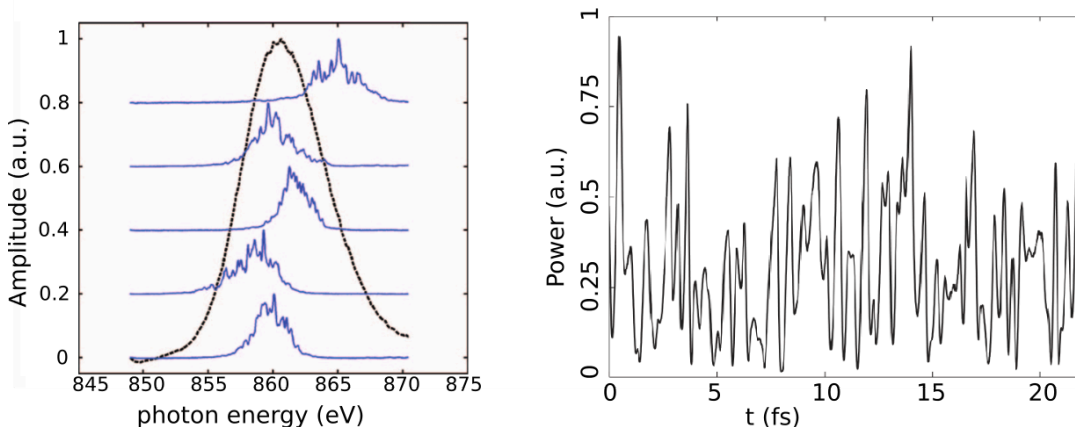
Figure 3.7: **SASE pulse characteristics. Left:** A selection of single-shot spectra in blue, measured at the soft X-ray and materials beamline at LCLS with the black line showing the average spectrum of 3000 shots [62]. The single-shot spectral scattering is clearly visible as well as the overall average in form of the Gaussian (black) SASE distribution. **Right:** A modeled temporal power profile with typical pulse-by-pulse fluctuations simulated for LCLS [58].

LCLS FEL.

3.2.5   Sample Delivery and Replacement

To utilize soft X-rays, vacuum conditions need to be met. Since one of the main interests of RIXS measurements on transition metal systems is the way function is created, which highly depends on the investigated complex's symmetry and environment, the state of the sample is of major importance. Due to this importance of the natural environments, which for biological or chemical systems is mostly the liquid phase, solid and liquid samples have to be introduced into the experiment. The latter, however, is not easily compatible with experiments in ultra-high vacuum. To circumvent this problem, a liquid jet delivery system is used when working with liquid samples. Hereby, the liquid is introduced into the vacuum through a small nozzle with a diameter of around 20 μm at typical flow rates of a few millimeter per minute. This ensures that the amount of sample introduced into the vacuum remains relatively small, which is essential for maintaining the vacuum condition required for soft X-ray transmission. For further improved vacuum conditions, the jet is directly aimed at freezing traps that capture and freeze most of the liquid, thus reducing the amount of sample flying through the experimental chamber. The velocity v of the jet, resulting from the liquid being pressed through the nozzle with the radius opening r and the flow F, can be determined by

$$v = \frac{F}{\pi r^2} \ [64].$$

(3.35)

Consequently, for typical nozzle sizes of around 10 μm to 30 μm, the resulting velocity amounts to approximately 30 m/s. At these velocities, the jet is defined by two parts: a laminar flow region for a few millimeters just below the nozzle, and the formation of droplets behind the laminar flow region [64]. As stated above, these droplets have to be trapped to prevent evaporation. The laminar area provides a region of bulk-like liquid, that can be coincided with the X-ray beam to probe the liquid phase of the sample.

Another issue occuring when working with intense photon pulses is sample damage [65, 66]. Since the X-ray photons interacting with the sample generate free electrons through the Auger process as explained in Sec. 3.1.2, a substantial

amount of energy is induced, which generates long living disturbances such as vibrations, ionizations, and consequently, bond and structure breaking. This is not a problem when working with a liquid jet as long as the jet speed exchanging the sample volume exceeds the repetition rate of the light source. For the repetition rate of 120 Hz typical for LCLS and a focus size of 100 μm^2, the sample is refreshed for every pulse at a jet speed of $v > 1.20$ m/s, which is easily achievable through typical flow speeds of about 30 m/s. For solid samples, this has to be addressed by not only decreasing the repetition rate, but also by moving the sample to a new spot in between each pulses. However, for solid samples it is much harder to refresh the light-matter interaction spot as a solid sample has to be moved with a steady light interaction region to preserve the beam focus. For the experiment described in Chapter 5, a new sample is introduced into the interaction region for every shot through sample holder movement which ensures a new sample for each shot but significantly reduces the number of FEL shots collected in the experiment as. Alternatively for lower FEL intensities or for samples with less pulse induced damage, it is possible to scan the solid sample through the beam as we did in [67, 68].

3.2.6 Spatial and Temporal Overlap

One of the most interesting application of FEL pulses is the unique possibility to perform time-resolved X-ray experiments with intense pulses in the femtosecond time range. To enable this, the interaction region, explained in the last section, has to be overlapped with a laser pulse to enable a classical pump-probe scheme. This proves a non-trivial problem that has to be solved. Throughout the work of this thesis, three steps are necessary to perform the stated experiments. First, the X-ray pulse focus has to be overlapped with the sample, which, for a liquid jet, is performed through a fluorescence yield measurement while performing an x-y-scan with the jet. For a solid sample, this is done through a transmission measurement behind a pinhole at the position of the sample. The optimum focus position of the FEL is, in both cases, the maximized signal. Next, a precise overlap between the laser and the X-ray focal spot needs to be created and maintained throughout the experiment. For this, the same procedure as for the X-ray pulse focus sample overlap is performed. In addition, an induced reflection change measurement is performed for the temporal overlap at the jet position, as explained in [69]. It is crucial to maximize the spatial and temporal overlap to

obtain meaningful experimental results with a high excited state signal. Lastly, in order to attribute for the single FEL pulse timing jitter originating from the stochastic source of the pulse, a cross correlator between the laser and FEL pulse timing is used as explained in [70, 71].

3.2.7   Spectrometer

For X-ray emission studies, a decomposition of the emitted radiation can be achieved by dispersing the emitted radiation at spherical gratings. In order to minimize the aberrations of spherical gratings, H.A. Rowland introduced the theoretical basis for the Rowland circle geometry [72], which is shown in Fig. 3.8. In this geometry, the spherical grating with a radius of 2R is positioned on a circle of radius R, the so called Rowland circle. If the photon source is positioned exactly on the edge of this circle, focusing of the energetically resolved photons will occur along this specific circle. This focusing can be described via the grating equation [72]

$$n \cdot \lambda = -d \left(sin\alpha - sin\beta \right), \tag{3.36}$$

where λ is the incident wavelength, n the diffraction order, d the grating line density, α the incident, and β the diffracted angle. It should be noted that the diffraction order is directly correlated to the energy resolution, as higher order diffractions disperse energies to a higher degree. This leads to a higher energy resolution with subsequently lower intensity [73]. In Fig. 3.8 one can see the X-ray source on the right, illuminating the spherical grating. This radiation is then dispersed and focused on wavelength dependent spots on the circle. As indicated, the detector is of planar geometry, which reduces the resolution due to the capture of unfocused photons in the area alongside the circle. This effect can be reduced by moving the detector to a position on the circle, where its center coincides with the focus of the central wavelength of interest.

For measurements during this work, unless stated otherwise, a Nordgren-type soft X-ray emission spectrometer consisting of an entrance slit, three grazing-incidence spherical gratings, and a movable detector is used [74, 75]. The detector unit assembles a micro channel plate stacked with a deflector plated on top of a phosphor screen. Outside the vacuum system is a charge coupled device (CCD) camera focused onto the phosphor screen. According to [76], the overall
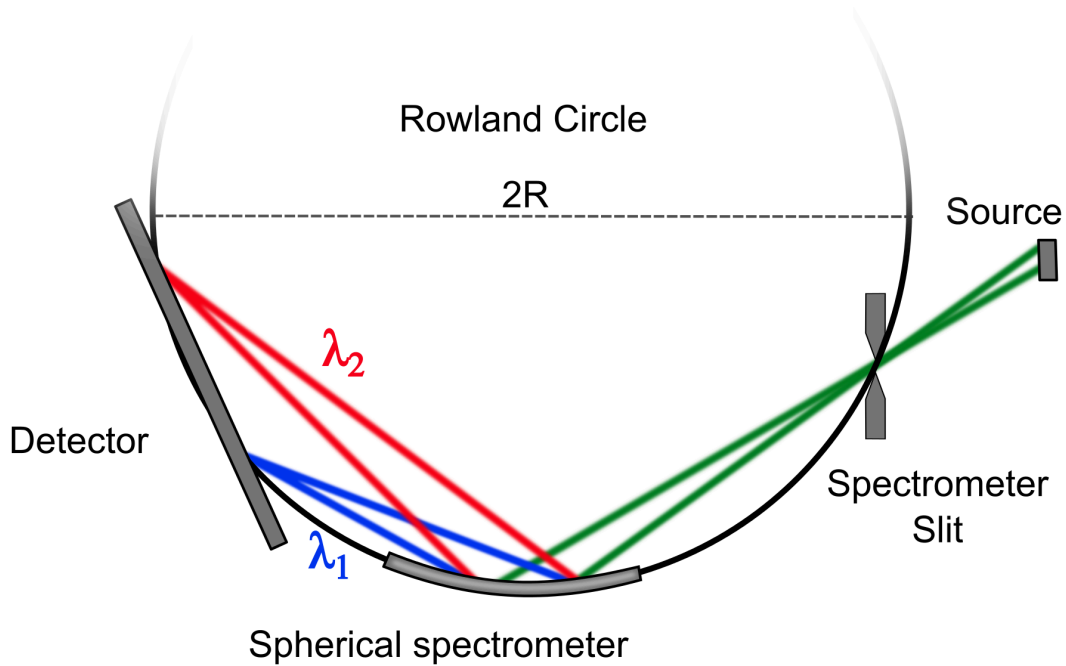
Figure 3.8: **The Rowland circle geometry, which is applied in the spectrometer.** The light emitted from the source (for example the interaction region in the sample indicated in green) falls through the spectrometer entrance slit on the spherical grating. The grating focuses the light on different spots on the Rowland circle depending on its wavelength, as indicated in red and blue. The detector is placed on the Rowland circle to maximize the resolution at a chosen wavelength. The resolution reduces when receiving wavelengths that are focused on Rowland circle positions far from the detector position and are, therefore, unfocused on the detector.

spectrometer efficiency is 10^{-7}, which accounts for the grating efficiency, the geometrical acceptance, and the detector efficiency.

Chapter 4

Implications of Intense Photon Fields on Soft X-ray Spectroscopies

As a result of the implementation and development of modern X-ray sources with an ever increasing peak brightness (compare Fig. 3.4), the X-ray-matter interactions increase in complexity due to the onset of non-linear effects. Although evoking new challenges for an equally in complexity growing data analysis, this also opens up new opportunities of transferring spectroscopic methods from the non-linear optical regime to X-ray spectroscopy.

With the now established FEL sources, photon-hungry spectroscopic methods such as RIXS or coherent diffractive imaging [77] become more and more exploitable for low sample volumes and ultra-short time resolved experiments [78, 79, 80]. These types of experiments, however, still demand a high photon intensity in a small sample volume in order to be feasible, as discussed in Sec. 3.2. This results in the requirement of an increased light field strength, which in turn pushes the light-matter interaction into regimes where the light field might induce a non-linear response. The occurrence of non-linear effects was observed in various experiments during the last years [29, 37, 81, 82, 83, 84, 85]. As these effects may also occur in classic spectroscopic experiments not aimed at these non-linear aspects, this asks for a discussion on the implied effects of intense light fields on commonly applied spectroscopic methods. This field is rather new to the X-ray spectroscopy community, hence it is rarely noted that non-linear implications can complicate experimental findings.

For this reason, this chapter focuses on the implications of intense photon fields on soft X-ray spectroscopies. In particular, the light field driven change of light-matter interaction is discussed based on the emergence of the first order non-linear effect of stimulated emission within a single light pulse. Before venturing into the discussion of the recently observed stimulated effects and their implications on modern spectroscopy, a short introduction into the treatment of non-linear light-matter interactions seems important. To understand this aspect, an introduction into the well established concept of the non-linear susceptibility is given, followed by a discussion of the intensities in FEL experiments with a special focus on the relation between spontaneous and stimulated emission. Secondly, we will discuss how the onset of stimulated emission changes the pulse propagation through a sample, and how it affects scattering and transmission. A special focus is put on the continually changing interplay of spontaneous emission, stimulated emission, and Auger decay, which manifests itself in the observation of effects such as self-induced transparency, self-focusing, scattering breakdown, and pulse induced damage. We believe that these phenomena will play a key role not only for carrying out new experiments, but even for the re-interpretation of already published data from a new point of view. To emphasize how the increasing intensity can be a double-edged sword for experimental interpretations, the above mentioned effects are discussed using the examples of some experiments which may have been affected by these [86]. Finally, we briefly review recent advances in the area of multidimensional X-ray spectroscopy.

4.1   Light-Matter Interactions at High X-Ray Fluences

4.1.1   Non-Linear Susceptibility

The classical approach to non-linear light-matter interactions connects the generalized electric polarization $\vec{P}(\vec{r}, t)$ of a system with the field strength $\vec{E}(\vec{r}, t)$ of an applied optical field through the wave equations

$$\left[\nabla^2 + \frac{\partial^2}{c^2 \partial t}\right] \vec{E}(\vec{r}, t) = -\frac{4\pi}{c^2}\frac{\partial^2}{\partial t^2}\vec{P}(\vec{r}, t) \tag{4.1}$$

$$\nabla \vec{E}(\vec{r}, t) = -4\pi \nabla \vec{P}(\vec{r}, t) \ , \tag{4.2}$$

which originate from Maxwell's equations. Here, the polarization includes not only the electric dipole, but also all multipole contributions of the interacting atom, molecule, or matter [87]. In case of linear optics and weak fields, the induced polarization

$$\vec{P} = \epsilon_0 \chi^{(1)} \vec{E} \tag{4.3}$$

is linear in $\vec{E}$ with the linear susceptibility $\chi^{(1)}$ and the vacuum permittivity ϵ_0. Following the common description, the polarization and electric field strength are expanded into their Fourier components

$$\vec{E}(\vec{r}, t) = \sum_n \vec{E}(\omega_n), \tag{4.4}$$

$$\vec{P}(\vec{r}, t) = \sum_n \vec{P}(\omega_n) \tag{4.5}$$

$$\text{with} \quad \vec{E}(\pm\omega) = \frac{1}{2}\vec{\xi}_n e^{\pm i\vec{k}\vec{r}} \ . \tag{4.6}$$

Accordingly, the polarization can be written as a power series with the nth order susceptibility tensor $\vec{\xi}^n$.

$$\vec{P}(\omega) = \vec{\chi}^{(1)}\vec{E}_{(\omega_i)} \tag{4.7}$$

$$+ \sum_{j,k} \chi^{(2)}(\omega_i = \omega_j + \omega_k) : \vec{E}_j \vec{E}_k \tag{4.8}$$

$$+ \sum_{j,k,l} \vec{\chi}^{(3)}(\omega_i = \omega_j + \omega_k + \omega_l) : \vec{E}(\omega_j)\vec{E}(\omega_k)\vec{E}(\omega_l) \tag{4.9}$$

$$+ \dots \tag{4.10}$$

Note that the susceptibility tensor's dependence on $\vec{k}$ is neglected owing to the electric dipole approximation $e^{i\vec{k}\vec{r}} \approx 1$, which is typically applied in soft X-ray spectroscopies. For understanding non-linear X-ray-matter interactions within this approach, it is key to determine the susceptibility tensor, which is, however, not easily achievable, but gives a full description of any non-linear phenomena if done correctly.

In the following discussion, we concentrate on the third order susceptibility, since the described processes all fall within the interactions described by this term, i.e. stimulated Raman or Stokes scattering and (four) wave mixing. For an estimation of $\chi^{(3)}$, one can use the centro-symmetric an-harmonic oscillator model presented by Boyd ([88]), adapted to the electronic Raman scattering case

$$\chi^{(3)}(\omega_2 = \omega_2 + \omega_1 - \omega_2)/N \tag{4.11}$$

$$\approx \frac{e^4 \omega_0^2}{\epsilon_0 m^3 r_a^2} \left(\frac{1}{\omega_0^2 - \omega_2^2 - 2i\gamma\omega_2} \right)^2 \left| \frac{1}{\omega_0^2 - \omega_1^2 - 2i\gamma\omega_i} \right|^2 \ \text{[31]}. \tag{4.12}$$

As shown by Patterson, the model shows quite good agreement with detailed calculations from other models [31]. Boyd classifies two types of interactions, one where the initial and final electronic state remains unchanged, and one where the material experiences a transmission into a different electronic state [88]. These processes are called parametric and non-parametric, respectively. The important point here is that a parametric process can be described by the real part of the susceptibility, whereas a non-parametric process can be described by the complex part of the susceptibility.

Two different approaches to treating light-matter interactions are common. The classical one, as briefly introduced above, relies on the calculation of non-linear susceptibilities through the induced polarization, whereas the quantum mechanical approach relies on the calculation of transition rates and cross sections, as described in Chapter 3. Further theoretical discussions and developments on non-linear X-ray-matter interactions go beyond the scope of this discussion, but there are interesting discussions about the treatment of non-linear interactions. Out of these I would like to point your attention to an interesting study that generalizes the Kramers-Heisenberg cross section (Eq. 3.20), to enable its application within the non-linear regime, and thus enabling calculations of non-linear X-ray cross sections through the susceptibility [89].

4.1.2 Stimulated vs. Spontaneous Emission

As discussed in Sec. 3.1.2, light-matter interactions are commonly described through their respective cross sections. To understand how light-matter interactions change with rising pulse intensity, a formalism to treat the decay cross sections in an intensity dependent way is being discussed in the following. The

formalism to treat stimulated scattering at optical frequencies, as derived by Lee and Albrecht [90], was recently applied to the X-ray regime by Patterson [31], who discussed the extended possibilities of such effects and estimated approximate magnitudes of the experimental parameters, required in order to observe stimulated scattering. In this treatment, the spontaneous emission is regarded as a stimulated emission of the vacuum or zero point field, respectively.

$$\frac{\delta^2 \sigma_{stim}}{\delta\Omega\delta\omega_2} = \frac{\hbar\omega_1\omega_2}{2\epsilon_0 c^2} F(\omega_2) \frac{Im(\chi^{(3)})}{\rho} \tag{4.13}$$

Equation 4.13 describes the stimulated scattering cross section of an incident photon at frequency ω_1 into the frequency interval $[\omega_2, \omega_2 + \delta\omega_2]$ and the solid angle $\delta\Omega$ in the presence of a photon field at frequency ω_2 that is given by the spectral photon flux $F(\omega_2)$. The medium is represented by the third order susceptibility $\chi^{(3)}$ and the density of scattering centers ρ. Schreck et al. applied this formalism to a dense medium that excludes saturation effects [30]. Thereby, they derived the following expression for the total scattering cross section as

$$\sigma_{total} = \sigma_{spon} \left(\underbrace{1}_{\sigma_{spon}} + \underbrace{\frac{1 - \omega_{fy}}{\omega_{fy}}}_{\sigma_{Auger}} + \underbrace{\frac{4\pi^2 c^2}{\omega_2^2} F(\omega_2)}_{\sigma_{stim}} \right) , \tag{4.14}$$

where the fluorescence yield ω_{fy} determines the ratio between the spontaneous emission and the Auger cross section. The light-matter interaction in this formalism can be understood as driven through a perturbation which induces the interaction process. In the case of Auger decay, the driving force is the strong Coulomb field of the nuclei. In the case of spontaneous emission, it is the zero point electromagnetic (vacuum) field or the usually weak photon field, respectively. When the electromagnetic field becomes comparably strong as the Coulomb field, the spontaneous emission becomes stronger than the Auger decay, which results in an increased emission cross section, here indicated through the stimulated emission cross section [30]. This idea enables a comparison of the different contributions to the total scattering cross section for different experimental parameters, as shown in Fig. 4.1.

First, it can be seen that the ratio between the spontaneous and the stimulated cross section changes with the resonant excitation energy. In the soft X-ray regime, Auger decay dominates over spontaneous emission, whereas in the hard
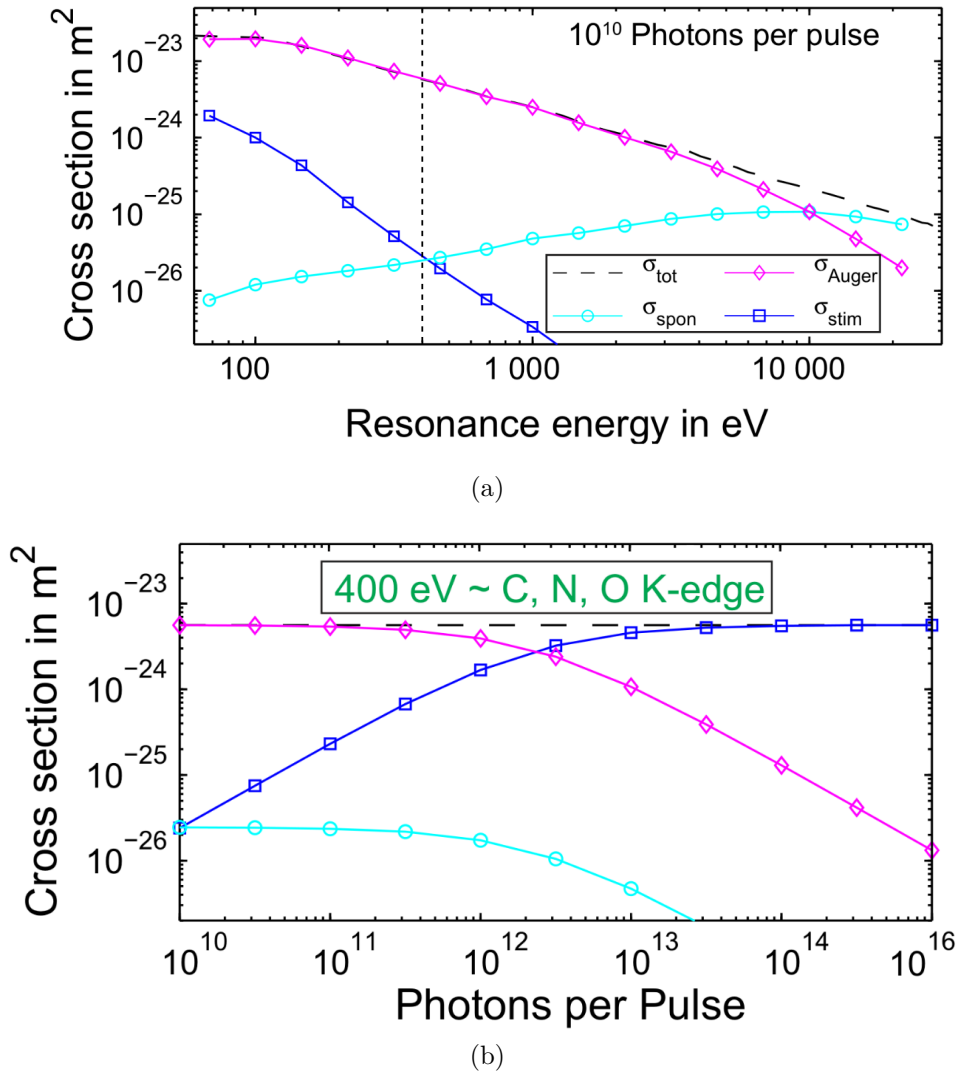
(a)

(b)

Figure 4.1: **(a):** The ratio between the individual contributing cross sections is shown in relation to the incident photon energy. The total cross section (black) is the sum of the spontaneous (cyan), stimulated (blue) and Auger(pink) cross section. **(b):** Contributing cross sections at a fixed incident energy versus incident photon flux. The simulated cross sections where calculated for a 10 fs pulse of 0.5% bandwidth and a focal size of 50 μm^2. The figure was adapted from [30] with courtesy from S. Schreck.

X-ray regime at around 10 keV, spontaneous decay starts to exceed Auger decay, as shown in Fig. 4.1 on the left-hand side. Secondly, the stimulated cross section rises with increasing photon flux and starts to surpass the Auger decay at around 10^{12} photons per pulse, which is the estimation for photon numbers within a short LCLS pulse and, consequently, within the range of observable processes [47]. The corresponding resonance energy of 400 eV in Fig. 4.1 top is indicated by a dashed line as a guide to the eye. The simulations of the cross

section distributions were performed with an estimated focus size of 50 μm^2. The capabilities for X-ray focal spot sizes are way below this, going down to orders around ≈ 1 μm^2, which further increases the effective photon flux [91]. The stimulated cross section decreases with increasing photon energy, indicating that stimulated scattering is more likely observable at smaller photon energies. Nonetheless, this has indirectly been observed at hard X-ray energies, as shown in Fig. 4.3 and discussed below.

4.2 Implications of Single Pulse Self-Induced Effects on Soft X-ray Spectroscopies

In this section, the implications of non-linear, especially stimulated, effects on X-ray spectroscopies are discussed. All effects discussed here are compared to experimental evidence. Self-induced effects are those occurring during the interaction of one pulse with the sample on the timescale of the pulse length, and are, hence, induced by the pulse itself. Fluences on the order of 10^{10} photons per pulse which are estimated to equalize the amount of stimulated and spontaneous effects (Fig. 4.1), are achievable at FEL and even sometimes at modern synchrotron sources [47]. Therefore, it is critical to understand what happens when stimulated effects start to overtake and thereby change the experimental outcome. Here we discuss three aspects of stimulated scattering, namely self-induced transparency, self-focusing, and the breakdown of scattering intensity before first applications of stimulated scattering are shown.

4.2.1 Self-Induced Transparency or Saturable Absorption

The effect of saturable absorption is well known from non-linear optical spectroscopy and takes place in almost any medium if the incident pulse fluence is close to the damage threshold of the sample. It is either called saturable absorption [92] or self-induced transparency [93]. In either case, the self-induced transparency is created by the strong excitation of the sample, meaning that almost every possible absorption event takes place. When the sample is stripped of electrons in the core level, the basic requirements for an absorption process are not fulfilled anymore and thereby the photon passes unaffected through the

sample. To be fair, a complete excitation is difficult to realize, but still has been observed for multi-ionization experiments at FEL sources [94, 95]. However, the saturation of absorption starts to set in when a significant amount of electrons is excited, which is discussed in common non-linear optics literature, such as for example [88]. As indicated above though, stimulated emission also plays a crucial role related to this effect. When the light field strength increases, the

(a)

(b)

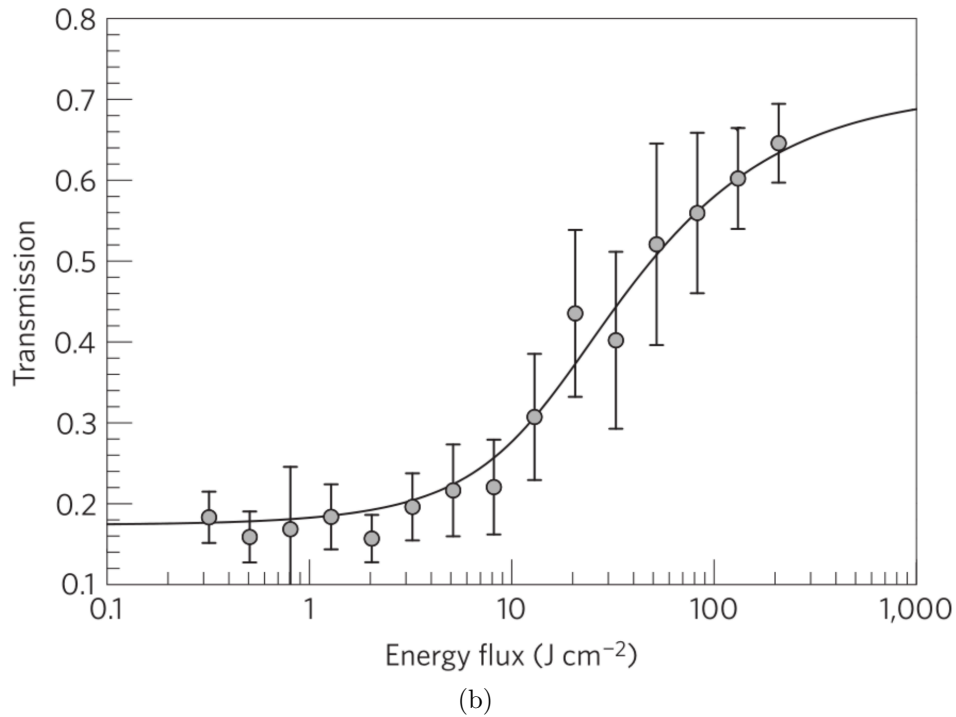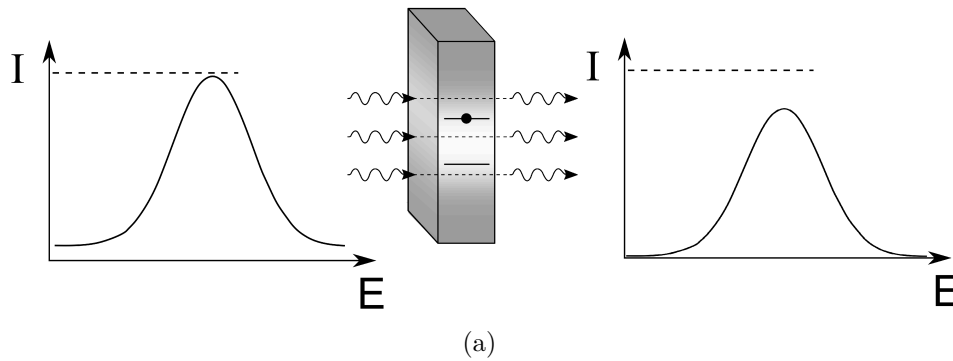Figure 4.2: **(a):** Schematic illustration of self-induced transparency. The front of the pulse excites the majority of electrons within the sample, thus rendering it transparent for the following photons while only loosing a fraction of its total intensity I through absorption. **(b):** The experimental data was recorded by Nagler et al. at the Al L-edge (92 eV) and shows fluence dependent self-induced transparency [84].

probability of stimulated scattering also increases. Any stimulated photon is indistinguishable from its stimulating photon, therefore the stimulated one travels in the same direction as the latter one, effectively increasing the intensity in the forward direction of the beam. The more stimulated photons there are, the higher is the effective transparency in the sample. Additionally, the sample can only absorb a maximum number of photons up to an excited state population of around 50 %, where the amount of absorptions and stimulated emissions merges. Such a behavior has been simulated by Stöhr et al. for thin Co films at the Co L-edge [37], where they stated this to be observable at today's FEL light sources for short pulses.

The principle of self-induced transparency is shown in Fig. 4.2, where the schematic pulse-sample interaction is shown to the top. At the bottom, a measurement by Nagler et al. can be seen, illustrating the fluence-dependent change of the sample transmission in thin Al-films at the Al L-edge (92 eV) [84]. Fig. 4.2 clearly shows an increase in transparency in dependence of the incident fluence as explained above. In the discussion around Fig. 4.1, the occurrence of stimulated emissions was stated to be more likely for lower X-ray energies, however, the phenomenon has also been observed at hard X-ray energies at the iron K-edge (7.1 keV) [81] and in neon gas targets [96]. In the case of a low density gas target, the authors explain the transparency by the complete ionization of the gas, which is a second possible pathway for the light pulse to render the sample effectively transparent.

Whether all interacting atoms are striped off their inner shell atoms or the majority of the sample is in a core excited state, the effect on the transmission of the pulse is the same: it becomes more transparent. Would the same amount of energy absorbed by the front of the pulse be injected back into the pulse through stimulated emission, the sample would become completely transparent.

4.2.2 Self-Focusing through Saturable Absorption or Stimulation

Whenever saturable absorption occurs for a Gaussian shaped pulse, the transmitted pulse will experience self-focusing, as indicated schematically in Fig. 4.3. It can be seen that the pulse absorbs approximately the same number of photons along its transverse profile, which in turn results in a narrower transmitted profile (Fig. 4.3 top). This so-called self-focusing of the incident pulse was ob-

(a)

(b)
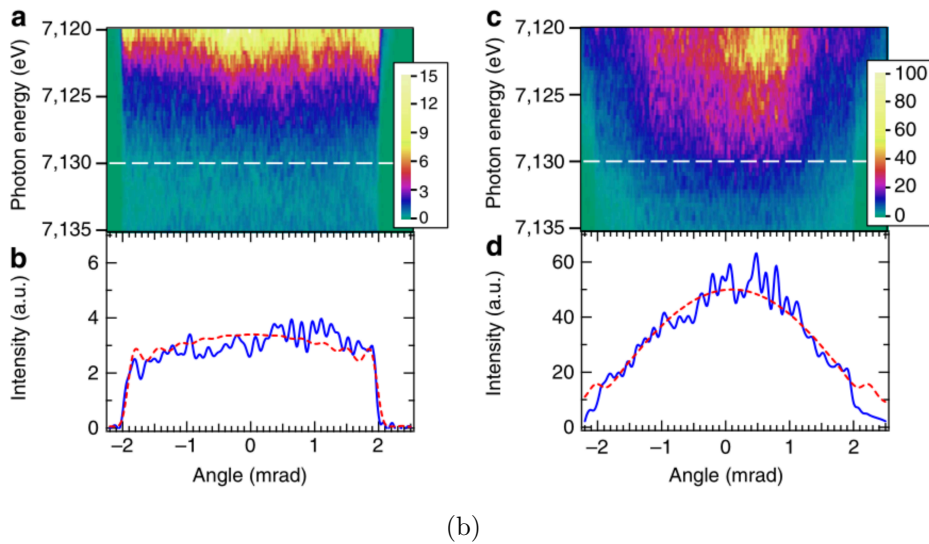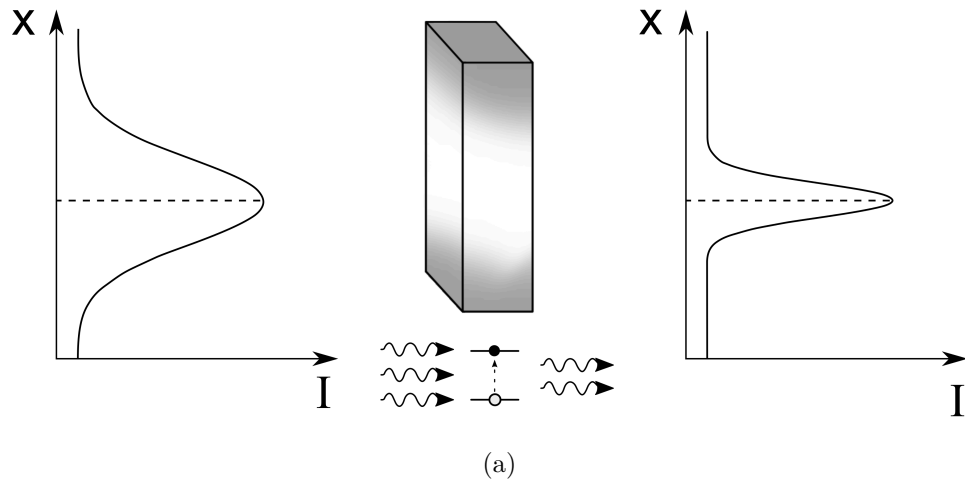
Figure 4.3: **(a):** A schematic explanation of self-focusing through saturable absorption. When intense pulses pass through a material with saturable absorption behavior, the transmitted pulse is focused, as shown at the top. At the bottom, experimental data by Yoneda et al. is shown. In this paper, they noticed the focusing effect in angular resolved transmission spectra at the iron K-edge (7130 eV) [81].

served by Yoneda et al. at the iron K-edge (7130 eV), as shown in Fig. 4.3 at the bottom. In addition to that, a second aspect has to be considered. As indicated in Fig. 4.1, the cross section for stimulated scattering increases with increasing incident fluence. This results in a change of the ratio between spontaneous and stimulated emissions, as discussed in [30]. Since all stimulated photons are indistinguishable from the stimulating field, the occurrence of stimulation results in an increase in forward scattering, as explained in Sec. 4.2.1. Because stimula-

tion depends on the photon field strength, it occurs predominantly at the center of the incident Gaussian profile, thereby increasing the induced transparency and effectively also the self-focusing effect. In non-linear optics, self-focusing is merely due to the intensity dependent refractive index changes, which reflects intensity into the area with the lowest refractive index and thus effectively into the area with the highest light field intensity. To realize focusing for X-ray pulses, this concept can be expanded to include the effect of stimulation and saturable absorption and may, as Yoneda et al. point out [81], be used to improve X-ray pulse fronts and focal sizes.

4.2.3 Scattering Breakdown

Another important self-induced change in the light-matter interaction is the breakdown of scattering signals, as indicated in Fig. 4.4. As discussed above (Sec. 4.2.1), the emergence of stimulated emission strongly depends on the incident photon fields strength. Since stimulated emission is a forward directed scattering and the overall scattering is mostly dependent on the absorption cross section, the presence of stimulation reduces the rate of spontaneously emitted photons available for scattering. Additionally, saturable absorption effectively lowers the absorption cross section, which in turn reduces the total amount of scattering processes. All the above together result in a reduction of scattering intensity independent of the reaction of the material to the pulse, and thus independent of the experimental setup. This could be of particular interest for the demagnetization dynamics discussion, as it affects especially magnetic scattering experiments.

The scattering breakdown effect was independently observed by Müller et al. [97] and Wu et al. [98] in different magnetic scattering experiments. Both observations are shown in Fig. 4.4 at the bottom, and in both cases the scattering signal reduces as the incident fluence increases. This example shows how classical interpretations of these experiments may be difficult due to potentially overlapping effects: stimulated scattering reduces the overall scattering signal as it pushing photons in the forward direction, whereas magnetic demagnetization is well known to reduce the scattering signal by itself.

To improve the understanding of this interplay of effects, Stöhr et al. developed a model to investigate the effective excited state population within a two level system, which gives rise to the domination of stimulated channels at
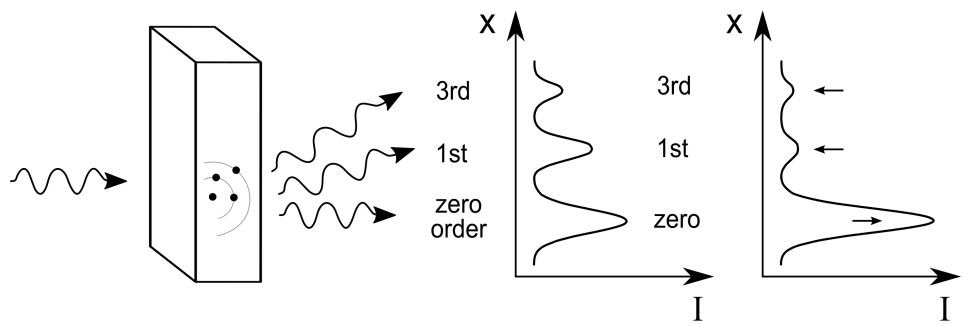
(a)
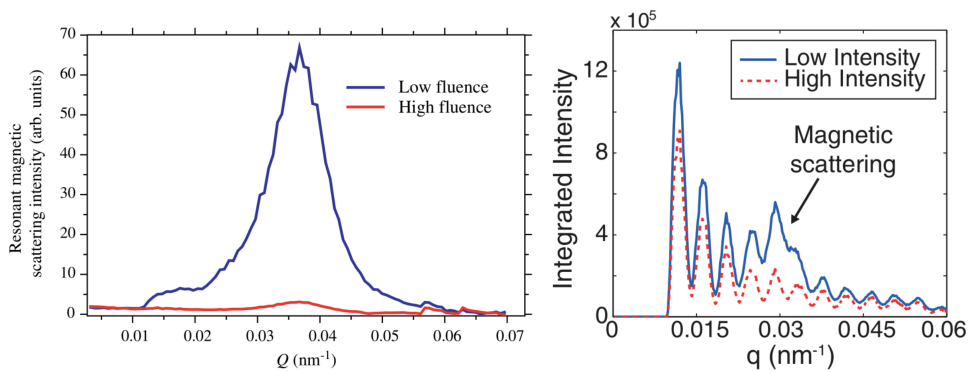
(b)

Figure 4.4: **(a):**The schematic shows a typical scattering experiment for two cases of different incident fluences. When the incident pulse induces transparency or stimulation in the sample, spontaneous emission is suppressed, which pushes the transmitted light intensity into the forward direction. **(b):** Two magnetic scattering experiments by Müller et al. (left) and Wu et al. (right) are shown, where they observed the decrease of scattering intensity by increasing the incident pulse fluence [97, 98].

the cost of scattering (or the spontaneous channel for that matter) [37]. At this point, it cannot be said whether this effect changes the common interpretation of a scattering change as a direct proof of magnetization or demagnetization [99, 100], but it has to be taken into account when trying to understand scattering intensity dependent results. However, there is also a way to directly observe the onset of stimulated emission, namely the measurement of the spectral distribution of the transmitted direct beam. In case of stimulated emission, not only a transparent sample will be observed, but the stimulation within an absorption band will also result in an increase of transmitted intensity at the lower end of the absorption edge. This is due to the fact that at the lower end of the absorption band, it is more likely to create an inversion, which is a result of ultra fast

electron cascades as simulated by Ziaja et al. [101]. In this paper, they show that ultrafast electron cascades affect the sample already within the first femtoseconds after excitation, and that these cascades are dominated by low energy electron scattering, which shakes up the occupied electrons around the Fermi energy and therefore effectively increases the possibility of an electron-hole pair recombination at the lower energy end of the absorption band.

4.3 Experimental Evidence of Stimulated Scattering and Beyond

The experiments in the discussion above give clear indications of the presence of stimulated scattering. However, Sec. 4.2 did not discuss the occurrence of stimulation itself, but rather experimental evidence pointing towards it. As discussed by Schreck et al. [30], stimulated emission depends on the photon field strength and on the incident photon energy. In Fig. 4.1 to the top, the dependence of the stimulated scattering cross-section from the incident photon energy is shown. The higher the photon energy becomes, the smaller is the stimulated scattering cross section. Hence it seems reasonable that the first observation of amplified spontaneous emission in the soft X-ray regime reported by Beye et al. [29], occurred at the silicon L-edge (around 115 eV) in crystalline silicon. Here they observed an amplification of the fluorescence yield signal that could be backtracked to the geometry of the excited volume in the sample, which then indicated the amplification of spontaneous emission along the excited sample volume. The first direct observation of stimulated resonant X-ray Raman scattering was observed at an atomic gas target by C. Weninger et al. [102].

4.3.1 Atomic Inner-Shell X-ray Laser

The onset of stimulated scattering opens new ways to generate fully coherent X-ray lasers through the stimulation of inner-shell transitions, which could generate X-ray pulses with full temporal coherence, ultra-short pulse duration, and extreme spectral brightness [83]. For this idea to work, the FEL pumps a gas target, which in the following relaxes within the core hole lifetime. But as in a classical laser, the FEL pump generates an inversion which enables the spontaneous emission from the target to be amplified through stimulated scattering, which results in a completely coherent inner-shell laser pulse. This has been

reported for a 1.46 nm wavelength transition at single ionized neon gas targets by Rohringer et al. [83], and for a wavelength of 1.5 Å at solid copper targets by Yoneda et al. [82]. As explained above, for example in Fig. 4.1 or [30], stimulated scattering in the hard X-ray regime is much less efficient. To still enable X-ray lasing in this regime, a seed is needed in order to amplify the emission at the seed wavelength. This is the technique Yoneda et al. exploited in [82]. To make these X-ray inner-shell lasers relevant for actual applications, one needs to expand their capabilities to a wider range of wavelengths. In their paper Kimberg et al. provided a study on lasing in diatomic molecules that expands these capabilities to a whole new set of possible lasing wavelengths [103]. This development is quite interesting, since it enables X-ray pulses at selected wavelengths with an extremely narrow bandwidth and pulse length.

4.3.2   Towards Controlled Multi-Pulse X-ray Spectroscopy

The logical conclusion of the evolving field of non-linear X-ray spectroscopy is to expand the experimental capabilities to multi-pulse experiments. The concept of four-wave mixing is one of the most promising ones, as discussed by Mukamel et al. [104, 105, 106]. In these publications, Mukamel et al. also discuss the theory behind four-wave mixing, including the experimental requirements. This technique could extend the possibilities of X-ray spectroscopies by the capabilities of non-linear optics. The authors also mention that the required control over two incident pulses could potentially be achieved through stimulated RIXS, which will be introduced in the next chapter. A number of other aspects of X-ray multi-pulse experiments have also been the focus of various groups, as described in the following.

The first step on the route to controlled non-linear spectroscopy is the achievement of any type of wave mixing in the X-ray regime. It was almost half a century ago that Eisenberger et al. and Freund et al. described the modulation of X-ray photons through optical/small wavelength photons and predicted the experimental observations we see today [107, 108, 109]. The first observation of optical and X-ray wave mixing was recently reported by Glover et al. [110]. They managed to perform sum-frequency generation between an X-ray and an optical photon. Consequential, the observation of sum-frequency generation leads to the question whether parametric down-conversion is feasible, since it is the inverse wave mixing process. And indeed, it has been observed

in the extreme ultra-violett (XUV) region by Tamasaku et al. [85] and in the X-ray regime by Shwartz et al. [111]. Mixing of an optical and an X-ray photon was observed, therefore the next step is the mixing of two X-ray photons. The simplest step of X-ray-X-ray mixing is second harmonic generation. This process was reported by Shwartz et al. [112] for hard X-ray pulses at LCLS. The first report of a successful four-wave mixing experiment at an FEL source was published by Bencivenga et al. [113]. They were able to realize four-wave mixing experiments in the XUV regime, showing the principal feasibility of FEL light sources for such experiments.

4.4   Summary

This chapter has discussed the occurrence of non-linear effects in the X-ray regime, using the example of the onset of stimulated emission. Since this is the first order of non-linear effects occurring due to the presence of intense photon fields, it will subsequently be relevant for the first set of controlled non-linear experiments in the X-ray regime. The fluences where stimulation occurs are well within the range of modern FEL facilities. A way to understand the impact of simulation is the concept of the intensity dependent decay cross sections which where discussed in detail. As a result of the shifting decay cross sections from Auger and spontaneous emission towards stimulated emission, a number of experimental observations occurred. All these observations open the way to transfer experimental capabilities from the non-linear optical field to the X-ray-matter interactions. However, to enable the utilization of these techniques, we have to improve our understanding of single-pulse self-induced effects. As a first experimental aspect, the observation of self-induced transparency or saturable absorption due to the high number of photons in the X-ray pulse and the full excitation of the medium were discussed. This was followed by a discussion on self-focusing through saturable absorption or stimulation. Since this effect is a direct result of the self-induced transparency, with the transparency having a lateral profile through the sample, the effect reduces from the central (high intensity) portions of the pulse towards the edge resulting in an effectively narrower transmitted pulse. Finally, the reduction of scattering intensity due to the increasing occurrence of stimulated scattering was discussed. This effects shifts the ratio of scattered photons to transmitted photons towards the transmission due to the nature of stimulation being directed parallel to the incident pulse.

All these aspects have to be taken into account when attempting to interpret experiments performed at extremely high photon densities within the X-ray regime. However, there are already groups trying to push the idea of multidimensional spectroscopy such as higher harmonic generation, parametric conversion, and four-wave mixing in the X-ray regime. These First findings where discussed in the final part of this chapter. As stimulated scattering is a promising candidate to push the limits of RIXS to higher selectivity and improved photon yields, the next chapter focuses on an experimental approach to reveal these available transition channels.

Chapter 5

Stimulated RIXS: Single-Shot Spectroscopy and Scattering Reveal Hidden Channels in Magnetic CoPd Thin Films

RIXS is a powerful tool to study a broad variety of systems. Since it allows to investigate charge, vibronic, spin, and orbital degrees of freedom, as discussed in Chapter 3, there is a strong interest to exploit this spectroscopic tool for the investigation of different materials. The major drawback of RIXS is the low fluorescence yield of less then 1% in the soft X-ray regime, which is surpassed by the Auger decay that generally covers $\approx 99\%$ of the relaxation processes [49]. This leads to the need for high photon densities or rather long measurement times not feasible for time resolved experiments. The limited number of FEL sources available and the relevance of RIXS measurements for the understanding of complexer molecular dynamics increases the interest in improving the RIXS photon output in any possible way. Therefore, it is of fundamental interest for the future development of RIXS measurements to increase the fluorescence yield. As a result of the tremendous advances in FEL performance in terms of pulse

People who contributed to this experiment, the analysis and discussions:
Zhao Chen[1,*], Dan Highley[1,*], Markus Hantschmann[2,*], Martin Beye[3], Joachim Stöhr[1] and Alexander Föhlisch[2].
1 Stanford Linear Accelerator Center, 2575 Sand Hill Rd, Menlo Park, CA 94025, USA
2 Helmholtz-Zentrum Berlin, Institute for Methods and Instrumentation for Synchrotron Radiation Research, 12489 Berlin, Germany
3 Desy Photon Science, Notkestr. 85, 22607 HAMBURG, Germany
* Contributed equally

intensity and control over the pulse parameters such as shape, energy, length, and coherence, for example, new opportunities to enhance the fluorescence yield or the amount of gathered information opened up.

The idea of a stochastic pump-probe RIXS scheme proposed by Rohringer et al. [114], for instance, intends to use the stochastic distribution of the SASE pulses in combination with an X-ray pump-probe scheme to expand the amount of extracted information. The other approach, investigated in this thesis, is the amplification of the RIXS signal through stimulated emission, where the fluorescence channel of interest is amplified by an external electrical field. This can be the photon field of the incoming pulse or the photon field of the spontaneous emission channel, for example. The effect of stimulated scattering, first observed by Beye et al.[29] and C. Weniger et al.[102], turned out to be a promising approach, since this effect directly boosts the cross section of the fluorescence decay and thereby decreases the Auger decay efficiency as shown in [30]. It is of particular interest to search for direct experimental evidence of stimulated RIXS and a way to exploit this to increase the photon yield of the relevant interaction channels in the investigated system.

In this chapter, an experimental approach to reveal the feasibility of stimulated RIXS will be discussed. For this purpose, a single-shot RIXS experiment on magnetic CoPd samples was designed and performed at the LCLS FEL source. The experiment, as well as the results will be discussed and are to be published soon. In this experiment, a first direct observation of stimulated RIXS in a solid sample is presented, continuing on the path given by the first observation of amplified spontaneous emission in the X-ray regime by Beye et al. [29]. The chapter finishes with the first publication originating from this experiment, whocj focuses on the scattering loss and increase in transparency discussed in detail below [115].

5.1   Boosting the Fluorescence Channel While Suppressing the Auger Channel

For RIXS, the fluorescence emission channel is the channel that transports the information about the medium, as discussed in Chapter 3. Since a core excited system decays through either spontaneous emission or Auger decay, the ratio

between the two determines the amount of information, that is the number of photons extractable through the RIXS process. Typically $\approx 99\%$ of the core holes decay through Auger decay and only $\approx 1\%$ decay through spontaneous emission. Considering that spontaneous emission is an isotropic process, only a fraction of this 1% of all decays can be captured in a RIXS measurement. The question that arises is, whether it is possible to increase the fluorescence channel's cross section or decrease the Auger decay cross section. The first process capable of doing this is the stimulated emission, as we discussed from the intensity dependent cross sections in Sec. 4.1.2. Considering the possibility to stimulate the fluorescence channel, this ultimately leads to an increased RIXS cross section while effectively suppressing the Auger cross section.

The stimulated emission cross section is, furthermore, dependent on the third-order non-linear susceptibility $\chi^{(3)}$ and the number of scattering centers in the medium ρ. The resulting relationship between the cross sections for different X-ray energies and light field power densities was shown in Fig. 4.1 in dependence of the incident fields power density or photon numbers, respectively. In Fig. 5.1, the intensity dependent cross sections around the energy of common transition metal L-edges, such as Fe or Co for example, can be seen. The different sub-figures show different incident pulses X-ray energies, chosen to be on the order of typical material absorption edges. It is clearly visible that the Auger and spontaneous cross section decrease with increasing incident field strength, while the stimulated cross section increases, leaving the total cross section unchanged as the model depicts. For incident photon numbers between $10^{12} - 10^{13}$ photons per pulse, strong changes in the cross sections can be observed. These photon counts are achievable at single short LCLS pulses [47]. Since the total relaxation cross section depends on the absorption cross section, it is clear that the process of resonant excitation must be investigated in order to be able to observe the changes induced by this effect. In addition, it should be noted that by increasing the stimulated emission cross section, the scattering is pushed into the forward direction, resulting in a change from the isotropic scattering towards a forward dominated scattering scheme. This increased forward scattering at the cost of the isotropic scattering has to be observable in the form of a fluence dependent scattering decrease.

In order to demonstrate stimulated RIXS experimentally, a material system showing some kind of non-linear interaction in the soft X-ray regime was to be
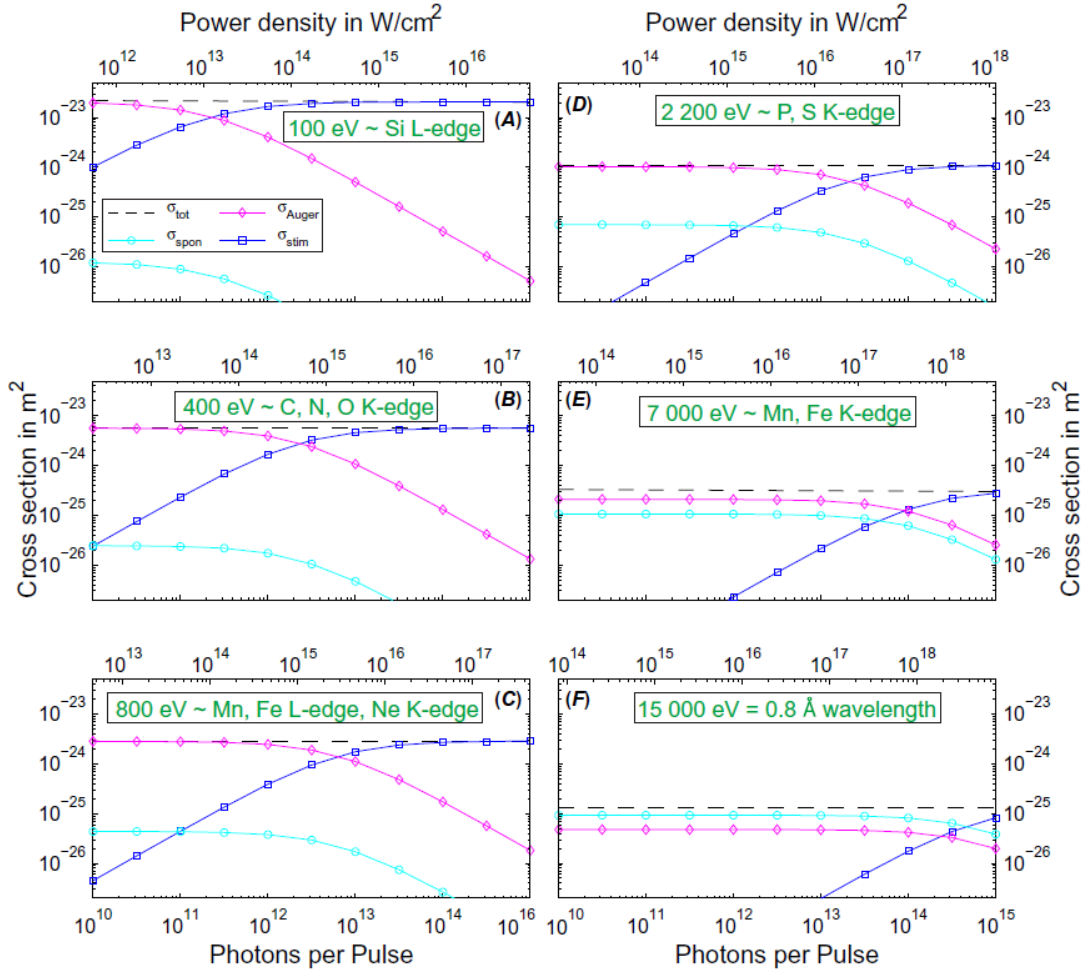
Figure 5.1:   **Intensity dependent Cross-sections versus the incident power density for a variety of typical material edges from [30].** In all sub-figures 1(a)-(f) the relations between the different relaxation cross sections are shown. The lower x axis gives the intensity in photons per incident pulse, and the upper x axis shows the power density in W/cm^2. The black dashed line gives to the total relaxation cross section, while the others refer to the Auger cross section (pink), the spontaneous cross section (cyan), and the stimulated cross section (blue), respectively. For all X-ray material edges, the spontaneous and Auger cross sections decrease with increasing incident field strength, whereas the stimulated cross section increases instead. The higher the photon energy (increasing from (a) to (f)), the higher the required field strength to achieve the same cross section changes.

found. It has recently been reported by Wu et al.[98] that they observed a decrease in the X-ray diffraction intensity induced by intense X-ray pulses tuned to the Co L_3 resonance in magnetic CoPd multilayers. This observation indicates exactly the scattering breakdown expected when stimulated RIXS occurs in a material system, and provides, therefore, the starting point for our experiment described in the next section 5.2.

5.2   Experimental Approach

In order to understand the interplay between the different relaxation channels, an experiment being capable of recording X-ray scattering as a measure of the spontaneous emission as well as the spectral information of the direct beam transmitted through the sample was designed, giving a measure of the stimulated emission channel. The corresponding experiment was performed at the Atomic Molecular and Optical Science (AMO) endstation [91] at the LCLS. It was designed to simultaneously obtain pulse by pulse information on the charge and spin interaction in the magnetic sample. The experimental schematics are shown in Fig. 5.2. The FEL provides linearly polarized SASE pulses of 5 fs pulse length and 10^{13} photons per pulse at a photon energy of 778.8 eV with a bandwidth of 1 eV tuned for the Co L_3-edge excitation.

The Kirkpatrick-Baez (KB) optic focuses the pulses to ≈ 10 μm^2 at the sample position. These pulses are then split and spatially separated by a split and delay line [116], which is only used for splitting purposes, into a probe pulse and a normalization pulse. The probe pulse travels through the CoPd sample, while the spatially separated normalization pulse travels through an empty SiN membrane. The directly transmitted pulses continue both through a hole in between the two PnCCDs (Pn for pinhole) and enter the spectrometer described in [117]. The alteration to the mentioned spectrometer is a CCD focused onto a YAG screen instead of the MCP (compare Chapter 3.2.7 and [76]). This enables intense single-shot observations with a high dynamic range compared to sensitive low photon-count measurements in the original spectrometer setup. In our experiment, the direct beams are dispersed on a grating and then sent onto a YAG screen, where a CCD captures the spectral information, as shown in the Fig. 5.2.

The image on the YAG screen in Fig. 5.2 is a typical single-shot spectrum of both beams as measured during the experiment. In this setup, the spatial
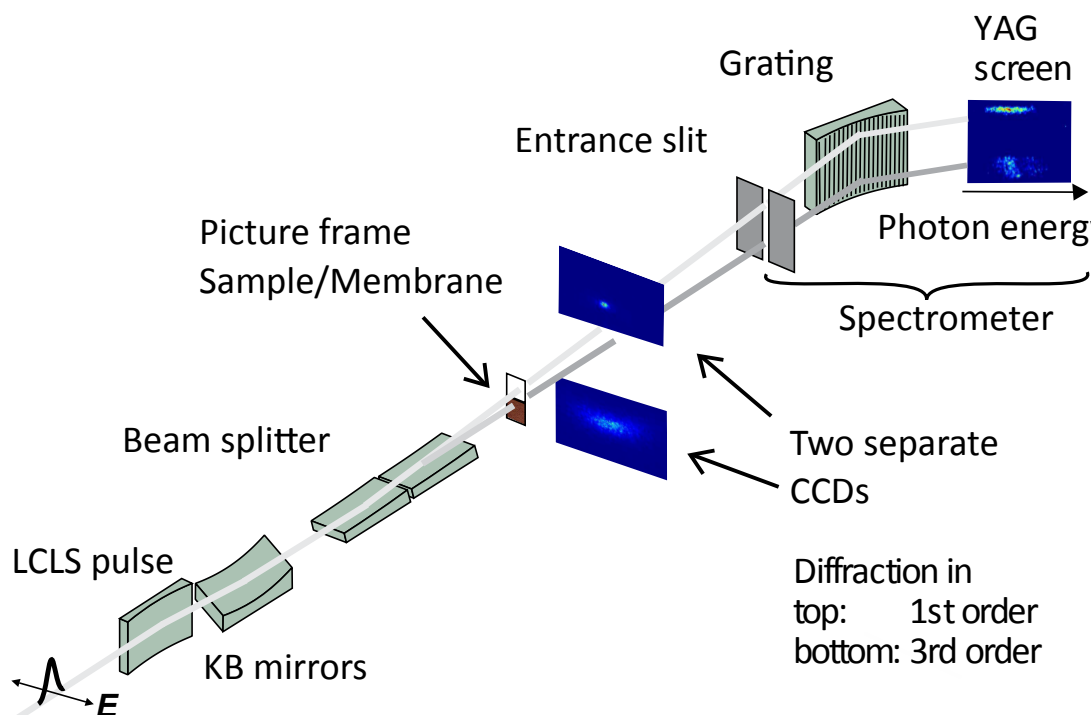
Figure 5.2: **Schematic stimulated RIXS experimental setup.** The FEL pulses are spatially separated to pass through either a sample or a dummy-membrane. The two beams continue through a hole in between the two separated CCDs that collect the scattering signal. One CCD is positioned in a manner to collect the first order scattering, while the other one collects the third order scattering, respectively. The direct beam enters a spectrometer consisting of an entrance slit, a grating, and a YAG screen. A CCD is focused onto the YAG screen, where the spectral information of the incident beam and the transmitted beam is recorded.

separation is key, as it enables a single-shot measurement of the energy, the bandwidth, and the transmission intensity, which additionally opens a way to single-shot normalization. Apart from the spectral information, the two PnC-CDs measure the sample's first and third order diffraction, thereby collecting information about the antiferromagnetic domains in the long range and the short range, corresponding to the first order scattering and the third order scattering, respectively.

5.2.1 Magnetic Thin Film CoPd Samples

The experiment was performed with magnetic thin film samples CoPd on SiN membranes. This sample system was chosen because of a report on an unexpected scattering signal breakdown at the Co L_3-edge by Wu et al. [98]. In their experiment, the magnetic speckle pattern was significantly reduced by the

incident FEL pulses compared to equivalent synchrotron measurements. This indicates the sort of non-linear response to an incident light field which we aim to investigate. Comparing with Fig. 5.1 around 800 eV we expect a comparable strong RIXS signal (spontaneous emission) to the stimulated signal (stimulated emission) around photon numbers of 10^{11} per pulse in a $50x50$ μm focus area (compare Sec. 4.1.2).

Our samples were characterized for normalization spectra regarding absorption and emission at the Stanford Synchrotron Radiation Light-source (SSRL) facility at the coherent scattering station at beamline 13. First, they were magnetized by an external magnetic field in order to form stripe domains instead of random worm domain patterns. This is done to push the scattering intensity into Bragg peaks instead of rings, which would typically occur for a random scattering alignment of a certain domain size [2]. These Bragg peaks push the entire scattering intensity to the position of the PnCCDs, thus improving the signal to noise ratio on these PnCCDs. Then, the samples were mounted next to an empty SiN membrane, which serves as a dummy transmission membrane to enable single-shot normalization of the sample and no-sample spectra, as shown in Fig. 5.2. The experiment was performed in collaboration with the Stöhr group from Stanford University, who has extensively studied this material system before, as it is of importance in the field of ultrafast demagnetization of an anti-ferromagnetic material [118].

5.2.2 Stochastic Fluctuation of the Incident SASE Pulses

For this experiment, an ideal pulse would be monochromatic with a bandwidth small enough to select different areas of the absorption edge, for instance the rising edge or the absorption maximum, for excitation. On top of that, it has to be short in the time domain, namely on the order of the Auger lifetime which is $\approx 1 - 2$ fs in Co, and has to be coherent over the entire pulse duration. A high photon flux for the maximization of the induced non-linear effects is also crucial due to the high intensity dependent onset of non-linear effects, as explained in Section 5.1. Due to the geometry of the beam splitter, the pulse position or beam path has to be stable for every single pulse.

The pulses provided by the FEL are created by the self-amplified spontaneous

emission process, which produces short, transversely coherent pulses, with strong statistical fluctuations as explained in [119] and in Chapter 3.2.4. Due to their spiky structure, SASE pulses are temporally rather incoherent. High fluences are crucial to induce non-linear effects, so this was the first priority for our experiment. To increase the fluence, the pulses are focused to a very small focal size of $\approx 10\ \mu m^2$, which was scanned before every experimental run in order to enable a calculation of the shot-to-shot fluence values. These small focus sizes are only achievable at the AMO endstation at LCLS [91]. The compromise at this endstation is the availability of a very small X-ray focus and the split and delay station at the cost of a missing monochromator [116]. To make up for this, the pulse's bandwidth is increased to cover roughly the whole absorption edge. However, since the pulses are still created in a SASE scheme, the pulse's energy fluctuates substantially from pulse to pulse. The experiment was performed with pulses of 5 fs FWHM pulse length and coherence times expected to be over the whole pulse or 5 fs. In Fig. 5.3 the typical fluctuations of pulses with the same coherence length and FWHM in the time domain are shown, calculated as introduced in [119]. All pulses have a nominal FWHM pulse length of 2.5 fs. At the same time, it is clearly visible that the intensities and the distributions in the time domain differ considerably from pulse to pulse. These fluctuations increase the difficulty of a clear interpretation of the results, and have to be taken into
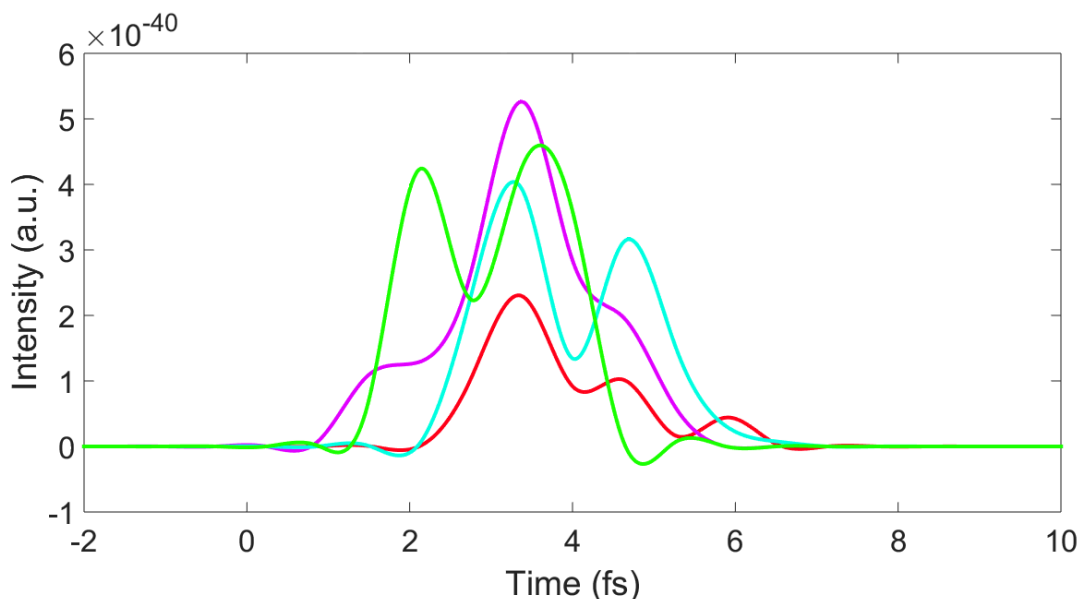

Figure 5.3: **Schematic of the varying SASE pulses.** Four different exemplary LCLS pulses in the time domain for nominally 2.5 fs FWHM pulses at an incident fluence of 100 mJ/(cm²fs) [119].

account for any comparison. Since the incident pulse's spectrum is measured, it is fortunately possible to bin the results not only by incident fluence, but also by incident spectrum. This enables sorting out incident pulses with a spectrum off the absorption edge or with multiple SASE spikes. A simulated distribution of varying SASE pulses is used for the range of theory input points in section 5.3.2, based on a method for the estimation of SASE fluctuations [119].

5.3 Results and Discussion

The data collected in the experiment are strongly convoluted. To understand the variety of effects that might contribute to the results a step by step analysis is necessary. In Fig. 5.4, the collected data are illustrated. One can see the initial pulse's spectra, the transmitted spectra, and the scattered intensity. In both cases, the single pulse shows the spiky SASE structure whereas the sum of multiple SASE pulses results in the Gaussian shape typical of SASE statistics [119]. The transmitted sum of all pulses clearly shows the expected Cobalt absorption edge at 778 eV. Such a behavior is expected for a classical synchrotron experiment, but it does not reveal the single pulse interaction within the sample. In order to understand the dynamics in this experiment and the effects accompanying stimulated RIXS, the phenomena of saturable absorption and scattering breakdown are discussed first. Since these two effects are necessary, but not a sufficient conditions for stimulated RIXS. They will always occur when stimulated RIXS is happening. Following these, the first direct observation of stimulated RIXS and a discussion of the difficulties in understanding the dynamics within the CoPd sample is presented.

5.3.1 Self-Induced Transparency and Saturable Absorption

With increasing intensity of the incident X-ray beam, the Co absorption edge starts to disappear until it vanishes completely for very high fluences, resulting in an effectively transparent sample. Fig. 5.5 shows the normalized sample transmission in dependence of the incident photon fluence and the photon energy. It can clearly be seen that the sample's absorption decreases with increasing intensity of the incident X-ray beam. While the sample still shows a pronounced Co absorption edge for a low fluence of 42 mJ/(cm^{2}fs), the absorption edge has
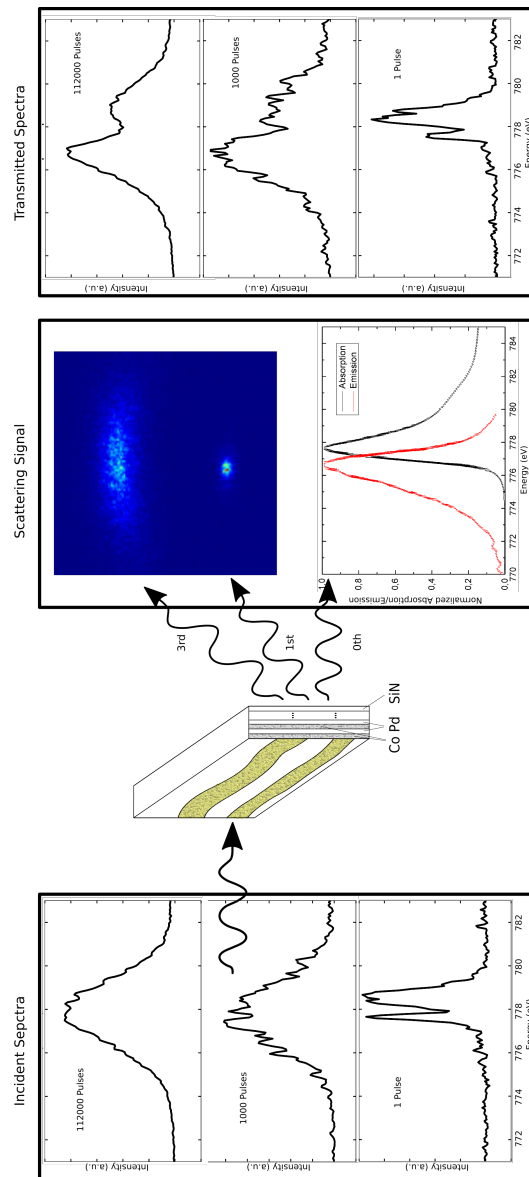
Figure 5.4: **Data collection scheme with raw data for incident and transmitted pulse as well as scattering in 1st and 3rd order.** The graphic shows the raw data as collected for the incident pulse (left) and the transmitted pulse (right) as well as the scattering signal on the PnCCD in first and third order (blue image). The spectra for the incident and transmitted pulses are shown for a single pulse (bottom), 1000 pulses (middle) and all 112000 pulses (top). A the single SASE pulses add up to a typical Gaussian distribution around the absorption edge. The transmitted pulse clearly shows the dip of the absorption edge in the Gaussian distribution of the SASE pulses. The sample schematic is also illustrated with the magnetic stripe domains that pushes the scattering signal into the spots as seen on the PnCCD image. Also indicated is the linear absorption and emission of the sample. This picture gives a general idea of the collected data.

completely disappeared for the spectrum recorded at substantially higher fluences of 1600 mJ/(cm²fs). It should, however, be noted that even at relatively low fluences an average reduction of the transmission loss of 38%, compared to the reference synchrotron measurements performed at the coherent scattering endstation at beamline 13 at SSRL, can be observed. As a consequence, more photons arrive on the spectrometer, resulting in an increase in photon numbers in the forward direction.

The effect described above is either called saturable absorption [92] or self-induced transparency [93] throughout the literature. In the following, the term self induced transparency will be used for this phenomenon. It can be understood in a simple two level system, where a linear absorption takes place for a relaxed system with 100% of the states in the ground level. If the incident pulse populates 50% of the states into the excited level, the same number of photons is absorbed and stimulated, respectively, and the sample is transparent for the following photons. Ideal transparency would occur when the induced absorption during the first half of the pulse is followed by a coherent induced emission during the second half of the pulse, inducing the absorbed amount of energy back into the beam direction [93].

To gain a deeper understanding of the onset of this effect in the soft X-ray regime, Stöhr and Scherz introduced an expansion of Beer-Lambert's law [37]

$$I_{trans}^q = I_0^q e^{\sigma_{abs}^q \rho_a d},\tag{5.1}$$

that is commonly used to estimate the transmitted intensity through a sample of known thickness d and atomic number density ρ_a with a polarization dependent (q) incident I_0^q and I_{trans}^q transmitted intensity and the X-ray absorption cross section σ_{abs}^q as explained in Chapter 3. According to equation 5.1, the transmitted intensity decays exponentially with the number of atoms in the beam and their absorption cross section. Following the discussion in [37], a modified Beer-Lambert law that includes a non-linear atomic scattering length can be derived through a dispersion correction, changing the Beer-Lambert law to

$$I_{trans}^q = I_0^q e^{-2\lambda(f_0''^q + 2f_{NL}''^q)\rho_a d},\tag{5.2}$$

where the spontaneous absorption cross section becomes $\sigma_{abs} = 2\lambda[f_0''^q + 2f_{NL}''^q]$. This cross section now depends on the atomic scattering length $f_0''^q$ and the
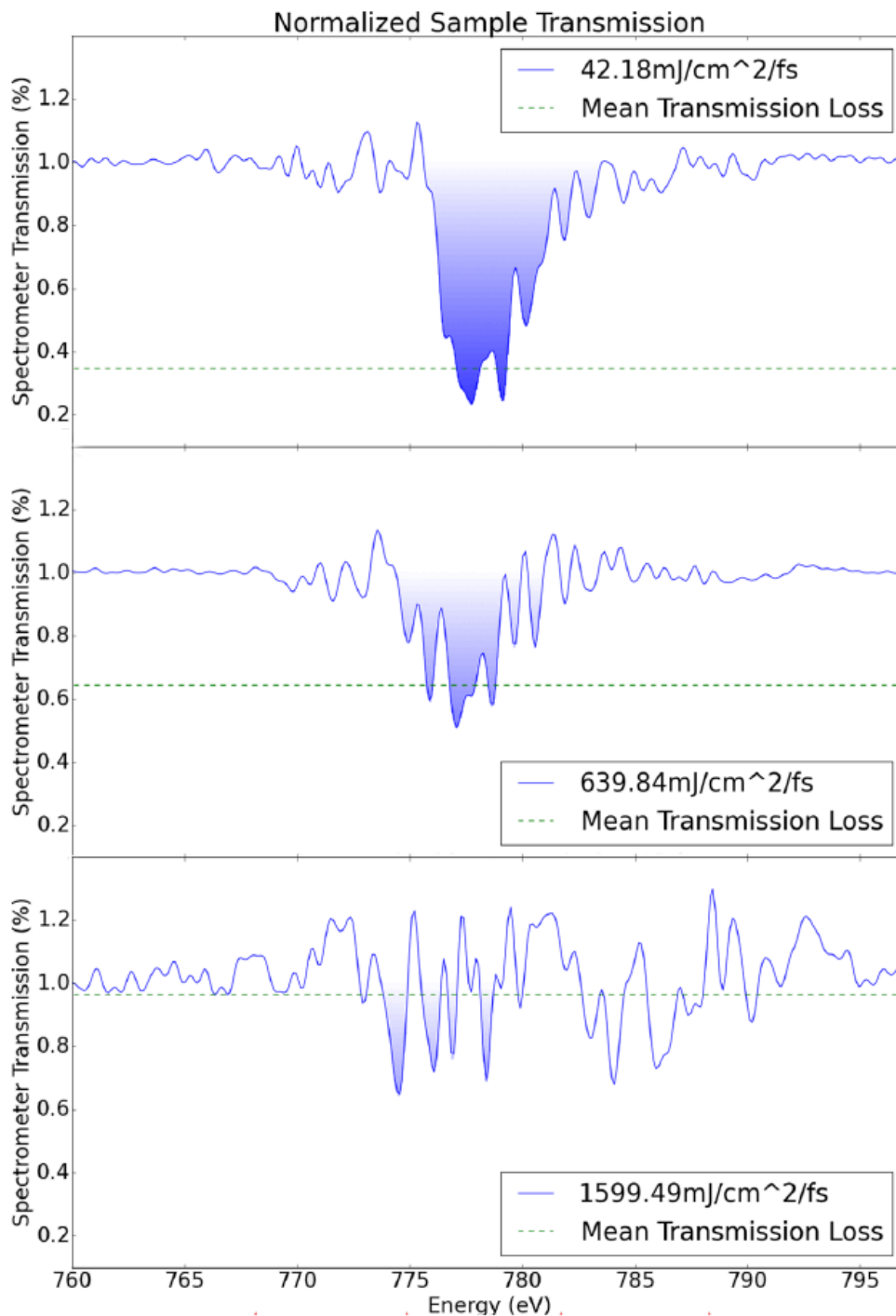
Figure 5.5: **Single-shot spectra for three different X-ray pulse fluences.**
For a low fluence (top), the typical Co absorption edge can be seen, whereas for
a medium fluence (middle), the absorption edge already starts to disappear and
vanishes eventually completely for a very high fluence (bottom). Additionally,
the transmission change for the respective fluences is indicated by the dashed
line. For the low fluence, the transmission change of 38% increases to 65%
for medium fluences, whereas for very high fluences the sample becomes almost
transparent (98% transmission change). The obtained spectra and transmis-
sion change values are averaged over all single-shot spectra within the fluence
magnitude given in the graph.

Figure 5.6: Numerically derived effective excited state population of the Co L_3-core two level system as a function of incident intensity for different coherence times τ_c [37]. Resonant excitation, an incident linearly polarized transform limited pulse and typical Co material parameters were assumed in the simulation. The three black lines indicate the fluences stated in the experimental measurements.
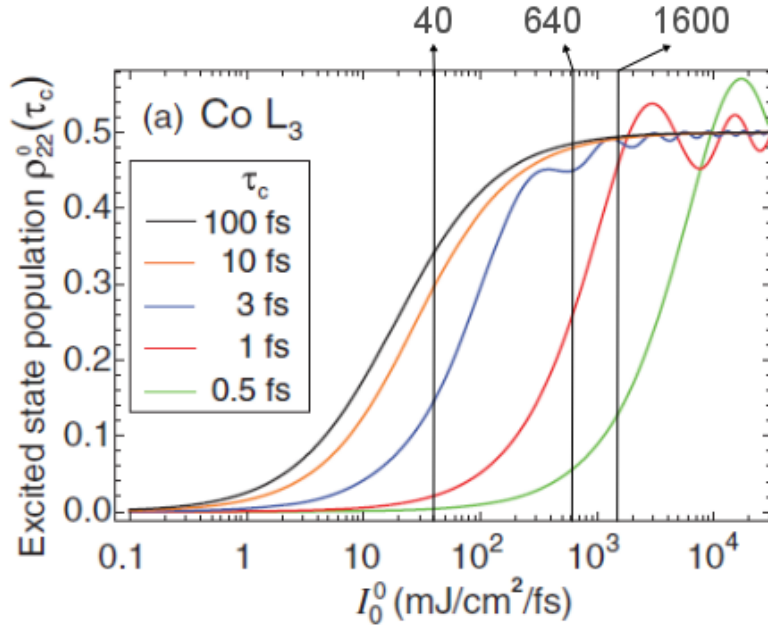
stimulated non-linear part $2f_{NL}''^q$, which depends on the excited state population. This excited state population can be obtained from the Bloch equations, integrated over the coherence length of the incident pulse.

The resulting effective excited state population for the Co L_3-edge are shown in Fig. 5.6 in relation to the incident photon flux and the pulse's coherence length. The material parameters are typical Co parameters for a 20 nm thick magnetic film and a resonant excitation with a transform limited incident pulse, as given in [37]. Since an effective excited state population of 50% corresponds to a transparent sample as explained above, and an excited state population of 0% relates to a sample with a linear absorption or a transparency change of 0%, the excited state population and the induced transparency change ΔT can be related through

$$\Delta T = 2\rho_{22} \ . \tag{5.3}$$

This relation enables a qualitative comparison of the experimental findings (Fig. 5.5) with the theoretical predictions (Fig. 5.6).

The measured fluences are indicated in the theoretical depiction Fig. 5.6 through the black lines at the stated fluences. For incident fluences around 40 mJ/(cm²fs), a transmission change of $\approx 38\%$ was observed which relates to an excited state population of 0.19. For the higher fluence values of about 640 mJ/(cm²fs) and 1600 mJ/(cm²fs), and the observed transmission changes of 65% and $\approx 98\%$, an excited state population of about 0.325 and 0.49, respectively, are expected. These values can be compared with the theoretical predictions for different pulses as indicated in Fig. 5.6. To see the estimated excited state population in the theory for the same fluences, an incident pulse in between 3 fs and 1 fs coherence time is needed (in between the red and the blue curve). Since the experimental values are averaged over a series of single shots, some fluctuations are expected.

So in conclusion, we observed self-induced transparency in the soft X-ray regime and could show by comparison of induced transparency to excited state population that the theory proposed in [37] supports our experimental findings for coherence times shorter than the expected 5 fs.

5.3.2   Scattering Breakdown

Wu et al. [98] observed a decrease in scattering induced by the incident X-ray radiation and attributed it to the onset of stimulated scattering. As we investigated the same material at higher incident fluences, we expect to monitor this scattering breakdown as well. In addition, the logical conclusion from the effect of induced transparency observed and described in Section 5.3.1 would be a reduction in the amount of scattered photons, since less photons interact with the scattering material. This is a step less than Wu et al. went with their interpretation. For the observation of a disappearing scattering, no stimulated emission has to be present in the interaction, however, stimulated emission is a logical expansion, as can be seen later on.

The first and third order scattering were recorded as described in Section 5.2. Unfortunately, the data quality of the third order scattering is quite poor, the following analysis is, hence, concentrated on the first order scattering. Fig. 5.7 illustrates the measured first order scattering intensity on the lefthand side

in blue. The orange line depicts the low intensity scattering signal for 5 fs long pulses as measured for low intensities (average for the lowest intensity shots). From this figure, two key observations can be made: first, the scattering signal decreases with increasing fluence, and secondly, the values at a fixed incident fluence vary substantially.

From the scattering perspective, the forward direction signal can be referred to as zero order scattering. Since a scattering breakdown in higher order signals
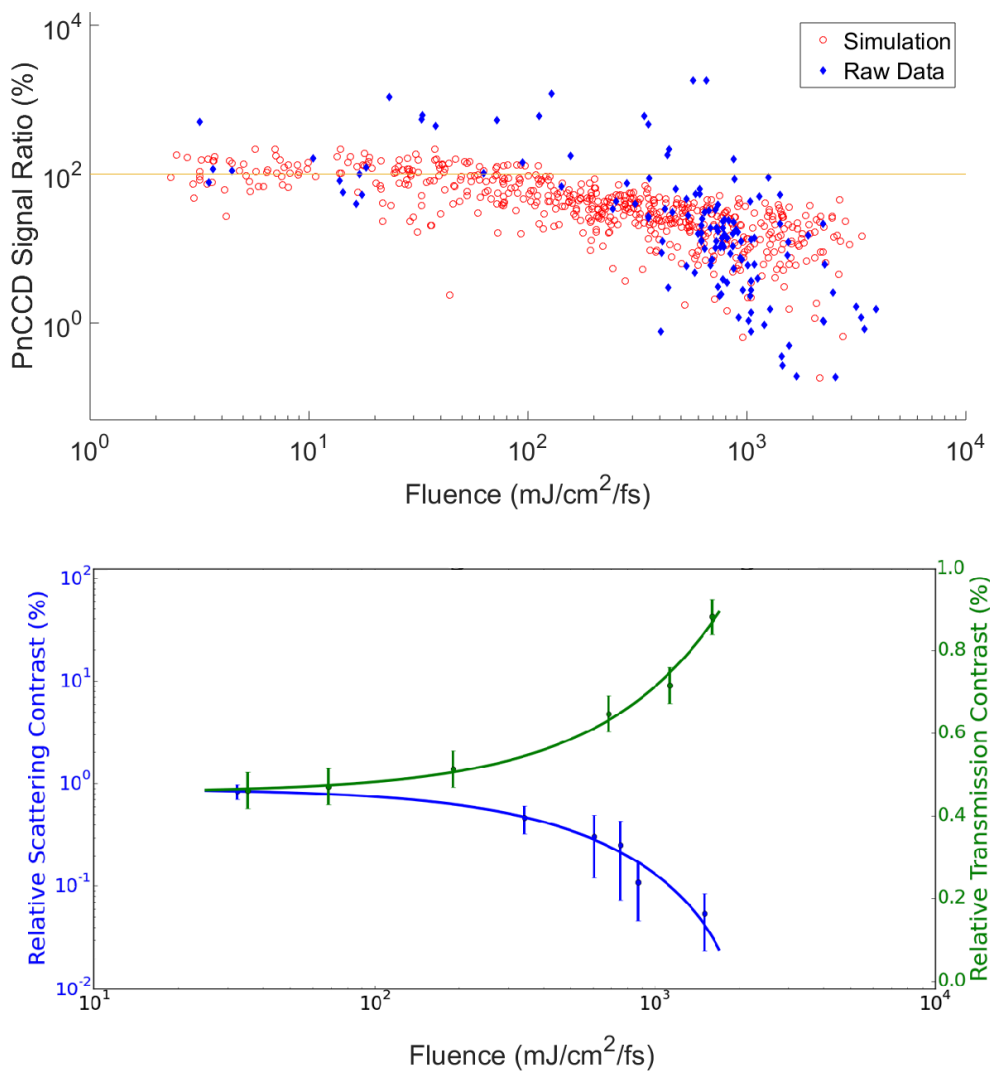
Figure 5.7: **Scattering signal in first order in relation to the incident fluence. Top:** The first order scattering signal is shown in blue in relation to the pulse's incident fluence. In red one can see the simulation of 5 fs pulses with a coherence length of 1 fs and a statistical scattering of the incident spectrum, as indicated in chapter 5.2.2. **Bottom:** The relative scattering contrast and the relative transmission (zero order scattering contrast) are shown in relation to the incident fluence.

(> 0) is equivalent to an increase in zero order scattering, the relative ratio of first order scattering to zero order scattering (labeled as relative scattering contrast) is shown in Fig. 5.7 on the righthand side. The measured points are averaged values with a deviation indicated by the error bars and connected by a fit as a guide to the eye. Since the evaluation of the scattering signal is limited to the first order scattering in our experiment, all scattered intensity has to be found in either first or zero order scattering, thus giving the total scattered intensity I_{total} as the sum

$$\int I_{total} = \int I_{zero} + \int I_{first}.$$ (5.4)

So, if the first order scattering signal decreases, the zero order scattering signal, consequently, has to increase, leaving the total scattered intensity I_{total} constant. This effect can clearly be recognized in Fig. 5.7 on the righthand side, where a decrease in the relative scattering contrast results in an increase in the relative transmission contrast.

To understand the scattering signal shown in Fig. 5.7 (top), we follow the theory introduced in the previous section [37]. For incident pulses of 5 fs FWHM and a coherence time of 1 fs and the stochastic scattering of the SASE pulse distribution indicated in 5.2.2, it is possible to calculate the excited state population during the pulse transmittance, as explained in Section 5.3.1. Doing so for every different SASE pulse, a different excited state population can be determined, which then again results in a different scattering signal. The resulting simulated scattering distribution is shown in Fig. 5.7 (left) in red. An overall agreement with the decrease of the scattering intensity in relation to the incident fluence can be found, and the variety in scattering signals at comparable fluence levels can be understood as the fluctuation in SASE pulse parameters. The theory can replicate the experimental findings extraordinarily well. This proves the theory to be very accurate for this particular system.

5.3.3 Observation of Stimulated RIXS

The experimental findings explained above indicate the X-ray induced change of the fundamental light-matter interaction, but do not give evidence of stimulated scattering. In this section, the first direct observation of stimulated RIXS in a

solid sample is presented, followed by a description of the interpretation problems that occur in this type of sample system. Also another finding is presented, that can not be explained by stimulated RIXS or the above discussed ideas. The section finishes with an outlook on the challenges that lie ahead.

To extract the information leading to Fig. 5.5, we use the findings of the last two sections 5.3.1 and 5.3.2 to further bin the data sets measured on the spectrometer. We now know that the incident fluence controls the strength of the non-linear effect, and that the scattering signal also indicates whether the sample is strongly excited or rather in the linear regime. The sample transparency was extracted using a broad average over shots with a comparable incident fluence in the same way the scattering data set was organized. Now the incident pulses are binned by fluence as before, and, since the single SASE shots vary strongly in energy, the pulses are also binned by their central energy determined by a Gaussian fit in the no-sample reference spectrum. These presorted pulses as well as their reference spectra are then binned and compared as shown in Fig. 5.5.

Three different binning options are shown in Fig.5.8. The top of the figures bins all pulses with a very low fluence on the order of 5 mJ/(cm^{2}fs). The dashed line shows the averaged incident spectrum, whereas the black line shows the by a factor of 10 expanded difference spectrum to the no-sample reference beam. For very low fluences, there is almost no visible difference between linear transmission and the measured transmission, which indicates the interaction to be in the linear regime. For increased incident intensities as shown in the middle and at the bottom in Fig. 5.5, there is a significant difference to the linear absorption visible depending on the incident photon energy. In both cases, the incident fluence is high enough to induce a strong induced non-linear reaction in the sample, as observed in the previous sections. The incident fluences between $1000-1500$ mJ/(cm^{2}fs) create a to a greater or lesser extend transparent sample, as shown in Fig. 5.5, while the scattering signal also decreases by two orders of magnitude as shown in Fig. 5.7. Furthermore, the predictions from the non-linear Beer-Lambert law for these fluences indicate an effective excited state population on the order of $\approx 40-50\%$ in the core-valence two level system, calculated in [37]. The actual interaction happening here is hard to decouple, since there are multiple possible reaction pathways within the excited CoPd multilayer and the experiment lacks selectivity to concentrate on one. Addition-
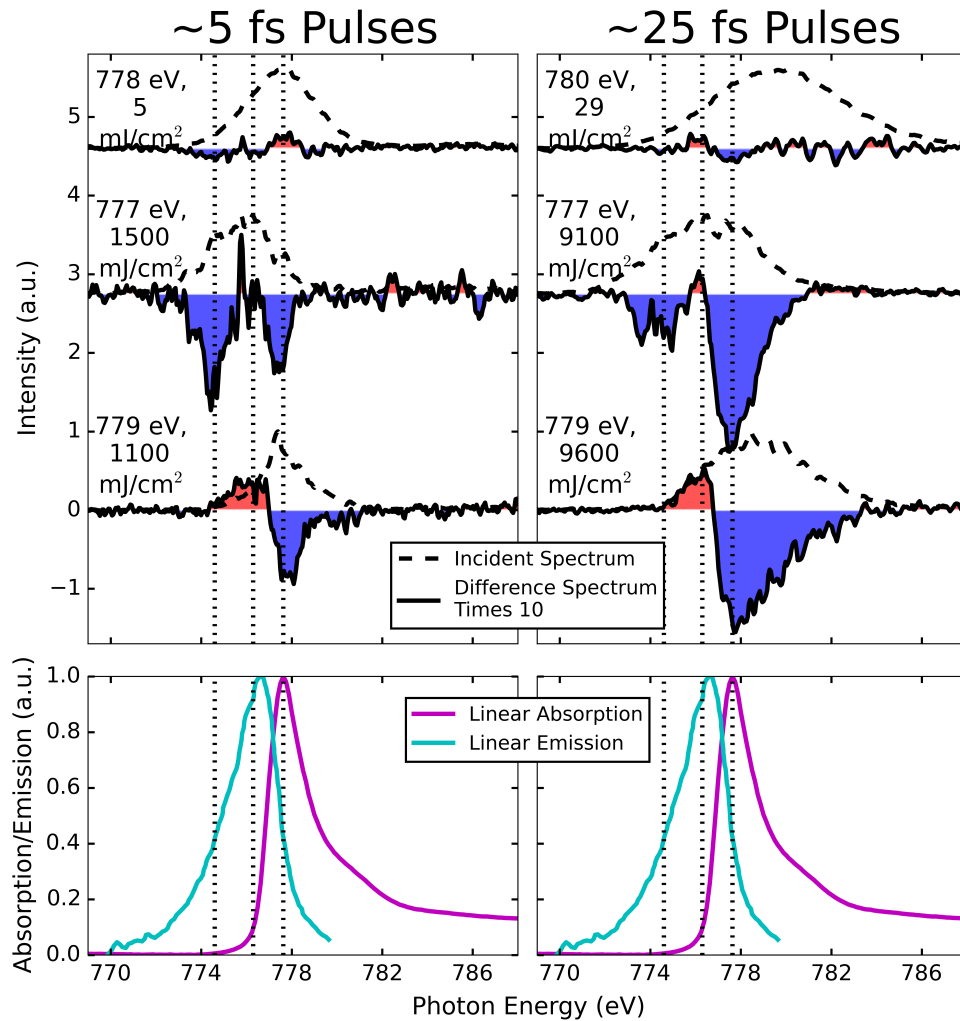
Figure 5.8: **Averaged spectral response to ultrashort high intensity pulses.** The CoPd multilayer response to 5 fs pulses of different fluences and different incident central energies is shown on the left. The energies shown there are given by a Gaussian fit of the averaged spectrum. The averaged incident spectrum is given by the dashed line, while the difference transmission spectrum is shown as the solid black line 10 times enhanced. The differences from Zero are colored in blue for a decrease in absorption and in red for an increase in absorption. For low fluences around $5 \frac{mJ}{cm^2}$ (top), we expect no non-linear reaction, which is confirmed by the lack of difference. For high fluences, slightly detuned to incident energies below the absorption edge (middle), the absorption decreases, which means an increase in transmission. For pulses with incident energies tuned to the absorption edge (bottom), the situation is more complicated. In the beginning of the edge and slightly below one can see an increase in absorption, while the main absorption decreases as in the detuned case. On the right, the linear absorption and emission are shown in pink and cyan, respectively. The dashed vertical lines from left to right indicate the onset of absorption, the maximum of the linear emission, and the maximum of absorption (or center of the absorption edge) in both pictures.

ally, the sample has a broad density of states and an electronic system that is governed by the magnetic domains, which form complicated, ultrafast demagnetization behavior [118].

To try and understand the intense pulse-sample interaction, Fig. 5.8 shows two cases for high incident fluences. For the first case in the middle of the figure, the incident spectrum is about as broad as the absorption edge, but slightly detuned to a lower energy, whereas for the other case at the bottom, the bandwidth is relatively small compared to the latter and the photon energy roughly hits the center of the absorption edge. As can be clearly seen in Fig. 5.8, the systems response to the two different incomming pulses differs substantially. If the incident pulse is detuned to the lower end of the absorption edge around 777 eV, the resulting transmission spectrum shows three different areas. On the edge centered around 778 eV the absorption decreases as well as for the area just below the absorption edge, around 774 eV. It should be noted that a decrease of absorption is equivalent to an increase in transmitted intensity. However, around the rising front of the absorption edge (indicated by the dashed line in the middle) the system reacts as in the linear case, showing almost no difference to the linear absorption (Fig. 5.8 top). This indicates two effects with opposing consequences occuring around the absorption edge. A rise in transmission intensity at a certain photon energy distribution is a direct proof of the existence of stimulated RIXS. This merges with the theoretical predictions from the two earlier stated discussions of the onset of stimulated scattering by Stöhr et al. [37], and the changing relation of the relaxation cross section that takes intensity from the spontaneous and Auger channel by increasing the stimulated emission cross section, as discussed in Schreck et. al [30]. These two theories explain the rise in transmission (blue colored area), which we initially expected and could now experimentally prove.

The amplitude of the stimulated scattering, or rather the absorption decrease, seems to follow the envelope of the incident photon field, except for the dip in the middle. This area coincides spectrally with the linear emission of the sample, indicating that the increase of absorption is either connected to the linear emission of the sample, or to the nearby Fermi level and the unoccupied valence states above defining the absorption edge. In the case where the incident energy is tuned to the absorption edge as shown in the bottom spectrum in Fig.
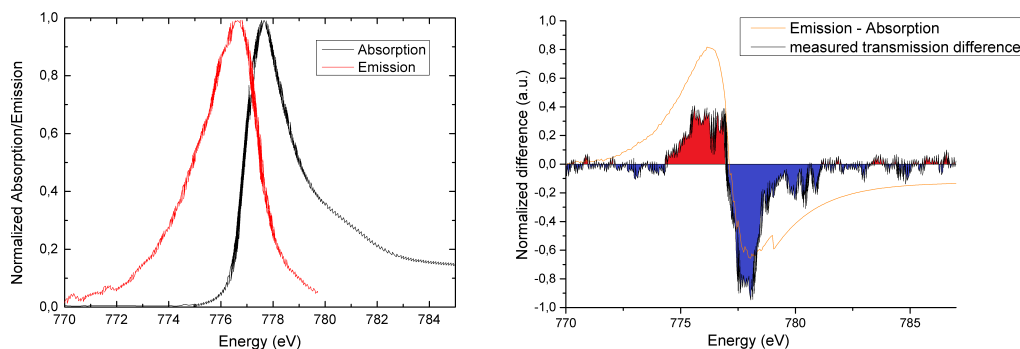
Figure 5.9:   **Linear emission and absorption at the Co L$_3$-edge and its difference in comparison to the transmission change induced in the CoPd sample. Left** The normalized linear emission (red) and absorption (black) is shown for a Co magnetic sample around the Co L$_3$ absorption edge. **right** The transmitted intensity is estimated through the difference between the emission (positive contribution) and the absorption (negative contribution) and shown as the orange line. The measured transmission difference is given as the black line with increase colored in red and decrease colored in blue as in Fig. 5.8 (bottom left), respectively. The simple estimation for the transmission difference in orange agrees well with the measured difference, given its simple approach.

5.8, the main absorption decreases, resulting in a higher transmission intensity in the same way as it does in the middle spectra, whereas the absorption on the rising side of the absorption edge shows an increase in absorption, resulting in a decrease of transmitted intensity. This finding is problematic for a clear interpretation. The decrease of absorption on the absorption edge indicates the presence of stimulated scattering, but the increase of absorption at lower incident energies gives rise to a new, counteracting effect.

One idea to explain this is an increase in unoccupied states just below the Fermi level, caused by the X-ray induced electron cascade that opens new absorption channels as predicted by Ziaja et al. [101]. Their theory states that electron cascades which follow X-ray absorption, are dominated by low energy electrons which saturate in numbers within $10 - 100$ fs. In their model they find a start of the electron cascade within the first few femtoseconds. For our case that would mean that even within the pulse length, low energy electrons are being excited, effectively changing the density of state occupation around the Fermi level by distributing electrons from the occupied valence states into the unoccupied states. This opens up new unoccupied states below the absorption

edge, which in turn open new absorption channels. This effectively increases the absorption for these energies, while decreasing the absorption for energies just above the absorption edge. Other observations that can be understood in a comparable way were made in [120, 121].

A simple approach to understand these changes in transmitted intensity within the absorption band can be made by comparing these areas with the linear absorption and the linear emission as indicated in the bottom graph in Fig. 5.9. First of all it is noticeable that the maximum of the increase coincides with the maximum of the linear emission and the minimum of the decreasing area coincides with the maximum of the linear absorption, as indicated by the vertical lines in Fig. 5.8. To ease the comparison the dashed lines are drawn at the position of the linear absorption and emission maxima, respectively.
A simple estimation is performed, where the linear emission represents the density of states (DOS) of the occupied valence states, and the linear absorption represents the DOS of the unoccupied valence states. As explained above, the low energy electron excitations change the occupation of states around the Fermi level, effectively occupying states above the Fermi level while depopulating states below the Fermi level. In a first attempt, we assume the transmitted intensity to change according to $I_{change} \approx Emission - Absorption$. This is shown in Fig. 5.9 (right hand side) in orange together with the measured absorption difference. The increase and decrease in the measured absorption are colored in red and blue, respectively. It seems that at a first glance the estimation shows a pretty close correlation to the experimental findings as shown in Fig. 5.9 on the left hand side. Additionally, it is clearly visible that the blue area exceeds the red area, which indicates the presence of stimulated scattering.

5.3.4 The Ultrafast Self-Induced X-Ray Transparency and Loss of Magnetic Diffraction

Here is the first manuscript from the project. The majority of the results is covered in the chapter above.

Ultrafast Self-Induced X-Ray Transparency and Loss of Magnetic Diffraction

Z. Chen,[1] D. J. Higley,[2] M. Beye,[3] M. Hantschmann,[4] V. Mehta,[5] O. Hellwig,[6, 7] A. Mitra,[8, 9]
S. Bonetti,[10] M. Bucher,[8] S. Carron,[8] T. Chase,[11] E. Jal,[8] R. Kukreja,[12] T. Liu,[1] A. H.
Reid,[8] G. L. Dakovski,[8] A. Föhlisch,[4] W. F. Schlotter,[8] H. A. Dürr,[8] and J. Stöhr[13, *]

[1]*Dept. of Physics, Stanford University, Stanford, CA 94305, USA*
[2]*Dept. of Applied Physics, Stanford University, Stanford, CA 94305, USA*
[3]*Dept. of Photon Science, DESY, Notkestraße 85, D-22607 Hamburg, Germany*
[4]*Dept. of Materials and Energy Science, Helmholtz Zentrum Berlin, D-14109 Berlin, Germany*
[5]*San Jose Research Center, HGST a Western Digital company, San Jose, CA 95135, USA*
[6]*Institute of Physics, Technische Universität Chemnitz, D-09107 Chemnitz, Germany*
[7]*Institute of Ion Beam Physics and Materials Research,*
Helmholtz-Zentrum Dresden-Rossendorf, 01328 Dresden, Germany
[8]*SLAC National Accelerator Laboratory, 2575 Sand Hill Road, Menlo Park, CA 94025, USA*
[9]*Department of Physics, University of Warwick, Coventry; United Kingdom*
[10]*Dept. of Physics, Stockholm University, S-10691 Stockholm, Sweden*
[11]*Dept. of Applied Physics, Stanford University, Stanford, CA, 94305 USA*
[12]*Dept. of Mat. Sci. and Eng., University of California Davis, Davis, CA 95616, USA*
[13]*SLAC National Accelerator Laboratory and Dept. of Photon Science, Stanford, CA 94035, USA*
(Dated: May 9, 2018)

We report the ultrafast concurrent disappearance of the resonant Co L_3 x-ray absorption and diffraction contrast for a Co/Pd multilayer film using $\simeq 2.5$ fs and $\simeq 25$ fs self amplified spontaneous emission (SASE) pulses of increasing intensity. At ~ 1 J/cm^2/fs the diffracted intensity has decreased by a factor of 10^2 and the sample has becomes effectively transparent. The dependence of the stimulated sample response on the incident intensity, the coherence time and energy jitter of the SASE pulses is quantitatively accounted for by a statistical description of the pulses and treating the sample dynamics by the optical Bloch equations.

PACS numbers 75.70.-i, 75.50-Cc, 78.70.-Dm

With the advent of x-ray free electron lasers, studies of the non-linear electronic response of matter have become possible. In particular, the stimulated *inelastic* x-ray response of matter has been observed through the stimulated amplification of spontaneous emission [1–3] and stimulated x-ray Raman scattering [4].

A particular important x-ray process that links the two fundamental x-ray processes of *absorption* and *elastic scattering* involves the *resonant* excitation of electrons from a core shell to empty valence states. After excitation, the created core hole decays *spontaneously* by emission of Auger electrons or characteristic x-rays, with Auger decay resulting in irreversible conversion of photons into electrons. The fraction of radiative decays, the x-ray fluorescence yield, varies significantly with atomic number Z and the core shell involved. It is less than 1% for the K-shell of the chemically important low-Z elements C, N and O and the L-shell of the important $3d$ transition metals such as Fe, Co, Ni and Cu [5].

Resonant x-ray processes are widely used in both spectroscopy and diffraction imaging since they maximize cross sections and provide atomic, chemical [6] and magnetic [7] specificity. X-ray absorption and resonant x-ray scattering are described by the $\mathbf{p} \cdot \mathbf{A}$ interaction Hamiltonian with absorption treated by first and scattering by

second order perturbation theory [7]. The goal of the present paper is the experimental demonstration of the theoretically conjectured link between the two processes [8, 9] and the importance of controlling the interplay between the two processes through energy and coherence time tuning of the incident field.

Previous experiments only revealed the out-of-beam diffraction aspects [10]. The predicted x-ray transparency through stimulation could not be observed directly since the centrally transmitted beam was blocked to protect the position sensitive CCD detector. Here this limitation is overcome by using the novel experimental arrangement shown in Fig. 1. It allows us to perform a simultaneous study, pulse-by-pulse, of the transmitted intensity in the forward direction and the out-of-beam diffracted intensity arising from nanoscale magnetic stripe domains.

Our studies use broad bandpass self amplified spontaneous emission (SASE) pulses which allow access to a wide intensity range covering three orders of magnitude. They confirm theoretical predictions and reveal strict requirements for controlling the stimulation process in terms of intensity, coherence time and energy tuning.

As samples we used, as before [10], magnetic Co/Pd multilayers deposited via sputtering on SiN windows with a metal layer sequence Ta(1.5)/Pd(3)/[Co(1)Pd(0.7)]x25/Pd(2), where the thicknesses in round brackets are in nm. As part of the fabrication process, the samples were placed in an

---

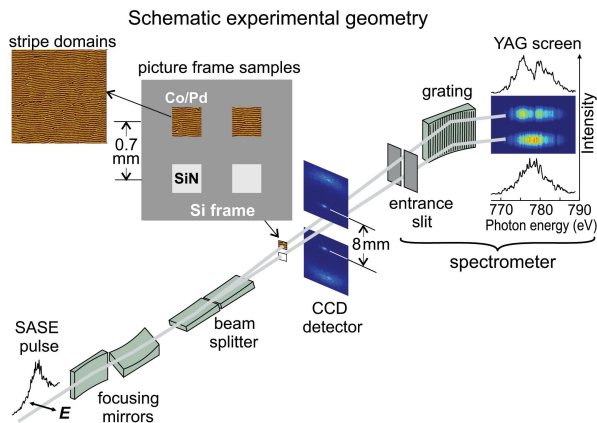*Electronic address: Email:stohr@stanford.edu

FIG. 1: (color online) Experimental geometry for simultaneous pulse-by-pulse measurements of the transmitted and diffracted response of a Co/Pd thin film. Incident SASE pulses of ~ 2.5 fs or ~ 25 fs length are focussed onto the sample plane and split by the sharp edge of a mirror, with one half propagating through a Co/Pd/SiN sample in a picture frame and the other through a pure SiN reference film for normalization purposes. The horizontal magnetic stripe domains in Co/Pd produce strong first and third order Bragg diffraction peaks on a pnCCD detector [11]. The spatially separated undiffracted beams are allowed to propagate into a downstream spectrometer. A grating disperses the two offset beams onto a yttrium aluminum garnet (YAG) fluorescence screen, yielding separate single-shot sample and reference spectra around the Co L_3 resonance. The shown spectra and first and third order diffraction images are real data averaged over several pulses.

oscillatory in-plane magnetic field, where the amplitude of the field was slowly attenuated every cycle. Such a process created well-defined magnetic stripes of ~ 150nm length scale at remanence, as shown in Fig. 1. The samples containing a total of 25 nm Co had $\simeq 30\%$ transmission at the Co L_3 resonance.

The linearly polarized SASE pulses of either ~ 2.5 fs or ~ 25 fs temporal length were generated at the Linac Coherent Light Source (LCLS) and steered into the AMO endstation [12]. The central energy of the x-ray pulses of approximately 5 eV total width was set to the nominal Co L_3 resonance of 778 eV and rastered through modulation of the electron beam energy to cover a range of about 20 eV. A calibrated gas detector provided an absolute measure of the integrated incident intensity I_{ref} for each pulse. A mirror with a sharp edge split the SASE pulse into two statistically identical halves [13], one transmitted through a Co/Pd/SiN sample in a 300μm picture frame and the other through an identical offset picture frame containing a pure SiN membrane for reference. A pair of upstream Kirkpatrick-Baez mirrors focused the beam to $\sim 15\mu$m diameter spots in the sample plane, as verified by a pinhole scan.

Two movable halves of a pnCCD imaging detector intercepted the first and third-order diffraction pattern of

the magnetic stripe domains, with a 8 mm separation of the first order diffraction spots. We utilized the integrated intensity of the first order diffracted spot denoted I_d, but the first and third order intensities closely tracked each other.

The centrally transmitted beams from both the Co/Pd sample, $I_t(\hbar\omega)$, and the reference beam through the SiN membrane, $I_0(\hbar\omega)$, passed through a gap between the two halves of the pnCCD detectors. Their energy resolved spectra were recorded by a grating spectrometer which dispersed the intensity with a resolving power of ~ 1000 onto an optically fluorescent YAG crystal imaged by a camera.

All intensities were first normalized to the *absolute* integrated incident intensity I_{ref}. A second *relative* pulse-by-pulse normalization was then accomplished by use of the energy resolved reference spectrum $I_0(\hbar\omega)$ of the centrally transmitted reference beam, yielding the central spectroscopy signal $S_t(\hbar\omega) = I_t/I_0$ and the diffracted contrast signal $S_d = I_d/I_0$. The extraction of the spectroscopy signal $S(\hbar\omega) = I_t(\hbar\omega)/I_0(\hbar\omega)$ had to be refined because the reference spectrum $I_0(\hbar\omega)$ dropped to zero near the end of the scan range $\mathcal{E}_0 \pm 10$ eV as shown on the top right of Fig. 1.

To eliminate singularities we therefore show in Fig. 2 the signal $S(\hbar\omega) = C[S'(\hbar\omega) - 1] + 1$ where $S'(\hbar\omega) = (I'_t + C)/(I'_0 + C)$ and $C = 10 \gg I'_t, I'_0$. This normalization scheme emphasizes the behavior of the transmitted signal near the resonance. While an incoming intensity of 42 mJ/cm^2/fs produces a prominent L_3 absorption feature, as expected in the linear regime, an increase in intensity reduces the resonance and at 1600 mJ/cm^2/fs no absorption feature can be discerned.

The change in the centrally transmitted intensity revealed by Fig. 2 is replotted as a function of incident intensity as solid blue circles connected by a blue line in Fig. 3. Due to the poor statistics of the spectrometer signal the shown data points represent an average over several shots. In the lower panel of the figure we also show on the same intensity scale the change of the magnetic diffraction contrast as solid red circles. In this case the data points represent single shots.

The changes of the in-beam transmitted and out-of-beam diffracted signals shown in Fig. 3 may potentially contain contributions from different microscopic mechanisms. Firstly, the energy deposited in the core excitations can be quickly released into the electronic system on the femtosecond timescale via Auger decays and ensuing electron-electron scattering as proposed by Schreck et al. [14]. The resulting reshuffling of valence electrons from below to above the Fermi level could lead to a decrease in the absorption at the Co resonance and hence an increase of transmission. Secondly, ultrafast demagnetization would completely reduce the magnetic diffraction contrast on a longer timescale of > 200 fs [15], but small changes [16] may be present on the 2.5–25 fs timescale of our pulses. Thirdly, impulsive (by the beam itself) stimulated elastic forward scattering has previously been
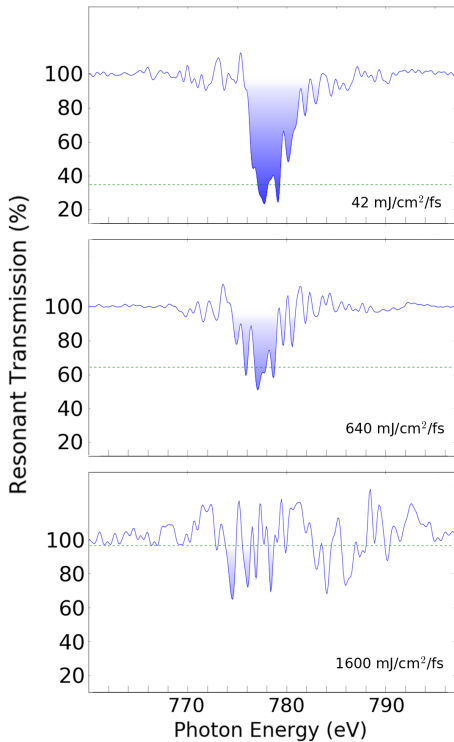
FIG. 2: (color online) Normalized transmission signal $S = C(S' - 1) + 1$ defined in the text for three different incident intensities around the Co L_3 resonance for a Co/Pd multilayer sample. Each spectrum represents an averaged spectrum across multiple shots in a certain fluence range. With increasing intensity the absorption peak clearly revealed at the lowest intensity is suppressed at it has vanished at the highest intensity of $1600\,\mathrm{mJ/cm^2/fs}$ revealing x-ray transparency.
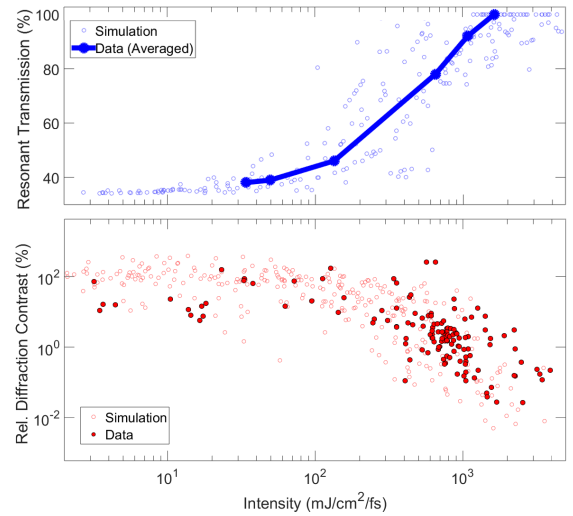

FIG. 3: (color online) Top: Comparison of the change in the transmitted intensity due to stimulation as a function of incident intensity. At a given intensity, we show the normalized *simulated* shot-by-shot transmitted intensity as open blue circles while the normalized *experimentally* observed intensity is an average over multiple shots (solid blue line). Bottom: Intensity dependent shot-by-shot observed and simulated diffracted intensities plotted on a log scale to emphasize the large statistical noise due to the used SASE pulses. All shown experimental and simulated data are based on the same number of combined single-shot data for 2.5 fs and 25 fs pulses.

shown to reduce absorption (increase transmission) at the expense of out of beam diffraction [8, 10].

While contributions of the first two mechanisms of valence electron reshuffling and ultrafast demagnetization cannot be excluded, we here explain our observations in terms of stimulated forward scattering. This model extends well-established quantum optical concepts to the x-ray regime by modelling the electronic structure of the sample as a two-level system where resonant transitions occur between the $2p_{3/2}$ core and empty $3d$ valence states. Remarkably, we will show that all features of the current experimental data can be quantitatively reproduced.

In the stimulated scattering model [8, 10], the interplay between resonant absorption and stimulated elastic scattering is well described by the optical Bloch equations for a two-level system. In essence each atom forms a two level system with a core level forming the lower energy state and a valence level the upper state. Before arrival of the x-ray pulse, only the lower state is popu-

lated, expressed by a population $\rho_{11} = 1$, while the upper state has a population $\rho_{22} = 0$, where $\rho_{11} + \rho_{22} = 1$. With increasing incident intensity the solutions of the Bloch equations determine the changes of the populations toward the equilibrium limit $\rho_{11} = \rho_{22} = 0.5$.

The population equilibrium, where there is a complete balance between up and down transitions, is reliably reached if the incident energy is tuned to the exact resonance value and the incident fields have a coherence time τ_{coh} longer than the core hole life time $t_\Gamma = \hbar/\Gamma$, where Γ is the total spontaneous (Auger plus radiative) energy decay width of the core hole ($\Gamma = 0.43\,\mathrm{eV}$ and $t_\Gamma = 1.5\,\mathrm{fs}$ for Co L_3). This was accomplished in a previous study [10] by use of a monochromator which by energy filtering of the incident SASE pulses fixed the incident photon energy to the resonance value $\mathcal{E}_0$ and the resulting small bandwidth $\Delta\mathcal{E}_0 \simeq 0.2\,\mathrm{eV}$ yielded a sufficiently long coherence time of about 10 fs. For the case of a thin film one also needs to consider that the total atomic system of areal number density N_a/A responds coherently, lowering the stimulated onset by a value of $\mathcal{G}_{\mathrm{coh}} = N_\mathrm{a}\lambda^2/(4\pi A)$, where λ is the wavelength. For the Co L_3 resonance in Co metal we have $\mathcal{G}_{\mathrm{coh}} \simeq 360$ [8].

In the present study, no monochromator was used so that the pulses had an intrinsic coherence time $\tau_{\mathrm{coh}} \sim 1\,\mathrm{fs}$

associated with the spikes in the incident SASE pulses. In addition, each SASE pulse of approximately 5 eV width only contained a fraction of photons at the resonance energy, while most of them were detuned from the resonance energy. SASE pulses of specified pulse length and central intensity were simulated as described in [17]. The simulations yield a parameter set $I_0, \tau_{\mathrm{coh}}, \Delta\mathcal{E}$ for each *spike* within the total SASE pulse, where $\Delta\mathcal{E} = \hbar\omega - \mathcal{E}_0$ is the detuning energy from resonance. We assumed *independent* SASE spikes and solved the optical Bloch equations for each coherent spike, with the total pulse response being the sum of the individual spike responses. Inhomogeneous broadening effects were taken into account as prescribed by [18, 19]. Examples of simulated SASE pulses for various beam parameters are shown in the inset of Figure 4 below. The simulations gave a histogram of coherence times peaked in the $\tau_{\mathrm{coh}} \simeq 0.5 - 1$ fs range for both 2.5 fs and 25 fs pulses in good accord with experimental results [20]. The stimulated response was therefore similar for both pulse lengths with the larger number of spikes in the 25 fs pulses simply yielding a better defined statistical average (see below).

Solution of the optical Bloch equations yielded the pulse averaged excited state population $\rho_{22}(I_0, \hbar\omega, \tau_{\mathrm{coh}})$ given by [10],

$$\rho_{22} = -\beta_0 \frac{\alpha I_0 \Gamma_x \rho_a d\lambda^5/(32\pi^3 c)}{(\hbar\omega - \mathcal{E}_0)^2 + (\Gamma/2)^2 + \alpha I_0 \Gamma_x \rho_a d\lambda^5/(16\pi^3 c)} \quad (1)$$

where $\beta_0(\hbar\omega)$ is the dimensionless optical absorption parameter describing the spontaneous Co L_3 response, $\alpha = 0.5$ a dimensionless parameter that accounts for the layer-by-layer propagated absorption and stimulation response through the Co film of thickness $d = 25$ nm, I_0 (dimension [energy/(area×time)]) the incident intensity, $\Gamma_x = 0.96$ meV the Co L_3 dipole transition energy width for linearly polarized x-rays, $\rho_a = 90.9$ nm^{-3} the number density of Co atoms, $\lambda = 1.59$ nm the resonant wavelength, $c = 300$ nm/fs the speed of light, and $\Gamma = 430$ meV the core hole energy decay width.

The change of the (in-beam) transmitted intensity due to stimulation relative to the transmitted intensity due to spontaneous processes is given by [8],

$$\frac{I_t^{\mathrm{stim}}}{I_t^{\mathrm{spon}}} = \frac{e^{-2[\beta_0(1-2\rho_{22})]kd}}{e^{-2\beta_0 kd}} \quad (2)$$

where $k = 2\pi/\lambda$ is the photon wavevector. The change in first-order diffracted magnetic response is given by [10]

$$\frac{I_d^{\mathrm{stim}}}{I_d^{\mathrm{spon}}} = \frac{1 - e^{-2\beta_0(1-2\rho_{22})kd}}{1 - e^{-2\beta_0 kd}}$$
$$\times \frac{\cosh(2\Delta\beta_0[1-2\rho_{22}]kd) - \cos(2\Delta\delta_0[1-2\rho_{22}]kd)}{\cosh(2\Delta\beta_0 kd) - \cos(2\Delta\delta_0 kd)} \quad (3)$$

where $\delta_0(\hbar\omega)$ is the dimensionless spontaneous optical dispersion parameter and $\Delta\beta_0, \Delta\delta_0$ the magnetism induced changes of the optical parameters. The exponential prefactors in (2) and (3) reveal the complementary behavior of in-beam transmitted and out-of beam

diffracted intensities which are determined by a change in the spontaneous absorption coefficient β_0 in the presence of stimulation to $\beta_0(1 - 2\rho_{22})$. The last term in (3) reveals that magnetic diffraction depends on changes in both the absorptive $\Delta\beta_0$ and dispersive $\Delta\delta_0$ magnetic sample response.

The results of our simulations are superimposed on the experimental data in Fig. 3, with single-shot transmission intensities shown as open blue circles and diffraction intensities as open red circles. The origin of the large
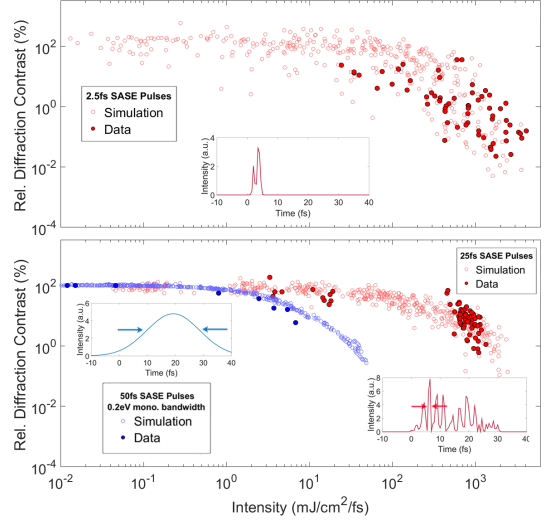

FIG. 4: (color online) Simulations juxtaposed with experimental data for various beam parameters. Top: Simulations and data for 2.5 fs SASE pulses, with a representative simulated pulse plotted in the inset. Bottom: Simulations and data for 25 fs SASE pulses with (blue) and without (red) monochromatization, with representative simulated pulses for both cases plotted in the insets. The response of the longer 25 fs SASE pulses follows the same mean value as the response of the shorter 2.5 fs pulses, but with lower standard deviation by a factor of $\approx \sqrt{10}$, consistent with our independent SASE spike assumption. Monochromatized data utilizing 50 fs pulses are taken from Wu et al. [10].

variance in the stimulated response is mainly due to a combination of the short coherence time and photon energy spread of the individual coherent spikes in the SASE pulses. First, the short intrinsic coherence time of the spikes within the SASE pulses prevents the electronic system to reach a consistent ρ_{22} value, which is only reached in equilibrium when τ_{coh} is significantly longer than the femtosecond core hole life time $t_\Gamma = \hbar/\Gamma$ [8]. Second, the different photon energies of the individual spikes lead to a spread in detuning energies $\hbar\omega - \mathcal{E}_0$ in (1) and therefore in ρ_{22}. The energy spread associated with the temporal spikes in a single pulse is enhanced by the shot-by-shot jitter in the central energy of the SASE pulses caused by pulse-to-pulse jitter of the electron beam energy. The stimulation effect on the magnetic diffraction contrast as

a function of pulse length and coherence time is illustrated in more detail in Fig. 4.

By comparison of the experimental and simulated data shown in red for $\tau_1 = 2.5\,\mathrm{fs}$ and $\tau_2 = 25\,\mathrm{fs}$ pulses in Fig. 4 we see that both pulses have a similar dependence of the diffraction contrast with incident intensity, but the response variance is significantly smaller for the longer pulses. The reduction factor of the variance is found to be close to $\sqrt{\tau_2/\tau_1} = \sqrt{10}$, consistent with the independent SASE spike assumption and the larger number of spikes in the 25 fs pulses that leads to improved noise statistics.

In the bottom half of Fig. 4 we also compare the stimulated response for our non-monochromatic SASE pulses with the results obtained with monochromatized pulses by Wu et al. [10], shown in blue. Besides greatly reduced noise due to the longer coherence time of the monochromatic pulses of $\Delta\mathcal{E}_0 = 0.2\,\mathrm{eV}$ (see blue inset), the onset of stimulated diffraction is lowered by a factor of about 100 by the elimination of energy jitter $\hbar\omega - \mathcal{E}_0$ since the photon energy is fixed to the resonance energy by the monochromator. This behavior is in good accord with that predicted by Fig. 2 in Ref. [8].

Our main results are summarized in Fig. 5, where we plot the averaged response signals in both the transmission and diffraction channels, obtained by simple spline fits to the data. In the absence of stimulation, both plotted relative transmission and diffraction intensities would be constant as a function of the incident intensity, reflecting a linear scaling of the spontaneous response. As discussed above, the plotted transmission response emphasises the change of the peak of the Co L_3 resonance, and thus also represents an quasi-elastic response. The figure reflects the complementary, opposing nonlinear responses in the two channels. The pnCCD diffraction signal is attenuated by 2 orders of magnitude, while forward transmission increases from the spontaneous value of 30% to the stimulated value of $\sim 100\%$.
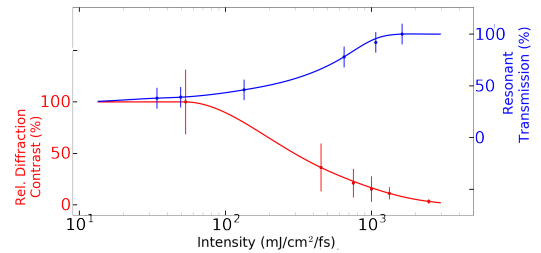

FIG. 5: (color online) Summary results of the observed transmission (blue) and magnetic diffraction (red) contrast relative to the conventional spontaneous response as a function of incident intensity. The shown curves are simple spline fits of the data. With incident intensity the transmission increases from $\sim$30%, characteristic of the Co L_3 resonance response of a 25 nm Co film to 100% corresponding to complete x-ray transparency. The diffraction contrast behaves oppositely, decreasing by about two orders of magnitude.

In summary, our measurements reveal the observation of complete x-ray transparency for a solid sample predicted in Ref. [8]. Together with previous diffraction results [10], our work also reveals the key dependence of stimulated effects on intensity, coherence time, and resonance tuning of the photon energy.

[1] N. Rohringer et al., Nature **481**, 488 (2012).
[2] M. Beye et al., Nature **501**, 191 (2013).
[3] T. Kroll et al., Phys. Rev. Lett. **120**, 133203 (2018).
[4] C. Weninger et al., Phys. Rev. Lett. **111**, 233902 (2013).
[5] J. H. Hubbell, P. N. Trehan, N. Singh, B. Chand, D. Mehta, M. L. Garg, R. R. Garg, S. Singh, and S. Puri, J. Phys. Ref. Data **23**, 339 (1994).
[6] J. Stöhr, *NEXAFS Spectroscopy* (Springer, Heidelberg, 1992).
[7] J. Stöhr and H. C. Siegmann, *Magnetism: From Fundamentals to Nanoscale Dynamics* (Springer, Heidelberg, 2006).
[8] J. Stöhr, A. Scherz: Phys. Rev. Lett. **115**, 107402 (2015); *Phys. Rev. Lett.* **116**, 019902 (2016).
[9] J. Stöhr, Phys. Rev. Lett. **118**, 024801 (2017).
[10] B. Wu, T. Wang, C. E. Graves, D. Zhu, W. F. Schlotter, J. J. Turner, O. Hellwig, Z. Chen, H. A. Dürr, A. Scherz, et al., Phys. Rev. Lett. **117**, 027401 (2016).
[11] O. Hellwig, G. Denbeaux, J. Kortright, and E. E. Fullerton, Physica B: Condensed Matter **336**, 136 (2003).
[12] C. Bostedt, S. Boutet, D. M. Fritz, Z. Huang, H. J. Lee, H. T. Lemke, A. Robert, W. F. Schlotter, J. J. Turner, and G. J. Williams, Rev. Mod. Phys. **88**, 015007 (2016).
[13] J. C. Castagna et al., Journal of Physics: Conference Series **425**, 152021 (2013).
[14] S. Schreck et al., Phys. Rev. Lett. **113**, 153002 (2014).
[15] C. Boeglin et al., Nature **465**, 458 (2010).
[16] V. Shokeen, M. S. Piaia, J.-Y. Bigot, T. Müller, P. Elliott, J. K. Dewhurst, S. Sharma, and E. K. U. Gross, Phys. Rev. Lett. **119**, 107203 (2017).
[17] E. L. Saldin, E. A. Schneidmiller, and M. V. Yurkov, New J. Phys. **12**, 035010 (2010).
[18] R. A. Smith, Proceedings of the Royal Society A: Mathematical, Physical and Engineering Sciences **362**, 1 (1978).
[19] R. A. Smith, Proceedings of the Royal Society A: Mathematical, Physical and Engineering Sciences **362**, 13 (1978).
[20] I. A. Vartanyants et al., Phys. Rev. Lett **107**, 144801 (2011).

5.4 Conclusion and Outlook

Our experiment aimed towards finding experimental evidence of the existence of stimulated RIXS in fluence regimes readily achievable for state of the art light sources, and towards evaluating its relevance for further developments of spectroscopic methods. Our experimental results show the feasibility of this idea by presenting the first direct observation of stimulated RIXS. If the photon field becomes stronger than the background field [30], the events of stimulated emission start to outnumber those of spontaneous emission and eventually even the Auger decay. This results in an increase in direct forward scattering at the cost of spontaneous scattering as shown in Section 5.3.3. It is important to note that the stimulation is suppressed close to the Fermi level. We interpret this through the induction of partially occupied states around the Fermi level, induced by ultrafast electron cascades.

Furthermore, the effects of induced transparency and the scattering breakdown were discussed. These effects accompany stimulated RIXS naturally, since they are based on an increased excited state population, but they set in at lower incident fluences, as shown in Section 5.3.1 and Section 5.3.2. These effects are particularly relevant for any spectroscopic method being carried out in comparatively low fluence regimes from $\approx 20 \frac{mJ}{cm^2 fs}$ upwards, because they change the linear transmission and the scattering cross sections, which are commonly understood as fixed, material dependent interaction constants. It becomes, therefore, clear that the strong incident X-ray field changes the photon matter interaction substantially by inducing fluence dependent changes to the absorption and emission cross sections [30], which has to be taken into account when interpreting transmission or scattering spectroscopy at FEL light sources.

Our experiment helped understanding and describing stimulated RIXS and the correspondingly required X-ray fluence regimes, thereby providing a new basis for even further advanced experiments based on this physical process. A promising idea to exploit these findings is a four wave mixing approach as discussed in, for example [106, 122, 123]. An experiment as proposed in [106, 122, 123] requires two X-ray pulses, one pump pulse to excite the system and create core holes, and another one with an energy tuned to the transition of interest, stimulating the emission from this channel. For this type of ex-

periment, both pulses have to arrive on the sample within the coherence time, in other words within a few femtoseconds, which is nearly impossible for separately generated pulses. However, there are promising reports of two color FEL pulses already being commissioned at LCLS [124]. Another obstacle relates to the control over the incident pulse parameters, because a wave mixing experiment based on fluctuating and lowly reproducible SASE pulses is likely to fail. There have been encouraging news of progress in seeding FEL pulses, as explained in Chapter 3, as it could substantially reduce the fluctuations, improve the temporal coherence, as well as narrow the bandwidth of the pulses even further [125]. The first implementation of seeded FEL pulses have been demonstrated at FERMI [63]. An upgrade in order to enable seeded pulses at the LCLS II facility is also expected to happen. These new developments raise hopes to move another step closer towards the application of stimulated RIXS.

Chapter 6

A Rate Model Approach for FEL Pulse Induced Transmissions Changes, Saturable Absorption, X-Ray Transparency, and Stimulated Emission

The previous chapter discussed the experimental findings of our stimulated scattering experiment. This chapter is now focused on developing a simulation approach through a rate model to further understand our observations. As the CoPd multilayer exhibits especially many states close to the Fermi energy, these states will play an important role for the spectroscopic characteristics discussed before, therefore the model must include the DOS close to the Fermi energy and must be able to understand the occupation changes and their effects on the experimental channels, namely scattering and resonant inelastic scattering. As an unexpected increase in photons below the absorption edge and an increase in absorption above the absorption edge were observed, these have to be reproduced as well as the scattering breakdown observed in first and third order scattering.

As the use of FEL sources increases, so do the findings mentioning nonlinear phenomena occurring at these experiments, such as saturable absorption, induced transparency and scattering breakdowns. These are well known among

the laser community, but are still rarely understood and expected among the X-ray community and to date lack tools and theories to accurately predict the respective experimental parameters and results. This chapter presents a simple theoretical framework to access short X-ray pulse induced light-matter interactions which occur at intense short X-ray pulses as available at FEL sources. The introduced approach allows to investigate effects such as saturable absorption, induced transparency and scattering suppression, stimulated emission, and transmission spectra, while including the density of state influence relevant to soft X-ray spectroscopy in, for example, transition metal complexes or functional materials. This computationally efficient rate model based approach is intuitively adaptable to most solid state sample systems in the soft X-ray spectrum with the potential to be extended for liquid and gas sample systems as well. The feasibility of the model to estimate the named effects and the influence of the density of state is demonstrated using the example of CoPd transition metal systems at the Co edge. It is hoped that this work will make an important contribution for the preparation, performance, and understanding of FEL based high intensity and short pulse experiments, especially on functional materials in the soft X-ray spectrum.

6.1 Model Introduction

The past two decades have lead to a rapid establishment of FEL applications for the utilization of ultra-fast and extremely bright photon sources in the extreme ultra-violet to hard X-ray photon regime at sources such as Fermi Elettra, Flash, SACLA, or LCLS, and with new sources such as XFEL or SwissFEL due to commence operation in the near future. These sources enable new experiments and impressive insights into the very heart of matter through techniques such as scattering before destruction [126], pump probe experiments utilizing different combinations of two color X-rays or optical pump-probe setups [127, 78, 128], and many more. To enable these experiments and insights, higher photon densities and shorter pulse lengths have been pushed, which also opened the experimental window into non-linear X-ray-matter interactions. There, a whole new world of effects has been observed and reported, including multiple photon absorption [129], stimulated scattering [130, 127], saturable absorption [131] as well as parametric conversion [132]. These effects, however, are still unexpected and unaccounted for in the X-ray community, although, the field of optical laser

science has long been familiar with these effects [133] and thus has established models to account for high pulse power light-matter interaction [134, 135]. As X-ray experiments are often seen as the toolbox to gain new insights into the systems under investigation rather than insights into the nature of light-matter interactions, these new effects are delaying the extreme potential of ultra-fast X-ray science to enhance our knowledge in chemical reaction dynamics and pathways, heterogeneous catalysis, photosynthesis, and solid state phase transitions, for example.

There have of course been efforts to create theories to handle these effects and to understand them in detail, utilizing various techniques from solving the Maxwell-Bloch equations [136], to a Maxwell-Liouville-von Neumann approach [130, 137, 138], and a rate-equation based approach [139, 140]. Although these models are powerful and work well for their specific use case (presented for gas or cluster targets), they are also computationally demanding and need extensive expertise to be adapted to different systems. As FEL science moves towards more applied areas of physical and chemical sciences, this exceeds the scope of many experimental proposals. Here it becomes obvious that there is still a need of a quick and simpler to use toolbox to get a realistic estimation of the expected interactions for varying experimental conditions, especially for functional materials with a high density of states (DOS) around the absorption edge. We decided to build up on the knowledge of optical laser science and transfer this to a simple and easy to expand toolkit that functions well for this type of soft X-ray-matter interaction experiments and can enable a fast window into high intensity soft X-ray FEL science.

This paper is organized as follows: First, the rate model is introduced with its various aspects and relevant setup parameters including the intensity dependent cross sections and the density of state estimation for the absorption band. Secondly, the dynamics of a pulse transmission are being discussed with respect to the internal occupation changes, the intensity dependent rate changes, and the spectral effects of the individual channels. Lastly, the spectral changes of a transmitted pulse are investigated with their dependency on the incident pulse's energy, intensity, and the sample's density of states. The paper finishes with a comparison to the scattering breakdown observed by Chen et al. [115].

6.2 Rate Model Approach

The model discussion is started from a well established set of rate equations whose derivations and applications can be found in for example [133, 141, 134]. The presented approach is based on a three band/state system containing a core state, an intermediate non-radiative decay state, and the absorption band, which is common in functional materials and can be partly occupied, as shown in Fig. 6.1 a). For simplicity, the core and the intermediate state are not energy resolved, i.e. from the core state, every state in the absorption band can be reached (compare Fig. 6.1 b/c)) and every state in the absorption band can decay into the core or intermediate state (compare Fig. 6.1c)). The intermediate state works as a relaxation state for all non-radiative decay mechanisms. In the soft X-ray regime, this decay mechanism is dominated by the Auger decay. This implementation is different from simulations presented by Hatada and Di Cicco [139, 140], as the modeling approach considers the DOS in the absorption band, thus enabling energy resolved information on spectral changes and spec-
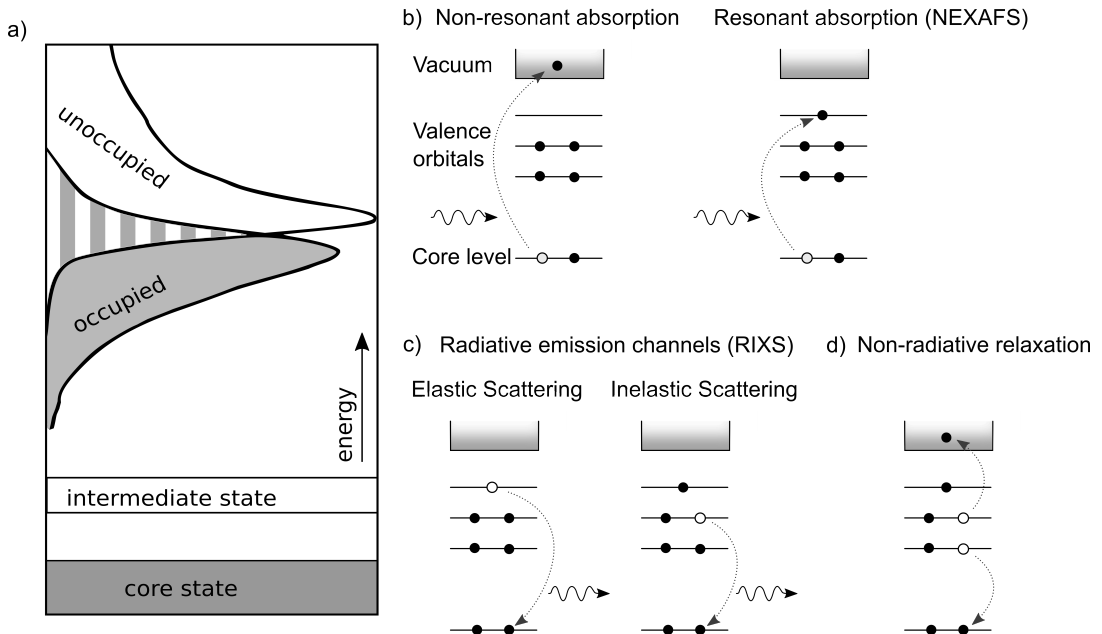
Figure 6.1: The initial setup of the model's sample system system and the implemented energy conversion channels. In any X-ray matter interaction, a core state electron is being excited into an absorption state or band, which then decays back into the core state, or into a non-radiative intermediate state. The absorption band can be partitioned into occupied and unoccupied states. The example displays a typical L-edge type of system, which is used for most examples in the following.

troscopic features induced by the X-ray pulse. Furthermore, the model considers an intensity driven cross section as discussed by Patterson [142] and extended by Schreck et al. [30].

6.2.1   Rate Equations

The basis of the here introduced rate equation system is the time evolution of the population number of the three bands and states (N_{Core}, N_{Band}, $N_{Intermediate}$), respectively, and their interaction channels (Fig. 6.1b)-d)). Following the text-book formalism [133], this leads to:

$$\frac{\partial N_{Core}(t)}{\partial t} = \sum^{E}[-R_{Abs}(E,t) + R_{Stim}(E,t) + R_{Spon}(E,t) + R_{Decay}(t)]$$

(6.1)

$$\frac{\partial N_{Band}(E,t)}{\partial t} = R_{Abs}(E,t) - R_{Stim}(E,t) - R_{Spon}(E,t) - R_{Aug}(E,t)$$ (6.2)

$$\frac{\partial N_{Intermediate}(t)}{\partial t} = R_{Aug}(t) - R_{Decay}(t)$$ (6.3)

The three levels can be populated or depopulated by the processes shown in Fig. 6.1 (b-d), namely absorption R_{Abs}, spontaneous R_{Spon} and stimulated R_{Stim} emission, and non-radiative decay R_{Decay}, here given as the number of events at the given time and energy. The core state, as mentioned above, is energy independent in this model, therefore the sum is taken over all energy channels to obtain the total population change. The core state in this model can be depopulated through absorption and repopulated through spontaneous emission, stimulated emission, and the decay of the intermediate states, respectively. The absorption band is implemented as an ensemble of states that can be partially occupied, as shown in Fig. 6.2. The absorption band is populated through absorption and depleted via stimulated emission, spontaneous emission, and Auger decay. As the transmission of short X-ray pulses of the order of femtoseconds is simulated in the soft X-ray regime, non-radiative decays are dominated by Auger decay (Fig. 6.1 d)), thus other non-radiative decays are not included in the current model. Therefore, the intermediate state can decay into the core state through non-radiative relaxation and can be populated through the absorption band via the Auger decay. With the exception of the decay from the intermediate state to the core state, all interactions are time and energy resolved.
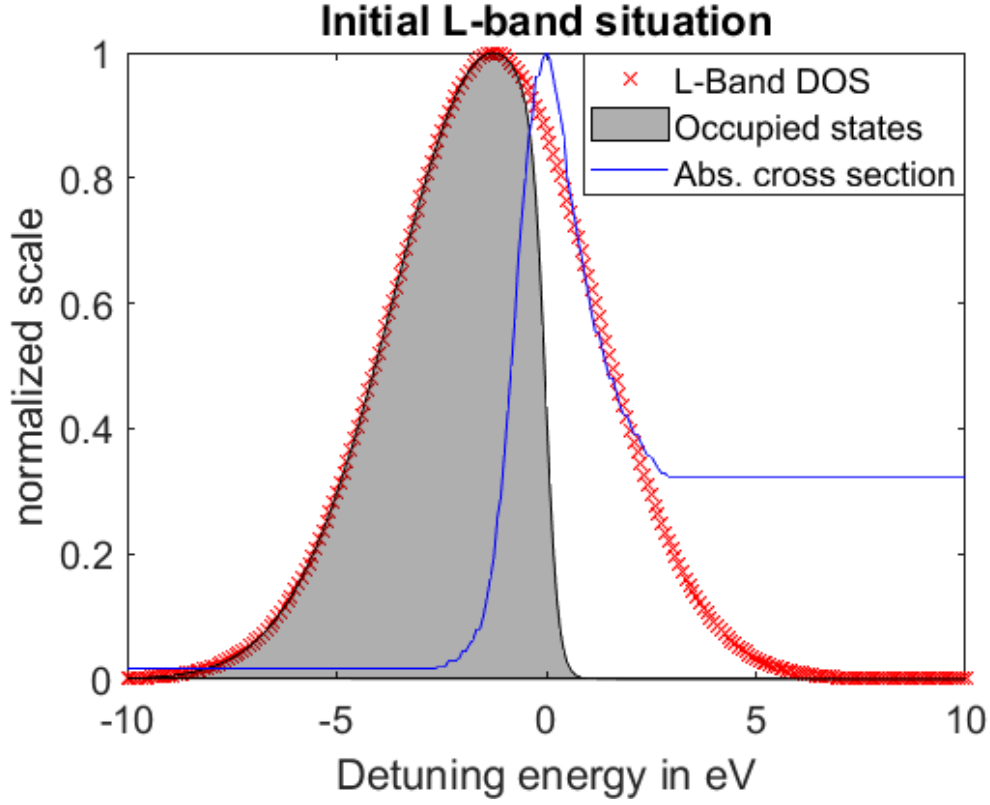
Figure 6.2: Initial band occupation for a Co L-edge simulation. Width and distribution have been create to be comparable to [143] for Co through a Gaussian, convoluted with a Fermi-Dirac distribution. The gray area represents initially occupied states, while the white area represents free unoccupied states. The red curve indicates the available states at the given energy, while the blue curve gives the absorption cross section at the Co L-edge.

The interstate transition events are given by the following equations:

$$R_{Abs}(E, t) = I(E, t) \cdot \frac{\lambda A}{hc} \cdot \sigma_{abs}(E) \cdot f_{Abs}(E, t) \tag{6.4}$$

$$R_{Spon}(E, t) = I(E, t) \cdot \frac{\lambda A}{hc} \sigma_{Spon}(E) \cdot N_{Band}(E, t) \cdot f_{Spon}(E, t) \tag{6.5}$$

$$R_{Auger}(E, t) = I(E, t) \cdot \frac{\lambda A}{hc} \sigma_{Auger}(E) \cdot N_{Band}(E, t) \cdot f_{Aug}(E, t) \tag{6.6}$$

$$R_{Stim}(E, t) = I(E, t) \cdot \frac{\lambda A}{hc} \sigma_{Stim}(E) \cdot N_{Band}(E, t) \cdot f_{Stim}(E, t) \tag{6.7}$$

$$R_{Decay}(t) = \frac{N_{intermediate}(t)}{\tau_{non-radiative}} \tag{6.8}$$

These event numbers depend mainly on three factors: first, the incident pulse $I(E, t)$ with the photon distribution in time and energy, second, the respective interaction cross sections $\sigma(E)$ or decay times τ as further discussed in the next

section, and finally, the occupation factors $f(E,t)$ between the involved states. The incident pulse is taken in terms of total number of photons at a given energy and time, as shown in Eq. 6.11. The occupation factor f is given by the product of the relative occupations of the two involved states, for example, the occupation factor for absorption becomes the product of the occupied core state occupation and the available unoccupied absorption state occupation:

$$f_{abs}(E,t) = \frac{N_{Core}(t)}{max(N_{Core})} \cdot (1 - \frac{N_{Band}(E,t)}{max(N_{Band}(E,t))})$$ (6.9)

The other variables have the usual meaning, with A being the incident pulse focus size.

6.2.2   Decay Cross Sections

The decay cross sections are implemented as described by Schreck et al. [30], where the authors show how they can be determined from the total absorption cross section, the photon energy and the present photon field. More specifically, the total absorption cross section has to decay through one of the decay channels, thus the sum of decay cross sections has to equal the total absorption cross section:

$$\sigma_{Abs} = \sigma_{Aug} + \sigma_{Spon} + \sigma_{Stim}$$ (6.10)

The resulting cross section distribution for different photon numbers can be seen in Fig. 6.3, where they have been calculated for a 10 fs incident pulse with varying photon number at 788 eV. The maximum is given by the absorption cross section (violet line) at a given energy, but changes with the absorption cross section over the absorption band (compare Fig. 6.2 blue line). The distribution of decay cross sections is dependent on the energy and the total number of photons. As the sample is treated in a one-dimensional way, the total number of photons present is treated as the sum of all photons that have passed into the sample within a given time t. Therefore, the decay cross sections (compare Fig. 6.3) will initially start at the lower end of photon numbers and will stop changing when reaching the total number of photons within the pulse when the pulse has effectively been transmitted. This leads to a somewhat distorted decay behavior after the pulse has passed. However, as the focus of these simulations is on the light-sample interaction during the pulse and not the sample recovery behavior,

this should not pose an issue. As one can see in Fig. 6.3, the majority of the decay cross section is given by the Auger decay, which holds true for the soft X-ray regime, yet for higher photon energies, the majority of decays switches from Auger to spontaneous emission, as expected and shown in [30]. For increasing photon numbers, the photon field dependent stimulated cross section increases, thus suppressing the spontaneous and Auger decay cross sections. This concept is completely implemented into Eqs.(4.14 and 6.10), and a full derivation can be found in Schreck et al. [30].
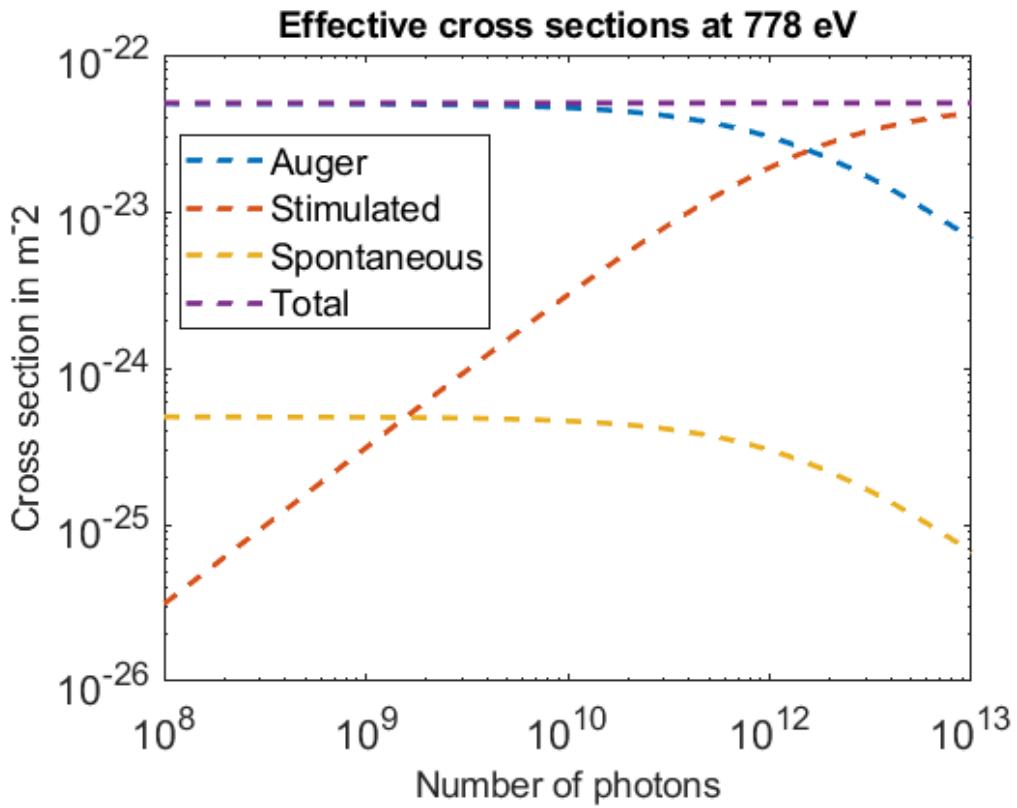
Figure 6.3: An example of the decay cross sections used in the model, here for a photon pulse at 778 eV. Depending on the number of photons within a pulse the distribution of decay cross sections are changing, whilst the total decay cross section equaling the total absorption cross section and the sum of all decay cross sections, stay constant. Towards higher photon numbers, the auger and spontaneous cross section are being suppressed for the benefit of the stimulated cross section. The equations are based on the model developed by Schreck et al. [30] and have been implemented into the here introduced model.

The absorption cross section is commonly known for most sample systems, however as FEL pulses can saturate absorption and induce transparency [131, 144, 115], the absorption cross section may not be treatable like an interac-

tion constant, but can change with the incident pulse intensity. These types of changes have been discussed by Stöhr et al. [145] for a 2-level system. It is possible to implement a time, intensity, or absorbed energy dependent change into the absorption cross section in the modeling approach. This affects all rates, as the decay rates depend on the absorption cross section for example through the opening of core level holes. For this purpose, a factor decreasing and increasing the overall absorption cross section with the transmitted pulse intensity was tested and was found to affect the timing (delay or accelerate) of the dynamics, but not the spectral position of the changes. Thus for the following, we do not implement this factor affecting the absorption cross section.

6.2.3   The Incident Pulse

For the incident pulse we used a Gaussian shaped light pulse in the time and energy regime. The pulse can be written in terms of intensity $I(E,t)$ or photon number N_{Photon} at a certain energy and time, as given in Eq. 6.11 and 6.12, respectively. Here I_0 is the incident intensity in mJ/(cm^{2}fs), with σ_t and σ_E being the time and energy width of the pulse, and A being the focus size. The pulse can be shifted in the time domain using the time offset t_{Off}, and in energy using the energy offset E_{off}.

$$I(E,t) = I_0 \cdot \exp\left(-\frac{1}{2} \cdot (\frac{t - t_{off}}{\sigma_t})^2\right) \cdot exp\left(-\frac{1}{2} \cdot (\frac{E - E_{off}}{\sigma_E})^2\right) \qquad (6.11)$$

$$N_{Photon}(E,t) = I(E,t) \cdot \frac{\lambda A}{hc} \qquad (6.12)$$

To simulate the spectral changes after transmission, we look at the time evolution of the transmitted pulse's photon numbers $Pulse_{trans}$ in time and energy (Eq. 6.13), which depends on the incident pulse $I(E,t)$ and the two channels ($R_{Abs}(E,t)$ and $R_{Stim}(E,t)$) depleting and refilling photons.

$$\frac{\partial Pulse_{trans}(E,t)}{\partial t} = I(E,t)\frac{\lambda A}{hc} - R_{Abs}(E,t) + R_{Stim}(E,t) \qquad (6.13)$$

For the model it is of course feasible to adapt the pulse to represent typical SASE patterns with multiple spikes at different energies and varying time delays, although they are not straightforward to compare as the occupation changes strongly depend on the spectral distribution of these SASE pulses. Hence for the

first demonstration of the model, Gaussian shaped pulses that vary in intensity, time, energy, and width are utilized.

6.2.4   Absorption Band DOS

To estimate the available states in the interaction region, the interaction volume is calculated from the sample dimensions and the pulse focus as $V_{interaction} = A \cdot d$, with the focal size A and the sample thickness d. Multiplying this with the atom density ρ_{Atom} yields an estimate for the number of atoms in the interaction volume. From this one obtains an estimate for the maximum number of states in the core level and the interaction band through the electron count of the respective orbital, i.e. times 2 for the core level and times the number of electrons n_e in the absorption band. This obviously leads to an initial occupation number of the core and interaction band which in turn enables to follow relative occupation changes. To account for the DOS in the absorption band around the edge, one can either take a full DOS for the initial distribution, or take an XES measurement as a measure of occupied states and an XAS measurement as a measure for unoccupied states in the absorption band. For most material systems, this information is well known, for example a Co L-edge is described in [143] and reproduced in Fig. 6.2. This distribution is approximated through a Gaussian distribution, reflecting the total number of states in the absorption band at the given energy, which then is multiplied with a Fermi-Dirac distribution, to get an initial distribution for occupied, unoccupied, and total available states at the different absorption edge energies, as displayed in Fig. 6.2. In the presented example, the gray area shows the initial occupation of states around the absorption edge, whereas the red line represents the available states at a given energy. For visualization, the absorption cross section, which has been adapted from [145] for the Co L-edge of a CoPd multi-layer, is shown in blue. For the ratio of occupied and unoccupied states, the ratio of electrons in the absorption band was found to be a rather good measure. For example for a Co L-edge, there are 7 out of 10 d-electrons, yielding a pre-occupation of 70 % of the available states in the absorption band, which compares well to the situation measured for a Co film by Nillson et al.[143]. When discussing X-ray absorption or X-ray emission spectroscopy, the core hole screening effect and the Z+1 rule ?? have to be considered with different strengths for differ-ent material systems. As the RIXS process discussed here moves from an initial state via a transient

state back to said initial state, and the dynamic effects connected to core hole screening occur for nearly filled bands in the ground state **??**, which is not the case here, we consider the core hole screening to be negligible for the discussions below.

6.2.5   Occupation Dynamics

Now a Gaussian shaped pulse being transmitted through the described sample system is considered. This results in an occupation dynamic, as displayed in Fig. 6.4. Here one can see how the incident pulse depopulates the ground state (blue) while increasing the occupation of the excited states in the absorption band, shown as a sum of all states (yellow) and a single state at the central resonance 778 eV (red). As time goes on, the excited states decay while reoccupying the ground state through stimulated and spontaneous emission and the intermediate relaxed state (purple) through Auger decay. In the following, no decay is considered from the relaxed state back into the core hole ground state as we focus on the immediate pulse matter interaction and not on the slower relaxation behavior.
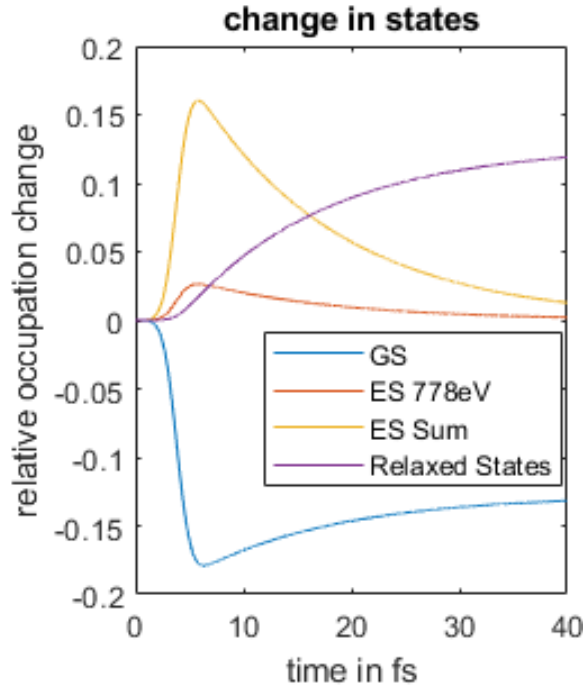
Figure 6.4: The relative occupation change in the different states is shown for a 5 fs, 2 eV FWHM pulse with 10 mJ/(cm^{2}fs) Intensity is shown. As the pulse travels through the sample, the ground state (blue) occupation is converted into excited state or absorption band population (red and yellow). Over time, the Auger decay starts to occupy the intermediate relaxed states (purple), thus depopulating the majority of the excitation band and preventing it from recombining into the core hole ground state.

6.3   Model Applications; CoPd multi-layer samples under short high intensity pulses

To illustrate how the model can be applied for short pulse high fluence X-ray spectroscopy experiments, we choose a typical transition metal Co L-Edge spectroscopic situation as described in [144], which has shown changes in transparency and scattering in past FEL experiments [115, 144, 146]. As the CoPd system has a high DOS around the Fermi level, we expect the impact of the DOS on the transaction rates to be high compared to other typical soft X-ray spectroscopic systems. We streamline the SASE pulses from typical FEL experiments by using a resonant Gaussian shaped pulse of variable intensity, energy and length, as this significantly simplifies the interpretation of the simulation results and enables a much better understanding of the model's dynamics.

6.3.1   Transmission and Induced Transparency

In Fig. 6.5, the transmission of a resonant 2 eV FWHM pulse is shown for varying central pulse energies relative to the resonance (778 eV). The transmission is defined as the difference between the sum of all incident photons and the sum of all transmitted photons. The transmission for all pulses increases for higher incident pulse intensities, starting with a linear increase for lower incident intensities (inset) before slowly saturating towards (almost) full transparency at higher intensities. The general transmission increase is due to two reasons in the model. First, the ground state population gets depleted more strongly with increasing intensity, which reduces the probability of further absorptions through the population factor f. Second, the higher the incident intensity gets, the higher becomes the probability for stimulated emission events, which work as a counterbalance to absorption as they 'add' photons to the transmitted pulse, thus effectively increasing the transparency. The transparency depends on the incident photon distribution, being higher for a pulse that has reduced overlap with unoccupied absorption band states, which is the case for all detuned pulses. For a +1 eV detuned pulse (pink), the photon distribution only overlaps by about 30 % with empty absorption band states (as illustrated by the white area in Fig. 6.2), therefore the transparency at low incident pulse intensities is approximately doubled compared to the resonant pulse. The resonant
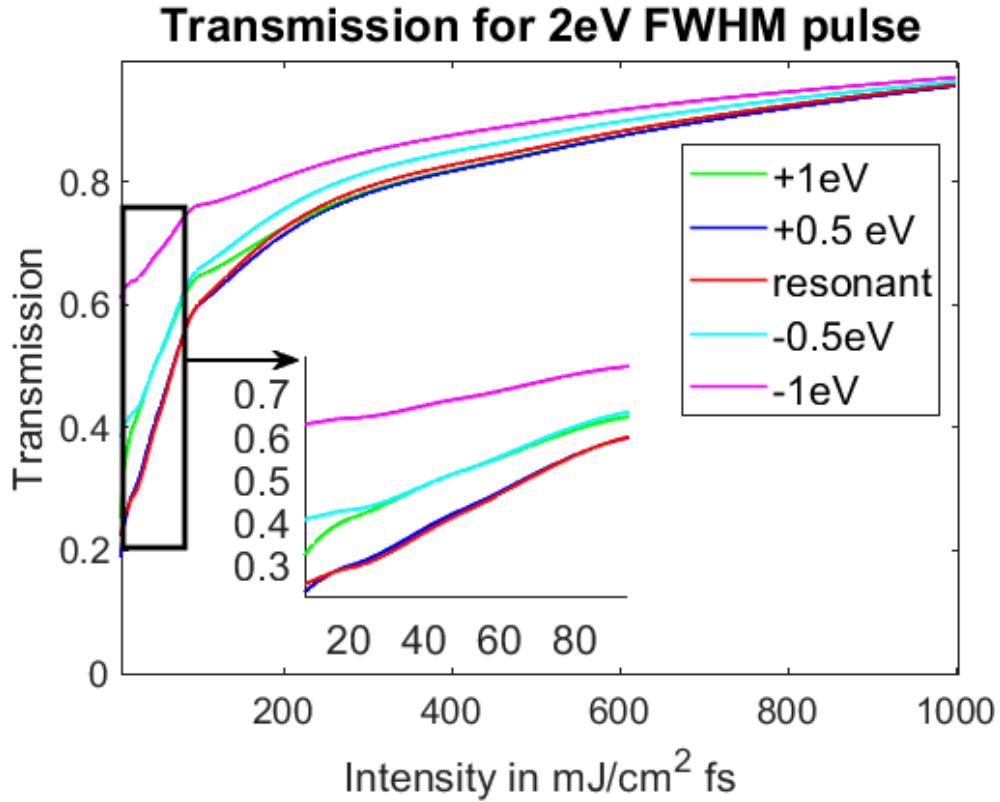
Figure 6.5: The transmission of an incident pulse is shown for a resonant (red) and detuned (other colors) 2 eV FWHM pulse. The resonant pulse (red) shows the lowest initial transmission, as most photons overlap with the majority of empty absorption band states, whereas the detuned pulses overlap with less available absorption band states (positive detuned, green and blue), or more already occupied states (negative detuned, cyan and pink). For low intensities (inset) all pulses show a linear transmission increase with increasing pulse intensity, but for higher intensities, the transmission converges towards an effectively fully transparent sample.

pulse (red) and the 0.5 eV positively detuned pulse (blue) have almost the same transparency evolution, as they both highly overlap with the absorption cross section, which reflects the width of the strongest absorption area (compare with the absorption cross section (blue) in Fig. 6.2).

6.3.2   Intensity Dependent Absorption and Stimulation

To compare the absorption and stimulation channel, Fig. 6.6 shows the respective number of events, which is defined as the sum of all channel events, here calculated for a 2 fs long resonant pulse. As the pulse intensity increases, so do
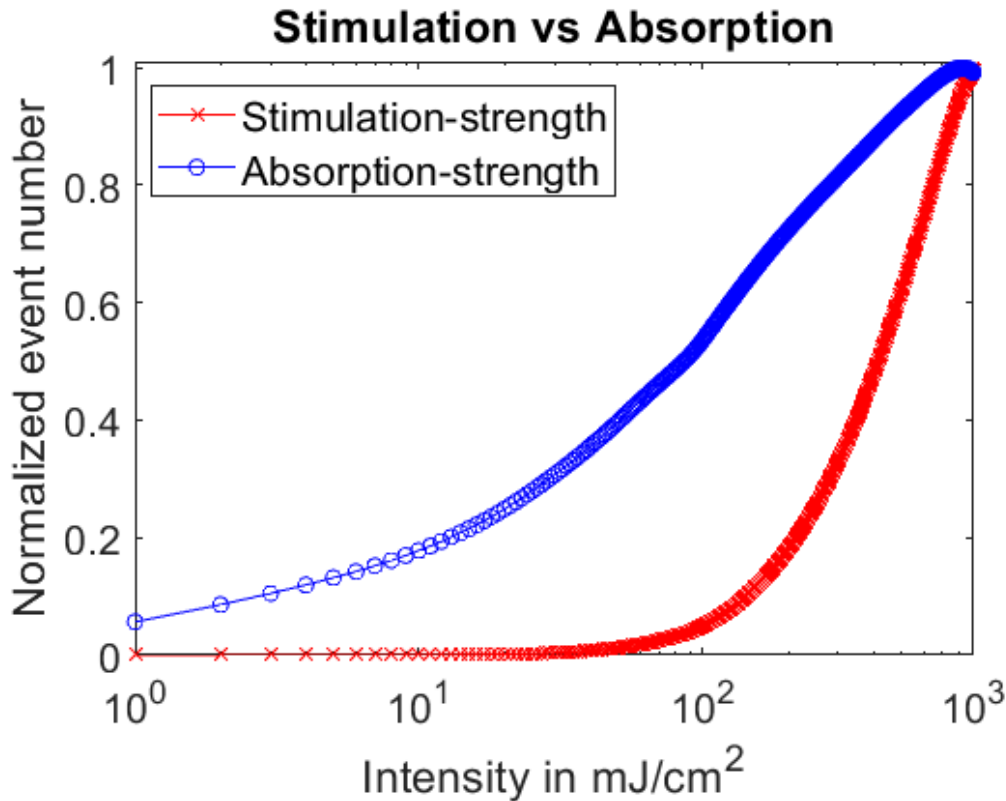
Figure 6.6: The intensity dependent relative amount of stimulated or absorption events, respectively, simulated for a 2 fs long resonant pulse of 2 eV FWHM. The absorption increases with the incident pulse intensity, whereas the stimulation only starts to set in for high intensities, but then amplifies rapidly. The event numbers have been normalized to the maximum number of events for each channel, respectively. This is done for easier visualization of the two event numbers, as absorption is occurring at far higher rate than the stimulation. The exact strength of the two channels depends on a number of factors. This image should visualize the trend between the linear increase in absorption and the non-linear increase in stimulated events.

the two optical channels, however, while the absorption increases steadily with increasing intensity, the stimulation only starts to kick in above 100 mJ/(cm²fs). This effect of the superlinear increase in stimulated emission with higher intensity is analogous to the light-versus-current characteristic in, for example, semiconductor lasers (Reference **??** Fig: 5 and 6). Also, the respective events do not occur at the same photon energies, which leads to an asymmetric sample reaction in state changes, as will be discussed in more detail in Sec. 6.3.3. But let us discuss two other aspects first: The decay events relative to the created core holes, and the spectral evolution of the absorption and stimulation channels.

Another quantity to understand the rate model dynamics is the number of decay events relative to the number of core holes created. In Fig. 6.7 the maximum number (peak) of stimulated events are shown relative to the number of core holes created through the pulse for different detuning energies relative to the resonance. The simulations where performed for a 5fs, 2eV FWHM pulse with varying intensity to create different amounts of core holes. This shows the trend that the more overlap the pulse has with the pre-occupied states in the valence band (in this case a negative detuning energy), the more stimulated events are being triggered. However, this shows the peak number of events for a single time-step at these detuning energies to visualize the impact of detuning and therefore the overlapp with the unoccupied and pre-occupied valence states. For the trend of the total number of events, compare this with Fig.
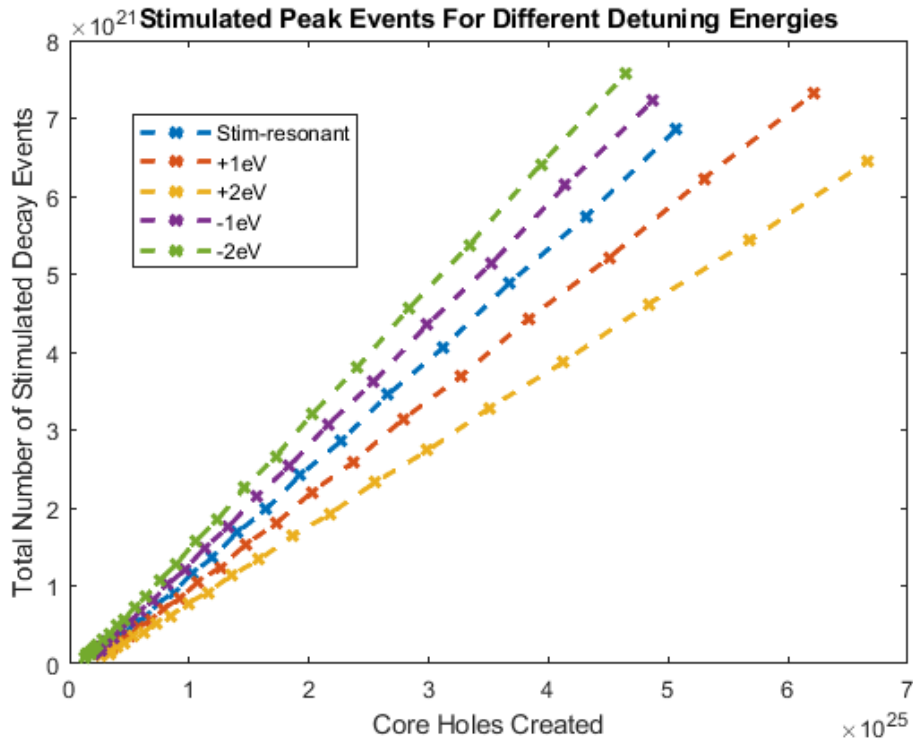
Figure 6.7: Stimulated peak events are shown for different detuning energies of a Gaussian pulse in dependence of the total number of core holes created. This was simulated for varying incident intensity for a 2fs, 2eV FWHM pulse with different detuning energies relative to the resonance. For the trend of the total number of events compare this with Fig. 6.8.

6.8. Here, the trend of the total number of Auger decays and the total number of stimulated emissions are shown in dependence of the total number of core holes created. One can see that the detuning has only a minor role on the total

number of events. However, the length of the pulse and the simulation time has a strong effect on the relative intensities. In this case the simulations where performed for a 2 eV FWHM pulse with 5 fs length, and a 40fs simulation time. The incident pulse maximum was delayed by 10 fs to cover the full ramp-up in the simulations. As the graph shows, the total number of stimulated emission events stays below the total number of core holes created, as it has to be expected. Although not exactly visible here, the same is true for the sum of Auger decays and stimulated emission events.
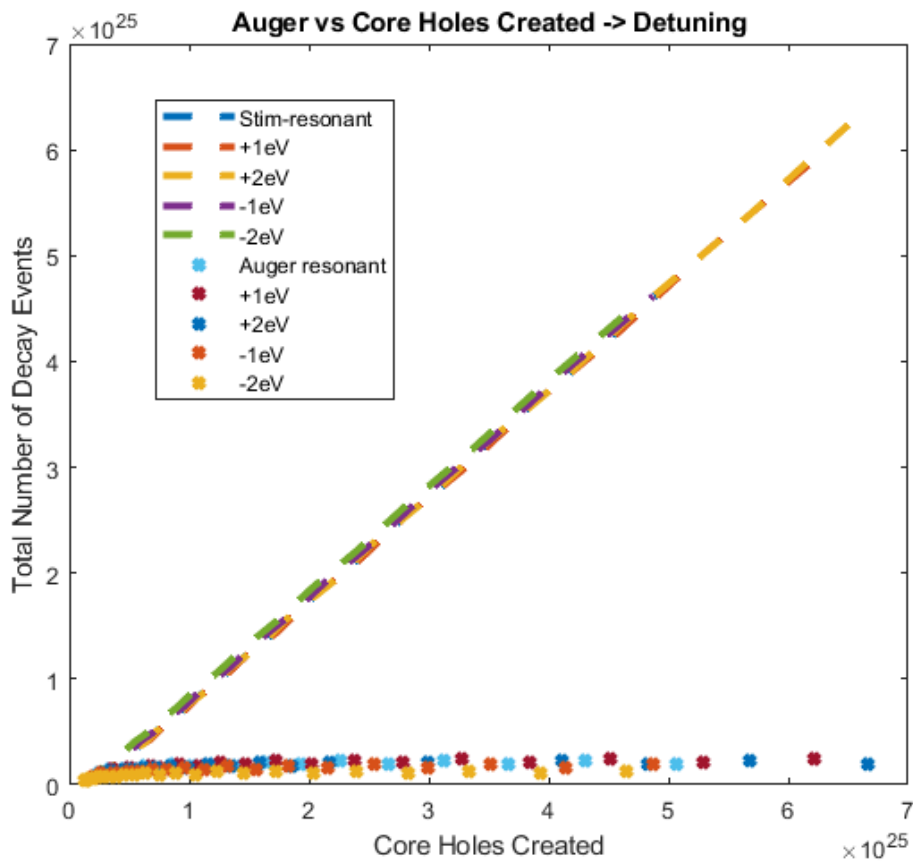
Figure 6.8: Here, the trend of the total number of Auger decays and the total number of stimulated emissions are shown in dependence of the total number of core holes created. The simulations where performed for a 2 eV FWHM pulse with 5 fs length, and a 40fs simulation time, and the number of events summed over the simulation time. The simulations have also been performed for different detuning energies, but as shown here, the effect of detuning is minimal on the total number of decay events.

As shown in Fig. 6.8, the total number of decay events does not relate to the detuning energy of the incident pulse. Let us discuss now how the spectral dis-

tribution of the absorption and stimulation act for a resonant Gaussian incident pulse. Now we compare the spectral evolution of the absorption and stimulation channels, which are shown in Fig. 6.9 and Fig. 6.10 respectively. Since the spectral changes are normalized, only relative changes can be seen here. The spectral distribution of absorption events shifts from the higher end of the absorption edge towards the lower end, thus occurring more frequently in spectral areas with more pre-occupied L-band states. Also, the overall absorption distribution is more pronounced and steeper around $1 - 2$ eV, however this is a feature of the normalization, as for increasing numbers of absorption events this quenches the lower numbers. Note that this effect is not observable at the lower energy end of the distribution, hinting to an asymmetric absorption behavior, which is to be expected given the asymmetric pre-occupation of the absorption band (compare white and gray area in Fig. 6.2). For the spectral distribution of stimulation events, the shift only occurs in an asymmetric way towards higher intensities. Comparing Fig. 6.9 and Fig. 6.10, one can see that the stimulation distribution is shifted to lower energies compared to the absorption distribution. As these two have the opposite effect on the transmitted photons (i.e. stimulation adds photons to the transmitted pulse while absorption removes them), this leads to a change in the transmitted photon distribution, which is discussed in the following section.

6.3.3   Spectral Changes in Transmission

To compare the strength of these two channels at the respective photon energies, we compare the relative difference given by $\frac{\#R_{Abs}(E) - \#R_{Stim}(E)}{\#R_{Abs}(E)}$, which gives a measure for the relative change of the linear transmission at the given photon energies for this setup. An example for the resulting relative differences is shown in Fig. 6.11 for a resonant pulse of 2 eV FWHM and varying incident intensities. The overall difference increases as the incident intensity increases and, therefore, the strength of the stimulation channel grows. The asymmetric change is obvious and can be separated into two different areas. The first is the main peak, which coincides with the bulk of the pre-occupied L-band states and hence with an area of less absorptions. This area can, for higher intensities, contribute to an increased transmission and ultimately for an effective increase in the number of photons transmitted even above the incident photon count. This area would give

rise to the amplification of the incident pulse through stimulated emission, very much like a typical semiconductor optical amplifier. The main surprise here is how far below the resonance this area occurs. In this case the maximum change is around -2 eV.
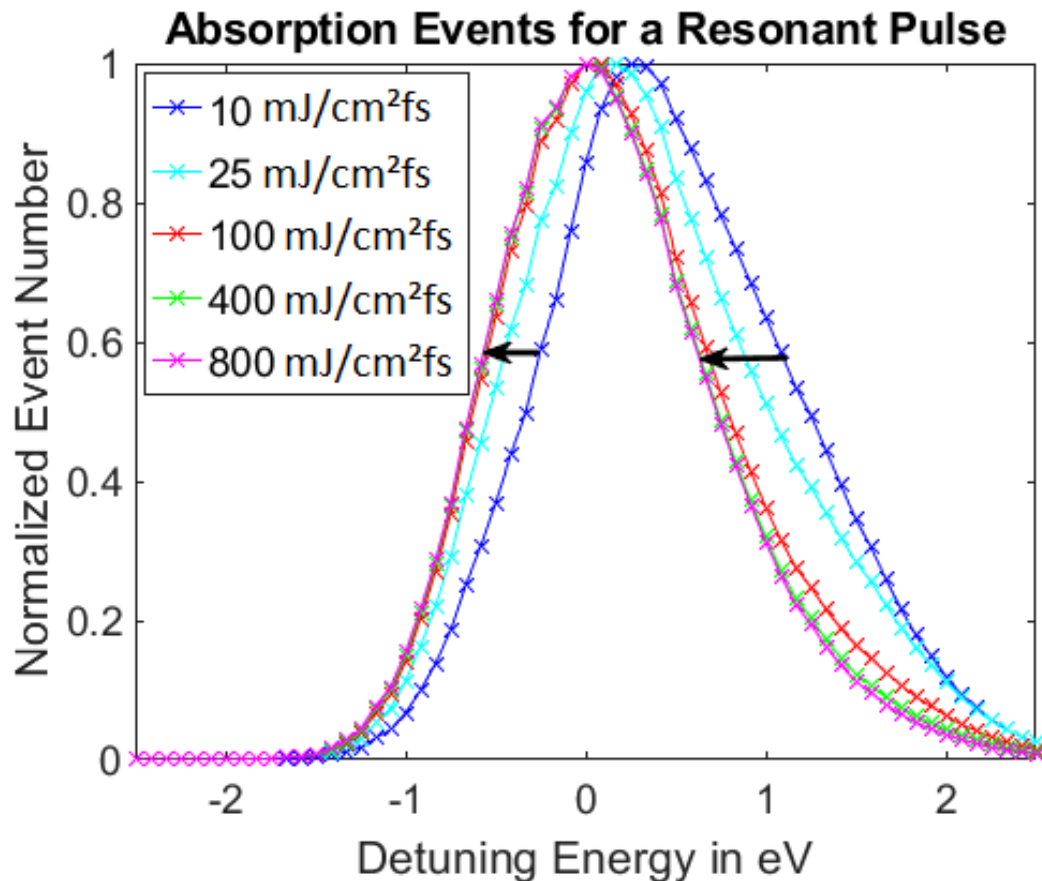
Figure 6.9: This figure shows the relative spectral changes of the absorption for different incident pulse intensities. The change in the spectral absorption distribution shifts towards lower energies with increasing incident intensity until it saturates around the green (400 mJ/(cm²fs)) distribution. The absorption distribution also narrows, as can be seen from red to green/pink at the right flank of the distribution.

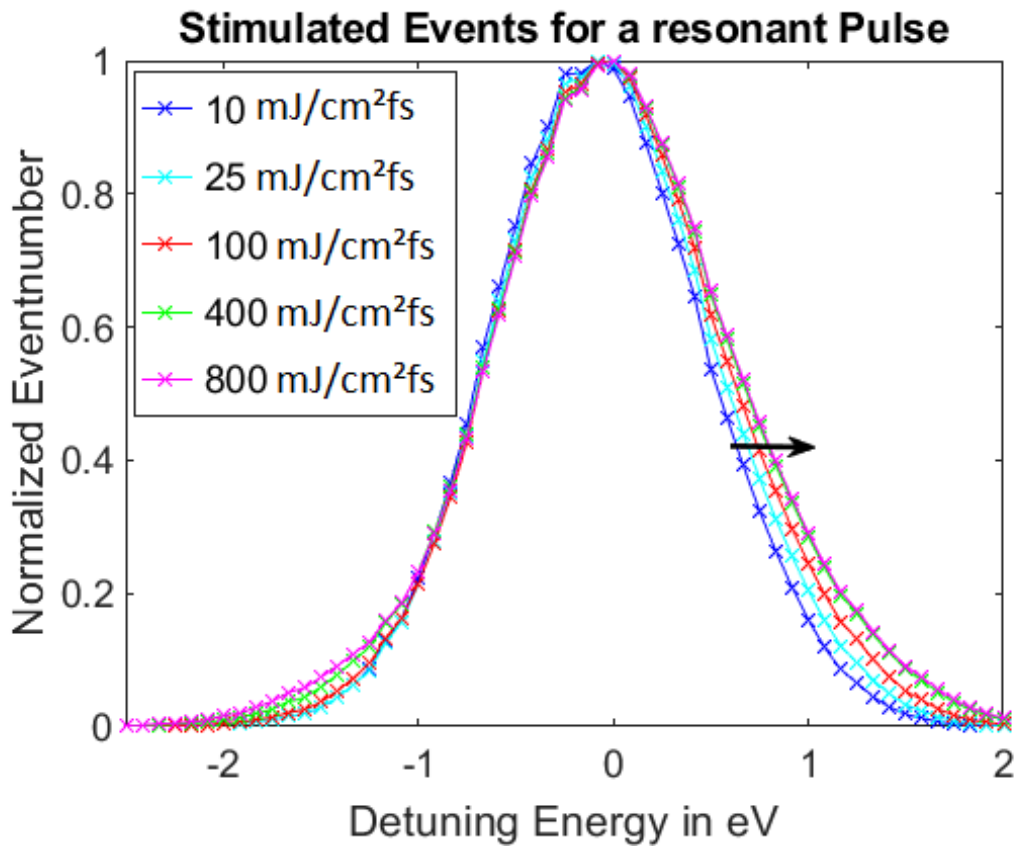Figure 6.10: This figure shows the relative spectral changes of the stimulated channel for different incident pulse intensities. The stimulated distribution does not shift but broadens with increasing incident intensity towards higher incident intensities, thus working as a counterweight to the absorption distribution shift through the increased depopulation of excited states through stimulated emission.
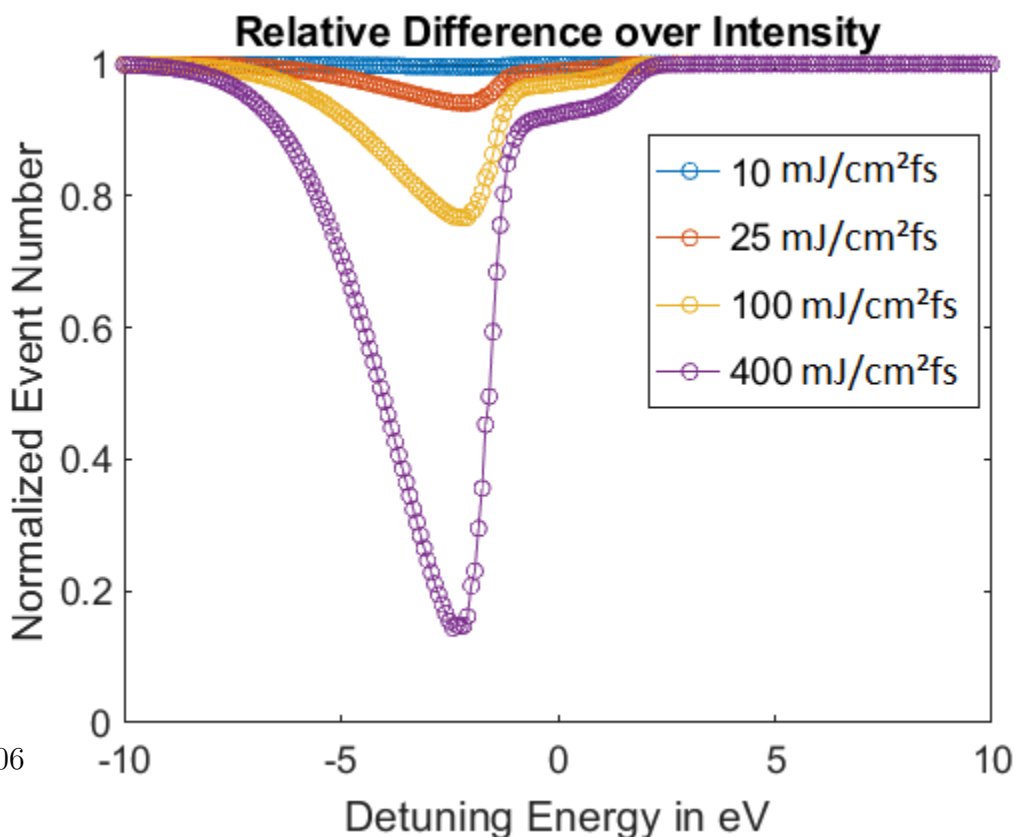
The second interesting relative difference is the plateau-like reduction just around the resonant energy. This is caused by the overlap of the stimulated distribution and the absorption distribution, as shown in Fig. 6.9 and Fig. 6.10, counteracting each other with respect to the transmission. The stimulated emission is far weaker than the absorption, but still increases the transmitted photons in these spectral areas, resulting in an effective increase in transmitted photons. This reduction in absorption can be measured in transmission experiments and has indeed been reported by Chen et al., who measured the transmission of a CoPd thin film L-edge spectra for ultra-fast short X-ray pulses [115]. However, as reported by Highley et al., effects beyond stimulated scattering such as for example electron cascades within the valence band could change the influence of stimulated scattering on these systems [146].

Fig. 6.12 shows the effect of detuning on the described difference for a 200 mJ/(cm²fs) pulse of 2 eV FWHM, with the detuning being an energy shift of the incident pulse with respect to the resonance at 778 eV. As mentioned in Sec. 6.3.1, the resonant (yellow) and slightly positively detuned (+0.5 eV red) pulse examples are almost identical, as they both have a very high overlap with the absorption cross section. This leads to a higher activity in absorption, increasing the number of occupied L-band states, while depopulating the core levels and ultimately leading to more stimulated emission and thus a higher relative difference. The other detuned pulses exhibit a lower amount of absorption events, but the more relevant feature is the fact that the main peak follows the pulse detuning direction. However, as the detuning from the resonance for all examples is larger than the shift, while the highest difference is well below the highest photon peak, the total relative difference has to be understood as a convolution of incident photon distribution, pre-occupation distribution, the stimulated and absorption distribution, and the effective transmission.

One could argue that the Auger decay strength must also have an effect on the spectral difference, as it will also occur in an asymmetric way, since the L-band occupation is higher for the pre-occupied area of the absorption band thus leading to more Auger decays in the model. However, this was found to only have a minor impact on the differences, as the Auger decay works like a countereffect against the stimulated emission through the depletion of excited states, but in turn gets suppressed by the stimulated emission at higher intensities (compare

Fig. 6.3). Also this effect is already included in the stimulated distribution here, as Auger decay and stimulated emission are linked through their respective cross sections. The two spectral features in Fig. 6.11 and Fig. 6.12 are experimentally observable as a decrease in absorption, but under different conditions: As the main difference (around -2 eV detuning energy) strongly depends on the tuning of the incident pulse, this will be easier to observe under monochromatic conditions. Conversely, the plateau-like decrease around 0 to 2 eV is robust to the incident pulse energy distribution and should thus be observable in SASE operation.
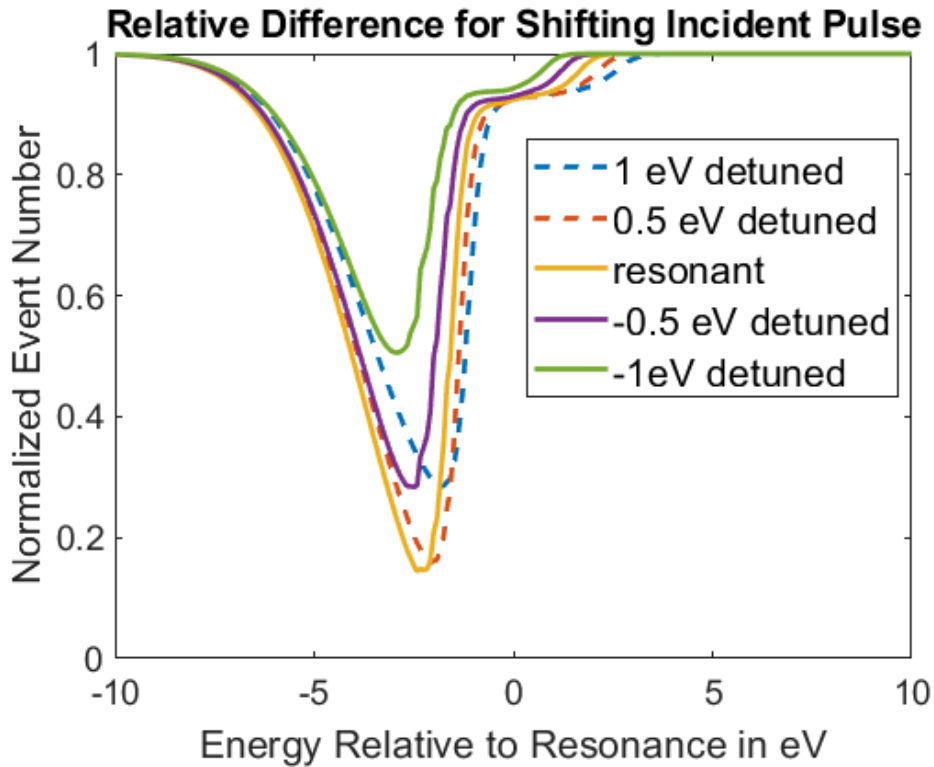
Figure 6.12: The relative differences of the stimulated and absorption channel strengths are shown as $\frac{abs-stim}{abs}$, for different detuning energies. One can see the how detuning of the incident pulse for an Intensity of 200 mJ/(cm^{2}fs) changes this relative difference. The maximum of the difference follows the detuning direction while the overall difference reduces for both detuning directions. Note that there is a plateau like area around the resonance that does not change in strength for different detuned pulses. This effectively reduces the observed absorption while increasing the transmitted photons at these energies compared to lower incident intensity pulses.

6.3.4   Transmitted Photon Distribution and Stimulated Signature

The previously discussed changes in the internal cross channel rates of course result in differences in the transmitted photon distribution, which are shown in Fig. 6.13 and Fig. 6.14, respectively. Fig. 6.13 shows a photon difference map between the transmitted pulse and the incident pulse ($N_{photon}(transmitted)(E) - N_{photon}(incident)(E)$) compare Eq. 6.12), which has been normalized to values between 1 and -1 for better visualization. The change in the transmitted spectral distribution can be compared for rising intensities. The blue feature corresponds to the absorption edge and a reduction in transmitted photons, whereas the red feature corresponds to an increase in transmitted photons compared to the incident pulse. Note that the stimulated edge occurs 1.5 to 2 eV below the resonant absorption edge (778 eV). Fig. 6.14 shows cuts of the un-normalized photon differences, bringing the rise through stimulation in relation to the dip through absorption. The image displays changing intensity from lower intensity (blue) to higher intensity (red). With rising intensity, more photons get absorbed, leading to a deeper absorption edge but also a rise in the stimulated feature, as shown in the inset. This results in a steeper low energy flank and ultimately a reduction in absorption edge width. However, the overall absorption overshadows the amount of stimulated photons.
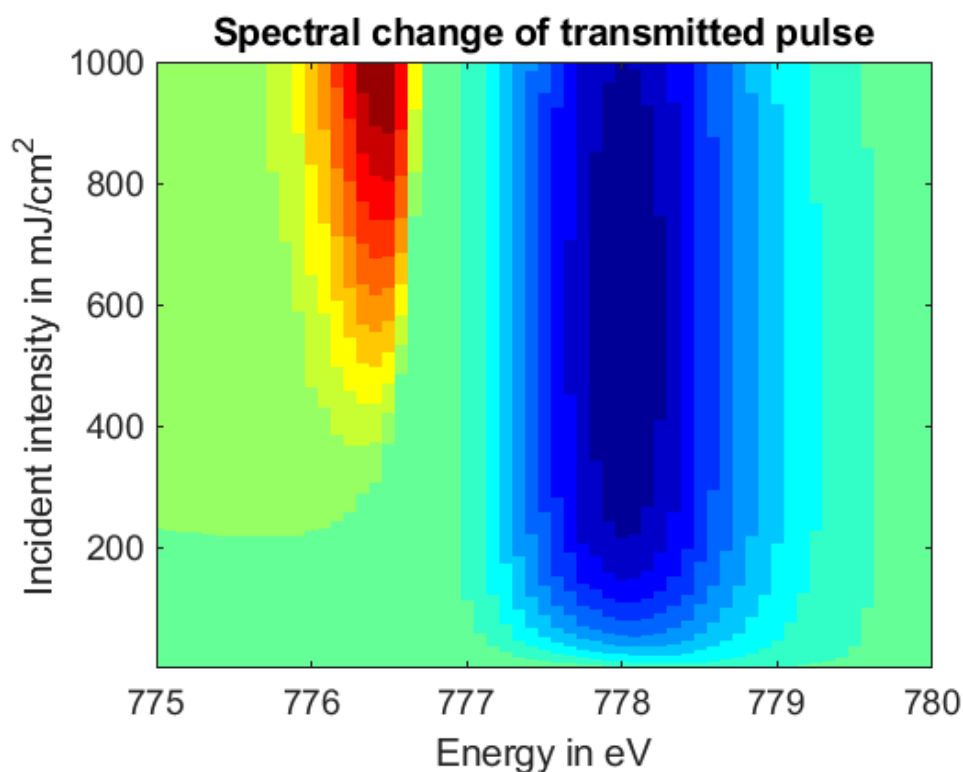
Figure 6.13: The image shows a difference map of the transmitted number of photons compared to the incident number of photons at the given energy. The map has been calculated for a resonant 2 eV FWHM pulse and is normalized to changes between 1 (red) and -1 (blue) to visualize the stimulated features appearance. The red feature corresponds to a higher photon number after transmission, whereas the blue feature corresponds to the typical expected absorption edge. The stimulated feature appears 1.5 eV below the absorption edge.

As discussed above, the position of the stimulated edge is dominated by the initial band structure and mostly affected by the position of the incident pulse through the overlap with pre-occupied states and the overlap with the incident intensity. Therefore, a SASE pulse with for ex-ample two spikes, one on the absorption edge and one 2 eV below the edge, should induce a strong stimulation for the lower energy spike. This of course becomes feasible to achieve with the new emerging two color FEL conditions [27] at various FEL sources around the world, which will strongly increase the control over the experimental conditions in FEL experiments compared to SASE operation.
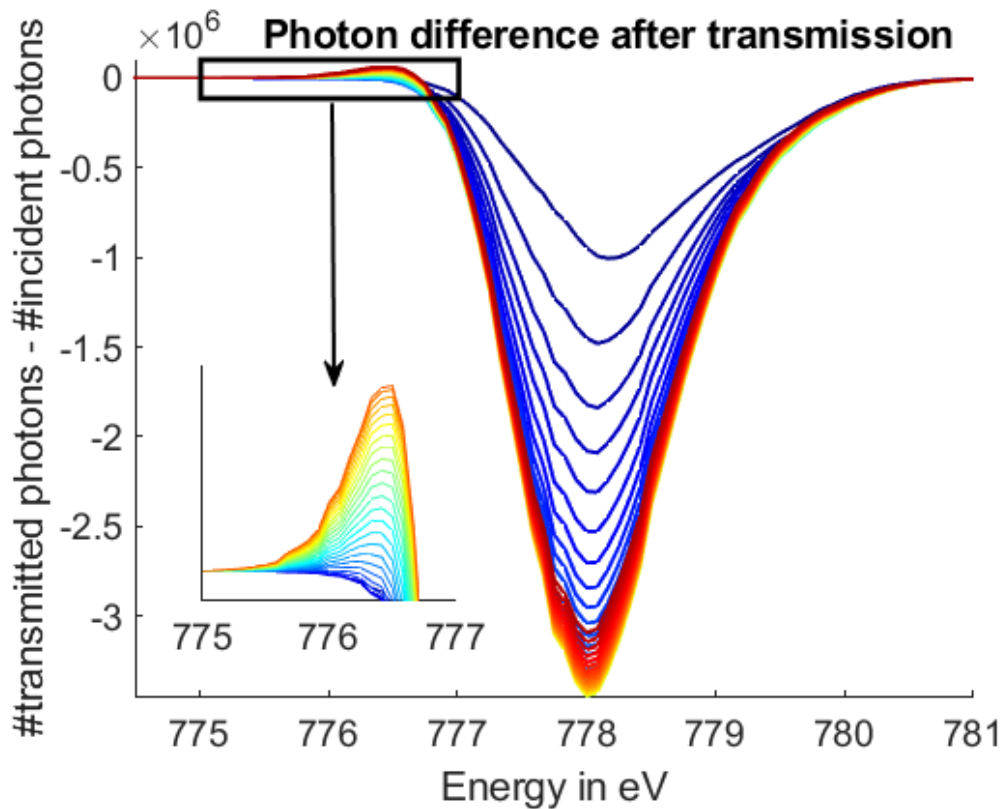
Figure 6.14: The un-normalized data-set for the photon difference after transmission displayed from low (blue) to high (red) intensity, brings the increase in transmitted photons in relation to the decrease through absorption. As the absorption edge becomes deeper, the stimulated edge rises, resulting in a reduction in the (low energy) width of the absorption edge and a steeper low energy flank.

6.3.5 Stimulation Impact on Scattering: Scattering Breakdown

A last aspect to be discussed is the effect increased stimulated emission has on X-ray scattering. As stimulated emission emits in the pulse (forward) direction and reduces the amount of spontaneous decays with increasing intensity, it also reduces the scattering signal, which is primarily caused by these spontaneous decays. This effect quenches the pulse in the forward direction, increasing the transmission (compare Sec. 6.3.1) and reducing the 360° scattering. In Fig. **??**, the blue curve shows the fraction stimulated emission takes from the total amount of decay events for a varying incident intensity of a 2 eV FWHM resonant pulse. As discussed before, the fraction of stimulated emission increases rapidly with increasing incident intensity, while suppressing the Auger and the spontaneous decay channel. The increase of stimulated events correlates with

the measured decrease in diffraction contrast by Chen et al. [115] (which is for comparison shown in orange).
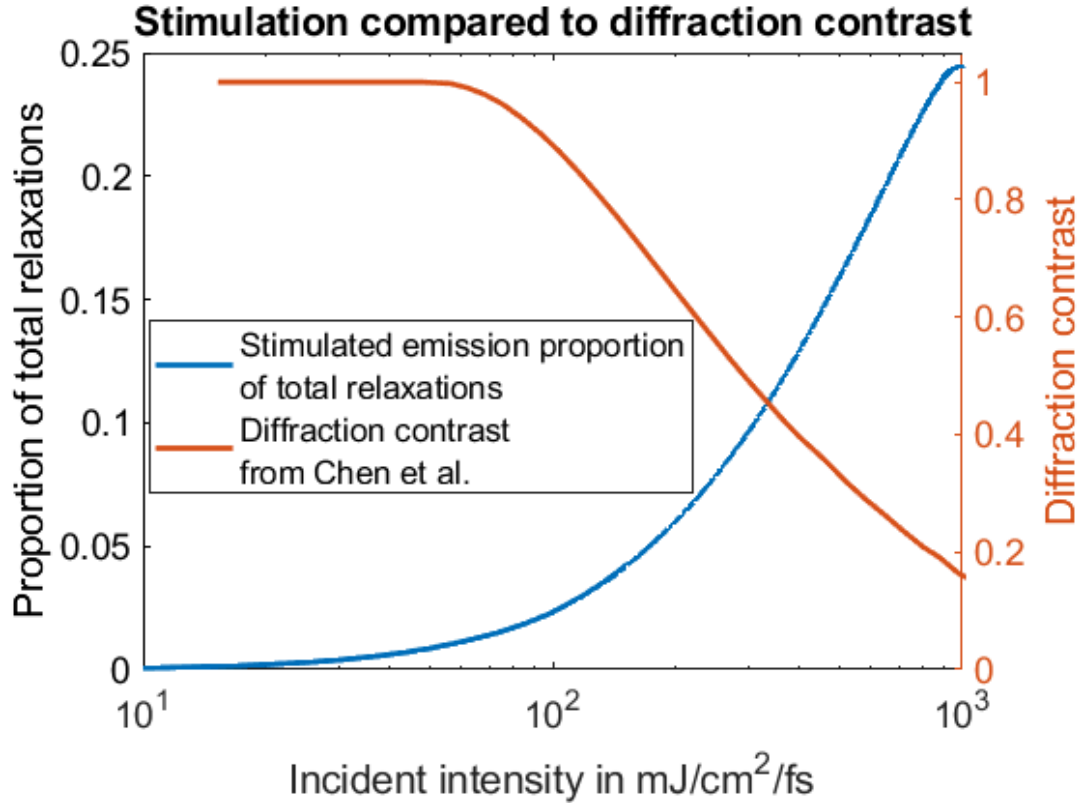
Figure 6.15: This figure shows a comparison of the diffraction contrast measured by Chen et al.[115] (orange) to the proportion of stimulated decays as a fraction of the total occurring decays for a resonant 2 eV FWHM pulse and varying incident intensity (blue). The decrease in diffraction contrast correlates extraordinarily well to the calculation of increasing stimulated emission events, which corresponds to an increase in forward transmission of light at the cost of scattered (spontaneous) emitted light

6.4   Model Limitations and Possible Extensions

To facilitate the occupation dynamics and pulse transmission calculations as outlined in the previous sections, it is necessary to keep the computational complexity relatively low in order to obtain simulation results in a reasonable amount of time. For example, a single pulse transmission calculation in the described way for a 10 fs long pulse and a 40 fs physical simulation time takes about 15 seconds of run time in the here presented system. This way it is feasible to investigate numerous parameter sets and to gather information about trends in

a realistic time frame. The complexity and capabilities of the model are thus always a trade-off.

First and foremost, the described model could be expanded in the depth dimension by implementing depth information about varying occupation dynamics, comparable to the approach by Hatada et al. [139]. This would add information in the form of a depth profile of occupation dynamics and could show different 'front' or 'end' behavior of the samples-pulse interaction, and thus could improve our understanding of how the light-matter interaction is changing while a pulse is being transmitted through the sample. Additionally, this could make the DOS microscopically accurate, enabling the implementation of local impurities or defects to understand their contribution to saturation behavior. In the current model setup, however, a depth dimension with a given number of x depth points along the pulse direction would increase the numerical simulation time of each single pulse x-fold. Hence, this new parameter dimension could improve the quality of information gained from the model at the cost of a massive increase in computational time. Since Hatada et al. [139] have already developed a model that looks at the depth information, the approach of this work concentrates on the so far little studied topic of spectral information instead.

The same trade-off applies to the potential of internal valence band energy conversions and low energy valence band excitations or decays by means of phonons, for example. These may play an important role in some systems on femtosecond timescales, such as the ultrafast electron cascades in diamond Ziaja et al. reported [147]. However, for the investigation of stimulated RIXS in CoPd multilayers as described in chapter 5, the effects of internal conversions were not expected to play a dominant role due to two reasons. First, the short pulse lengths applied in the experiment do not give these other decay mechanisms enough time to be observed, as these occur on a much longer timescale (around 20 fs [147]) compared with the direct pulse induced effects of the order of the pulse length (i.e. 2 fs). Second, the comparison of the two different experimental pulse length sets (2 fs versus 20 fs) does not show a major difference regarding their timing and decay behavior (compare chapter 5.3.3 and appendix 8-2). If other decay mechanisms played a dominant role, the pulse length comparison should differ quite significantly, as it would increase the available time for these

slower decay types to be observed. Still, the occurrence of internal valence band energy conversions plays possibly a more important role in other systems and could technically be implemented into the model in a next step. To date though, the exact way to implement and weigh potential low energy decays and conversions on femtosecond timescales within the valence band is not fully understood yet. In the model presented in this work, these effects as well as higher order interactions are neglected, so that their impact are not observed in the model's current setup.

A last discussion point is the implementation of the cross sections in the model. Since these were derived for equilibrium systems that are dominated by Auger decay (compare [148] and [31]), they may not hold true for every system in the way implemented here. For soft X-ray spectroscopy, Auger decay is the dominant decay mechanism, hence for the discussed case around the Co-L-edge this will not be an issue. For hard X-ray spectroscopies, in contrast, the decay cross sections are dominated by the spontaneous emission, hence these cross sections may not be valid the way they are implemented although a correction factor dependent on the fluorescence yield is already implemented in the cross sections. Additionally, non-radiative decays are ignored in the current setup which, again, works in the soft X-ray case, but potentially needs adaption for hard X-ray experiments due to for example compton scattering. Another last point is the cross sections' internal dependency on the incident intensity, as explained in Sec. 6.2.1. This leads to a coupling of the intensity-driven cross sections and the intensity-defined photon numbers for the stimulated emission as

$$R_{Stim} \propto I_{phontonnumber} \cdot I_{cross-section} \cdot correction(I). \qquad (6.14)$$

With the intensity dependencies arising from the photon number, the cross section, and the cross section consistency factor, respectively. As the correction factor is connected to the absorption cross section, Fig:6.6 shows the intensity dependency of the stimulated emission (in red, comparable to a common L-I curve) and indirectly the correction factor (blue). One can see the superlinear increase for the stimulation strength which is consistent with classical laser physics around the laser threshold. The exact analytical description of the cross sections is not resolved and needs further research as of today. It would also be possible to implement quantum mechanically calculated exchange rates or cross

sections. However, this again leads to the discussion about computational efficiency and additionally about the model's complexity and usability, especially as quantum mechanical calculations are typically complex and need extensive time investment to be realized correctly.

6.5   Accessibility of Surface States through Stimulated Resonant X-Ray Scattering

Now we take a look at surface states, which are an interesting feature due to the relevance of the surface in any interface related reactions for example in catalytic processes [67, 68]. However, they are experimentally very hard to grasp and as the of today available tools are angle resolved photo-electron spectroscopy [149] and tunneling microscopy [150, 149]. Other tools, such as near edge X-ray absorption fluorescence spectroscopy (NEXAFS) or RIXS are powerful and well established in material science to investigate time resolved behavior of reaction dynamics [28] such as catalysis [67], which are likely to be heavily dependent on the nature of states near a catalytic surface where the reaction takes place. It would be a strong enhancement of experimental capabilities to enable NEXAFS or RIXS to detect the nature of surface states and differentiate them from their bulk counterparts.

It is well established that bulk DOS is different from the surface DOS due to the different coordination number of atoms in the surface and bulk, respectively, leading to a smaller valence-electron density in the surface region, which in turn results in a surface core level shift. These shifts in Fermi energy are especially strong for metals with d-valence electron levels close to the Fermi energy. Historically this has been investigated through photo-electron spectroscopy and were discussed extensively by others like the standard textbook on photo-electron spectroscopy by Hüfner [151, 152]. As a shift of the Fermi energy redistributes the DOS for surface states compared to the bulk, this should in principle also be visible through spectroscopy methods such as RIXS, however until today they could not be observed. This section presents a theoretical discussion on spectroscopic fingerprints of surface states with respect to how they can be revealed through stimulated RIXS at FEL light sources.

6.5.1 Numerical Implementation of the Fermi Level or DOS Shift

As demonstrated in the previous section 6.3, the introduced rate model is able to reproduce spectral changes of transmitted resonant X-ray pulses and helps to understand the interplay of Auger decay and stimulated scattering in solid state sample and intense light field interactions. This was shown at the example of a CoPd multilayer, representing a recent stimulated resonant scattering experiment [115, 146]. These capabilities are now being extended by amending the initial absorption band distribution in order to account for shifts of the
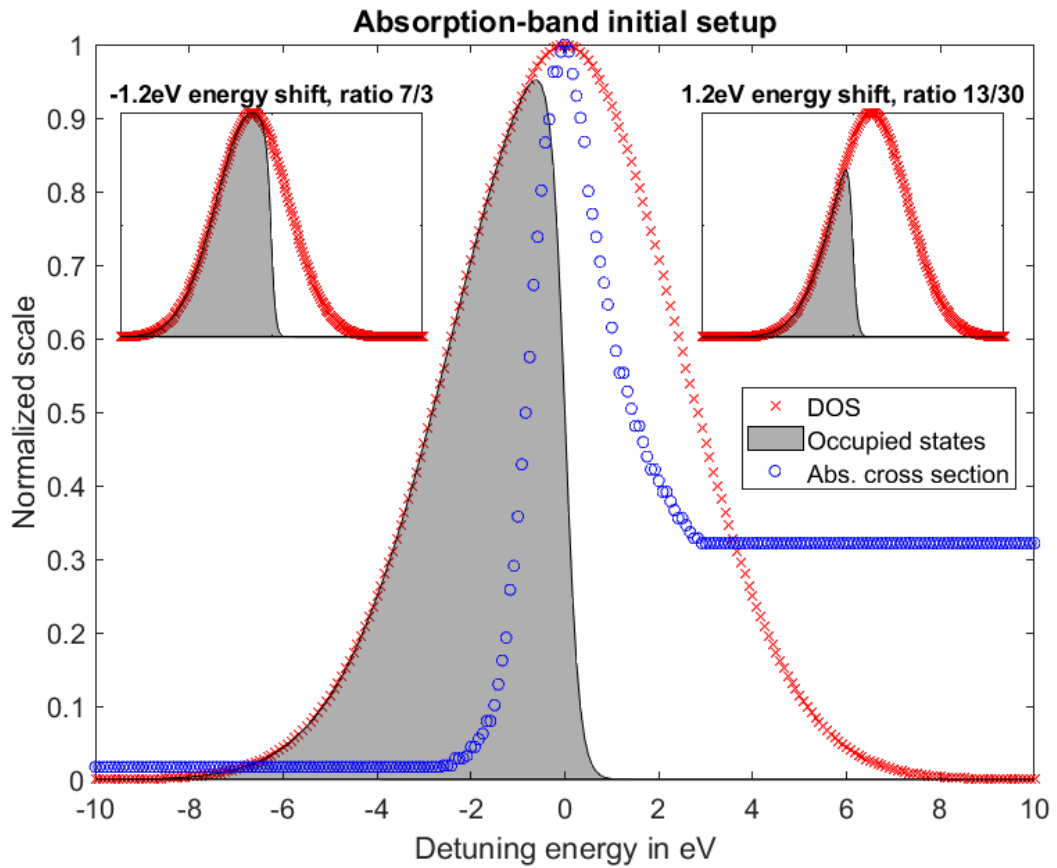
Figure 6.16: The initial setup of the absorption band's DOS. For simplicity, a Gaussian shaped density of state correlated with a Fermi-Dirac-distribution around the resonant energy is used as a distribution of occupied, unoccupied, and available states in the absorption band. The enveloping Gaussian distribution of available states is shifted to change the ratio of occupied to unoccupied states, while the absorption cross section is considered constant around the resonance. For the absorption cross section, we take values for the Co L-3 Edge as a typical d-valence-electron transition metal.

Fermi energy by changing the initial absorption band occupation distribution. As mentioned above, shifts of the Fermi energy occur in the surface states of d-valence electron metals, but the DOS can also change due to the number of element specific valence electrons. Co, for example, has 7 out of 10 d-electrons occupied compared to Ni, which has an additional one. However, in their recent discussion Chen et al. for example figured out an valence band occupation of 75% to be realistic for Co [153]. To account for both options, the shift of the Fermi energy and the changing of the occupied-to-unoccupied states ratio in the absorption band, a generic Gaussian DOS as used in Section 6.2.4 and shown in Fig. 6.16 is defined. As in Section 6.2.4, the Gaussian DOS ($\sigma =$2.4 eV) describes the available states in the absorption band, where the occupied states are given by the product of this Gaussian with a Fermi-distribution at the resonance as shown in the graph. By shifting the enveloping Gaussian to higher or lower energies, the Fermi energy or the ratio of occupied to unoccupied states is effectively changed. While shifting the Gaussian distribution, the Fermi-distribution and thus the resonant energy are, however, kept in place. Additionally, the ratio of occupied over unoccupied states is defined as a new parameter for the simulation in order to visualize the effect different materials will have on the occurrence, strength, and position of a stimulated fingerprint.

This concept is shown in Fig:6.16, where three example distributions are displayed. One for the ratio 1 (central), meaning an equal number of occupied and unoccupied states, and two exemplary shifts of 1.2 eV and -1.2 eV, respectively. The shift of -1.2 eV also represents ratio of occupied to unoccupied states of 7:3, which is the ratio in the valence band of Co (7 out of 10 d-electrons in the valence shell), while the shift of 1.2 eV equals a ratio of 13:30 (close to Mo). For all initial setups, the same absorption cross sections displayed in Fig. 6.16 (blue) are being used. The resonant energy equals the highest absorption cross section and the position in the absorption band, where the initial occupation is 50 %. For the absorption cross section, values for Co are taken from Stöhr et al. [37]. The energy shift of the Gaussian is defined as 0 when the number of occupied and unoccupied states in the valence band are equal at a ratio of 1 (1:1).

6.5.2   Influence on the Absorption Edge

In order to investigate the impact of a Fermi level shift on the spectroscopic fingerprints around the absorption edge, a resonant Gaussian pulse as in 6.2.3

is transmitted through this adapted system. The pulse is chosen to have a duration of 5 fs with 2^{11} photons and an FWHM of 3 eV to cover the entire absorption edge. This corresponds to an intensity of $\approx$ 200 mJ/(cm^2 fs) at the Co L-3 edge, which is at modern FEL sources well achievable in the soft X-ray regime [91, 47]. As the pulse passes through the sample, the pulse gets absorbed where unoccupied states are available, scatters at the sample, and can induce stimulated emission where preoccupied states in the valence band are present. Yet, the availability of core holes after absorption also enables the pre-occupied states to decay through non-radiative Auger decay. Here, the discussion is focused on the difference of photons in the incident pulse and photons after transmission, as can be seen in Fig. 6.17. This photon difference is then normalized to the highest decrease in photons after transmission, i.e. the highest number of absorption events (deep blue), to better visualize the relative photon number change induced by the shifting DOS. The absorption
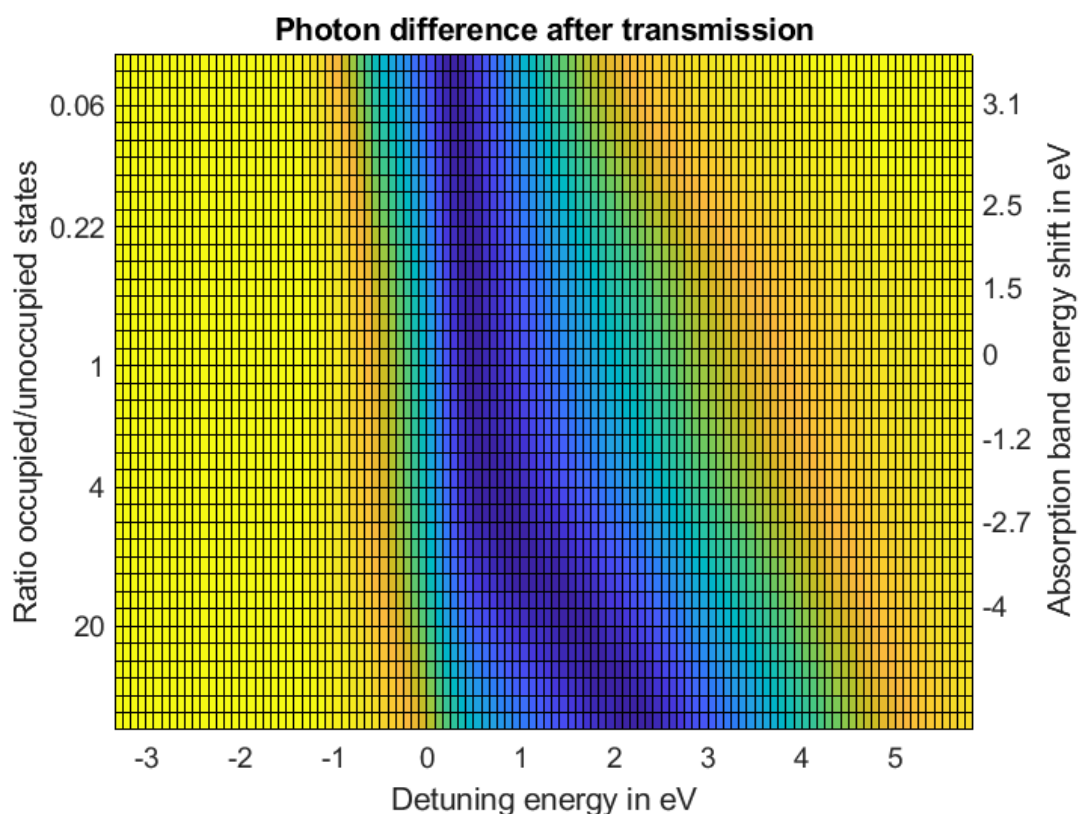

Figure 6.17: Effect of the shifting DOS on the absorption edge in the sample in terms of photon-difference after transmission. The detuning energy of zero corresponds to the peak of absorption cross section and a half filled absorption band, respectively. The transmission was simulated for a resonant Gaussian pulse of 2 eV FWHM and an intensity of 200 mJ/(cm^{2}fs).

edge is visible as the blue dip for different ratios (left axis) and energy shifts (right axis). There are two effects to be noted here. First, the absorption edge minimum shifts towards lower incident energies for decreasing ratios (or positive DOS shifts), and secondly, the absorption edge widens for higher ratios.

While the broadening at high ratios is an effect of the smaller availability of unoccupied states for absorption events due to the mostly occupied valence band. The remaining unoccupied states exist in the right corner of the DOS (compare Fig:6.16 top left), which flattens the distribution of available states and in turn leads to a wider distribution of absorption events on the visible scale. This effect is a mere scaling effect, as there are less overall absorption events for higher ratios due to the lower number of available empty states in the valence band and the number of events is normed to the lowest value (compare Fig. 6.17 dark blue). For the lowest ratio the number of initially occupied states goes towards zero, hence the absorption events represent the incident pulse shape multiplied with the DOS shape. The main absorption dip for the majority of ratios steadily occurs at 0.5 eV, with the exception of the very high ratios above 10. Therefore these ratios are not being simulated in the following.

6.5.3   Influence on Stimulated Scattering

For the lowest occupied-to-unoccupied-states ratio, or highest number of initially unoccupied states, respectively, the sample exhibits almost no induced stimulation events or Auger decays above the amount expected for a synchrotron pulse. This becomes clear in Fig. 6.18, where a stimulated increase of transmitted photons below the absorption edge is displayed. As mentioned above (Sec: 6.5.2), for the two extremes at high or low ratios, the absorption distribution is dominated by the unavailability of unoccupied states states (high ratio), and the unavailability of initially occupied states for other decay channels (low ratio). Henceforth, efforts are concentrated on ratio differences between 0.05 and 10. For these ratios, the stimulated enhancement below the absorption edge in Fig. 6.18, which occurs due to the initially occupied states decaying through stimulated emission, is investigated. In Fig: 6.18, one can see again two effects. First, the stimulated increase is stronger for higher values while disappearing for lower values, and secondly, the stimulated feature decreases for higher ratios while shifting to lower energies after reaching a maximum at an approximate occupied-to-unoccupied-states ratio of 4. While the number of ab-

Stimulated enhancement after transmission
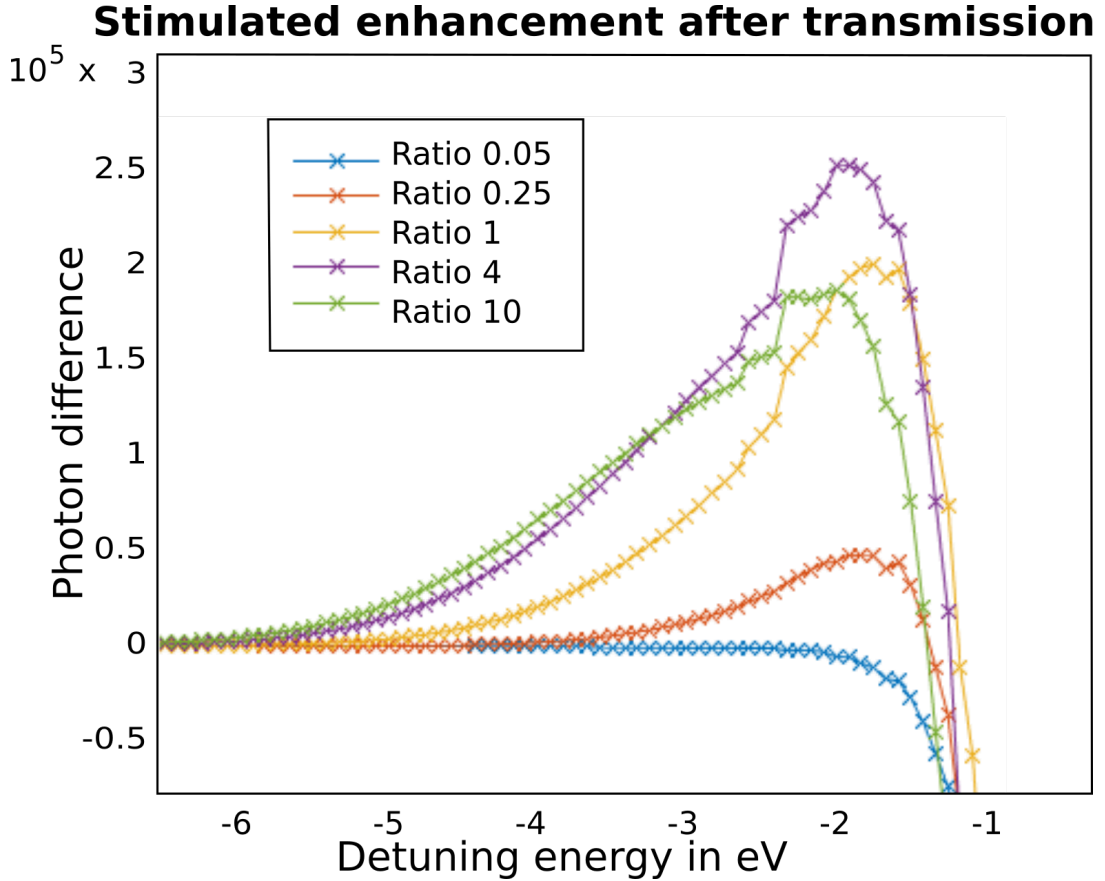
Figure 6.18: Dependence of a stimulated enhancement below the absorption edge from the DOS shift. For very low ratios the stimulated enhancement is small or not existent (blue and red), while for higher ratios the stimulated feature rises to a maximum around ratio 4 (violet), before it decreases while shifting to lower incident energies for even higher ratios (green). The image displays the difference in the number of photon after transmission in absolute photon counts.

sorption events peak at 0.5 eV for all these ratios, the stimulated emission peaks around -2 eV($\pm$0.5).

A photon difference of 10^5 is detectable with modern differencing methods as well as shifts of a some 10 meV, hence these effects could be observed in well designed FEL experiments thus separating spectroscopic bulk information from interface (surface-bulk or layer-layer) information.

6.5.4   Influence on the Stimulated Fingerprint

To improve our understanding of the constraints for potential experiments, it makes sense to look at the effect of the DOS shift on the strength of the three different decay channels, namely spontaneous emission, auger decay, and stimulated emission, especially to further understand the substance of the stimulated
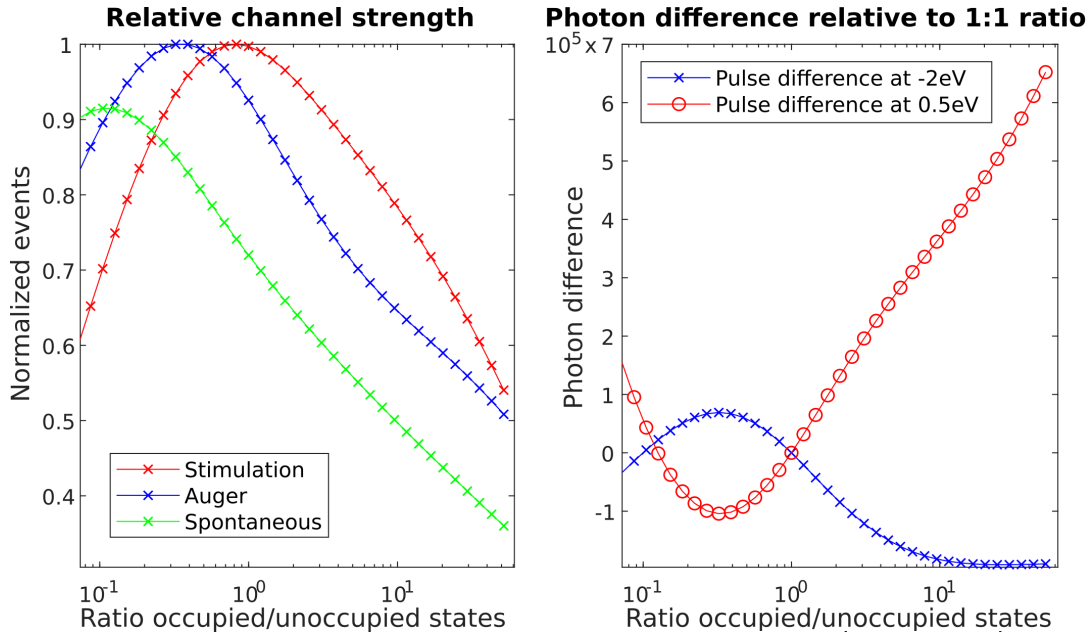
Figure 6.19: Left: The normalized strength of the different decay channels for all incident energies is shown for different ratios. One can see the maximum for all channels to be at different ratios. Right: The difference of photons after transmission compared to the transmission at the ratio 1:1 is displayed for two incident energies, 0.5 eV (red) and -2 eV (blue), respectively. While the photon difference at 0.5 eV corresponds to the shift in the absorption edge, the difference at -2 eV corresponds to the enhancement through stimulated emission below the absorption edge.

feature at -2 eV.

The channel strength (sum over all events) is displayed in Fig. 6.19 to the left. The three decay channels have varying strengths for different ratios. In the soft X-ray regime, Auger decay is usually the strongest channel, yet for this setup and photon number, stimulated emission surpasses the Auger decay for ratios above 0.6, which correlates well with the increasing stimulated feature from Fig. 6.18. With the total number of events decreasing for higher ratios as discussed above, the total channel strength decreases as well. As the stimulated emission is the strongest channel above a ratio of 0.6, the stimulated enhancement is strong as well. When spontaneous emission is stronger than stimulated emission (at around a ratio of 0.25) the stimulated feature disappears. Auger decay just takes radiative decays from the system and reduces the overall transmitted photons by re-opening absorption band states for re-absorption. Auger decay occurs more frequently at energies with a higher occupation in the absorption band, but has only a limited effect on the shape and position of the

stimulated enhancement.

In Fig. 6.19 on the right, the difference of transmitted photons at the energies -2 eV and 0.5 eV is shown in relation to the values at an occupied-to-unoccupied-states ratio of 1 (Ratio(1) - Ratio(x)), hence it shows the difference in transmittance at the given energies compared to the values of the ratio 1:1. These energies correlate to the peak of stimulated enhancement (blue) and absorption (red). As the difference is displayed relative to the ratio 1:1, the image effectively shows the detectable signal difference at two energies if the DOS shifts from the bulk ratio of 1:1 to higher or lower ratios, respectively. As the 1:1 ratio already shows a rather strong stimulated signal, the stimulated ratio can shift in both directions: decreasing towards lower ratios (or a positive energy shift), which increases the photon difference as the decreasing ratio lowers the stimulated signal, or increasing towards higher ratios, which increases the number of transmitted photons and thus decreases the photon difference towards negative values. The combination with the transmitted photon difference at the absorption edge, which changes in the opposite direction compared with the stimulated feature, yields two detectable fingerprints for a DOS shift.

In order to visualize this effect in a real experiment, one would need to design it with a material that firstly exhibits a strong Fermi shift in surface states compared to the bulk, secondly has to potential to be grown as a multilyer (or thin film) and bulk material, and thirdly has a ratio above 0.7 as the change in photon counts here is strong for small ratio changes. In other words, the experiment would have to choose a material with a valence band DOS occupied to unoccupied ratio on the flank where both, the stimulated signal (compare Fig. 6.19 right in red) and the absorption signal (compare Fig. 6.19 right in blue) change with changing ratio. For example the CoPd multilayers used in the experiment (Sec: 5) have a occupied to unoccupied valence state ratio of 2.3 and should thus be ideal to observe this stimulated fingerprint in a well controlled (not SASE) experiment that would compare a bulk Co spectra with a multilayer Co spectra (or a bulk Co sample under a very small angle to increase the surface effect for that matter).

6.6 Chapter Summary

This chapter has presented a rate model approach to simulate the interaction of FEL pulses with solid sample systems in order to understand the impact of effects such as stimulated scattering, induced transparency, and scattering breakdown in the soft X-ray spectrum. The model is easily adaptable to different material systems, especially solid state systems, includes intensity dependent cross sections, and the DOS of the absorption band. Although the presented model is strongly simplified compared to full quantum mechanical treatments, the introduced approach is capable of reproducing the impact intensity-driven stimulated emission in FEL experiments has on scattering, spectroscopy, and transmission, while being computationally efficient and more quickly to perform. Based on this model, simulations of the transmission of Gaussian shaped pulses through a CoPd multilayer thin film, which has a high DOS around the L-edge and has been demonstrated to show non-linear behavior, were presented. It was demonstrated how the interplay of the DOS and the pulse's energy and intensity drive the pulse-sample interaction in this system, and have demonstrated how induced transparency develops with intensity dependent absorption and stimulation rates, inducing an increase in transmission in the sample system. Furthermore, it was shown that the spectral distribution of absorption and stimulation events occur at different energies, thus inducing an asymmetric photon distribution change during transmission. This asymmetric behavior has been investigated in detail with respect to the incident pulse's intensity and energy, resulting in two key findings: first, a decrease in absorption on the main absorption resonance, which is in accordance with recent experimental findings, and secondly, the appearance of an increase in transmission 1-2 eV below the absorption edge dominated by stimulated emission. This stimulated feature can lead to an amplification of the incident pulse in a narrow spectral range, but is highly dependent on the incident pulse's energy, thus only being observable under very controlled experimental conditions. We also discussed the increase of stimulated events at higher incident pulse intensities were compared with the experimentally observed decrease in diffraction contrast and conclude that the increase in stimulated emission events leads to a decrease in scattering events. It still is an experimental challenge to detect changes of 10^7 photons in a pulse of 10^{12} photons, requiring a resolution power of 100000 necessary to detect the stimulated increase, however with differencing methods and modern spectrome-

ters this is already feasible[154, 155].

Lastly we discussed the dependence of the stimulated fingerprint under a Fermi shift in the valence band, as it occurs for example in surface states. We imagined detecting the increase and decrease of the stimulated fingerprint with a controlled pulse enabling to track a shifting DOS. This dependency can be observable in well designed experiment which may open a new path to separate information on the bulk DOS from the surface or interface DOS of a material. Section 6.1 to Sec:6.3 are under review at the journal for electron spectroscopy and represent Paper B (compare Sec:1).

Chapter 7

Summary and Conclusion

In this thesis the influence of stimulated scattering on soft X-ray RIXS experiments at FEL sources was investigated. After discussing the potential of the RIXS process and the experimental capabilities surrounding it in chapter 3, we ventured into the space of free electron laser science and the implications of intense photon fields on spectroscopic techniques in chapter 4. In the latter, recent experimental findings in the field of non-linear X-ray matter interactions where discussed and put into perspective relative to the impact the photon fields have or may have had on the respective experiments. In particular, we discussed the impact of the photon field on the decay cross sections (Auger-decay, spontaneous decay, and stimulated emission), which changes the relative strengths of the three channels pushing the spontaneous emission and Auger decay down while increasing the simulated emission with rising photon field strength. This in turn leads to experimental effects observable in among others self induced transparency, saturable absorption, a breakdown in scattering signal or a self focusing effect, which are being discussed in section 4.2.

To further our understanding of these effects and enable a rigorous investigation of their impact on RIXS spectroscopy, scattering, as well as to potentially open new experimental capabilities, we designed an experiment on magnetic CoPd thin films, which was discussed in chapter 5. This experiment was developed specifically to enable normalized single shot comparisons of Co L-edge spectroscopy (direct beam RIXS) and scattering (1st and 3rd order magnetic stripe pattern), which in turn enables very good signal to noise ratios that can reveal new features originally invisible to typical RIXS approaches. With this setup, it was possible to investigate the breakdown in scattering signal relative to the incident intensity (compare section 5.3.2), observe and investigate the

spectral aspects of stimulated RIXS (compare section 5.3.3). It was possible to link the decrease in scattering signal and an increase in transparency to the increase in incident pulse intensity, which through the spectroscopic data could be linked to an increase in stimulated scattering in the beam direction. Additionally, we where able to observe spectroscopic stimulated features (increase in transmission) that appear on the lower energy end of the absorption edge.

These changes are now simulated especially the stimulated scattering aspect of this experiment. To enable this, a rate equation model based on semiconductor optical amplifiers (coherent pulse passing through an excited or excitable known medium) was developed and evolved to fit into our X-ray spectroscopy setup. Additionally the model was developed to enable relative quick simulations (compared to quantum mechanical calculations) based on a known incident pulse, the absorption cross section of the medium, and the initial density of states, which are usually well known or measurable parameters for most material systems.

Using our rate equation approach, we were able to calculate the valence band DOS dynamics induced by the incident pulse during the pulse transmission, and simulate the effect of stimulated scattering on the samples dynamics. Here the interplay of spontaneous emission, Auger decay and stimulated scattering revealed spectroscopic features for stimulated scattering different from the other decay mechanisms spectral fingerprints, which could open new potential experimental channels. We investigated the impact of stimulated scattering on the transmission, the scattering signal, the spectroscopy of direct beam RIXS, and the resulting changes in transmitted spectral information. At the lower end of the transmitted spectrum we were able to identify a specific feature caused by stimulated scattering, which could also be observed in the original experiment. This stimulated fingerprint was further investigated in the final part of this thesis, where the effect of a DOS shift on this was analyzed as well as the optimal DOS setting to maximize the photon difference caused by the stimulated fingerprint to eventually find a good material system for a future verification of the results on an independent system. The simulation technique seems to be quite capable to reproduce results for FEL experiments on solid sample systems at least on the tested L-edge. Additionally it is much easier and quicker to perform the simulations and gather relevant statistics for multiple experimental settings compared to for example simulations based on a maxwell-bloch approach. Also the rate equation model is pretty flexible to adapt to new situations, such as

inner valence electron cascades or other conversions within the valence band. Finally the model is capable to include more states, as shown with the multi-state valence setup including intermediate decay states as discussed above. This enables a detailed description of larger interaction ensembles like in solid state samples and their interaction with the light pulse on a makroskopic level. We believe this approach can help design and improve experiments for extremely low signal to noise setups, such as for example in heterogeneous catalysis or time resolved RIXS experiments. Additionally the stimulated fingerprint has the potential to act as a new marker for FEL direct beam experiments to control if the sample is still in the correct state or has changed, or to probe small signal changes due to DOS shifts which can occur in surface states as discussed above. Overall this thesis is another small piece in the puzzle to enable and establish a new stimulated RIXS technique that can overcome the dissadvantages of RIXS while opening one of the most powerful probing techniques to new experimental levels.

So long and thanks for all the fish!

Chapter 8

Appendix

Here I include one manuscript that, as of today the 19th of Maz 2022, is has been accepted for publication in the journal of physics communication. The manuscript 'Stimulated resonant X-ray scattering in a solid' includes further results from the stimulated scattering experiment on CoPd multilayers presented in chapter 5. The manuscript focuses on the spectral differences created with different initial pulse configurations and compares the rate equation based model (6) with a three level Maxwell Bloch approach.

Stimulated Resonant Inelastic X-Ray Scattering in a Solid

Daniel J. Higley,[1, 2, *] Zhao Chen,[1, 3] Markus Hantschmann,[4] Martin Beye,[5] Alex H. Reid,[1] Virat Mehta,[6]
Olav Hellwig,[6, 7, 8] Georgi L. Dakovski,[1] Ankush Mitra,[1, 9] Robin Engel,[5] Tim Maxwell,[1] Yuantao Ding,[1]
Stefano Bonetti,[1, 10] Maximilian Bucher,[1] Sebastian Carron,[1] Tyler Chase,[1, 2] Emmanuelle Jal,[1] Roopali
Kukreja,[1, 11] Tianmin Liu,[1, 3] Alexander Föhlisch,[4] Hermann A. Dürr,[1] William F. Schlotter,[1] and Joachim Stöhr[1, †]

[1]*SLAC National Accelerator Laboratory, 2575 Sand Hill Road, Menlo Park, California 94025, USA*
[2]*Department of Applied Physics, Stanford University, Stanford, California 94305, USA*
[3]*Department of Physics, Stanford University, Stanford, California 94305, USA*
[4]*Department of Materials and Energy Science, Helmholtz-Zentrum Berlin, D-14109 Berlin, Germany*
[5]*Department of Photon Science, DESY, Notkestraße 85, D-22607 Hamburg, Germany*
[6]*San Jose Research Center, HGST a Western Digital Company,*
3403 Yerba Buena Rd., San Jose, California 95135, USA
[7]*Institute of Physics, Chemnitz University of Technology, 09107 Chemnitz, Germany*
[8]*Institute of Ion Beam Physics and Materials Research,*
Helmholtz-Zentrum Dresden-Rossendorf, 01328 Dresden, Germany
[9]*Department of Physics, University of Warwick, Coventry CV4 7AL, United Kingdom*
[10]*Department of Physics, Stockholm University, S-10691 Stockholm, Sweden*
[11]*Department of Materials Science and Engineering,*
University of California Davis, Davis, California 95616, USA

When materials are exposed to X-ray pulses with sufficiently high intensity various nonlinear effects can occur. Among the most fundamental of these is stimulated inelastic X-ray scattering, where inelastic scattering of one X-ray photon is stimulated by another X-ray photon with a different energy. Here, we report observations of stimulated Resonant Inelastic X-ray Scattering (RIXS) near the Co L_3 edge in solid Co/Pd multilayer samples. The stimulated RIXS is observed through the X-ray fluence and photon energy dependence of the transmission of high intensity X-ray pulses through the samples. With 1330 mJ/cm^2, 5 fs duration X-ray pulses the number of stimulated RIXS photons we detect per X-ray photon incident on our samples is nearly a million times more than that which could be detected for spontaneous RIXS using standard grating-based X-ray spectrometers. These results pave the way for the development of nonlinear X-ray techniques that use stimulated RIXS in condensed matter.

INTRODUCTION

In spontaneous Resonant Inelastic X-ray Scattering (RIXS), an X-ray photon is resonantly absorbed in matter through a core-to-valence transition and a second X-ray photon is spontaneously emitted through a valence-to-core transition. In recent decades, spontaneous RIXS measurement has risen to prominence as a powerful technique for studying the elementary excitations of matter [1]. Despite this, typical spontaneous RIXS instrumentation only detects around one RIXS photon for every 10^8 X-ray photons absorbed by a sample [2], limiting the accuracy and parameter range of measurements. Stimulated RIXS is governed by the same material processes as spontaneous RIXS, but the photon emission part is stimulated by another real X-ray photon rather than occurring spontaneously. In stimulated RIXS, the emitted X-ray photon has the same energy and momentum as the stimulating X-ray photon rather than having a random direction as for spontaneous RIXS. Thus, stimulated RIXS could be used to overcome the low photon throughput of spontaneous RIXS. Moreover, stimulated RIXS is viewed as a building block of experimentally difficult, but powerful nonlinear X-ray techniques [3].

With the advent of X-ray Free Electron Lasers

(XFELs) [4–6], it has become possible to generate X-ray pulses with sufficient intensity for stimulated RIXS to reach measurable strengths. Pioneering studies have used these unique high intensity X-ray sources to study stimulated X-ray core-to-core emission [7–10], stimulated elastic scattering [11] and stimulated resonant extreme ultraviolet scattering [12]. Stimulated RIXS studies have so far been limited to the gas phase and either relied on amplification of an initially very weak photon source [13] or detected the molecular products of stimulated RIXS instead of the resultant X-rays [14, 15]. Much of the most interesting and technologically important physics and chemistry, however, occurs in condensed phases where stimulated RIXS has not yet been demonstrated. This is primarily due to the increased challenges in condensed matter of competing X-ray-induced nonlinearities caused by the decay of high energy electrons created following X-ray absorption [12, 14, 16–18].

Here, we present measurements of the intensity dependence of stimulated RIXS driven entirely by XFEL-generated X-ray pulses in solid Co/Pd magnetic multilayers. We accurately normalize our data by using an X-ray beam splitter to split off part of each X-ray pulse for a measurement of the spectra of X-rays incident on samples. Further, we reduce the impact on our measurements
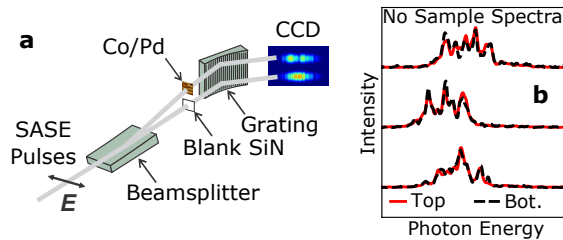
FIG. 1. Experimental setup for broad bandwidth nonlinear absorption spectroscopy with Self-Amplified Spontaneous Emission (SASE) pulses. (a) Simplified schematic of the experimental setup (see [11] for a more complete schematic). The X-ray beam is split into two components with an X-ray beam splitter. One of the X-ray beams passes through a membrane without sample while the other passes through a membrane with a Co/Pd magnetic multilayer sample. The beams emerging from the membranes in the forward direction are measured with a grating-based spectrometer. (b) Example single-shot spectra recorded without a sample present. The spectra recorded from each beam align very well, demonstrating our ability to accurately determine the photon energy content of X-rays incident on samples from the spectra recorded on the branch without a sample in the X-ray path.

of electronic dynamics within the X-ray pulse duration by using short, 5 fs Full-Width-at-Half-Maximum (FWHM) duration X-ray pulses, although stimulated RIXS is still seen with longer 25 fs duration X-ray pulses, albeit with reduced strength. In a previous paper, we described magnetic scattering and transmission measurements made with the same experimental setup that could be modeled through stimulated resonant elastic scattering with an assumed intensity-dependent enhancement factor [19], but potential sample changes within the X-ray pulse duration were not ruled out [11]. In this report, in contrast, we perform a more detailed spectroscopic analysis which reveals stimulated RIXS.

RESULTS

Experimental Setup

Fig. 1a shows a schematic of the experimental setup. Linearly polarized X-ray pulses were generated through self-amplified spontaneous emission at the Linac Coherent Light Source (LCLS) XFEL [5, 6]. The central X-ray photon energy was set near 778 eV, the peak absorption intensity of the Co L_3 resonance. The average X-ray pulse duration was 5 fs FWHM for a short pulse duration mode and 25 fs FWHM for a long pulse duration mode (see methods). The X-ray fluence at the sample ranged from 0.1 through 9500 mJ/cm^2 (see methods). When the X-ray fluence exceeded the single-shot sample damage threshold, the sample was replaced every few X-

ray shots. only the first shot on each sample was used in examining the effects of interaction with Co/Pd multilayers on the X-ray pulses. Measurements where the fluence was well below the sample permanent damage threshold were recorded at the full 120 Hz repetition of LCLS with the sample replaced every few minutes.

The generated X-ray pulses were directed to the AMO hutch [20]. There, the X-ray pulses were split into two similar intensity components [21]. These beams came to a focus near a chip containing 100 nm thick silicon nitride membrane windows. Half of the membranes had Co/Pd multilayer samples deposited on top. The samples were sputter deposited and had the metal layer sequence Ta(15)/Pd(3)/[Co(1)Pd(0.7)]x25/Pd(2), where the thicknesses in parentheses are in nm. One part of the split X-ray pulse passed through a membrane with sample deposited on top, while the other passed through a membrane without sample, acting as a reference. The samples scattered some X-rays that were detected with CCDs [11] (not shown in schematic). The X-rays emerging from the membranes in the forward direction passed were detected at separate positions of a spectrometer with ≈1000 resolving power (see methods). As shown in Fig. 1, the photon energy content of the two X-ray beams was very similar, which enabled accurate normalization of our nonlinear X-ray absorption spectra, overcoming difficulties of earlier studies [17].

Nonlinear X-Ray Absorption Spectra

Fig. 2 summarizes our results. Parts a and b are identical and show the low fluence absorption and emission strengths. The absorption was recorded at the SSRL synchrotron light source with the same samples as used for the high fluence measurements, while the emission spectrum was taken from previous reportedly data on Co metal [22]. Parts c and d show spectra recorded at LCLS as a function of pulse duration, central photon energy and average X-ray fluence. For each case, we show two spectra. The dashed spectra labelled 'Incident' are the spectra from the part of the X-ray pulses that travelled through reference membranes without Co/Pd. The solid spectra labelled 'Nonlin.' (nonlinear) show the difference between the measured spectrum of the parts of the X-ray pulses that travelled through Co/Pd membranes and the expected spectrum for this case if the sample exhibited its low fluence linear response (as obtained by multiplying the incident spectrum by the low fluence sample transmission). Supplementary Fig. 1 shows the calculation of these spectra from experimental data and their relationship to traditional X-ray absorption spectra in more detail.

The nonlinear spectra are negligible for low fluences, showing that our setup accurately measures the change in X-ray pulses upon propagation through our samples. For
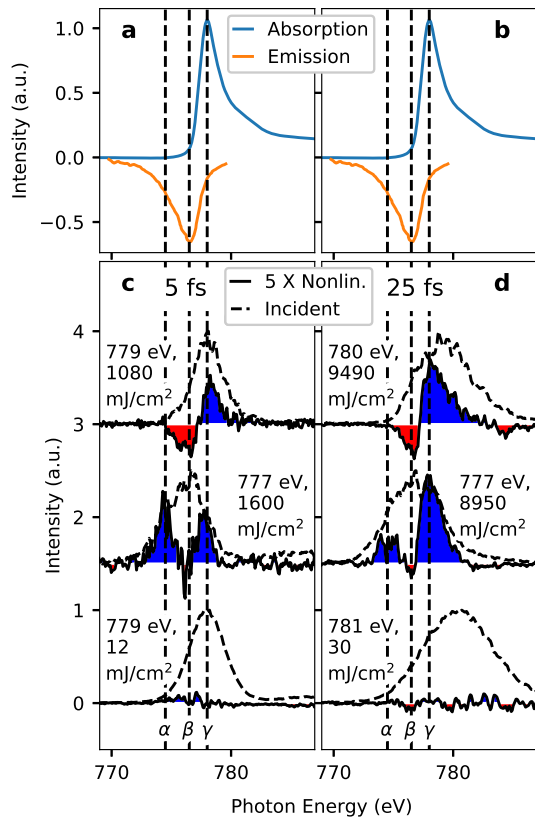
FIG. 2. Change of X-ray spectra (photon energy content) upon propagation through Co/Pd as a function of pulse duration, central photon energy and fluence. (a) and (b) show the absorption and emission of Co near the Co L_3 resonance in the low fluence limit, as recorded at synchrotron light sources. (c) shows results for 5 fs average X-ray pulse duration, while (d) shows results for 25 fs average X-ray pulse duration. The spectra incident on the samples are estimated from the measurement of the X-rays that did not travel through a sample, and the nonlinear spectra (Nonlin.) show the difference between the spectra emerging from samples and that expected with a linear sample response. The nonlinear spectra are positive where there are more photons exiting the sample than expected with a linear sample response (blue filled) and negative where there are less photons exiting the sample than expected with a linear sample response (red filled). The photon energies where different nonlinear features occur are highlighted with dashed vertical lines and labeled at the bottom of the figure.

the high fluence cases, the nonlinear spectra are still negligible well away from the Co L_3 resonance. In the vicinity of the Co L_3 resonance, however, there are strong deviations from zero. We identify three distinct features, as indicated with dashed vertical lines in Fig. 2 and labeled at the bottom of the figure. First, and most significantly

for this report, the number of photons emerging from the sample a few eV below the absorption resonance, at 774.5 eV, increases relative to a linear sample response (feature α). As we show below, this is due to stimulated resonant inelastic X-ray scattering. Second, the number of photons emerging from the samples at the low photon energy side of the Co L_3 resonance (776.5 eV) decreases (feature β). Finally, the number of photons emerging from the sample at the peak and high photon energy side of the Co L_3 resonance (778 eV) increases (feature γ).

The high fluence data for both short and long duration X-ray pulses was binned by the X-ray pulse central photon energies through binning by the XFEL electron beam energy which is strongly correlated with the central photon energy of the resultant X-ray pulse [23]. Feature γ appears in both spectra. For the higher central photon energy data, the stimulated RIXS signal (feature α) is absent, while feature β is enhanced. For the lower central photon energy spectrum, in contrast, the stimulated RIXS signal is pronounced and feature β is greatly reduced. The short and long duration X-ray pulses have similar X-ray intensities and show qualitatively the same features, but feature α is reduced in strength for the long pulse duration data relative to the short pulse duration data while feature γ is increased in strength.

Stimulated Inelastic Scattering Efficiency

Fig. 3 displays the X-ray fluence and pulse duration dependence of the stimulated inelastic scattering efficiency, which we define to be the number of photons emitted through stimulated inelastic scattering divided by the number of photons that would have been resonantly absorbed assuming a linear sample response. To estimate this from the experimental data, we first integrated over feature alpha (773 eV to 775.5 eV) then divided by the number of photons that would be absorbed with a linear sample response, as calculated with the incident spectra. Next, in order to correct for small differences in the two X-ray branches, we subtracted the same quantity calculated under the same conditions, but with neither beam propagating through a sample and the incident spectrum multiplied by the low fluence sample transmission. This method of estimating the efficiency from the experimental data doesn't take X-ray-induced valence electronic redistribution into account and the true stimulated inelastic scattering efficiency could be a few times higher, as discussed further below. The vertical error bars are an estimate of the standard error in the absence of nonlinear effects (see methods) and the horizontal error bars show the estimated 30 percent uncertainty in the absolute fluence calibration. The estimated stimulated inelastic scattering efficiency increases with increasing X-ray fluence, reaching more than five percent for the 1330 mJ/cm^2, 5
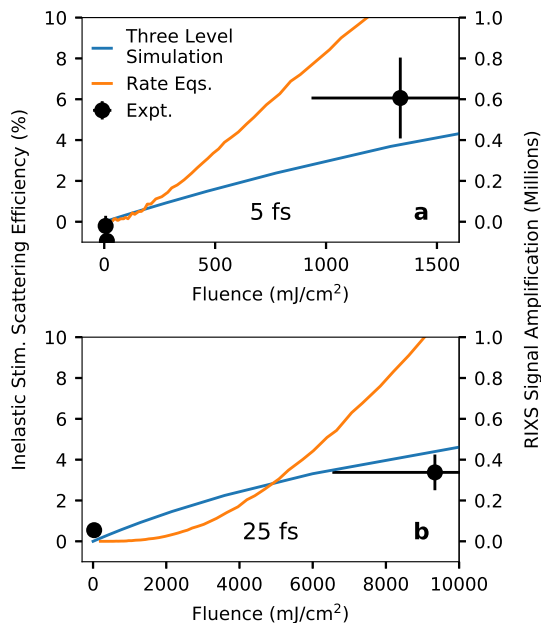
FIG. 3. Fluence and pulse duration dependence of experimentally estimated and simulated stimulated inelastic scattering efficiency (defined to be the number of stimulated inelastic scattering processes divided by the number of photons that would be resonantly absorbed assuming a linear sample response). For each case, we also show the corresponding RIXS signal amplification, which we define to be the ratio of the number of stimulated RIXS photons we detect per X-ray photon incident on our sample divided by that which could be detected with spontaneous RIXS using standard grating-based spectrometers.

fs X-ray pulses. The figure also shows model calculations as described further below.

DISCUSSION

The nonlinearities in X-ray absorption that we observe can be explained as a combination of resonant nonlinear X-ray effects involving the Co L_3 resonance, as shown schematically in Fig. 4. Our sample has no absorption edges near and below the photon energies we use and, as such, nonlinearities of non-resonant absorption are expected to be very weak [24–26]. The most important electrons in the nonlinear resonant processes are the 3d valence electrons which form a continuous density of states near the Fermi level, E_f, and the tightly bound Co $2p_{3/2}$ core electrons (Fig. 4a). As the sample is excited through X-ray absorption and evolves, it interacts with subsequent X-ray photons differently, which gives nonlinearities in the X-ray absorption. Importantly for

all study, of all these resonant nonlinear processes, only stimulated RIXS gives an increase in the number of photons emerging from the sample a few eV below the Co L_3 absorption resonance, as seen in feature α.

When an X-ray photon is absorbed at the Co L_3 resonance (778 eV), it excites one of the Co $2p_{3/2}$ core electrons into an unoccupied valence state of primarily 3d character (Fig. 4b). From here, another X-ray photon can stimulate a valence electron to fill the core hole, giving increased photons emerging from the sample below the absorption resonance (stimulated RIXS, giving feature α) and within the absorption resonance (stimulated elastic scattering, contributing to feature γ). In addition, the resonant absorption strength can also be reduced due to the shift of the Co $2p_{3/2}$ absorption edge. Such absorption edge shifts could also be caused by the ionization of other tightly bound electrons in the evolution of the sample following X-ray excitation [27], but these shifts should also impact the non-resonant absorption strength above the Co L_3 absorption resonance, which is not seen in our data, indicating that these shifts are not a dominant contributor to feature γ in our data.

If the Co $2p_{3/2}$ core hole is not filled through stimulated resonant scattering, then it will decay in 1.5 fs, primarily via Auger decay, a process that fills 99.3 percent of core holes in the low X-ray fluence limit [28, 29]. In Co/Pd the transfer of energy from initial X-ray absorption-induced excitation to electronic excitations within 2 eV of the Fermi level takes place in ≈ 13 fs [16]. Through this process, the occupation of states is decreased below the Fermi level and increased above it (Fig. 4c). This valence electron redistribution opens up new X-ray absorption channels for X-rays with photon energies below the peak of the absorption resonance (giving feature β) while eliminating others with energies near the peak of the absorption resonance (contributing to feature γ). The significant degree of X-ray-induced electronic excitation could also result in more subtle changes of the electronic density of states, but a recent investigation indicated that such effects are not strong for the degree of excitation we investigate here [30].

The photon energy dependence of the strength of stimulated RIXS reveals some interesting aspects. The stimulated RIXS signal is only strong when the X-ray intensity is strong at the photon energies where it occurs. This shows that the stimulated RIXS processes are driven by X-rays with photon energies that are already strongly present in the incident X-ray pulses, differentiating our results from the amplification of spontaneous emission [12] or amplification of initially very weak parts of an X-ray beam [13] previously studied. The peak of the stimulated RIXS signal (774.5 eV) is also not close to that of spontaneous RIXS (776.5 eV), deviating from what one may initially expect.

We propose that the difference in peak locations of the stimulated and spontaneous RIXS intensities is due to
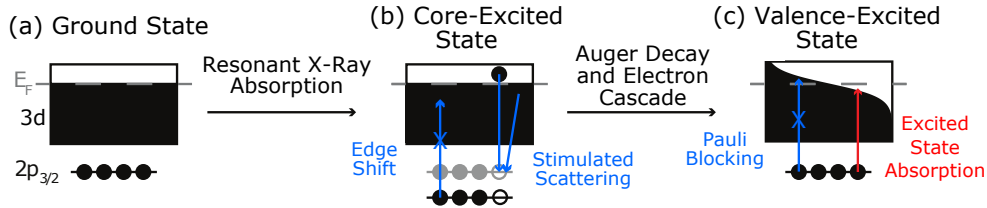
FIG. 4. Schematic of X-ray-induced evolution of the electronic state of a Co atom in a Co/Pd sample and corresponding nonlinear X-ray processes that can occur. Processes that increase the number of photons exiting from a sample with respect to the ground state are shown with blue arrows while those that decrease the number of photons emerging from a sample with respect to the ground state are shown with red arrows. (a) Ground state electronic structure. (b) Core-excited state that follows resonant X-ray absorption at the Co L$_3$ resonance. (c) Valence-excited state that follows relaxation of the core-excited state to few eV valence excitations in $\approx$ 13 fs.

the competition of the stimulated RIXS signal with increased absorption strength into states below the Fermi level from electron redistribution. At energies just below the photon energy for core to Fermi level excitations, the absorption changes from electron redistribution dominate the stimulated RIXS signal. At lower photon energies, however, both holes and electrons decay very rapidly in metallic Co, even in comparison to our several fs X-ray pulse durations. For example, electrons 1 eV above the Fermi level have been measured to decay in less than 5 fs in metallic Co, and the decay time is predicted to decrease rapidly as the energy from the Fermi level is further increased [31]. The photon energies where the experimental stimulated RIXS signal is strong give about one third of the integrated spontaneous RIXS strength, and thus we expect that the true stimulated RIXS strength is roughly three times stronger than the strength of feature α.

To quantiatively compare the strength of feature α to that expected for stimulated RIXS, we simulated the stimulated RIXS efficiency within a three level Maxwell-Bloch model as well as a rate equations model (see methods for details). The results are compared to experiment in Fig. 3. Both simulations are within a factor of a few of the experimental measurements. Taking into account this factor of 3, the experimental results are very close to what is expected within the rate Eqs. model. For the 25 fs duration X-ray pulses, the experimental results are shifted lower relative to the simulations than for the 5 fs duration X-ray pulses, which is likely due to the increased X-ray fluence and time available for X-ray induced valence electronic redistribution.

The number of stimulated RIXS photons that we measure per X-ray photon incident on our samples is far higher than that for conventional measurements of spontaneous RIXS. The efficiency of spontaneous RIXS at the Co L$_3$ edge is 0.8 percent [29], about an eighth of the maximum efficiency of stimulated RIXS reported here. In the case of spontaneous RIXS, however, the photons are emitted in all directions, and only a small fraction of

them are collected in a typical experimental measurement. (A collection efficiency of 10^{-6} is typical [2].) For stimulated RIXS, in contrast, photons are emitted in the same direction as the stimulating beam and thus, with appropriate experiment design, the vast majority of stimulated RIXS photons can be in the acceptance area and angle of a spectrometer. With suitable spectrometer design, around ten percent of stimulated RIXS photons could be measured, limited only by grating and CCD efficiency. Thus, our results demonstrate that through stimulated RIXS we could measure around 1 RIXS photon for every 200 photons absorbed in our sample, nearly a million times more than the single RIXS photon detected for every 10^8 photons absorbed in a sample with conventional spontaneous RIXS measurements [2]. This RIXS signal amplification is shown on the right side of Fig. 3.

We have reported observations of stimulated resonant inelastic X-ray scattering in a solid. The nearly a million-fold amplification of the RIXS signal shows the potential of stimulated RIXS to greatly enhance the throughput of RIXS studies, which could extend the feasible parameter coverage of RIXS investigations. For example, measuring the dependence of RIXS on many material compositions in static studies or on many time delays in pump-probe measurements. Nonetheless, the RIXS signal we observe co-occurs with nonlinear spectral changes of comparable strength due to X-ray-induced electronic dynamics within the X-ray pulse duration. For stimulated RIXS to be a robust technique, future studies must demonstrate that these effects can be mitigated or accounted for to an acceptable degree. One could imagine, for example, characterizing the nonlinearities due to X-ray-induced electronic dynamics from another, non-resonant pump pulse, and using even shorter X-ray pulse durations as are now available [32]. In addition, our study did not probe the angular dependence of stimulated RIXS, which would require further experimental development. Going beyond stimulated RIXS, our study could be a demonstration of the first step in condensed phases of proposed nonlinear

X-ray spectroscopies where excitations are created with stimulated RIXS then probed with subsequent X-ray or other pulses [33, 34].

METHODS

Adjustment and determination of X-ray fluence

The X-ray fluence at the sample was adjusted by changing the attenuation of a gas attenuator [35] before the sample as well changing the spot size at the sample. The pulse energy at the sample was determined from the X-ray pulse energy measured with a gas detector [35]. The X-ray transmission efficiency from the gas detectors to the sample location was estimated to be 10 percent. The X-ray spot size at the sample membrane was measured through pinhole scans, given a size of either 15 by 15 μm, or 20 by 150 μm, depending on the setting of the X-ray focusing mirrors.

Characterization of X-ray pulse duration

The average duration of X-ray pulses produced by LCLS in different modes was estimated using two different methods. The methods are complementary in that the first sets an upper limit on average pulse duration while the second sets a lower method. In the first method, an X-band Transverse Deflecting Cavity (XTCAV) measured the energy and temporal distribution of electrons in electron bunches after those bunches were used in the production of X-rays. The intensity profile of X-ray pulses was then estimated from these measurements [36]. This confirmed the 25 fs FWHM duration of the longer pulses and set an upper limit of 10 fs on the duration of the shorter pulses. In the second method, averaged pulse duration were estimated from the statistical correlation of X-ray spectra [37, 38]. For the same operating modes as used for collecting data on the Co/Pd samples, we recorded spectra using the spectrometer of the SXR beamline [39]. For robustness of this analysis method, we limited the analysis to X-ray pulses where the central electron energy of the electron bunch generating the X-ray pulse was within the middle 10 percent of observed values. This gave a lower limit of 4.7 fs on the duration of the shorter pulses and 8.5 fs on that of the longer pulses.

Retrieval of X-ray spectra

Spectra were obtained from spectrometer CCD images by selecting the relevant region on the imaging detector and projecting along the axis of photon energy dispersion. The photon energy was calibrated by adjusting the coefficients of a linear relationship between spectrometer pixel position and photon energy such that a low fluence absorption spectrum measured at LCLS agreed with that measured on the same sample at beamline 13.3 of the SSRL synchrotron light source.

Vertical Error Bars of Fig. 3

The vertical error bars of Fig. 3 show the estimated standard error of the measured stimulated inelastic scattering efficiency in the absence of nonlinear effects. To perform this calculation for the data with fluences above the sample damage fluence (higher than ≈ 50 mJ/cm^2), the spectra of X-rays that passed through blown up samples were first multiplied by the linear sample transmission. Next, bootstrapped [40] sets of these spectra were formed by sampling these spectra with replacement n times, where n is the number of spectra recorded with an intact sample for each data set. The stimulated inelastic scattering efficiency was calculated for each of these sets and the standard deviation of these gives the vertical error bars. For the data with fluences below the sample damage threshold, nonlinear processes were assumed to not contribute greatly to the error and the standard error of the intact sample data obtained using the bootstrap procedure was used for the error bars.

Three-Level Maxwell-Bloch Simulations

We used a one-dimensional three level Maxwell-Bloch model to estimate the strength of stimulated resonant inelastic X-ray scattering (see [41] for an overview of this and related models). Multilevel Maxwell-Bloch models have been successfully used to describe the propagation of light through a variety of media that can be adequately treated as discrete, few-level systems, including the propagation of strong resonant X-ray pulses through atomic and molecular gases [17, 42].

We follow [41] for our calculations. We write the amplitudes of the X-ray electric field as the real part of a slowly varying envelope, $\mathcal{E}(z,t)$ times a rapidly oscillating phase factor (Eq. 21.3 of [41]),

$$E(z,t) = \mathrm{Re}\left[\mathcal{E}(z,t)e^{i(kz-\omega t)}\right], \qquad (1)$$

where Re[x] denotes the real part of x, k is the X-ray wavenumber, z is propagation distance, ω is the X-ray

angular frequency and t is time. The material polarization (which is determined from the material state, as described below) is written in the same manner

$$P(z,t) = \text{Re}\left[\mathcal{P}(z,t)e^{i(kz-\omega t)}\right], \tag{2}$$

where $\mathcal{P}(z,t)$ is the polarization envelope. Making the slowly varying envelope approximation and the change of variables

$$Z = z, \; T = t - z/v \tag{3}$$

gives an equation for the evolution of the envelope of the X-ray electric field [41]

$$\frac{\partial}{\partial Z}\mathcal{E}(Z,T) = i\frac{\omega}{2c\epsilon_0}\mathcal{P}(Z,T). \tag{4}$$

Assuming the material polarization does not depend strongly on Z, we can integrate this equation to get an approximate expression for the field of the X-ray pulse exiting the sample (where the sample extends from $Z = 0$ to l),

$$\mathcal{E}(l,T) = \mathcal{E}(0,T) + i\frac{\omega l}{2c\epsilon_0}\mathcal{P}(0,T). \tag{5}$$

As our sample is only 1 optical depth thick at the peak of the Co L3 absorption resonance, we do not expect this approximation to distort the results by a large factor.

Now we describe how we calculate the evolution of the Co/Pd material state. For this, we model the Co/Pd as a slab of discrete three-level atoms. The slab has the same thickness as our samples and the same density of three-level atoms as density of Co atoms in the actual samples. The three levels represent a ground state with energy $E_1 = 0$ eV, a core-excited state with energy $E_2 = 778$ eV (coinciding with the peak of the Co L$_3$ resonance) and a valence-excited state with energy $E_3 = 2$ eV (coinciding with a typical 3d excitation energy). The dipolar coupling between the ground state and the core-excited state is d_{12}. The dipolar coupling between the core-excited state and the valence-excited state is d_{23}. We chose the dipolar couplings in accordance with the linear X-ray absorption cross sections of our samples, as described at the end of this section. We let $\rho_{nm}(t)$ denote the element in the nth row and mth column of the density matrix in the basis of eigenstates of the three-level atom in the absence of an applied X-ray field. From Eq. 16.107 of [41], we define a rotating coordinate representation of the density matrix through

$$\rho_{nm}(t) = s_{nm}(t)e^{i\xi_m(t)-\xi_n(t)}. \tag{6}$$

Here, $\xi_i(t)$ are arbitrary phase factors chosen to be conveinent for the problem to be solved. We choose these according to Eq. 13.14 of [41] with a single X-ray pulse acting to both excite and stimulate decay,

$$\hbar\xi_1(t) = 0, \; \hbar\xi_2(t) = \omega t, \; \hbar\xi_3(t) = 0, \tag{7}$$

where ω is the angular frequency of the applied X-ray field and $\hbar$ is Planck's constant divided by 2π. From Eqs. 13.8, 13.27 and 13.29 of [41], we have a matrix which describes the time evolution of the system,

$$W = \frac{1}{2}\begin{bmatrix} 0 & \Omega_P^* & 0 \\ \Omega_P & 2\Delta_P & \Omega_S \\ 0 & \Omega_S^* & 2\Delta_R \end{bmatrix}, \tag{8}$$

with the complex, time-dependent Rabi frequencies defined as

$$\Omega_P = -d_{12}\mathcal{E}/\hbar, \tag{9}$$

and

$$\Omega_S = -d_{23}\mathcal{E}/\hbar. \tag{10}$$

The detunings are

$$\Delta_P = E_2 - E_1 - \hbar\omega = 0, \tag{11}$$

and

$$\Delta_R = E_3 - E_1. \tag{12}$$

The evolution of the density matrix elements is given by Eq. 16.116 of [41],

$$\frac{d}{dt}s_{m'm} = -i\sum_n \left[W_{m'n}(t)s_{nm}(t) - s_{m'n}(t)W_{nm}(t)\right]$$
$$- \sum_{nn'}\Gamma_{m'mn'n}s_{n'n}(t), \tag{13}$$

where Γ is a tensor chosen to phenomenologically model Auger decay. The entries of Γ are

$$\Gamma_{2222} = -\Gamma_{1122} = \Gamma_A, \tag{14}$$

$$\Gamma_{1212} = \Gamma_{2121} = \Gamma_{2323} = \Gamma_{3232} = \frac{\Gamma_A}{2}, \tag{15}$$

and zero otherwise. Once we have calculated $s(t)$ for a particular time, we calculate the envelope of the material polarization for that time from Eq. (21.94) of [41]

$$\mathcal{P}(t) = 2N\left(d_{12}s_{21}(t) + d_{32}s_{23}(t)\right). \tag{16}$$

We chose the dipole matrix element between the ground state and core excited state such that the integrated absorption cross section in the low fluence limit is the same as it is experimentally for Co metal and the width of the resonance is set by Auger decay. [19] derived that the peak absorption cross section for such a resonance is 18 Mb. We then obtained the corresponding dipole matrix element using [43]. Using Eq. (2.9.8) and (2.5.18) of [43], along with the definition of the absorption cross section as the extinction coefficient divided

by the atomic density, we obtain a formula for the absorption cross section at the peak of the resonance,

$$\sigma(\omega_0) = \frac{2\pi c^2 \gamma_{sp}}{\omega_0^2 \gamma}, \tag{17}$$

where c is the speed of light, ω_0 is the angular frequency at the center of the resonance, γ is half of the angular frequency FWHM of the absorption resonance, and γ_{sp} is a parameter proportional to the square of the dipole matrix element. In particular, γ_{sp} is given by Eq. (2.5.11) of [43] as

$$\gamma_{sp} = \frac{e^2 \omega_0^2 d_{12}^2}{6\pi \epsilon_0 \hbar c^3}, \tag{18}$$

where ϵ_0 is the permittivity of free space, and e is the charge of an electron. Combining these gives

$$d_{12} = \sqrt{\frac{3\sigma(\omega_0)\gamma\epsilon_0\hbar c}{\omega_0 e^2}} = 4.04 \times 10^{-12} \text{ m}. \tag{19}$$

The dipole matrix element between the model core and valence excited states was set to $d_{23} = \sqrt{3}d_{12}$, in correspondence with there being three times more occupied 3d than unoccupied 3d states in solid cobalt [44].

We now have the necessary equations to solve for the field of an X-ray pulse exiting a sample. We used the method of [45] to generate simulated SASE pulses with 4 eV bandwidth and either 5 or 25 fs pulse durations. For each pulse duration, we simulated the interaction of the X-ray pulses with 20 different randomly generated SASE pulses and averaged the results. We assume the sample starts in the ground state,

$$s(0) = \begin{bmatrix} 1 & 0 & 0 \\ 0 & 0 & 0 \\ 0 & 0 & 0 \end{bmatrix}. \tag{20}$$

Next, we use Eq. 13 to solve for the evolution of the sample, then Eq. 16 to calculate the polarization as a function of time. Finally, we calculate the X-ray field exiting the sample from Eq. 5. The spectra of X-rays incident and exiting a sample is obtained from these time domain quantities by taking a Fourier transform. The resulting spectra are shown in Supplementary Fig. 2 and the stimulated inelastic scattering efficiency quantified in Fig. 3.

We also performed simulations which incorporate an assumed enhancement factor of stimulated elastic scattering as proposed in [19]. For these simulations, the difference in polarization of the sample between its calculated nonlinear response and its polarization if it responded linearly was multiplied by the enhancement factor of [19] calculated with the average intensity of the X-ray pulse weighted by its intensity. The results are shown in Supplementary Fig. 3 and cause the main absorption resonance to decrease more rapidly with increasing X-ray intensity, but did not impact the stimulated inelastic scattering for the parameters we used.

Rate Equations Simulations

The rate equation model estimations were based on a 3-level/band model that includes the core states, intermediate non-radiative decay states and the valence states. The three levels are connected through rates describing absorption, spontaneous emission, stimulated emission and Auger decay. An example of the resulting rate equations for the valence band is

$$\frac{\partial N_{Band}(E,t)}{\partial t} = R_{Abs}(E,t) - R_{Stim}(E,t) \\ - R_{Spon}(E,t) - R_{Aug}(E,t), \tag{21}$$

where $N_{band}(E,t)$ is the occupation of the valence band as a function of energy, E, and time, t. The occupation increases through absorption $R_{Abs}(E,t)$, but decreases through spontaneous emission $R_{Spon}(E,t)$, Auger decay $R_{Aug}(E,t)$, and stimulated emission $R_{Stim}(E,t)$. The absorption band DOS was approximated with a Gaussian. The initial occupations of valence states was set by a Fermi-Dirac distribution. The ratio of occupied to unoccupied states was was approximated as 7 to 3. The event count for stimulated emission between two states with energy difference E and at time t, for example, was given by

$$R_{Stim}(E,t) = \sigma_{Stim}(E, I(E,t))N_{Band}(E,t) \\ \times f_{Stim}(E,t). \tag{22}$$

This depends on the incident X-ray intensity, written in terms of the number of photons, $I(E,t)\frac{\lambda A}{hc}$, the stimulated emission cross section, $\sigma_{Stim}(E)$, the number of available (occupied) states $N_{Band}(E,t)$, and an occupation factor $f_{Stim}(E,t)$ depicting the relative occupation between the two states (given in Eq. 24 below). The other symbols are c for the speed of light in a vacuum, h for Planck's constant, λ for the X-ray wavelength, and A for the area of the X-ray pulse at the sample.

From Schreck et al. [46], the intensity dependent core hole decay cross sections are related to the total absorption cross section σ_{total} as

$$\sigma_{total} = \sigma_{spon} \left(\underbrace{1}_{\sigma_{spon}} + \underbrace{\frac{1 - \omega_{fy}}{\omega_{fy}}}_{\sigma_{Auger}} + \underbrace{\frac{4\pi^2 c^2}{\omega_2^2}F(\omega_2)}_{\sigma_{stim}} \right). \tag{23}$$

As the stimulated cross section depends on the X-ray strength, increasing with increasing photon densities, the others cross sections also depend on the incident X-ray strength. Here, $F(\omega_2)$ is the spectral photon flux (photons per area, time and frequency interval) and ω_{fy} is the fluorescence yield. The occupation difference between the

two involved states is included through the occupation factor f as

$$f_{abs}(E,t) = \frac{N_{Core}(t)}{max(N_{Core})} \cdot (1 - \frac{N_{Band}(E,t)}{max(N_{Band}(E,t))}) \tag{24}$$

This example shows the occupation factor of the absorption process, given as the relative core state occupation multiplied with the relative absorption band occupation (inverted, as empty states are relevant for absorption). To estimate a inelastic stimulated scattering efficiency, the relative amount of stimulated events compared to the total number of decay events was calculated over a 40fs simulation time for 5, and 25 fs pulses respectively. For each incident fluence point, a number of 1000 Gaussian shaped resonant pulses with a randomized width and energy jitter of up to $\pm 1eV$ were calculated.

* dhigley@alumni.stanford.edu

† stohr@slac.stanford.edu

[1] L. J. P. Ament, M. van Veenendaal, T. P. Devereaux, J. P. Hill, and J. van den Brink, Resonant inelastic x-ray scattering studies of elementary excitations, Rev. Mod. Phys. **83**, 705 (2011).

[2] G. Ghiringhelli and L. Braicovich, Magnetic excitations of layered cuprates studied by rixs at cu l3 edge, J. Electron Spectrosc. Relat. Phenom. **188**, 26 (2013).

[3] N. Rohringer, X-ray raman scattering: a building block for nonlinear spectroscopy, Philos. Trans. R. Soc. A **377**, 20170471 (2019).

[4] B. W. McNeil and N. R. Thompson, X-ray free-electron lasers, Nat. Photonics **4**, 814 (2010).

[5] P. Emma, R. Akre, J. Arthur, R. Bionta, C. Bostedt, J. Bozek, A. Brachmann, P. Bucksbaum, R. Coffee, F.-J. Decker, et al., First lasing and operation of an ångstrom-wavelength free-electron laser, Nat. Photonics **4**, 641 (2010).

[6] C. Bostedt, S. Boutet, D. M. Fritz, Z. Huang, H. J. Lee, H. T. Lemke, A. Robert, W. F. Schlotter, J. J. Turner, and G. J. Williams, Linac coherent light source: The first five years, Rev. Mod. Phys. **88**, 015007 (2016).

[7] N. Rohringer, D. Ryan, R. A. London, M. Purvis, F. Albert, J. Dunn, J. D. Bozek, C. Bostedt, A. Graf, R. Hill, et al., Atomic inner-shell x-ray laser at 1.46 nanometres pumped by an x-ray free-electron laser, Nature **481**, 488 (2012).

[8] H. Yoneda, Y. Inubushi, K. Nagamine, Y. Michine, H. Ohashi, H. Yumoto, K. Yamauchi, H. Mimura, H. Kitamura, T. Katayama, et al., Atomic inner-shell laser at 1.5-ångström wavelength pumped by an x-ray free-electron laser, Nature **524**, 446 (2015).

[9] T. Kroll, C. Weninger, R. Alonso-Mori, D. Sokaras, D. Zhu, L. Mercadier, V. P. Majety, A. Marinelli, A. Lutman, M. W. Guetg, et al., Stimulated x-ray emission spectroscopy in transition metal complexes, Phys. Rev. Lett. **120**, 133203 (2018).

[10] T. Kroll, C. Weninger, F. D. Fuller, M. W. Guetg, A. Benediktovitch, Y. Zhang, A. Marinelli, R. Alonso-Mori, A. Aquila, M. Liang, et al., Observation of seeded mn k β stimulated x-ray emission using two-color x-ray free-electron laser pulses, Phys. Rev. Lett. **125**, 037404 (2020).

[11] Z. Chen, D. Higley, M. Beye, M. Hantschmann, V. Mehta, O. Hellwig, A. Mitra, S. Bonetti, M. Bucher, S. Carron, et al., Ultrafast self-induced x-ray transparency and loss of magnetic diffraction, Phys. Rev. Lett. **121**, 137403 (2018).

[12] M. Beye, S. Schreck, F. Sorgenfrei, C. Trabant, N. Pontius, C. Schüßler-Langeheine, W. Wurth, and A. Föhlisch, Stimulated x-ray emission for materials science, Nature **501**, 191 (2013).

[13] C. Weninger, M. Purvis, D. Ryan, R. A. London, J. D. Bozek, C. Bostedt, A. Graf, G. Brown, J. J. Rocca, and N. Rohringer, Stimulated electronic x-ray raman scattering, Phys. Rev. Lett. **111**, 233902 (2013).

[14] J. T. O'Neal, E. G. Champenois, S. Oberli, R. Obaid, A. Al-Haddad, J. Barnard, N. Berrah, R. Coffee, J. Duris, G. Galinis, et al., Electronic population transfer via impulsive stimulated x-ray raman scattering with attosecond soft-x-ray pulses, Phys. Rev. Lett. **125**, 073203 (2020).

[15] U. Eichmann, H. Rottke, S. Meise, J.-E. Rubensson, J. Söderström, M. Agåker, C. Såthe, M. Meyer, T. Baumann, R. Boll, et al., Photon-recoil imaging: Expanding the view of nonlinear x-ray physics, Science **369**, 1630 (2020).

[16] D. J. Higley, A. H. Reid, Z. Chen, L. Le Guyader, O. Hellwig, A. A. Lutman, T. Liu, P. Shafer, T. Chase, G. L. Dakovski, et al., Femtosecond x-ray induced changes of the electronic and magnetic response of solids from electron redistribution, Nat. Commun. **10**, 5289 (2019).

[17] V. Kimberg, A. Sanchez-Gonzalez, L. Mercadier, C. Weninger, A. Lutman, D. Ratner, R. Coffee, M. Bucher, M. Mucke, M. Agåker, et al., Stimulated x-ray raman scattering–a critical assessment of the building block of nonlinear x-ray spectroscopy, Faraday Discuss. **194**, 305 (2016).

[18] S. Schreck, M. Beye, J. A. Sellberg, T. McQueen, H. Laksmono, B. Kennedy, S. Eckert, D. Schlesinger, D. Nordlund, H. Ogasawara, R. G. Sierra, V. H. Segtnan, K. Kubicek, W. F. Schlotter, G. L. Dakovski, S. P. Moeller, U. Bergmann, S. Techert, L. G. M. Pettersson, P. Wernet, M. J. Bogan, Y. Harada, A. Nilsson, and A. Föhlisch, Reabsorption of soft x-ray emission at high x-ray free-electron laser fluences, Phys. Rev. Lett. **113**, 153002 (2014).

[19] J. Stöhr and A. Scherz, Creation of x-ray transparency of matter by stimulated elastic forward scattering, Phys. Rev. Lett. **115**, 107402 (2015).

[20] K. R. Ferguson, M. Bucher, J. D. Bozek, S. Carron, J.-C. Castagna, R. Coffee, G. I. Curiel, M. Holmes, J. Krzywinski, M. Messerschmidt, et al., The atomic, molecular and optical science instrument at the linac coherent light source, J. Synchrotron Radiat. **22**, 492 (2015).

[21] N. Berrah, L. Fang, B. F. Murphy, E. Kukk, T. Y. Osipov, R. Coffee, K. R. Ferguson, H. Xiong, J.-C. Castagna, V. S. Petrovic, et al., Two mirror x-ray pulse split and delay instrument for femtosecond time resolved investigations at the lcls free electron laser facility, Opt. Express **24**, 11768 (2016).

[22] A. Nilsson, J. Stöhr, T. Wiell, M. Aldén, P. Bennich, N. Wassdahl, M. Samant, S. Parkin, N. Mårtensson,

J. Nordgren, *et al.*, Determination of the electronic density of states near buried interfaces: Application to co/cu multilayers, Phys. Rev. B **54**, 2917 (1996).

[23] A. Sanchez-Gonzalez, P. Micaelli, C. Olivier, T. Barillot, M. Ilchen, A. Lutman, A. Marinelli, T. Maxwell, A. Achner, M. Agåker, *et al.*, Accurate prediction of x-ray pulse properties from a free-electron laser using machine learning, Nat. Commun. **8**, 15461 (2017).

[24] G. Nasreen, S. T. Manson, and P. C. Deshmukh, Photoionization of inner shells of the mg and ar isonuclear sequences, Phys. Rev. A **40**, 6091 (1989).

[25] M. Witthoeft, J. García, T. Kallman, M. Bautista, C. Mendoza, P. Palmeri, and P. Quinet, K-shell photoionization of na-like to cl-like ions of mg, si, s, ar, and ca, Astrophys. J., Suppl. Ser. **192**, 7 (2010).

[26] S. Vinko, O. Ciricosta, B. Cho, K. Engelhorn, H.-K. Chung, C. Brown, T. Burian, J. Chalupskỳ, R. Falcone, C. Graves, *et al.*, Creation and diagnosis of a solid-density plasma with an x-ray free-electron laser, Nature **482**, 59 (2012).

[27] L. Müller, C. Gutt, B. Pfau, S. Schaffert, J. Geilhufe, F. Büttner, J. Mohanty, S. Flewett, R. Treusch, S. Düsterer, *et al.*, Breakdown of the x-ray resonant magnetic scattering signal during intense pulses of extreme ultraviolet free-electron-laser radiation, Phys. Rev. Lett. **110**, 234801 (2013).

[28] M. O. Krause and J. Oliver, Natural widths of atomic k and l levels, k α x-ray lines and several kll auger lines, Journal of Physical and Chemical Reference Data **8**, 329 (1979).

[29] M. O. Krause, Atomic radiative and radiationless yields for k and l shells, Journal of physical and chemical reference data **8**, 307 (1979).

[30] O. S. Humphries, R. S. Marjoribanks, Q. Y. van den Berg, E. C. Galtier, M. F. Kasim, H. J. Lee, A. J. F. Miscampbell, B. Nagler, R. Royle, J. S. Wark, and S. M. Vinko, Probing the electronic structure of warm dense nickel via resonant inelastic x-ray scattering, Phys. Rev. Lett. **125**, 195001 (2020).

[31] R. Knorren, K. Bennemann, R. Burgermeister, and M. Aeschlimann, Dynamics of excited electrons in copper and ferromagnetic transition metals: Theory and experiment, Phys. Rev. B **61**, 9427 (2000).

[32] J. Duris, S. Li, T. Driver, E. G. Champenois, J. P. MacArthur, A. A. Lutman, Z. Zhang, P. Rosenberger, J. W. Aldrich, R. Coffee, *et al.*, Tunable isolated attosecond x-ray pulses with gigawatt peak power from a free-electron laser, Nat. Photonics **14**, 30 (2020).

[33] J. D. Biggs, Y. Zhang, D. Healion, and S. Mukamel, Watching energy transfer in metalloporphyrin heterodimers using stimulated x-ray raman spectroscopy, Proc. Natl. Acad. Sci. U.S.A. **110**, 15597 (2013).

[34] S. Mukamel, D. Healion, Y. Zhang, and J. D. Biggs, Multidimensional attosecond resonant x-ray spectroscopy of molecules: Lessons from the optical regime, Annu. Rev. Phys. Chem. **64**, 101 (2013).

[35] S. Moeller, J. Arthur, A. Brachmann, R. Coffee, F.-J. Decker, Y. Ding, D. Dowell, S. Edstrom, P. Emma, Y. Feng, *et al.*, Photon beamlines and diagnostics at lcls, Nucl. Instrum. Methods Phys. Res. A **635**, S6 (2011).

[36] C. Behrens, F.-J. Decker, Y. Ding, V. Dolgashev, J. Frisch, Z. Huang, P. Krejcik, H. Loos, A. Lutman, T. Maxwell, *et al.*, Few-femtosecond time-resolved measurements of x-ray free-electron lasers, Nat. Commun. **5**, 3762 (2014).

[37] A. Lutman, Y. Ding, Y. Feng, Z. Huang, M. Messerschmidt, J. Wu, and J. Krzywinski, Femtosecond x-ray free electron laser pulse duration measurement from spectral correlation function, Phys. Rev. Spec. Top. Accel. Beams **15**, 030705 (2012).

[38] R. Engel, S. Düsterer, G. Brenner, and U. Teubner, Quasi-real-time photon pulse duration measurement by analysis of fel radiation spectra, J. Synchrotron Radiat. **23**, 118 (2016).

[39] W. Schlotter, J. Turner, M. Rowen, P. Heimann, M. Holmes, O. Krupin, M. Messerschmidt, S. Moeller, J. Krzywinski, R. Soufli, *et al.*, The soft x-ray instrument for materials studies at the linac coherent light source x-ray free-electron laser, Review of Scientific Instruments **83**, 043107 (2012).

[40] B. Efron and R. Tibshirani, Bootstrap methods for standard errors, confidence intervals, and other measures of statistical accuracy, Statistical science , 54 (1986).

[41] B. W. Shore, *Manipulating quantum structures using laser pulses* (Cambridge University Press, 2011).

[42] C. Weninger and N. Rohringer, Stimulated resonant x-ray raman scattering with incoherent radiation, Phys. Rev. A **88**, 053421 (2013).

[43] R. Loudon, *The quantum theory of light* (Oxford University Press, 2000).

[44] C. Chen, Y. Idzerda, H.-J. Lin, N. Smith, G. Meigs, E. Chaban, G. Ho, E. Pellegrin, and F. Sette, Experimental confirmation of the x-ray magnetic circular dichroism sum rules for iron and cobalt, Phys. Rev. Lett. **75**, 152 (1995).

[45] T. Pfeifer, Y. Jiang, S. Düsterer, R. Moshammer, and J. Ullrich, Partial-coherence method to model experimental free-electron laser pulse statistics, Opt. Lett. **35**, 3441 (2010).

[46] S. Schreck, M. Beye, and A. Föhlisch, Implications of stimulated resonant x-ray scattering for spectroscopy, imaging, and diffraction in the regime from soft to hard x-rays, Journal of Modern Optics **62**, S34 (2015).

Bibliography

[1] A. H. Zewail, Femtochemistry: Atomic-scale dynamics of the chemical bond using ultrafast lasers (Nobel lecture), 2000.

[2] J. Stöhr and H. C. Siegmann, *Magnetism: From fundamentals to nanoscale dynamics*, 2006.

[3] J. D. Aiken and R. G. Finke, A review of modern transition-metal nanoclusters: Their synthesis, characterization, and applications in catalysis, 1999.

[4] D. Farrusseng, S. Aguado, and C. Pinel, Metal-organic frameworks: Opportunities for catalysis, 2009.

[5] Y.-C. Cheng and G. R. Fleming, Dynamics of light harvesting in photosynthesis., Annual review of physical chemistry **60**(2012 American Chemical Society (ACS).), 241–62 (2009).

[6] H. Mairbäurl and R. E. Weber, Oxygen transport by hemoglobin, Comprehensive Physiology **2**(2), 1463–1489 (2012).

[7] V. V. Yakovlev, G. I. Petrov, H. F. Zhang, G. D. Noojin, M. L. Denton, R. J. Thomas, and M. O. Scully, Stimulated Raman scattering: old physics, new applications., Journal of modern optics **56**(18-19), 1970–1973 (2009).

[8] P. Wernet, K. Kunnus, I. Josefsson, I. Rajkovic, W. Quevedo, M. Beye, S. Schreck, S. Grubel, M. Scholz, D. Nordlund, W. Zhang, R. W. Hartsock, W. F. Schlotter, J. J. Turner, B. Kennedy, F. Hennies, F. M. F. de Groot, K. J. Gaffney, S. Techert, M. Odelius, and A. Föhlisch, Orbital-specific mapping of the ligand exchange dynamics of Fe(CO)5 in solution, Nature **520**(7545), 78–81 (2015).

[9] H. Öström, A. Föhlisch, M. Nyberg, M. Weinelt, C. Heske, L. Pettersson, and A. Nilsson, Ethylene on Cu(110) and Ni(110): electronic structure and bonding derived from X-ray spectroscopy and theory, Surface Science **559**, 85–99 (2004).

[10] M. Dell'Angela, T. Anniyev, M. Beye, R. Coffee, A. Föhlisch, J. Gladh, T. Katayama, S. Kaya, O. Krupin, J. LaRue, A. Møgelhøj, D. Nordlund, J. K. Nørskov, H. Öberg, H. Ogasawara, H. Öström, L. G. M. Pettersson, W. F. Schlotter, J. A. Sellberg, F. Sorgenfrei, J. J. Turner, M. Wolf, W. Wurth, and A. Nilsson, Real-Time Observation of Surface Bond Breaking with an X-ray Laser, Science **339**(6125), 1302–1305 (2013).

[11] H.-J. Bäcker, J. Bahrdt, H. Dürr, V. Dürr, W. Eberhardt, A. Gaupp, E. Jaeschke, K. Holldack, S. Khan, D. Krämer, H.-C. Mertins, W. Peatman, G. Reichardt, T. Quast, M. Scheer, F. Senf, G. Wüstefeld, I. Hertel, F. Noack, W. Sandner, I. Will, and N. Zhavoronkoy, Layout of a femtosecond x-ray source at BESSY II, in *Proceedings of the IEEE Particle Accelerator Conference*, volume 2, 2003.

[12] M. Labat, M.-A. Tordeux, P. Hollander, P. Prigent, M.-E. Couprie, A. Nadji, D. Pédeau, J.-P. Ricaud, F. Dohou, L. Cassinari, O. Marcouillé, H. Abualrob, K. Tavakoli, D. Zerbib, J.-L. Marlats, A. Lestrade, M. Ros, L. Nadolski, J.-F. Lamarre, P. Betinelli, A. Buteau, N. Béchu, C. Herbeaux, P. Roy, J. Luning, T. Moreno, C. Laulhe, S. Ravy, M. Silly, F. Sirotti, and P. Morin, Commissioning progress of the femtoslicing at SOLEIL, in *IPAC 2014: Proceedings of the 5th International Particle Accelerator Conference*, 2014.

[13] B. W. J. McNeil and N. R. Thompson, X-ray free-electron lasers, Nature Photonics **4**(DECEMBER), 814–821 (2010).

[14] H. N. H. H. N. Chapman, A. Barty, M. J. M. Bogan, S. Boutet, M. Frank, P. Stefan, S. Marchesini, B. W. Woods, W. H. Benner, R. A. London, M. Kuhlmann, R. Treusch, T. Tschentscher, J. R. Schneider, E. Spiller, C. Bostedt, M. Hoener, D. A. Shapiro, K. O. Hodgson, D. V. D. Spoel, F. Burmeister, M. Bergh, C. Caleman, M. M. Seibert, R. W. Lee, N. Timneanu, J. Hajdu, S. Boutet, M. Frank, S. P. Hau-Riege, S. Marchesini, B. W. Woods, S. Bajt, W. H. Benner, R. A. London, E. Plönjes,

M. Kuhlmann, R. Treusch, S. Düsterer, T. Tschentscher, J. R. Schneider, E. Spiller, T. Möller, C. Bostedt, M. Hoener, D. A. Shapiro, K. O. Hodgson, D. van der Spoel, F. Burmeister, M. Bergh, C. Caleman, G. Huldt, M. M. Seibert, F. R. N. C. Maia, R. W. Lee, A. Szöke, N. Timneanu, and J. Hajdu, Femtosecond diffractive imaging with a soft-X-ray free-electron laser, Nature Physics **2**(12), 839–843 (2006).

[15] A. Aquila, M. S. Hunter, R. B. Doak, R. a. Kirian, P. Fromme, T. a. White, J. Andreasson, D. Arnlund, S. Bajt, T. R. M. Barends, M. Barthelmess, M. J. Bogan, C. Bostedt, H. Bottin, J. D. Bozek, C. Caleman, N. Coppola, J. Davidsson, D. P. DePonte, V. Elser, S. W. Epp, B. Erk, H. Fleckenstein, L. Foucar, M. Frank, R. Fromme, H. Graafsma, I. Grotjohann, L. Gumprecht, J. Hajdu, C. Y. Hampton, A. Hartmann, R. Hartmann, S. Hau-Riege, G. Hauser, H. Hirsemann, P. Holl, J. M. Holton, A. Hömke, L. Johansson, N. Kimmel, S. Kassemeyer, F. Krasniqi, K.-U. Kühnel, M. Liang, L. Lomb, E. Malmerberg, S. Marchesini, A. V. Martin, F. R. Maia, M. Messerschmidt, K. Nass, C. Reich, R. Neutze, D. Rolles, B. Rudek, A. Rudenko, I. Schlichting, C. Schmidt, K. E. Schmidt, J. Schulz, M. M. Seibert, R. L. Shoeman, R. Sierra, H. Soltau, D. Starodub, F. Stellato, S. Stern, L. Strüder, N. Timneanu, J. Ullrich, X. Wang, G. J. Williams, G. Weidenspointner, U. Weierstall, C. Wunderer, A. Barty, J. C. H. Spence, and H. N. Chapman, Time-resolved protein nanocrystallography using an X-ray free-electron laser, Optics Express **20**(3), 2706 (2012).

[16] K. H. Kim, J. G. Kim, S. Nozawa, T. Sato, K. Y. Oang, T. W. Kim, H. Ki, J. Jo, S. Park, C. Song, T. Sato, K. Ogawa, T. Togashi, K. Tono, M. Yabashi, T. Ishikawa, J. Kim, R. Ryoo, J. Kim, H. Ihee, and S.-i. Adachi, Direct observation of bond formation in solution with femtosecond X-ray scattering, Nature **518**(7539), 385–389 (2015).

[17] S. Mukamel, Multidimensional Femtosecond Correlation Spectroscopies of Electronic and Vibrational Excitations, Ann. Rev. Phys. Chem. **51**(11), 691–729 (2000).

[18] S. Tanaka and S. Mukamel, Coherent x-ray Raman spectroscopy: a nonlinear local probe for electronic excitations., Physical review letters **89**(4), 043001 (2002).

[19] M. Dantus, Coherent Nonlinear Spectroscopy: From Femtosecond Dynamics to Control, Annual Review of Physical Chemistry **52**(1), 639–679 (2001), PMID: 11326077.

[20] R. L. Swofford and A. C. Albrecht, Nonlinear Spectroscopy, Annual Review of Physical Chemistry **29**(1), 421–440 (1978).

[21] R. Frontiera and R. Mathies, Femtosecond stimulated Raman spectroscopy, Laser & Photonics Reviews **5**(1), 102 – 113 (2011).

[22] J. T. Fourkas, Multidimensional Raman spectroscopy, Advances in Chemical Physics **117**, 235–274 (2001).

[23] S. Mukamel, Y. Tanimura, and P. Hamm, Coherent Multidimensional Optical Spectroscopy, Accounts of Chemical Research **42**(9), 1207–1209 (2009).

[24] E. Allaria, R. Appio, L. Badano, W. Barletta, S. Bassanese, S. Biedron, A. Borga, E. Busetto, D. Castronovo, P. Cinquegrana, et al., Highly coherent and stable pulses from the FERMI seeded free-electron laser in the extreme ultraviolet, Nature Photonics **6**(10), 699–704 (2012).

[25] Y. Feng, J. Amann, D. Cocco, C. Field, J. Hastings, P. Heimann, Z. Huang, H. Loos, J. Welch, J. Wu, et al., System design for self-seeding the LCLS at soft X-ray energies, in *Proceedings of the 24th International FEL Conference, Nara, Japan*, 2012.

[26] A. Lutman, R. Coffee, Y. Ding, Z. Huang, J. Krzywinski, T. Maxwell, M. Messerschmidt, and H.-D. Nuhn, Experimental demonstration of femtosecond two-color x-ray free-electron lasers, Physical review letters **110**(13), 134801 (2013).

[27] T. Hara, Y. Inubushi, T. Katayama, T. Sato, H. Tanaka, T. Tanaka, T. Togashi, K. Togawa, K. Tono, M. Yabashi, et al., Two-colour hard X-ray free-electron laser with wide tunability, Nature communications **4**(1), 1–5 (2013).

[28] L. J. P. Ament, M. Van Veenendaal, T. P. Devereaux, J. P. Hill, and J. Van Den Brink, Resonant inelastic x-ray scattering studies of elementary excitations, Reviews of Modern Physics **83**(2), 705–767 (2011).

[29] M. Beye, S. Schreck, F. Sorgenfrei, C. Trabant, N. Pontius, C. Schüßler-Langeheine, W. Wurth, and a. Föhlisch, Stimulated X-ray emission for materials science., Nature **501**(7466), 191–4 (2013).

[30] S. Schreck, M. Beye, and A. Föhlisch, Implications of stimulated resonant X-ray scattering for spectroscopy, imaging, and diffraction in the regime from soft to hard X-rays, Journal of Modern Optics **62**(sup2), S41–S51 (2015).

[31] B. D. Patterson, Resource Letter on Stimulated Inelastic X-ray Scattering at an XFEL, Slac-Tn **026**(3) (2010).

[32] D. Healion, J. D. Biggs, and S. Mukamel, Manipulating one- and two-dimensional stimulated-x-ray resonant-Raman signals in molecules by pulse polarizations, Physical Review A - Atomic, Molecular, and Optical Physics **86**(3) (2012).

[33] A. Kotani and S. Shin, Resonant inelastic x-ray scattering spectra for electrons in solids, Rev. Mod. Phys. **73**(1), 203–246 (2001).

[34] E. Fill, Materials science: Boosting X-ray emission., Nature **501**(7466), 172–173 (2013).

[35] H. Haken, H. C. Wolf, and E. J. Brändas, *The Physics of Atoms and Quanta*, volume 54, 1995.

[36] M. Veenendaal, *Theory of Inelastic Scattering and Absorption of X-rays*, Cambridge University Press, 2015.

[37] J. Stöhr and A. Scherz, Creation of X-Ray Transparency of Matter by Stimulated Elastic Forward Scattering, Phys. Rev. Lett. **115**, 107402 (Sep 2015).

[38] P. W. Atkins and R. Friedman, Molecular Quantum Mechanics, Quantum **134**, 588 (2011).

[39] J. Sakurai, *Modern quantum mechanics*, Addison-Wesley, 1994.

[40] R. Moss, *Advanced Molecular Quantum Mechanics*, Chapman and Hall, 1973.

[41] H. A. Kramers and W. Heisenberg, Über die Streuung von Strahlung durch Atome, Zeitschrift für Physik **31**(1), 681–708 (1925).

[42] Interaction of Radiation with Matter, `http://www.ks.uiuc.edu/Services/Class/PHYS498TBP/EM1.pdf`, Accessed: 2017-02-04.

[43] J. Als-Nielsen and D. McMorrow, *Elements of Modern X-ray Physics*, John Wiley & Sons, Inc., 2011.

[44] D. Lee and A. Albrecht, *A Unified View of Raman Resonance Raman and Fluorescence Spectroscopy*, volume 12, Wiley Heyden, 1985.

[45] C. Pellegrini and J. Stöhr, X-Ray Free Electron Lasers: Principles, Properties and Applications, pages 1–16 (2009).

[46] P. H. Bucksbaum, R. Coffee, and N. Berrah, Chapter 5 - The First Atomic and Molecular Experiments at the Linac Coherent Light Source X-Ray Free Electron Laser, in *Advances in Atomic, Molecular, and Optical Physics*, edited by P. B. E. Arimondo and C. Lin, volume 60 of *Advances In Atomic, Molecular, and Optical Physics*, pages 239 – 289, Academic Press, 2011.

[47] LCLS parameters, `https://portal.slac.stanford.edu/sites/lclscore_public/Accelerator_Physics_Published_Documents/LCLS-parameters.pdf`, Accessed: 2017-02-01.

[48] M. M. Cid and J. Bravo, *Structure Elucidation in Organic Chemistry: The Search for the Right Tools*, 2015.

[49] M. O. Krause, Atomic radiative and radiationless yields for K and L shells, Journal of Physical and Chemical Reference Data **8**(2), 307–327 (1979).

[50] S. Schreck, *Potential Energy Surfaces, Femtosecond Dynamics and Nonlinear X-Ray-Matter Interactions from Resonant Inelastic Soft X-Ray Scattering*, PhD thesis, University Potsdam, 2014.

[51] BESSY parameter, `https://www.helmholtz-berlin.de/intern/nutzerplattform/betrieb-bessy/maschine/ring-parameter-tabelle_de.html`, Accessed: 2017-02-01.

[52] W. Peatman, *Gratings, Mirrors and Slits: Beamline Design for Soft X-Ray Synchrotron Radiation Sources*, CRC Press, 1997.

[53] D. Attwood, *Soft X-rays and Extreme Ultraviolet Radiation*, Cambridge University Press, 1999.

[54] I. Robinson, G. Gruebel, and S. Mochrie, X-ray beams with high coherence, New Journal of Physics **12** (2010).

[55] K.-J. Kim, S. Milton, and E. Gluskin, editors, Elsevier, Amsterdam, 2003.

[56] G. Brown, K. Halbach, J. Harris, and H. Winick, Wiggler and undulator magnets - A review, Nuclear Instruments and Methods In Physics Research **208**(1-3), 65–77 (1983).

[57] D. Rupp, *Ionization and plasma dynamics of single large xenon clusters in superintense xuv pulses*, volume Thesis, Technische Universität Berlin, 2013.

[58] Z. Huang and K.-J. Kim, Review of x-ray free-electron laser theory, Phys. Rev. ST Accel. Beams **10**, 034801 (Mar 2007).

[59] K.-J. Kim, Angular distribution of undulator power for an arbitrary deflection parameter K, Nuclear Instruments and Methods in Physics Research Section A: Accelerators, Spectrometers, Detectors and Associated Equipment **246**(1), 67 – 70 (1986).

[60] K. Sawhney, F. Senf, and W. Gudat, {PGM} beamline with constant energy resolution mode for U49-2 undulator at BESSY-II, Nuclear Instruments and Methods in Physics Research Section A: Accelerators, Spectrometers, Detectors and Associated Equipment **467–468, Part 1**, 466 – 469 (2001), 7th Int.Conf. on Synchrotron Radiation Instrumentation.

[61] R. J. Dejus, LCLS Prototype Undulator Report, DOE report (January) (2004).

[62] W. F. Schlotter, J. J. Turner, M. Rowen, P. Heimann, M. Holmes, O. Krupin, M. Messerschmidt, S. Moeller, J. Krzywinski, R. Soufli, M. Fernndez-Perea, N. Kelez, S. Lee, R. Coffee, G. Hays, M. Beye, N. Gerken, F. Sorgenfrei, S. Hau-Riege, L. Juha, J. Chalupsky, V. Hajkova, A. P. Mancuso, A. Singer, O. Yefanov, I. A. Vartanyants, G. Cadenazzi, B. Abbey, K. A. Nugent, H. Sinn, J. Lning, S. Schaffert, S. Eisebitt, W. S. Lee, A. Scherz, A. R. Nilsson, and W. Wurth, The soft x-ray instrument

for materials studies at the linac coherent light source x-ray free-electron laser, Review of Scientific Instruments **83**(4) (2012).

[63] E. Allaria, R. Appio, L. Badano, W. Barletta, S. Bassanese, S. Biedron, A. Borga, E. Busetto, D. Castronovo, P. Cinquegrana, S. Cleva, D. Cocco, M. Cornacchia, P. Craievich, I. Cudin, G. D'Auria, M. Dal Forno, M. Danailov, R. De Monte, G. De Ninno, P. Delgiusto, A. Demidovich, S. Di Mitri, B. Diviacco, A. Fabris, R. Fabris, W. Fawley, M. Ferianis, E. Ferrari, S. Ferry, L. Froehlich, P. Furlan, G. Gaio, F. Gelmetti, L. Giannessi, M. Giannini, R. Gobessi, R. Ivanov, E. Karantzoulis, M. Lonza, A. Lutman, B. Mahieu, M. Milloch, S. Milton, M. Musardo, I. Nikolov, S. Noe, F. Parmigiani, G. Penco, M. Petronio, L. Pivetta, M. Predonzani, F. Rossi, L. Rumiz, A. Salom, C. Scafuri, C. Serpico, P. Sigalotti, S. Spampinati, C. Spezzani, M. Svandrlik, C. Svetina, S. Tazzari, M. Trovo, R. Umer, A. Vascotto, M. Veronese, R. Visintini, M. Zaccaria, D. Zangrando, and M. Zangrando, Highly coherent and stable pulses from the FERMI seeded free-electron laser in the extreme ultraviolet, Nature Photonics **6**(10), 699–704 (2012).

[64] C. Weber, Zum Zerfall eines Flüssigkeitsstrahles, ZAMM Journal of Applied Mathematics and Mechanics / Zeitschrift fuer Angewandte Mathematik und Mechanik **11**(2), 136–154 (1931).

[65] K. Nass, L. Foucar, T. R. M. Barends, E. Hartmann, S. Botha, R. L. Shoeman, R. B. Doak, R. Alonso-Mori, A. Aquila, S. Bajt, A. Barty, R. Bean, K. R. Beyerlein, M. Bublitz, N. Drachmann, J. Gregersen, H. O. Jönsson, W. Kabsch, S. Kassemeyer, J. E. Koglin, M. Krumrey, D. Mattle, M. Messerschmidt, P. Nissen, L. Reinhard, O. Sitsel, D. Sokaras, G. J. Williams, S. Hau-Riege, N. Timneanu, C. Caleman, H. N. Chapman, S. Boutet, and I. Schlichting, Indications of radiation damage in ferredoxin microcrystals using high-intensity X-FEL beams, Journal of Synchrotron Radiation **22**(2), 225–238 (Mar 2015).

[66] H. O. Jönsson, N. Tîmneanu, C. Östlin, H. A. Scott, and C. Caleman, Simulations of radiation damage as a function of the temporal pulse profile in femtosecond X-ray protein crystallography, Journal of Synchrotron Radiation **22**(2), 256–266 (Mar 2015).

[67] H. Ostrom, H. Oberg, H. Xin, J. LaRue, M. Beye, M. Dell'Angela, J. Gladh, M. L. Ng, J. A. Sellberg, S. Kaya, G. Mercurio, D. Nordlund, M. Hantschmann, F. Hieke, D. Kuhn, W. F. Schlotter, G. L. Dakovski, J. J. Turner, M. P. Minitti, A. Mitra, S. P. Moeller, A. Föhlisch, M. Wolf, W. Wurth, M. Persson, J. K. Norskov, F. Abild-Pedersen, H. Ogasawara, L. G. M. Pettersson, and A. Nilsson, Probing the transition state region in catalytic CO oxidation on Ru, Science **347**(6225), 978–982 (2015).

[68] M. Beye, H. Oberg, H. Xin, G. L. Dakovski, M. Dell'angela, A. Föhlisch, J. Gladh, M. Hantschmann, et al., Chemical bond activation observed with an x-ray laser, The journal of physical chemistry letters **7**(18), 3647–3651 (2016).

[69] S. Eckert, M. Beye, A. Pietzsch, W. Quevedo, M. Hantschmann, M. Ochmann, M. Ross, M. P. Minitti, J. J. Turner, S. P. Moeller, W. F. Schlotter, G. L. Dakovski, M. Khalil, N. Huse, and A. Föhlisch, Principles of femtosecond X-ray/optical cross-correlation with X-ray induced transient optical reflectivity in solids, Applied Physics Letters **106**(6) (2015).

[70] C. Gahl, A. Azima, M. Beye, M. Deppe, K. Döbrich, U. Hasslinger, F. Hennies, A. Melnikov, M. Nagasono, A. Pietzsch, M. Wolf, W. Wurth, and A. Föhlisch, A femtosecond X-ray/optical cross-correlator, Nature Photonics **2**(3), 165–169 (2008).

[71] M. Beye, O. Krupin, G. Hays, A. H. Reid, D. Rupp, S. D. Jong, S. Lee, W. S. Lee, Y. D. Chuang, R. Coffee, J. P. Cryan, J. M. Glownia, A. F??hlisch, M. R. Holmes, A. R. Fry, W. E. White, C. Bostedt, A. O. Scherz, H. A. Durr, and W. F. Schlotter, X-ray pulse preserving single-shot optical cross-correlation method for improved experimental temporal resolution, Applied Physics Letters **100**(12) (2012).

[72] H. A. Rowland, XXXIX. Gratings in theory and practice, Philosophical Magazine Series 5 **35**(216), 397–419 (1893).

[73] W. Peatman, *Gratings, Mirrors and Slits: Beamline Design for Soft X-Ray Synchrotron Radiation Sources*, CRC Press, 1997.

[74] R. Nyholm and J. Nordgren, Design of a prtable large spectral range grazing incidence instrument, Nuclear Instruments and Methods in Physics Research **246**, 242–245 (1986).

[75] J. Nordgren, G. Bray, S. Cramm, R. Nyholm, J.-E. Rubensson, and N. Wassdahl, Soft x-ray emission spectroscopy using monochromatized synchrotron radiation (invited), Review of Scientific Instruments **60**, 1690–1696 (July 1989).

[76] J. Nordgren and J. Guo, Instrumentation for soft X-ray emission spectroscopy, Journal of Electron Spectroscopy and Related Phenomena **110**, 1–13 (2000).

[77] H. N. Chapman, S. Bajt, A. Barty, W. H. Benner, M. J. Bogan, M. Frank, R. A. London, S. Marchesini, E. Spiller, A. Szöke, B. W. Woods, J. Hajdu, M. Bergh, F. Burmeister, C. Caleman, G. Huldt, F. R. N. C. Maia, M. M. Seibert, D. V. D. Spoel, U. Uppsala, S. Uppsala, S. Boutet, K. O. Hodgson, M. Park, D. A. Shapiro, and U. C. Davis, Ultrafast Coherent Diffraction Imaging With X-Ray Free- Electron Lasers*, pages 1–7 (2006).

[78] R. M. Jay, J. Norell, S. Eckert, M. Hantschmann, M. Beye, B. Kennedy, W. Quevedo, W. F. Schlotter, G. L. Dakovski, M. P. Minitti, et al., Disentangling Transient Charge Density and Metal–Ligand Covalency in Photoexcited Ferricyanide with Femtosecond Resonant Inelastic Soft X-ray Scattering, The journal of physical chemistry letters **9**(12), 3538–3543 (2018).

[79] F. D. Fuller, S. Gul, R. Chatterjee, E. S. Burgie, I. D. Young, H. Lebrette, V. Srinivas, A. S. Brewster, T. Michels-Clark, J. A. Clinger, et al., Drop-on-demand sample delivery for studying biocatalysts in action at X-ray free-electron lasers, Nature Methods **14**(4), 443–449 (2017).

[80] I. D. Young, M. Ibrahim, R. Chatterjee, S. Gul, F. D. Fuller, S. Koroidov, A. S. Brewster, R. Tran, R. Alonso-Mori, T. Kroll, et al., Structure of photosystem II and substrate binding at room temperature, Nature **540**(7633), 453–457 (2016).

[81] H. Yoneda, Y. Inubushi, M. Yabashi, T. Katayama, T. Ishikawa, H. Ohashi, H. Yumoto, K. Yamauchi, H. Mimura, and H. Kitamura, Saturable absorption of intense hard X-rays in iron, Nature Communications **5**, 5080 (2014).

[82] H. Yoneda, Y. Inubushi, K. Nagamine, Y. Michine, H. Ohashi, H. Yumoto, K. Yamauchi, H. Mimura, H. Kitamura, T. Katayama, T. Ishikawa, and

M. Yabashi, Atomic inner-shell laser at 1.5-ångström wavelength pumped by an X-ray free-electron laser, Nature **524**(7566), 446–449 (2015).

[83] N. Rohringer, D. Ryan, R. A. London, M. Purvis, F. Albert, J. Dunn, J. D. Bozek, C. Bostedt, A. Graf, R. Hill, S. P. Hau-Riege, and J. J. Rocca, Atomic inner-shell X-ray laser at 1.46 nanometres pumped by an X-ray free-electron laser, Nature **481**(7382), 488–491 (2012).

[84] B. Nagler, U. Zastrau, R. R. Fäustlin, S. M. Vinko, T. Whitcher, a. J. Nelson, R. Sobierajski, J. Krzywinski, J. Chalupsky, E. Abreu, S. Bajt, T. Bornath, T. Burian, H. Chapman, J. Cihelka, T. Döppner, S. Düsterer, T. Dzelzainis, M. Fajardo, E. Förster, C. Fortmann, E. Galtier, S. H. Glenzer, S. Göde, G. Gregori, V. Hajkova, P. Heimann, L. Juha, M. Jurek, F. Y. Khattak, A. R. Khorsand, D. Klinger, M. Kozlova, T. Laarmann, H. J. Lee, R. W. Lee, K.-H. Meiwes-Broer, P. Mercere, W. J. Murphy, A. Przystawik, R. Redmer, H. Reinholz, D. Riley, G. Röpke, F. Rosmej, K. Saksl, R. Schott, R. Thiele, J. Tiggesbäumker, S. Toleikis, T. Tschentscher, I. Uschmann, H. J. Vollmer, and J. S. Wark, Turning solid aluminium transparent by intense soft X-ray photoionization, Nature Physics **5**(9), 693–696 (2009).

[85] K. Tamasaku, K. Sawada, E. Nishibori, and T. Ishikawa, Visualizing the local optical response to extreme-ultraviolet radiation with a resolution of $\lambda/380$, Nature Physics **7**(9), 705–708 (2011).

[86] J. Szlachetko, J. Hoszowska, and J.-C. e. a. Dousse, Establishing nonlinearity thresholds with ultraintense X-ray pulses, Scientific Reports **6:33292** (2016).

[87] Y. R. Shen, Recent advances in nonlinear optics, Reviews of Modern Physics **48**(1), 1–32 (1976).

[88] R. W. Boyd, Nonlinear Optics, Book , 613 (2008).

[89] O. Roslyak, C. A. Marx, and S. Mukamel, Generalized Kramers-Heisenberg expressions for stimulated Raman scattering and two-photon absorption, Physical Review A - Atomic, Molecular, and Optical Physics **79**(6) (2009).

[90] A. A. D Lee, A unified view of Raman, resonance Raman and fluorescence spectroscopy, in *Advances of IR and Raman Spectroscopy*, edited by R. Clark and R. Hester, pages 179–213, Wiley, 1985.

[91] K. R. Ferguson, M. Bucher, J. D. Bozek, S. Carron, J.-C. Castagna, R. Coffee, G. I. Curiel, M. Holmes, J. Krzywinski, M. Messerschmidt, et al., The Atomic, Molecular and Optical Science instrument at the Linac Coherent Light Source, J. Synchrotron Rad. **22**(3), 492–497 (2015).

[92] T. Pritchett, Models for Saturable and Reverse Saturable Absorption in Materials for Optical Limiting, ARL report (October) (2002).

[93] S. L. McCall and E. L. Hahn, Self-Induced Transparency, Physical Review **183**(2), 457–485 (1969).

[94] X-ray Laser strips Neon bare, http://today.slac.stanford.edu/feature/2009/lcls-amo-neon.asp, Accessed: 2017-05-01.

[95] L. Young, E. P. Kanter, B. Krässig, Y. Li, A. M. March, S. T. Pratt, R. Santra, S. H. Southworth, N. Rohringer, L. F. DiMauro, G. Doumy, C. A. Roedig, N. Berrah, L. Fang, M. Hoener, P. H. Bucksbaum, J. P. Cryan, S. Ghimire, J. M. Glownia, D. A. Reis, J. D. Bozek, C. Bostedt, and M. Messerschmidt, Femtosecond electronic response of atoms to ultra-intense X-rays, Nature **466**(7302), 56–61 (2010).

[96] L. Young, E. P. Kanter, B. Krässig, Y. Li, a. M. March, S. T. Pratt, R. Santra, S. H. Southworth, N. Rohringer, L. F. DiMauro, G. Doumy, C. a. Roedig, N. Berrah, L. Fang, M. Hoener, P. H. Bucksbaum, J. P. Cryan, S. Ghimire, J. M. Glownia, D. a. Reis, J. D. Bozek, C. Bostedt, and M. Messerschmidt, Femtosecond electronic response of atoms to ultra-intense X-rays, Nature **466**(7302), 56–61 (2010).

[97] L. Müller, C. Gutt, B. Pfau, S. Schaffert, J. Geilhufe, F. Büttner, J. Mohanty, S. Flewett, R. Treusch, S. Düsterer, H. Redlin, A. Al-Shemmary, M. Hille, A. Kobs, R. Frömter, H. P. Oepen, B. Ziaja, N. Medvedev, S. K. Son, R. Thiele, R. Santra, B. Vodungbo, J. Lüning, S. Eisebitt, and G. Grübel, Breakdown of the X-Ray resonant magnetic scattering signal during intense pulses of extreme ultraviolet free-electron-laser radiation, Physical Review Letters **110**(23), 1–5 (2013).

[98] B. Wu, T. Wang, C. E. Graves, D. Zhu, W. F. Schlotter, J. J. Turner, O. Hellwig, Z. Chen, H. A. Dürr, A. Scherz, and J. Stöhr, Elimination of X-Ray Diffraction through Stimulated X-Ray Transmission, Phys. Rev. Lett. **117**, 027401 (Jul 2016).

[99] C. von Korff Schmising, B. Pfau, M. Schneider, C. Günther, M. Giovannella, J. Perron, B. Vodungbo, L. Müller, F. Capotondi, E. Pedersoli, et al., Imaging ultrafast demagnetization dynamics after a spatially localized optical excitation, Physical review letters **112**(21), 217203 (2014).

[100] S. Eisebitt, J. Lüning, W. Schlotter, M. Lörgen, O. Hellwig, W. Eberhardt, and J. Stöhr, Lensless imaging of magnetic nanostructures by X-ray spectro-holography, Nature **432**(7019), 885–888 (2004).

[101] B. Ziaja, R. A. London, and J. Hajdu, Unified model of secondary electron cascades in diamond, Journal of Applied Physics **97**(6) (2005).

[102] C. Weninger, M. Purvis, D. Ryan, R. A. London, J. D. Bozek, C. Bostedt, A. Graf, G. Brown, J. J. Rocca, and N. Rohringer, Stimulated electronic X-ray Raman scattering, Physical Review Letters **111**(23), 2–6 (2013).

[103] V. Kimberg, S. B. Zhang, and N. Rohringer, X-ray lasing in diatomic molecules, Journal of Physics: Conference Series **488**(1), 012025 (2014).

[104] S. Tanaka and S. Mukamel, X-ray four-wave mixing in molecules, Journal of Chemical Physics **116**(5), 1877–1891 (2002).

[105] S. Mukamel, Multidimensional Stimulated Resonant Raman X-ray Spectroscopy of Molecules, in *Research in Optical Sciences*, page IT1D.1, 2012.

[106] M. Hartmann and S. Mukamel, Four Wave Mixing Spectroscopy, **99**(August) (1993).

[107] P.M.Eisenberger and S. McCall, Mixing of X-Ray and Optical Photons, Physical Review A **3**(3), 1145–1150 (1971).

[108] I. Freund, Nonlinear X-ray diffraction. Determination of valence electron charge distributions, Chemical Physics Letters **12**(4), 583–588 (1972).

[109] I. Freund and B. F. Levine, Optically modulated X-ray diffraction, Physical Review Letters **25**(18), 1241–1245 (1970).

[110] T. E. Glover, D. M. Fritz, M. Cammarata, T. K. Allison, S. Coh, J. M. Feldkamp, H. Lemke, D. Zhu, Y. Feng, R. N. Coffee, M. Fuchs, S. Ghimire, J. Chen, S. Shwartz, D. A. Reis, S. E. Harris, and J. B. Hastings, X-ray and optical wave mixing., Nature **488**(7413), 603–8 (2012).

[111] S. Shwartz, R. N. Coffee, J. M. Feldkamp, Y. Feng, J. B. Hastings, G. Y. Yin, and S. E. Harris, X-ray parametric down-conversion in the Langevin regime, Physical Review Letters **109**(1) (2012).

[112] S. Shwartz, M. Fuchs, J. B. Hastings, Y. Inubushi, T. Ishikawa, T. Katayama, D. A. Reis, T. Sato, K. Tono, M. Yabashi, S. Yudovich, and S. E. Harris, X-ray second harmonic generation, Physical Review Letters **112**(16) (2014).

[113] F. Bencivenga, R. Cucini, F. Capotondi, A. Battistoni, R. Mincigrucci, E. Giangrisostomi, A. Gessini, M. Manfredda, I. P. Nikolov, E. Pedersoli, E. Principi, C. Svetina, P. Parisse, F. Casolari, M. B. Danailov, M. Kiskinova, and C. Masciovecchio, Four-wave mixing experiments with extreme ultraviolet transient gratings, Nature **520**(7546), 205–208 (2015).

[114] V. Kimberg and N. Rohringer, Stochastic stimulated electronic x-ray Raman spectroscopy, (2015).

[115] Z. Chen, D. Higley, M. Beye, M. Hantschmann, V. Mehta, O. Hellwig, A. Mitra, S. Bonetti, M. Bucher, S. Carron, et al., Ultrafast self-induced x-ray transparency and loss of magnetic diffraction, Physical review letters **121**(13), 137403 (2018).

[116] B. F. Murphy, J.-C. Castagna, J. D. Bozek, and N. Berrah, Mirror-based soft x-ray split-and-delay system for femtosecond pump-probe experiments at LCLS, in *X-Ray Free-Electron Lasers: Beam Diagnostics, Beamline Instrumentation, and Applications*, volume 8504, pages 850409–850409–7, 2012.

[117] K. Kunnus, I. Rajkovic, S. Schreck, W. Quevedo, S. Eckert, M. Beye, E. Suljoti, C. Weniger, C. Kalus, S. Grübel, M. Scholz, D. Nordlund, W. Zhang, R. W. Hartsock, K. J. Gaffney, W. F. Schlotter, J. J. Turner, B. Kennedy, F. Hennies, S. Techert, P. Wernet, and A. Föhlisch, A

setup for resonant inelastic soft x-ray scattering on liquids at free elec-
tron laser light sources, The Review of scientific instruments **83**(2012),
123109 (2012).

[118] C. Boeglin, E. Beaurepaire, V. Halté, V. López-Flores, C. Stamm, N. Pon-
tius, H. a. Dürr, and J.-Y. Bigot, Distinguishing the ultrafast dynamics
of spin and orbital moments in solids., Nature **465**(7297), 458–61 (2010).

[119] E. L. Saldin, E. A. Schneidmiller, and M. V. Yurkov, Self-amplified sponta-
neous emission FEL with energy-chirped electron beam and its application
for generation of attosecond x-ray pulses, Phys. Rev. ST Accel. Beams **9**,
050702 (May 2006).

[120] S. Schreck, M. Beye, J. A. Sellberg, T. McQueen, H. Laksmono,
B. Kennedy, S. Eckert, D. Schlesinger, D. Nordlund, H. Ogasawara, R. G.
Sierra, V. H. Segtnan, K. Kubicek, W. F. Schlotter, G. L. Dakovski, S. P.
Moeller, U. Bergmann, S. Techert, L. G. M. Pettersson, P. Wernet, M. J.
Bogan, Y. Harada, A. Nilsson, and A. F??hlisch, Reabsorption of soft
X-ray emission at high X-ray free-electron laser fluences, Physical Review
Letters **113**(15), 1–6 (2014).

[121] S. M. Vinko, U. Zastrau, S. Mazevet, J. Andreasson, S. Bajt, T. Burian,
J. Chalupsky, H. N. Chapman, J. Cihelka, D. Doria, T. Döppner,
S. Düsterer, T. Dzelzainis, R. R. Fäustlin, C. Fortmann, E. Förster,
E. Galtier, S. H. Glenzer, S. Göde, G. Gregori, J. Hajdu, V. Hajkova,
P. A. Heimann, R. Irsig, L. Juha, M. Jurek, J. Krzywinski, T. Laarmann,
H. J. Lee, R. W. Lee, B. Li, K.-H. Meiwes-Broer, J. P. Mithen, B. Nagler,
A. J. Nelson, A. Przystawik, R. Redmer, D. Riley, F. Rosmej, R. Sobiera-
jski, F. Tavella, R. Thiele, J. Tiggesbäumker, S. Toleikis, T. Tschentscher,
L. Vysin, T. J. Whitcher, S. White, and J. S. Wark, Electronic Structure
of an XUV Photogenerated Solid-Density Aluminum Plasma, Phys. Rev.
Lett. **104**, 225001 (Jun 2010).

[122] S. Yokojima, T. Meier, V. Chernyak, and S. Mukamel, Femtosecond four-
wave-mixing spectroscopy of interacting magnetoexcitons in semiconduc-
tor quantum wells, Physical Review B **59**(19), 12584–12597 (1999).

[123] D. Healion, J. D. Biggs, and S. Mukamel, Manipulating one- and two-
dimensional stimulated-x-ray resonant-Raman signals in molecules by

pulse polarizations, Physical Review A - Atomic, Molecular, and Optical Physics **86**(3), 1–15 (2012).

[124] A. Marinelli, D. Ratner, A. A. Lutman, J. Turner, J. Welch, F.-J. Decker, H. Loos, C. Behrens, S. Gilevich, and A. A. Miahnahri, High-intensity double-pulse X-ray free-electron laser, Nature communications **6**, 1–6 (2015).

[125] D. Ratner, R. Abela, J. Amann, C. Behrens, D. Bohler, G. Bouchard, M. Boyes, C. Bostedt, D. Cocco, F. J. Decker, Y. Ding, C. Eckman, P. Emma, D. Fairley, Y. Feng, C. Field, G. Gassner, J. Hastings, N. Kelez, P. Heimann, Z. Huang, J. Krzywinski, H. Loos, A. Lutman, A. Marinelli, G. Marcus, T. Maxwell, P. Montanez, S. Moeller, D. Morton, N. Rodes, W. Schlotter, S. Serkez, T. Stevens, J. Turner, D. Walz, J. Welch, and J. Wu, Experimental Demonstration of a Soft X-Ray Self-Seeded Free-Electron Laser, Physical Review Letters **114**(5), 1–7 (2015).

[126] H. N. Chapman, A. Barty, M. J. Bogan, S. Boutet, M. Frank, S. P. Hau-Riege, S. Marchesini, B. W. Woods, S. Bajt, W. H. Benner, et al., Femtosecond diffractive imaging with a soft-X-ray free-electron laser, Nature Physics **2**(12), 839–843 (2006).

[127] M. Beye, S. Schreck, F. Sorgenfrei, C. Trabant, N. Pontius, C. Schüßler-Langeheine, W. Wurth, and A. Föhlisch, Stimulated X-ray emission for materials science, Nature **501**(7466), 191–194 (2013).

[128] S. Gerber, S.-L. Yang, D. Zhu, H. Soifer, J. Sobota, S. Rebec, J. Lee, T. Jia, B. Moritz, C. Jia, et al., Femtosecond electron-phonon lock-in by photoemission and x-ray free-electron laser, Science **357**(6346), 71–75 (2017).

[129] N. Rohringer, D. Ryan, R. A. London, M. Purvis, F. Albert, J. Dunn, J. D. Bozek, C. Bostedt, A. Graf, R. Hill, et al., Atomic inner-shell X-ray laser at 1.46 nanometres pumped by an X-ray free-electron laser, Nature **481**(7382), 488–491 (2012).

[130] C. Weninger, M. Purvis, D. Ryan, R. A. London, J. D. Bozek, C. Bostedt, A. Graf, G. Brown, J. J. Rocca, and N. Rohringer, Stimulated electronic x-ray Raman scattering, Physical review letters **111**(23), 233902 (2013).

[131] H. Yoneda, Y. Inubushi, M. Yabashi, T. Katayama, T. Ishikawa, H. Ohashi, H. Yumoto, K. Yamauchi, H. Mimura, and H. Kitamura, Saturable absorption of intense hard X-rays in iron, Nature communications **5**(1), 1–5 (2014).

[132] S. Shwartz, R. Coffee, J. Feldkamp, Y. Feng, J. Hastings, G. Yin, and S. Harris, X-ray parametric down-conversion in the Langevin regime, Physical review letters **109**(1), 013602 (2012).

[133] H. Statz and G. DeMars, Transients and oscillation pulses in masers, in *Quantum electronics*, page 530, 1960.

[134] C. Hantschmann, P. P. Vasil'ev, S. Chen, M. Liao, A. J. Seeds, H. Liu, R. V. Penty, and I. H. White, Gain switching of monolithic 1.3 μm InAs/GaAs quantum dot lasers on silicon, journal of lightwave technology **36**(18), 3837–3842 (2018).

[135] M. Sugawara, H. Ebe, N. Hatori, M. Ishida, Y. Arakawa, T. Akiyama, K. Otsubo, and Y. Nakata, Theory of optical signal amplification and processing by quantum-dot semiconductor optical amplifiers, Physical Review B **69**(23), 235332 (2004).

[136] Y.-P. Sun, J.-C. Liu, C.-K. Wang, and F. Gel'mukhanov, Propagation of a strong x-ray pulse: Pulse compression, stimulated Raman scattering, amplified spontaneous emission, lasing without inversion, and four-wave mixing, Phys. Rev. A **81**, 013812 (Jan 2010).

[137] N. Rohringer and R. London, Atomic inner-shell x-ray laser pumped by an x-ray free-electron laser, Phys. Rev. A **80**, 013809 (Jul 2009).

[138] C. Weninger and N. Rohringer, Stimulated resonant x-ray Raman scattering with incoherent radiation, Phys. Rev. A **88**, 053421 (Nov 2013).

[139] K. Hatada and A. Di Cicco, Modeling saturable absorption for ultra short X-ray pulses, Journal of Electron Spectroscopy and Related Phenomena **196**, 177–180 (2014).

[140] K. Hatada and A. Di Cicco, Modeling Non-Equilibrium Dynamics and Saturable Absorption Induced by Free Electron Laser Radiation, Applied Sciences **7**(8), 814 (2017).

[141] J. Carroll, J. Whiteaway, and D. Plumb, *Distributed feedback semiconductor laser*, 1999.

[142] B. D. Patterson and /SLAC, Resource Letter on Stimulated Inelastic X-ray Scattering at an XFEL, (9 2010).

[143] A. Nilsson, J. Stöhr, T. Wiell, M. Aldén, P. Bennich, N. Wassdahl, M. Samant, S. Parkin, N. Mårtensson, J. Nordgren, et al., Determination of the electronic density of states near buried interfaces: Application to Co/Cu multilayers, Physical Review B **54**(4), 2917 (1996).

[144] B. Wu, T. Wang, C. Graves, D. Zhu, W. Schlotter, J. Turner, O. Hellwig, Z. Chen, H. Dürr, A. Scherz, et al., Elimination of x-ray diffraction through stimulated x-ray transmission, Physical review letters **117**(2), 027401 (2016).

[145] J. Stöhr and A. Scherz, Creation of x-ray transparency of matter by stimulated elastic forward scattering, Physical review letters **115**(10), 107402 (2015).

[146] D. J. Higley, A. H. Reid, Z. Chen, L. Le Guyader, O. Hellwig, A. A. Lutman, T. Liu, P. Shafer, T. Chase, G. L. Dakovski, et al., Femtosecond X-ray induced changes of the electronic and magnetic response of solids from electron redistribution, Nature communications **10** (2019).

[147] B. Ziaja, A. Szöke, D. van der Spoel, and J. Hajdu, Space-time evolution of electron cascades in diamond, Physical Review B **66**(2), 024116 (2002).

[148] S. Schreck, M. Beye, and A. Föhlisch, Implications of stimulated resonant X-ray scattering for spectroscopy, imaging, and diffraction in the regime from soft to hard X-rays, Journal of Modern Optics **62**(sup2), S34–S45 (2015).

[149] T. Andreev, I. Barke, and H. Hövel, Adsorbed rare-gas layers on Au (111): Shift of the Shockley surface state studied with ultraviolet photoelectron spectroscopy and scanning tunneling spectroscopy, Physical Review B **70**(20), 205426 (2004).

[150] J. Li, W.-D. Schneider, S. Crampin, and R. Berndt, Tunnelling spectroscopy of surface state scattering and confinement, Surface science **422**(1-3), 95–106 (1999).

[151] S. Hüfner, *Photoelectron spectroscopy: principles and applications*, Springer Science & Business Media, 2013.

[152] E. Bertel and M. Donath, *Electronic surface and interface states on metallic systems*, World Scientific, 1995.

[153] C. T. Chen, Y. U. Idzerda, H.-J. Lin, N. V. Smith, G. Meigs, E. Chaban, G. H. Ho, E. Pellegrin, and F. Sette, Experimental Confirmation of the X-Ray Magnetic Circular Dichroism Sum Rules for Iron and Cobalt, Phys. Rev. Lett. **75**, 152–155 (Jul 1995).

[154] J. Dvorak, I. Jarrige, V. Bisogni, S. Coburn, and W. Leonhardt, Towards 10 meV resolution: The design of an ultrahigh resolution soft X-ray RIXS spectrometer, Review of Scientific Instruments **87**(11), 115109 (2016).

[155] M. M. Sala, C. Henriquet, L. Simonelli, R. Verbeni, and G. Monaco, High energy-resolution set-up for Ir L3 edge RIXS experiments, Journal of Electron Spectroscopy and Related Phenomena **188**, 150–154 (2013).